Problèmes direct et inverse de diffraction des ondes en milieu stratifié : du domaine des basses fréquences à la résonance

Marc Lambert

Université de Paris-Sud **UFR Scientifique d'Orsay**

Habilitation à Diriger des Recherches

présentée par

Marc Lambert

Sujet:

Problèmes direct et inverse de diffraction des ondes en milieu stratifié : du domaine des basses fréquences à la résonance

Soutenue le 19 décembre 2001

Président :	Jean-Charles Bolomey, Professeur des universités
Rapporteurs :	Mario Bertero, Professeur en sciences de l'information Marc Saillard, Professeur des universités Armand Wirgin, Directeur de recherche CNRS
Examinateurs :	Mathias Fink, Professeur des universités Dominique Lesselier, Directeur de recherche CNRS Dominique Placko, Professeur des universités

Laboratoire des Signaux et Systèmes, CNRS - Supélec - UPS

Remerciements

Je tiens en premier lieu à remercier respectivement P. Bertrand et G. Demoment, directeurs successifs du Laboratoire des Signaux et Systèmes où le travail présenté ici s'est déroulé.

Je tiens à exprimer ma profonde reconnaissance à D. Lesselier, Directeur de recherche au CNRS pour nos discussions sans cesse renouvelées sur des sujets divers et variés, ce travail lui devant plus que beaucoup. Qu'il trouve ici mon admiration la plus sincère.

Mes plus vifs remerciements vont à Monsieur M. Bertero, Professeur en Sciences de l'Information à l'université de Gênes, Monsieur M. Saillard, Professeur des universités à l'université de Provence et Monsieur A. Wirgin, Directeur de recherche au CNRS pour avoir accepté d'être les rapporteurs de ce travail. Je remercie également Messieurs J.-Ch. Bolomey, Professeur des universités à l'université Paris-Sud, M. Fink, Professeur des universités à l'université Denis Diderot et D. Placko, Professeur des universités à l'École Nationale Supérieure de Cachan de m'avoir fait l'honneur de participer à ce jury.

Je ne peux oublier l'ensemble des membres du laboratoire, stagiaires, doctorants et permanents, tant pour l'aide qu'ils m'ont apportée tout au long de ces années que pour les discussions intenses tenues autour d'une tasse de café ou de thé.

En tout premier lieu ceux avec qui j'ai directement travaillé, E. Bocly, B. Duchêne, J.-M. Geffrin, D. Martinez, G. Perrusson et C. Ramananjaona. Une mention spéciale à D. Dos Reis, premier doctorant dont j'ai suivi les travaux au jour le jour. Qu'il soit remercié pour sa patience devant mes demandes et sa capacité de travail pour y répondre.

Mes remerciements vont également aux autres membres du laboratoire et d'abord aux « anciens » déjà présents lors de ma thèse, F. Brouaye, L. Frémy, M. Hélier, A. Joisel, F. Jouvie, D. Lecointe, V. Monebhurrun, D. Picard et H. Roussel, auxquels se rajoutent les petits « nouveaux », N. Ribière Tharaud et A. Sangiovanni. Une mention spéciale également pour W. Tabbara dont les conseils pour la rédaction et la présentation de ce manuscrit ansi que sa correction m'ont été d'une aide précieuse.

Puis-je oublier les thésards, stagiaires, post-doctorant ou chercheur confirmé (D. de Badereau, V. Bertrand, L. Casavola, S. Deshayes, O. Merckel, B. Pliquet et A. Zyyiat) qui ont eu la chance de ne pas travailler directement avec moi mais grâce à qui l'ambiance de travail n'en a été que meilleure. Qu'ils en soient ici remerciés.

Rédiger de tels remerciements conduit nécessairement à des oublis, je ne doute pas qu'en les relisant d'ici quelques jours ou quelques semaines je m'aperçoive qu'il manque tel ou tel nom. Que celui ou celle qui sera victime de cet oubli veuille bien m'en excuser.

Propos liminaires

Les travaux présentés dans ce mémoire ont tous été effectués au sein du Laboratoire des Signaux et Systèmes (L2S) — aujourd'hui Unité Mixte du CNRS, de Supélec et de l'Université Paris-Sud — et plus particulièrement au sein de son Département de Recherche en Électromagnétisme (DRÉ) qui regroupe la Division Ondes du L2S et le Service Électromagnétisme de Supélec.

Ce manuscrit est divisé en trois parties :

- La première décrit de manière succincte mon parcours dans la recherche en présentant un bref CV, les encadrements de thèses, de stages de DEA, les enseignements et les collaborations auxquelles je participe ou ai participé ainsi que les participations à l'organisation de manifestations scientifiques.
- La deuxième présente les travaux effectués au L2S depuis mon entrée au CNRS ; les fils directeurs du manuscrit sont la résolution du problème inverse de diffraction des ondes et du problème direct qui lui est associé. Cette partie est divisée en deux chapitres traitant respectivement du problème bidimensionnel et du problème tridimensionnel. Dans chacun des chapitres plusieurs méthodes de résolution du problème direct et du problème inverse sont présentées, chacune décrite par un texte rappelant le contexte de la recherche et ses grandes lignes et chacune illustrée par un résultat extrait d'un article publié ou soumis.
- La troisième partie présente une sélection d'articles (publiés ou soumis) illustrant dans le détail ces méthodes, ces articles étant, comme de nécessaire, introduits dans la deuxième partie.

Première partie

Dossier Individuel

1

Curriculum vitae détaillé

Sommaire

1.1 Curriculum vitae

Marc LAMBERT
Courriel : marc.lambert@lss.supelec.fr

Né le 16 octobre 1966
Nationalité française

FORMATION UNIVERSITAIRE

1991/1993	**DOCTORAT EN SCIENCES**, Université Paris-Sud (Orsay) Spécialité : Optique et Photonique
1990	**D.E.A. D'OPTIQUE ET PHOTONIQUE**, Université Paris-Sud (Orsay), Mention Bien
1989	**MAÎTRISE DE PHYSIQUE FONDAMENTALE**, Université Paris-Sud (Orsay), Mention Assez Bien

EXPÉRIENCES PROFESSIONNELLES

Octobre 1995-	**CHARGÉ DE RECHERCHE CNRS**, Département de Recherche en Électromagnétisme, Laboratoire des Signaux et Systèmes (CNRS-Supélec-UPS) *Problèmes d'interaction ondes/structures et ondes/matériaux*

1995 (9 mois)	**INGÉNIEUR DE RECHERCHE**, Post-Doctorant, Bureau de Recherche Géologique et Minière (BRGM), Direction de la Recherche (Département Géophysique et Imagerie Géologique), Orléans *Modélisation numérique de problèmes électromagnétiques 3-D. Application à la géophysique de prospection.*
1993/1994	**ATTACHÉ TEMPORAIRE D'ENSEIGNEMENT ET DE RECHERCHE**, ATER, Université Paris-Sud (Orsay, Département de Physique) *Enseignements de physique générale en DEUG. Recherche effectuée au Laboratoire des Signaux et Systèmes (CNRS-Supélec-UPS).* Poursuite de la recherche effectuée lors de la thèse
1990/1993	**ALLOCATAIRE DE RECHERCHE**, Doctorant, Laboratoire des Signaux et Systèmes (CNRS-Supélec-UPS) *Thèse sous la direction de D. Lesselier (Directeur de Recherche CNRS). Développement d'algorithmes de résolution des problèmes direct et inverse de diffraction des ondes. Application à la caractérisation acoustique de fonds marins.*
1993 (3 mois)	**"SUMMER RESEARCH ASSISTANT"**, SACLANT Undersea Research Centre, Laboratoire de l'OTAN (Italie) *Travaux sous la direction de P. Gerstoft (Senior Scientist). Séjour effectué dans le cadre de la thèse. Mise au point et validation d'un algorithme génétique d'inversion développé à SACLANT à partir de données synthétiques et expérimentales.*
1991/1993	**MONITEUR DE L'ENSEIGNEMENT SUPÉRIEUR**, IUT Paris-Sud (Département de Mesures Physiques) *Enseignements de Physique. Service d'enseignement effectué en parallèle avec la thèse.*

ENSEIGNEMENT

depuis 2001	– 3 heures annuelles de cours en formation continue à Supélec : « Méthodes modernes de l'électromagnétisme » sur le problème inverse – 50 h de TD de physique générale en première année de DUT à l'IUT de Ville-d'Avray (Université Paris X (Nanterre))
depuis 1997	3 heures annuelles de cours en formation continue à Supélec : « Méthodes modernes de l'électromagnétisme » sur le problème direct
depuis 1996	10 heures annuelles de cours au DEA Méthodes Physiques en Télédétection (Université Denis Diderot *et al*) : « Obstacles et cibles »
1993/1994	**ATTACHÉ TEMPORAIRE D'ENSEIGNEMENT ET DE RECHERCHE**, ATER, Université Paris-Sud (Orsay, Département de Physique) *192 h d'enseignements de physique générale en 1ère année de DEUG.*
1991/1993	**MONITEUR DE L'ENSEIGNEMENT SUPÉRIEUR**, IUT Paris-Sud (Département de Mesures Physiques) *96 h annuelles d'enseignements de Physique (optique) en 1ère et 2ème année de DUT.*

DOMAINES DE COMPÉTENCE

ONDES ÉLECTROMAGNÉTIQUES OU ACOUSTIQUES

- Interaction ondes/structures et ondes/matériaux, diffraction des ondes par des configurations complexes 3-D
- Propagation des ondes dans des milieux complexes
- Problèmes directs et inverses de diffraction des ondes, méthodes intégrales
- Caractérisation électromagnétique ou acoustique de matériaux
- Contrôle non-destructif
- Imagerie électromagnétique ou ultrasonore

MODÉLISATION ET SIMULATION NUMÉRIQUES

ANALYSE NUMÉRIQUE

- Algorithmes d'optimisation locaux/globaux/stochastiques
- Méthodes de Moments
- Méthodes asymptotique et modale

INFORMATIQUE

- Langages de programmation : Fortran 77 et 90, C
- Systèmes d'exploitation : Unix, Macintosh

PUBLICATIONS (au 01/10/2001)

- 1 chapitre de livre
- 6 articles dans des actes de congrès édités (dont 1 soumis)
- 14 articles dans des revues avec comités de lecture (dont 2 à paraître et 1 soumis)
- 29 communications avec actes et comités de lecture
- 12 communications sans actes
- 1 rapport SACLANT (OTAN), 1 rapport de contrat (3 ans) DRET-DGA et 1 rapport de contrat (3 ans) CNRS-Supélec-BRGM

DIVERS

- Encadrement de stages de DEA (4)
- Participation à l'encadrement de thèses (deux en cours et une soutenue en 1999) et co-encadrement d'une thèse (soutenance le 6 décembre 2001)

	– Participation à un contrat de collaboration de recherche CNRS-BRGM (1996/1999), une Action Intégrée Franco-Hellénique PLATON (L2S-ICEHT/FORTH (1997/1998)) et une Action Intégrée Franco-Néerlandaise VAN GOGH (L2S-TUE/TTE (2001/..))
	– Rapporteur de 8 articles pour l'Institute of Physics Publishing (Journal of Physics D : Applied Physics, Inverse Problems), l'American Geophysical Union (Radio Science), l'Acoustical Society of America (Journal of the Acoustical Society of America (JASA)) et l'Institute of Electrical and Electronics Engineers (IEEE Transactions on Antennas and Propagation)
depuis novembre 2001	Membre suppléant de la Commission de Spécialistes 61/63ème section de l'Université Pierre et Marie Curie
1998/2001	Membre titulaire de la Commission de Spécialistes 61/63ème section de l'Université Pierre et Marie Curie
1998/2001	Membre suppléant de la Commission de Spécialistes 61/63ème section de l'Université Versailles Saint-Quentin-en-Yvelines.

1.2 Encadrements

Thèse

- G. Perrusson (octobre 1996 - octobre 1999), thèse effectuée au L2S, participation à l'encadrement avec D. Lesselier et B. Duchêne, « Caractérisation électromagnétique d'objets conducteurs enfouis. Application à la prospection géophysique. »
- D. Martinez, thèse effectuée à l'ONERA, participation à l'encadrement avec D. Lesselier pour le L2S et M. Lemistre pour l'ONERA, caractérisation de milieux anisotropes.
- D. Dos Reis (soutenance 6 décembre 2001), thèse effectuée au L2S, co-encadrement avec D. Lesselier, « Évaluation électromagnétique en régime diffusif de défauts et objets 3D enfouis : du modèle d'interaction à l'inversion de données ».
- C. Ramananjaona (octobre 1999 - octobre 2002), thèse effectuée au L2S, co-encadrement avec D. Lesselier (L2S) et la participation de J.-P. Zolésio, applications des ensembles de niveaux au contrôle non destructif.

Stage de DEA

- G. Perrusson (1996), DEA Méthodes Physiques en Télédétection, Université Denis Diderot (Paris VII), avec D. Lesselier et B. Duchêne, « Détection par induction électromagnétique d'objets conducteurs enfouis. Application à la prospection géophysique. »
- E. Bocly (1996), DEA Acoustique Physique, Université Denis Diderot (Paris VII), avec D. Lesselier, « Caractérisation d'objets cylindriques placés dans un guide d'ondes acoustique modélisant une situation de petits fonds marins. »
- D. Dos Reis (1998), DEA Méthodes Physiques en Télédétection, Université Denis Diderot (Paris VII), « Reconstruction en polarisation H d'objets enfouis. Application de l'approximation de Born. »

– C. Ramananjaona (1999), DEA Mathématiques de la Modélisation, Simulation et Application de la Physique, Université Versailles-Saint-Quentin-en-Yvelines, avec D. Lesselier, « Évaluation non destructive d'anomalies par méthode d'évolution contrôlée. »

Practical Training Agreement

– F. Müller (1998), Universität Gesamthochschule Kassel, avec D. Lesselier, « Vergleich verschiedener Approximationen des Reflexionsfaktors an einer inhomogenen Schicht. »

1.3 Enseignement

Moniteur de l'Enseignement Supérieur (1991-1993)

J'ai effectué en tant que moniteur et pendant deux années un service de 96 heures annuelles de Travaux Pratiques d'Optique au Département de Mesures Physiques (Institut Universitaire de Technologie de Paris-Sud) sous la direction de L. Leger (1ère année) et M. Gadenne (2ème année). Ces TP étaient divisés en une partie « rappels de cours » d'un quart d'heure à une demi-heure suivie de la partie « pratique » et ont porté, dans un premier temps, sur l'Optique Géométrique (relation de Snell-Descartes, le prisme, la lunette de Galilée et le microscope,...), puis, dans un deuxième temps sur l'Optique Ondulatoire (la diffraction de Fraunhoffer, le filtrage cohérent,...). J'ai eu, par ailleurs, la charge de la rédaction et de la correction des examens de TP.

J'ai également suivi pendant ces deux ans les stages de formation à l'Enseignement Supérieur dispensés par le Centre d'Initiation à l'Enseignement Supérieur sous la direction de B. Gatty et G. Torchet. En deuxième année et sur la demande de B. Gatty, j'ai participé à la formation des moniteurs de première année en tant qu'animateur-participant à une réunion de témoignages sur le monitorat.

Attaché Temporaire d'Enseignement et de Recherche (1993-94)

Nommé Attaché Temporaire d'Enseignement et de Recherche (A.T.E.R.) au Département de Physique (Université de Paris-Sud), mon enseignement s'est divisé en deux services parallèles :

– sous la direction de G. Rouanette, un enseignement de physique de 1ère année de DEUG B. J'ai encadré 2 groupes de Travaux Dirigés (42 h) et 3 groupes de TP (27 h). Le programme porte sur les Ondes (ondes propagatives et stationnaires, interférence, diffraction et effet Doppler), la Mécanique Quantique (atome de Bohr, dualité onde-corpuscule, ...) et la Physique Statistique (libre parcours moyen, ...). J'ai eu la charge de la rédaction d'un TD, de la rédaction et de la correction de deux interrogations comptant pour 50% de la note finale et de la correction du partiel final.
– sous la direction de J.-P. Chevillard, un encadrement en 1ère année de DEUG A. Il s'est agit d'encadrer les étudiants de l'option Mécanique et Programmation (durée 15 semaines à raison de 4 h/semaine par groupe de 15 étudiants). Dans cette option les étudiants ont réalisé deux expériences de mouvement dans un champ de force centrale sur table soufflante, la première à l'aide d'un ressort de longueur à vide presque nulle et la deuxième à l'aide d'un ressort de longueur à vide non nulle. Les points des trajectoires sont agrandis puis mesurés. La partie programmation sert à développer un programme en Pascal qui, à l'aide des mesures, permet la vérification des lois de la mécanique dans un champ de force centrale et, lorsque c'est possible, la détermination du coefficient de frottement à l'aide d'une théorie simplifiée.

Vacations (depuis 1996)

Je poursuis ma participation à l'enseignement sous forme de vacations.

- En DEA (Université Denis Diderot *et al.*)
  J'assure, depuis octobre 1996, une charge de cours dans le tronc commun du DEA de Méthodes Physiques en Télédétection (Université Denis Diderot *et al.*) qui dépend de l'École Doctorale des Sciences de l'Environnement de l'Ile de France. Ce module intitulé « Obstacles et cibles », d'une durée de 10 heures, a pour but de donner aux étudiants les bases nécessaires à la formulation et la résolution des problèmes de diffraction des ondes électromagnétiques. Ce cours a nécessité la rédaction d'un polycopié de plus de 60 pages et la rédaction et la correction chaque année d'un examen.
- Formation continue (Supélec)
  J'assure également, sur le même sujet et depuis 1997, 3 heures de cours dans une session de formation continue de Supélec intitulée « Les méthodes modernes de l'électromagnétisme et leurs applications » qui a nécessité la rédaction de près de 80 transparents, auxquels s'ajoute depuis 2001 3 heures de cours sur les problèmes inverses.
- En DUT (Université de Nanterre)
  J'assure depuis septembre 2001 une charge d'enseignement de 50 h de travaux dirigés de physique générale en première année de DUT à l'IUT Ville-d'Avray (qui dépend de l'Université de Nanterre (Paris X)). J'encadre un groupe de 25 étudiants. Le programme porte sur l'électrostatique, la magnétostatique et la mécanique dont il s'agit de présenter le cadre théorique et les équations s'y rattachant puis de les illustrer par des exemples.

1.4 Collaborations

Une partie significative de mes travaux s'est déroulée dans le cadre de contrats industriels et des actions intégrées qui ont permis des échanges fructueux avec des chercheurs français et étrangers, échanges qui se poursuivent à l'heure actuelle.

- **Contrat de collaboration de recherche CNRS-BRGM (1996-1999)** : ce contrat passé entre le BRGM et le CNRS a été établi après mon passage au BRGM en tant que post-doctorant en 1995. Son but était la poursuite des recherches déjà entamées sur l'inversion d'objets tridimensionnels en basse fréquence pour des applications de géophysique de prospection, recherche notamment approfondie lors de la thèse de G. Perrusson.
- **Action Intégrée Franco-Hellénique (PLATON) L2S-ICEHT-FORTH (1997-1999)** : cette collaboration entre le Laboratoire des Signaux et Systèmes et le Département de Mathématiques Appliquées de l'ICEHT-FORTH Patras a permis d'élaborer de nouvelles méthodes semi-analytiques de calcul du champ diffracté par un ellipsoïde enfoui dans un espace conducteur avec, ici encore, des applications de géophysique de prospection.
- **Contrat de collaboration de recherche CNRS-ONERA (Déc. 1997 - Déc 2000)** : cette collaboration porte sur la caractérisation de milieux stratifiés anisotropes, travail effectué notamment par D. Martinez lors de sa thèse à l'ONERA, thèse à l'encadrement de laquelle j'ai participé.
- **Programme de Recherche en Commun CNRS-NSF (1998-2000) (LMA-L2S-CMW)** : cette collaboration entre le Laboratoire de Mécanique et d'Acoustique de Marseille (en particulier les équipes Propagation et Imagerie (PI) et Acoustique Sous-Marine et Modélisation (ASM2)), le L2S et le Center of the Mathematics of Waves de l'Université du Delaware avait pour but l'identification par ondes acoustiques diffractées d'un objet dans une mer peu profonde.

- **Action Intégrée Franco-Néerlandaise (VAN GOGH) L2S-TUE-TTE (2001-)** : cette collaboration, qui a débuté en janvier 2001, avec l'Université d'Eindhoven porte sur l'évaluation non-destructive d'objets complexes enfouis dans des milieux complexes tant du point de vue modélisation, avec le développement de codes numériques, que du point de vue technique, avec le développement de prototypes expérimentaux de systèmes complexes d'imagerie.
- **VERDICT (Virtual Evaluation and Robust Detection for engIne Component non destructive Testing)** : Supélec (par l'intermédiaire du LGEP et du L2S) est part d'un projet RTD de l'Union Européenne, projet déposé en mars 2001 et retenu sur la liste complémentaire (décision de financement en attente). Ce projet regroupe 13 partenaires industriels (Snecma, Rolls-Royce, Turboméca, ...) et académiques (Université de Liège, City University, Supélec, ...). L'accent est mis sur les améliorations à apporter à l'évaluation non destructive de défauts dans des structures complexes (notamment les moteurs d'avions) et ce afin d'assurer une meilleure sécurité à moindre coût. Les quatre techniques majeures sont concernées (rayons X, Ultrasons, courants de Foucault et thermographie infrarouge). Pour sa part Supélec n'est impliqué que dans la partie concernant les courants de Foucault.

1.5 Participation à l'organisation de congrès scientifiques

Participation à l'organisation du congrès ISEM 2003 (International Symposium on Applied Electromagnetics and Mechanics) qui se tiendra à Versailles en mai 2003, congrès organisé sous la présidence de D. Lesselier (L2S) et A. Razek (LGEP). J'ai été choisi pour être l'un des deux secrétaires scientifiques de cette organisation, le second étant L. Pichon du LGEP ; environ 250 personnes sont attendues.

1.6 Divers

- Commission de Spécialistes : membre titulaire (1998-2001) puis suppléant (depuis novembre 2001) de la commission de spécialistes (61/63ème section) de l'université Pierre et Marie Curie et membre suppléant de la commission de spécialistes (61/63ème section) de l'université Versailles Saint-Quentin-en-Yvelines de 1998 à 2001.
- Rapporteur de 8 articles pour l'Institute of Physics Publishing (Journal of Physics D : Applied Physics, Inverse Problems), l'American Geophysical Union (Radio Science), l'Acoustical Society of America (Journal of the Acoustical Society of America (JASA)) et l'Institute of Electrical and Electronics Engineers (IEEE Transactions on Antennas and Propagation).

2

Liste de publications

Sont référencées ici les publications dont je suis auteur ou co-auteur avec le classement privilégié par le CNRS, T pour les thèses, L4 pour les chapitres de livre, L5 pour les articles dans des actes de congrès édités, A pour les articles dans des revues internationales avec comité de lecture, C pour les communications dans des congrès internationaux avec actes, CS pour les communications dans des congrès sans actes et RC pour les rapports de contrat. À cette dénomination se rajoute un numéro correspondant au numéro d'apparition dans cette liste de la publication (e.g., A.7 signifiant le 7ème article publié dans une revue internationale avec comité de lecture).

Thèse

[T.1] Marc Lambert, *Caractérisation de milieux plans stratifiés par sources localisées. Application au diagnostic acoustique du fond sous-marin*, Thèse de Doctorat, Université Paris-Sud (Orsay), 21 janvier 1994, Jury : G. Quentin, Professeur, Université Denis Diderot (président) ; M. Bruneau, Professeur, Université du Maine et P. Gerstoft, Senior Scientist, Saclant Centre (rapporteurs) ; J.-Ch. Bolomey, Professeur, Université Paris-Sud ; B. Duchêne, Chargé de Recherche CNRS ; D. Lesselier, Directeur de Recherche CNRS ; B. Poirée, Ingénieur, DRET/SDR.

Chapitre de livre

[L4.1] Bernard Bourgeois, Dominique Legendre, Marc Lambert et Grant Hendrickson, ARLETT : A Prototype Three-Component Borehole Electromagnetic System, M. L. Oristaglio et B. R. Spies (eds.), *Three-Dimensional Electromagnetics*, pp. 625–657, Society of Exploration Geophysicists (SEG), 1999.

Articles dans des actes de congrès édités

[L5.1] Marc Lambert, Peter Gerstoft, Andréa Caiti et Ralf Ambjørnsen, Estimation of bottom parameters from real data by genetic algorithms, O. Diachok, A. Caiti, P. Gerstoft et H. Schmidt (eds.), *Full Field Inversion Methods in Ocean and Seismic Acoustics*, pp. 159–164, Dordrecht, 1995, Kluwer Academic Publ., NATO Conference, Lerici, juin 1994.

[L5.2] Ralph E. Kleinman, Peter M. van den Berg, Bert Jan Kooij, Bernard Duchêne, Dominique Lesselier et Marc Lambert, Multifrequency version of the modified gradient algorithm for reconstruction of complex refractive indices, R. L. Barbour, M. J. Carvlin et M. A. Fiddy (eds.), *Computational, Experimental, and Numerical Methods for Solving Ill-Posed Inverse Imaging Problems : Medical and Nonmedical Applications*, pp. 76–87, Bellingham, 1997, SPIE.

[L5.3] Eric Bocly, Marc Lambert, Christophe Rozier et Dominique Lesselier, Optimal contour reconstruction of a sound-hard obstacle in a shallow water acoustic waveguide, A. Alippi et G. B. Cannelli (eds.), *Underwater Acoustics*, pp. 643–648, Rome, 1998, CNR-IDAC.

[L5.4] Bernard Duchêne, Marc Lambert et Dominique Lesselier, On the characterization of objects using rigorous inversion methods, M. Taroudakis et G. Makrakis (eds.), *Inverse Problems in Underwater Acoustics*, Lecture Notes in Physics, pp. 127–147, Berlin, 2001, Springer.

[L5.5] Daniel Dos Reis, Marc Lambert et Dominique Lesselier, On the modeling and inversion of 3-D inclusions in conductive media using extended Born models in the diffusive regime, T. Takagi et M. Uesaka (eds.), *Applied Electromagnetics and Mechanics*, JSAEM Studies in Applied Electromagnetics and Mechanics, pp. 481–482, Tokyo, mai 2001.

Soumis

[L5.6] Daniel Dos Reis, Marc Lambert et Dominique Lesselier, Eddy-current evaluation of 3-D defects in a metal plate, a first analysis of a contrast-source gradient method, F. Kojima (ed.), *Electromagnetic Non-Destructive Evaluation (V)*, Studies in Applied Electromagnetics and Mechanics, Amsterdam, 2002, *submitted*, IOS Press.

Articles dans des revues internationales à comité de lecture

[A.1] Marc Lambert et Dominique Lesselier, On the retrieval of the plane wave reflection coefficient of a seabed in shallow water, *Acta Acustica*, 3, 243–249, 1995.

[A.2] Marc Lambert, Rodrigo de Oliveira Bohbot et Dominique Lesselier, Born-type schemes for the acoustic probing of 1-D fluid media from time-harmonic planar reflection coefficients at two incidences, *J. Acoust. Soc. Am.*, 95, 243–253, 1996.

[A.3] Marc Lambert, TE scattering by cylindrical dielectric obstacle buried in half-space : a H-field-based solution method, *J. Electromagn. Waves Applic.*, 12, 1217–1239, 1998.

[A.4] Marc Lambert, Dominique Lesselier et Bert Jan Kooij, The retrieval of a buried cylindrical obstacle by a constrained modified gradient method in the H-polarization case and for Maxwellian materials, *Inverse Problems*, 14, 1265–1283, 1998, Featured article (for a semester, in the Journal Information Page for Inverse Problems of the WWW site of the Institute of Physics).

[A.5] Bert Jan Kooij, Marc Lambert et Dominique Lesselier, Non-linear inversion of a buried object in transverse electric scattering, *Radio Science*, 34, 1361–1371, 1999.

[A.6] Marc Lambert et Dominique Lesselier, Distributed source method for retrieval of the cross-sectional contour of an impenetrable cylindrical obstacle immersed in a shallow water waveguide, *ACUSTICA - Acustica united with Acta Acustica*, 86, 15–24, 2000.

[A.7] Gaële Perrusson, Marc Lambert, Dominique Lesselier, Antonis Charalambopulos et George Dassios, Electromagnetic scattering by a tri-axial homogeneous penetrable ellipsoid : low-frequency derivation and testing of the localized nonlinear approximation, *Radio Science*, 35, 463–481, 2000.

[A.8] Marc Lambert et Dominique Lesselier, Binary-constrained inversion of a buried cylindrical obstacle from complete and phaseless magnetic field, *Inverse Problems*, 16, 563–576, 2000.

[A.9] Gaële Perrusson, Dominique Lesselier, Marc Lambert, Bernard Bourgeois, Antonis Charalambopoulos et George Dassios, Conductive masses in a half-space Earth in the diffusive regime : Fast hybrid modeling of a low-contrast ellipsoid, *IEEE Trans. Geoscie. Remote Sensing (Special Issue on Computational Wave Issues in Remote Sensing, Imaging and Target Identification, Propagation and Inverse Scattering)*, 38, 1585–1599, 2000, Présélectionné à l'issue de l'URSI International Symposium on Electromagnetic Theory, Salonique, 1998.

[A.10] Christophe Ramananjaona, Marc Lambert, Dominique Lesselier et Jean-Paul Zolésio, Shape reconstruction of buried obstacles by controlled evolution of a level set : from a Min Max formulation to numerical experimentation, *Inverse Problems (Special Issue to celebrate Pierre Sabatier's 65th Birthday)*, 17, 1087–1111, 2001.

[A.11] Christophe Ramananjaona, Marc Lambert et Dominique Lesselier, Shape inversion from TM and TE real data by controlled evolution of level sets, *Inverse Problems (Special Section « Testing inversion algorithms against experimental data »)*, 17, 1585–1595, 2001.

[A.12] Daniel Dos Reis, Marc Lambert et Dominique Lesselier, On the modeling of 3-D inclusions in conductive media using extended Born models in the diffusive regime, *J. Applied Electromagnetics and Mechanics, à paraître* 2002.

[A.13] Daniel Dos Reis, Marc Lambert et Dominique Lesselier, Extended Born domain integral models of diffusive fields, *IEEE Trans. Magn., à paraitre* mars 2002.

Soumis

[A.14] Christophe Ramananjaona, Marc Lambert et Dominique Lesselier, On novel developments of controlled evolution of level-sets in the field of inverse shape problems, *Radio Science*, 2001, Présélectionné à l'issue de l'URSI International Symposium on Electromagnetic Theory, Victoria, 2001.

Conférences avec actes

[C.1] Marc Lambert, Rodrigo de Oliveira Bohbot et Dominique Lesselier, Caractérisation d'un sous-sol marin stratifié en situation de petits fonds par une méthode itérative, *Cinquantenaire du Laboratoire de Mécanique et d'Acoustique (Publication L.M.A. 125)*, pp. 133–143, juin 1991.

[C.2] Rodrigo Bohbot, Patricia Grassin, Xavier Demoulin, Marc Lambert, Dominique Lesselier et Walid Tabbara, Probing of stratified media : physically- and mathematically-based approximations, *Proc. 13th World Congress on Computation and Applied Mathematics*, pp. 477–478, Dublin, juillet 1991, Contribution invitée.

[C.3] Marc Lambert, Rodrigo Bohbot et Dominique Lesselier, Reconstruction des paramètres acoustiques d'un sous-sol marin stratifié à partir de son coefficient de réflexion, *J. Phys. IV (Suppl.III)*, pp. 945–948, Arcachon, avril 1992, 2ème Congrès de la Société Française d'Acoustique.

[C.4] Marc Lambert et Dominique Lesselier, On the acoustic probing of the sea bottom in shallow water from near-field data, *J. Acoust. Soc. Am.*, volume 93, page 2395, Ottawa, mai 1993, 125th Meeting of the Acoustical Society of America.

[C.5] Marc Lambert et Dominique Lesselier, Détermination des profils acoustiques d'un fond marin de faible profondeur à partir du champ observé dans le chenal en présence d'une source donnée, *J. Phys. IV (Suppl. III)*, pp. 1067–1070, Toulouse, mai 1994, 3ème Congrès de la Société Française d'Acoustique.

[C.6] Marc Lambert, Bernard Duchêne et Dominique Lesselier, Nonlinearized inversion of 2-D objects in a stratified embedding : the TE case, *Proc. Progress In Electromagnetics Research Symposium (PIERS'96)*, page 280, Innsbrück, juillet 1996.

[C.7] Marc Lambert, Bert Jan Kooij et Bernard Duchêne, Reconstruction of a buried penetrable object : the TE case, *Proc. Progress In Electromagnetics Research Symposium (PIERS'97)*, page 554, Cambridge, juillet 1997, Contribution invitée.

[C.8] Bert Jan Kooij et Marc Lambert, Nonlinear inversion of a buried object in TE-scattering, *Proc. IEEE AP-S International Symposium and URSI North American Radio Science Meeting*, pp. 2617–2620, Montréal, juillet 1997.

[C.9] Gaële Perrusson, Marc Lambert, Dominique Lesselier, Bernard Duchêne, Antonis Charalambopoulos et George Dassios, Electromagnetic scattering by a tri-axial homogeneous penetrable ellipsoid : Low-frequency analytical derivation and numerical testing of the localized nonlinear approximation, *Proc. URSI International Symposium on Electromagnetic Theory*, pp. 408–410, Salonique, mai 1998.

[C.10] Gaële Perrusson, Marc Lambert, Dominique Lesselier, Bernard Duchêne, George Dassios et Gregory Kamvyssas, On the identification of a simple conductive body buried in a conductive Earth at low frequencies, *Proc. URSI International Symposium on Electromagnetic Theory*, pp. 575–577, Salonique, mai 1998.

[C.11] Marc Lambert, Amélie Litman, Bernard Duchêne et Dominique Lesselier, The optimal reconstruction of buried obstacles by nonlinearized methods, *Proc. EUROEM'98*, Tel Aviv, juin 1998, Contribution invitée.

[C.12] Marc Lambert, Bernard Duchêne et Dominique Lesselier, Inverse scattering for 2-D targets : comparison of the TE- and TM-cases, *Proc. Progress in Electromagnetics Research Symposium (PIERS'98)*, page 449, Nantes, juillet 1998, Contribution invitée.

[C.13] Bert Jan Kooij et Marc Lambert, Nonlinear inversion of a buried object in TE-scattering, *Proc. Progress In Electromagnetics Research Symposium (PIERS'98)*, page 864, Nantes, juillet 1998.

[C.14] Gaële Perrusson, Marc Lambert, Dominique Lesselier, Bernard Duchêne, Antonis Charalambopoulos, George Dassios, Gregory Kamvyssas et Bernard Bourgeois, On the characterization of a conductive body in a conductive earth using low-frequency asymptotic analyses, *Proc. Progress In Electromagnetics Research Symposium (PIERS'98)*, page 867, Nantes, juillet 1998, Contribution invitée.

[C.15] Gaële Perrusson, Marc Lambert, Dominique Lesselier, Bernard Duchêne, Antonis Charalambopoulos, George Dassios, Gregory Kamvyssas et Bernard Bourgeois, Probing conductive masses in the induction regime : equivalent sources and bodies, *Proc. European Association of Geoscientists and Engineers Conference and Technical Exhibition (61th EAGE)*, pp. 2–10, Helsinki, juin 1999.

[C.16] Gaële Perrusson, Antonis Charalambopoulos, Bernard Bourgeois, Dominique Lesselier, Marc Lambert et George Dassios, The localized non linear approximation : a good recipe for low-contrast ellipsoidal bodies, *Proc. European Association of Geoscientists and Engineers Conference and Technical Exhibition (61th EAGE)*, pp. P–93, Helsinki, juin 1999.

[C.17] Marc Lambert et Dominique Lesselier, On some computational issues in nonlinearized wavefield inversion, *Proc. International Congress on Industrial and Applied Mathematics (ICIAM'99)*, page 137, Edinburgh, juillet 1999, Contribution invitée.

[C.18] Diégo Martinez, Michel Lemistre, Marc Lambert et Dominique Lesselier, Modelization of the electromagnetic behavior of multilayer carbone-epoxy materials, *Proc. International Conference on Composite Materials (ICCM'12)*, pp. CD–ROM, 6 pages, Paris, juillet 1999.

[C.19] Marc Lambert et Dominique Lesselier, The retrieval of a buried cylindrical obstacle by constrained modified gradient methods : the H-polarization case, *Proc. XXVIth URSI General Assembly*, page 125, Toronto, août 1999, Contribution invitée.

[C.20] Gaële Perrusson, Dominique Lesselier, Marc Lambert, Bernard Duchêne, Bernard Bourgeois, Antonis Charalambopoulos, George Dassios et Gregory Kamvyssas, The identification of conductive masses in the Earth. Theory, numerical modeling and inversion of real data at induction frequencies, *Proc. XXVIth URSI General Assembly*, page 407, Toronto, août 1999.

[C.21] Christophe Ramananjaona, Marc Lambert et Dominique Lesselier, Boundary shape reconstruction of obstacles from laboratory-controlled data at microwave frequencies, *Proc. Progress In Electromagnetics Research Symposium (PIERS'2000)*, page 252, Cambridge, juillet 2000, Contribution invitée.

[C.22] Jean-Michel Geffrin, Bernard Duchêne et Marc Lambert, On requirements for electromagnetic detection of immersed metallic structures, *Proc. Progress In Electromagnetics Research Symposium (PIERS'2000)*, page 102, Cambridge, juillet 2000, Contribution invitée.

[C.23] Daniel Dos Reis, Marc Lambert et Dominique Lesselier, On the use of contrast-source dyadic integral formulations for the modeling of eddy current non-destructive evaluation, *Proc. Progress In Electromagnetics Research Symposium (PIERS'2000)*, page 252, Cambridge, juillet 2000, Contribution invitée.

[C.24] Marc Lambert et Dominique Lesselier, A short tour of nonlinearized inversion methods, *Proc. Kleinheubacher Tagung, URSI Allemagne*, pp. 418–424, Kleinheubach, septembre 2000, Contribution invitée.

[C.25] Christophe Ramananjaona, Marc Lambert, Dominique Lesselier et Jean-Paul Zolésio, On the controlled evolution of level sets and its application to the retrieval of obstacles from microwave laboratory data, *Proc. 30th European Microwave Conference*, pp. 19–26, Paris, octobre 2000, Contribution invitée.

[C.26] Christophe Ramananjaona, Marc Lambert, Dominique Lesselier et Jean-Paul Zolésio, On novel developments of the controlled evolution of level sets in the field of inverse shape problems, *Proc. URSI International Symposium on Electromagnetic Theory*, pp. 459–461, Victoria, mai 2001.

[C.27] Daniel Dos Reis, Marc Lambert et Dominique Lesselier, Eddy-current evaluation of 3-D defects in a metal plate, a first analysis of a contrast-source gradient method, *Proc. 7th International Workshop on Electromagnetic Nondestructive Evaluation (ENDE)*, page 9, Kobé, mai 2001.

[C.28] Daniel Dos Reis, Marc Lambert et Dominique Lesselier, Extended Born domain integral models of diffusive fields, *Proc. 13th Conference on the Computation of Electromagnetic Field (COMPUMAG'01)*, volume IV, pp. 74–75, Évian, Juillet 2001.

[C.29] Christophe Ramananjaona, Marc Lambert, Dominique Lesselier et Jean-Paul Zolésio, On mathematical and computational issues in the electromagnetic inversion (TE mode) of buried

objects by controlled evolutions of level sets, *Proc. 3rd Congress of the International Society for Analysis, its Applications and Computation (ISAAC'01)*, page 225, Berlin, août 2001.

Conférences sans actes ou avec actes à diffusion restreinte, et séminaires

[CS.1] Rodrigo Bohbot, Marc Lambert, Dominique Lesselier et Walid Tabbara, Caractérisation des milieux plans stratifiés (problème inverse), Réunion du Groupe d'Étude sur la Propagation Acoustique, Paris, février 1991.

[CS.2] Rodrigo Bohbot, Marc Lambert, Dominique Lesselier et Walid Tabbara, Caractérisation des milieux plans stratifiés (problème inverse), Réunion du Groupe d'Étude sur la Propagation Acoustique, Paris, février 1992.

[CS.3] Marc Lambert, Caractérisation acoustique d'un fond marin, 1er Colloque Jeunes Chercheurs en Physique, Université Paris-Sud, mars 1993.

[CS.4] Dominique Lesselier, Marc Lambert, Rodrigo Bohbot, Christophe Rozier et Walid Tabbara, Caractérisation acoustique de milieux stratifiés plans. Application au diagnostic du fond, Réunion Groupe d'Études sur la Propagation Acoustique, Lyon, septembre 1995.

[CS.5] Marc Lambert et Bernard Bourgeois, Détection par induction électromagnétique d'objets conducteurs enfouis. Application à la prospection géophysique, 4ème Colloque Jeunes Chercheurs en Physique, Université Paris-Sud, mars 1996.

[CS.6] Bernard Duchêne, Marc Lambert, Dominique Lesselier, Amélie Litman, Vikass Monebhurrun, Christophe Rozier, Laurent Souriau, Tom S. Angell, Ralph E. Kleinman et Fadil Santosa, On the inversion of binary objects in a nonlinearized wavefield framework, 3ème Séminaire International Problèmes Inverses en Électromagnétisme et Acoustique, Clermont-Ferrand, Contribution invitée, juin 1997.

[CS.7] Marc Lambert et Dominique Lesselier, Integral methods and nonlinearized inversion of buried obstacles, 4ème Séminaire International Problèmes Inverses en Électromagnétisme et Acoustique, Clermont-Ferrand, Contribution invitée, mai 1999.

[CS.8] Marc Lambert, Dominique Lesselier et Bernard Duchêne, On the characterization of obstacles in shallow water using rigourous inversion methods, 1er Workshop on Inverse Problems in Underwater Acoustics, Heraklion, mai 1999.

[CS.9] Marc Lambert et Dominique Lesselier, Méthodes intégrales et inversion nonlinéaire d'obstacles enfouis, Séminaire Problèmes Inverses, INRIA, Rocquencourt, Contribution invitée, juin 1999.

[CS.10] Marc Lambert et Dominique Lesselier, On the characterization of 2-D buried obstacles by nonlinearized inversions, RCP264 Workshop Inverse Problems and Nonlinearity, Theory and Applications, Montpellier, Contribution invitée, juin 2000.

[CS.11] Christophe Ramananjaona, Marc Lambert, Dominique Lesselier et Jean-Paul Zolésio, Shape reconstruction by controlled evolution of a level set : from a min-max formulation to numerical experimentation, RCP264 Workshop Inverse Problems and Nonlinearity, Theory and Applications, Montpellier, Contribution invitée, juin 2000.

[CS.12] Christophe Ramananjaona, Marc Lambert, Dominique Lesselier et Jean-Paul Zolésio, Sur la reconstruction non-linéarisée du contour d'un objet cylindrique de paramètres électriques prescrits par l'utilisateur, Séminaire École Polytechnique, Contribution invitée, avril 2001.

Rapports

[RC.1] Marc Lambert, Dominique Lesselier et Rodrigo Bohbot, Caractérisation de milieux plans stratifiés (problème inverse), Rapport technique, Convention de Recherche 89/34/134, DRET-DGA, 1992, Rapport Interm. : février 1991, Rapport final : février 1992.

[RC.2] Marc Lambert, Inversion of seismo-acoustic synthetic and real data using genetic algorithms and a posteriori probability distributions, Memorandum SM-276, SACLANT Undersea Research Centre, La Spezia, Italie, mars 1994.

[RC.3] Gaële Perrusson, Dominique Lesselier, Marc Lambert et Bernard Duchêne, Caractérisation électromagnétique d'objets conducteurs enfouis. Application à la prospection géophysique, Contrat Supélec/CNRS/BRGM n° 041101400, Supélec-CNRS, 1998, 1er Compte-Rendu d'Activité, juin 1997, Rapport Interm. : décembre 1997, 2ème Compte-Rendu d'Activité, juin 1998, Rapport Interm. : décembre 1998, Rapport final : octobre 1999.

Deuxième partie

Travaux de recherche

Introduction

Le but de cette introduction est de replacer dans leur contexte les travaux développés depuis mon entrée au CNRS en 1995 sur les problèmes direct et inverse de diffraction des ondes en électromagnétisme et acoustique mais en aucun cas d'effectuer une présentation exhaustive de leurs difficultés théoriques et numériques et de leurs mises en œuvre. Si le lecteur souhaite approfondir ses connaissances sur l'inversion au sens large il pourra se référer, par exemple, à [Sabatier, 1987; Bertero et Pike, 1991; Bonnet, 1999; Sabatier, 2000] et aux centaines de références qui y sont faites.

Le cadre de mes travaux

Le problème peut être posé de la façon suivante : soit un ensemble de paramètres $\mathcal{P}$ (densité, masse, vitesse, permittivité, ...) lié à un ensemble d'observables $\mathcal{O}$ (vitesse, pression, champ électrique ou magnétique, ...) par l'intermédiaire de « lois de la nature » $\mathcal{L}$ et soit un modèle mathématique $\mathcal{M}$ plus ou moins sophistiqué permettant de décrire au mieux ces « lois de la nature » à l'aide d'équations mathématiques ; la résolution du « problème direct » consiste à calculer $\mathcal{O}$ à partir de $\mathcal{M}$ et $\mathcal{P}$ connus alors que le « problème inverse » consiste à remonter aux paramètres $\mathcal{P}$ à partir de la connaissance de mesures $\mathcal{O}$ et des lois $\mathcal{M}$.

Les champs d'application sont nombreux et variés comme le soulignent les contributions éclectiques présentées dans [Sabatier, 1987; Bertero et Pike, 1991; Bonnet, 1999; Sabatier, 2000] dont j'ai extrait certains exemples :

- Géophysique : identification de structures profondes à partir de mesures (sismiques ou électromagnétiques) obtenues en surface ou dans un nombre réduit de puits de forage.
- Contrôle non destructif : identification et caractérisation de défauts (fissure, délaminage, brûlure, ...) affectant une pièce, un ouvrage, une structure et pouvant en modifier le comportement attendu.
- Imagerie ou reconstruction : caractérisation d'un ensemble de matériaux à partir de la réponse qu'ils donnent à une sollicitation connue.
- Traitement d'images ou de signaux : amélioration d'une image ou d'un signal distordu(e) à cause de bruit (ex : déconvolution, turbulence atmosphérique, ...)
- Conception de systèmes de mesures, de capteurs : amélioration des capteurs et des configurations pour permettre une amélioration du signal mesuré.

Problème inverse

Parmi l'ensemble de ces applications je me suis concentré, ces dernières années, sur l'étude de la diffraction inverse des ondes et plus particulièrement sur le contrôle non-destructif et la caractérisation de structures et de matériaux à l'aide de sources électromagnétiques. Ce travail vise au développement et au test par modélisation et simulations numériques de méthodes de caractérisation non destructive d'objets complexes insérés dans un milieu hôte particulier. Ces objets sont vus par les perturbations qu'ils créent lorsque l'on éclaire leur hôte à l'aide de sources données. Ainsi les informations concernant les propriétés de ces objets (emplacements, tailles, formes, paramètres des matériaux constitutifs, etc.) sont présentes sous forme codée dans le signal mesuré par les récepteurs. Le « décodage » de ce signal, également appelé résolution du problème inverse, permet d'extraire de ce signal les paramètres d'intérêt de l'objet.

Ces problèmes de diffraction inverse sont en toute hypothèse non linéaires — les paramètres des objets ne dépendent pas linéairement des champs observés —, et mal posés — existence, unicité et continuité de la solution ne peuvent être assurées simultanément — ce qui d'un point de vue pratique fait entre autre que des petites perturbations des données peuvent conduire à de larges variations des paramètres reconstruits. À ces obstacles théoriques s'ajoutent ceux, plus classiques, liés aux imperfections des données (erreurs aléatoires ou systématiques) et des modèles (nous approximons une situation réelle, et l'inversion elle-même peut par exemple se faire en négligeant une partie des phénomènes de diffraction survenant entre l'hôte et les objets, telles des diffractions multiples).

Prenant en compte ce qui précède, mon but est donc de contribuer à la construction et à la mise en œuvre de méthodes de résolution de ces problèmes inverses des ondes qui conduisent à des solutions

- qui soient suffisamment précises pour être utiles et stables vis-à-vis des erreurs de modèle et de données, ce qui se fait grâce à des régularisations (typiquement opérant sur la norme des solutions, de leurs dérivées ou de fonctions résultant de l'application d'opérateurs particuliers sur ces solutions), et l'incorporation au départ de et/ou au cours de l'inversion d'informations *a priori* sur les objets (compacité, non-négativité, connexité, amplitudes bornées, etc.) ;
- qui puissent être obtenues assez rapidement, notamment dans le cas de structures complexes ou de tailles importantes, ce qui dépend bien sûr des ordinateurs utilisés et des méthodes numériques choisies.

Deux domaines ont été privilégiés :

- le domaine des basses fréquences dans lequel la longueur d'onde (ou, cas échéant, l'épaisseur de peau) dans le milieu hôte est grande devant la taille caractéristique de l'obstacle.
- le domaine de résonance dans lequel la longueur d'onde (ou, cas échéant, l'épaisseur de peau) dans le milieu hôte et la taille caractéristique de l'obstacle sont du même ordre de grandeur.

Problème direct

La résolution des problèmes directs de diffraction correspondants est une première étape nécessaire à tout problème inverse. Elle permet une validation de la formulation des champs électromagnétiques ou acoustiques choisie — par comparaison avec des résultats synthétiques obtenus dans la littérature par exemple ou expérimentaux obtenus soit au laboratoire soit chez nos partenaires —, l'acquisition de données synthétiques, une meilleure compréhension des phénomènes d'interaction mis en jeu et la possibilité de mettre en évidence les paramètres clés des objets et de leurs hôtes. En sus, ce travail conduit notamment à l'obtention de modules de calcul rapides utilisables au cours des inversions, un goulet d'étranglement dans les problèmes inverses des ondes résidant fréquemment dans l'obligation de calculs répétitifs — souvent coûteux — des champs pour des environnements donnés.

Configurations génériques

Deux configurations génériques ont été plus particulièrement étudiées :

- le milieu hôte est supposé homogène par morceaux, milieu que représente bien un empilement de strates homogènes d'interfaces parallèles planes. Les sources créent l'éclairement (nous sommes dans une situation active). Elles peuvent être planes générées à l'infini ou localisées — lignes et points sources, dipôles, boucles, ou dispositifs rayonnants plus élaborés — placées soit à la surface, à distance finie de la première interface (avec la possibilité qu'elles soient directement en contact avec elle), soit dans le milieu hôte, à l'intérieur d'une strate par exemple. Les récepteurs, en nombre limité, nous donnent accès au champ diffracté (ou d'anomalie) lié aux objets, et sont également placés soit à la surface soit dans le milieu hôte. Les données ainsi obtenues sont dites « d'aspect limité » puisqu'il n'est pas possible de tourner tout autour de l'hôte. Pour compenser partiellement cette perte d'information ces mesures sont effectuées, dans la mesure du possible, à plusieurs fréquences en régime harmonique et pour plusieurs géométries de sources et de récepteurs. Ainsi les résultats d'existence et d'unicité des inversions ne sont, à ma connaissance, connus que dans la configuration non restreinte du diffracteur en espace homogène et les difficultés sont pour nous aggravées par le fait que l'hôte n'est pas nécessairement un demi-espace homogène mais peut être stratifié.
- le milieu hôte est supposé homogène, situations d'espace libre, sources et récepteurs pouvant être soit répartis tout autour de l'obstacle — l'obstacle est alors « vu » de tous côtés — soit de part et d'autre — situation « d'aspect limité ».

Si ces configurations peuvent paraître simples par comparaison à la réalité, elles n'en demeurent pas moins riches de difficultés théoriques et numériques conduisant à des problèmes difficiles à résoudre. Elles sont également une première étape indispensable avant tout complexification du problème.

Formulations et méthodes

Les travaux présentés ici se situent, pour l'essentiel, dans l'optique d'une résolution de ces problèmes directs et inverses à partir de formulations intégrales de domaine ou de frontière des champs, ce qui met en évidence l'importance de l'écriture et du calcul des fonctions ou tenseurs de Green représentatifs des champs créés par des sources scalaires ou vectorielles élémentaires qui permettent de les formuler. L'utilisation maximale de transformées rapides de Fourier est une nécessité rendue possible par la structure de convolution (au moins partielle) de la plupart des formulations choisies. Ces formulations ont l'avantage de prendre en compte l'ensemble des phénomènes électromagnétiques ou acoustiques existant entre l'obstacle et le milieu environnant et de s'écrire sous une forme compacte mais elles cachent certaines difficultés théoriques et numériques. Cependant, l'étude d'approximations permettant soit d'accélérer les calculs numériques (Born, Born étendu, …), soit de poursuivre plus loin les calculs analytiques (développement basse fréquence lorsque la longueur d'onde est beaucoup plus grande que les dimensions caractéristiques de l'obstacle par exemple), ne sera pas pour autant négligée.

La caractérisation de tels objets diffractants au sein de milieux hôtes donnés (qui sont connus exactement ou le plus souvent avec une certaine imprécision) se fait par approximations dans des cas limites (fréquences assez basses et défauts de petites dimensions, interactions multiples réduites, surfaces parfaitement réfléchissantes) et de manière complète en règle générale. Parmi l'ensemble des méthodes d'inversion existantes les approches itératives déterministes ont été privilégiées : les

paramètres caractéristiques de ces objets sont alors déterminés par une succession de « petits déplacements » dans un espace de paramètres, de façon à minimiser une fonction coût représentative de l'écart entre données et champs associables à une configuration itérée à laquelle se rajoute, le cas échéant, des régularisations judicieusement choisies.

Le choix des paramètres à chercher est une des difficultés majeures de la résolution des problèmes inverses. Il repose sur un équilibre entre la rapidité attendue et/ou espérée des algorithmes, la complexité du modèle utilisé et la précision sur la solution souhaitée. Si une grande partie du travail effectué ici concerne la caractérisation complète (peu ou pas d'approximations), plusieurs approches conduisant à des solutions approchées ont cependant été envisagées :

- la recherche d'un obstacle équivalent : l'obstacle recherché est remplacé par un obstacle canonique équivalent (sphère, ellipsoïde, ...) dont la position, les paramètres électromagnétiques (conductivité, permittivité) et le volume sont alors à déterminer.
- la recherche de sources équivalentes : l'obstacle recherché est remplacé par une ou plusieurs sources équivalentes dont la ou les positions et la ou les amplitudes contiennent, sous des formes plus ou moins simples, des informations sur le volume, les paramètres électromagnétiques ou acoustiques, et la position de l'obstacle à reconstruire.

Plan de la seconde partie du manuscrit

Dans cette seconde partie est introduit l'ensemble des travaux auxquels je me suis intéressé. Dans la mesure du possible chaque section débute par un « état des lieux » au moment où le problème a été abordé et, lorsque nécessaire, les collaborations sont rappelées. Puis elle se poursuit par une présentation des solutions, innovations et/ou extensions qui ont été apportées. Elle se termine par une ou plusieurs références correspondant à une sélection d'articles publiés ou soumis (pour les travaux les plus récents) illustrant la méthode, sélection présentée dans la troisième partie. Dans cette seconde partie j'ai choisi de ne mettre aucune équation, espérant ainsi permettre à un lecteur moins averti de comprendre les méthodes sans être obligé d'aborder les formulations mathématiques. Tout lecteur souhaitant approfondir telle ou telle méthode peut cependant se référer aux articles de la troisième partie qui présentent, dans le détail, équations et résultats numériques correspondants.

Dans le premier chapitre de cette seconde partie (§ 3), le cas d'un objet dont une des dimensions est beaucoup plus grande que les autres a été privilégié — nous nous situons alors dans le cas bidimensionnel pour lequel, en électromagnétisme, les polarisations sont découplées (les polarisations fondamentales TE et TM étant alors à considérer). Des applications en électromagnétisme et en acoustique ont été visées, toutes dans le domaine de résonance (taille de l'objet de l'ordre de grandeur de la longueur d'onde). La résolution des problèmes direct et inverse est principalement basée sur une formulation intégrale de domaine de la solution de l'équation de propagation scalaire faisant intervenir la fonction de Green de l'espace stratifié. L'accent a été mis sur le cas plus compliqué et moins étudié de la polarisation TE (la seule composante non nulle du champ magnétique H étant orientée suivant la dimension la plus grande de l'obstacle). Un code de résolution du problème direct (§ 3.2) a été développé. Puis plusieurs algorithmes d'inversion basés sur des techniques variées ont été mis au point : le gradient modifié et ses variantes (§ 3.3), les sources distribuées (§ 3.4) et l'évolution d'ensembles de niveaux (§ 3.5).

Dans le second chapitre (§ 4), le problème des obstacles tridimensionnels de volume quelconque a été abordé (il faut alors tenir compte de la dépolarisation et du couplage TE-TM). Ce travail est également basé sur une expression intégrale de domaine de la solution de l'équation de propagation

vectorielle faisant intervenir les dyades de Green électrique-électrique et électrique-magnétique de l'espace stratifié. La résolution du problème direct est effectuée par deux approches complémentaires :

- Une solution dite « exacte » (§ 4.2) faisant appel à une méthode de moments a été développée, plusieurs approximations de type Born ont été expérimentées et les résultats obtenus comparés avec la solution exacte.
- une solution semi-analytique approchée (§ 4.3) du problème direct pour un ellipsoïde de faible ou moyen contraste par rapport à son environnement est obtenue grâce à l'utilisation couplée d'une approximation de type Born et un développement basse fréquence (Rayleigh) en faisant notamment appel à la théorie des harmoniques ellipsoïdales.

De la même façon deux approches différentes du problème inverse correspondant à deux applications distinctes ont été développées :

- « problème inverse de diffraction » (§ 4.4) : une cartographie d'une zone dans laquelle est supposée se trouver un défaut est effectuée à l'aide d'une méthode de type gradient modifié avec pour but l'application au contrôle non destructif par courants de Foucault, domaine de recherche abordé de longue date au L2S concernant la détection de fissures ou inclusions dans des plaques ou tubes métalliques.
- « problème inverse source » (§ 4.5) : des sources équivalentes à l'obstacle sont recherchées, leurs localisations et leurs amplitudes permettant, dans une certaine mesure, de remonter aux paramètres caractéristiques (taille, conductivité) de l'obstacle. Cette technique a été appliquée dans un problème de caractérisation à basse fréquence d'un sous-sol profond, problème abordé lors d'un séjour post-doctoral au BRGM (Bureau de Recherche Géologique et Minière) en 1995. Le but est de positionner et d'identifier un gisement minier potentiel enfoui dans le sous-sol lointain (quelques centaines de mètres) à partir de la mesure, dans un ou plusieurs puits de forage, des trois composantes du champ magnétique.

Un tel travail n'aurait pu être mené à bien sans de nombreuses collaborations au sein même du laboratoire ou dans des laboratoires extérieurs avec des stagiaires, doctorants ou chercheurs confirmés français ou étrangers comme en témoigne le fait que la plupart des publications sont co-signées. En tout premier lieu D. Lesselier qui, après avoir été mon directeur de thèse de 1990 à 1994, est devenu mon directeur de recherche lors de mes dix-huit mois de fonctionnaire stagiaire d'octobre 1995 à mai 1997 et avec qui je continue de travailler étroitement depuis. Je ne saurai oublier les stagiaires de DEA devenus, pour la plupart, doctorants au L2S et, pour la plus ancienne, Maître de Conférences à l'Université de Paris-Sud, avec par ordre chronologique G. Perrusson, E. Bocly, D. Dos Reis, D. Martinez et C. Ramananjaona. Je ne pourrai oublier les collaborations nombreuses avec des chercheurs français — B. Bourgeois du BRGM et M. Lemistre de l'ONERA — et étrangers — R. E. Kleinman de l'Université du Delaware, B. J. Kooij de l'Université de Delft, A. Charalambopoulos de l'Université de Salonique, G. Dassios et G. Kamvyssas de l'Université de Patras — au travers de collaborations variées (§ 1.4).

3

Évaluation non destructive d'objets axisymétriques

Sommaire

3.1 Introduction

La localisation et l'identification de défauts axisymétriques pénétrables ou impénétrables enfouis sont toujours d'une grande actualité dans la communauté scientifique internationale comme le montre l'importance de la littérature sur le sujet et sont d'application par exemple dans le cas où une des dimensions de l'objet est beaucoup plus grande que les autres (barre d'acier, tuyau, ...). Cette restriction au cas bidimensionnel a l'avantage, en électromagnétisme, de conduire à un découplage des polarisations Transverse Électrique (TE ou H) et Transverse Magnétique (TM ou E) et donc à une simplification des équations à résoudre. Je me suis plus particulièrement intéressé au cas, plus compliqué et plus rarement étudié, de la polarisation TE pour laquelle la seule composante non nulle du champ magnétique H est parallèle à l'axe du cylindre, le cas de la polarisation TM pour laquelle la seule composante non nulle du champ électrique E est parallèle à l'axe du cylindre n'étant pas négligé pour autant.

Deux configurations ont été étudiées (FIG. 3.1) :
- l'objet est enfoui dans un demi-espace stratifié, les sources et récepteurs étant situés au-dessus de l'interface séparant le milieu contenant l'objet de celui les contenant.
- l'objet, les sources et les récepteurs sont placés au sein d'une stratification plane jouant le rôle d'un guide d'ondes, les interfaces pouvant être parfaitement réfléchissantes ou non.

Nous nous situons donc dans le cas de données « d'aspect limité »

Plusieurs objectifs sont intéressants : cartographie des paramètres électromagnétiques dans le cas d'objets homogènes ou hétérogènes, reconstruction de forme dans le cas d'objets homogènes.

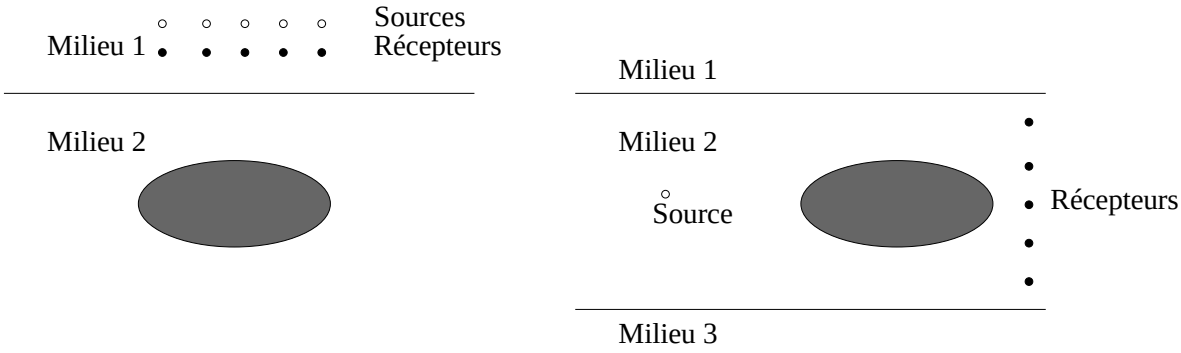

FIG. 3.1 – Schéma des deux configurations d'intérêt : à gauche la configuration stratifiée, à droite le guide d'ondes.

Formulations intégrales

Les travaux effectués ici font appel à des formulations intégrales de frontière ou de domaine. Elles sont obtenues par application du théorème de Green aux équations gouvernant la propagation des champs et leur choix dépend du problème à résoudre.

Intégrales de frontière

Cette formulation ne s'applique qu'aux cas d'obstacles homogènes ou homogènes par morceaux pénétrables ou non. Le champ dans tout l'espace ne s'exprime qu'à partir du champ et/ou de sa dérivée sur la frontière du ou des obstacles et de la fonction de Green du milieu hôte et/ou de sa dérivée normale à la frontière (principe de Huygens) par l'intermédiaire d'une intégrale de frontière. Il existe un grand nombre de formulations différentes [Kong, 1986] exprimant le champ électromagnétique, par exemple à partir des composantes tangentielles du champ E ou du champ H uniquement, ou d'un mélange des deux, ou encore d'un mélange de composantes tangentielles et normales ; certaines sont cependant à utiliser avec précaution car pouvant mener à des résultats erronés (apparition de fréquences de résonnance [Harrington, 1989]), les mêmes remarques étant valables en acoustique.

Du point de vue numérique, cette formulation ne nécessite que la discrétisation des frontières des obstacles et le calcul des champs sur cette frontière uniquement, d'où un nombre d'inconnues relativement faible.

Intégrales de domaine

Cette formulation est la plus générale, s'appliquant à la fois à des obstacles homogènes et inhomogènes pénétrables. Le champ dans tout l'espace est obtenu à partir du champ et/ou de sa dérivée dans le ou les obstacles, de la fonction de Green du milieu hôte et/ou de sa dérivée et d'une fonction contraste mesurant l'écart entre les paramètres électromagnétiques du milieu hôte et de l'obstacle par l'intermédiaire d'une intégrale de domaine. Il existe également différentes formulations, scalaires ou vectorielles[1], pour résoudre les problèmes rencontrés et notamment, dans le cas de la polarisation TE, deux formulations des champs sont possibles :

[1]Ceci dépend du choix de l'équation de propagation à résoudre. Des précisions sont apportées plus loin.

- une formulation en champ E conduisant à résoudre un problème vectoriel dont les inconnues sont alors les deux composantes transverses non-nulles du champ E. Elle a l'avantage de ne faire intervenir que les composantes de E et la fonction de Green ou ses gradients mais nécessite de travailler avec une équation intégrale vectorielle.
- une formulation en champ H conduisant à résoudre un problème scalaire dont l'inconnue est alors l'unique composante longitudinale non-nulle du champ H. Elle a l'avantage de ne faire intervenir qu'une équation intégrale scalaire mais l'inconvénient de dépendre non seulement des gradients de la fonction de Green mais également du gradient de H.

L'utilisation de formulations intégrales conduit à résoudre successivement deux équations intégrales :

- l'équation de couplage (ou d'état) qui lie le champ total (E ou H) dans l'obstacle au champ incident présent dans le milieu en l'absence d'obstacle et à lui-même ou à son gradient par l'intermédiaire de la fonction contraste mesurant l'écart entre les paramètres électromagnétiques du milieu hôte et de l'obstacle et de la fonction de Green de ce milieu hôte ou de son gradient.
- l'équation d'observation (ou de données) qui lie le champ mesuré sur les récepteurs au champ total dans l'obstacle ou à son gradient par l'intermédiaire de la fonction contraste et d'une autre fonction de Green ou de son gradient.

D'un point de vue numérique, cette formulation nécessite la discrétisation du domaine des obstacles et le calcul des champs dans ce domaine, d'où un nombre d'inconnues plus important que pour une formulation d'intégrale de frontière.

Fonction de Green

Le préalable est l'établissement d'une expression de la fonction de Green. Celle-ci n'est autre que la solution élémentaire de l'équation de propagation du champ pour une source élémentaire modélisée par une ligne source électrique ou magnétique. Dans le cas d'un milieu homogène la fonction de Green s'exprime uniquement par un terme dit singulier modélisant le rayonnement d'une ligne source dans un espace homogène et dont la formulation est connue analytiquement dans le domaine des fréquences spatiales et le domaine spatial. Pour celle de l'espace stratifié, à ce terme singulier s'ajoute un terme régulier prenant en compte les réflexions sur et les transmissions à travers les interfaces et dont la formulation analytique n'est connue que dans le domaine des fréquences spatiales. Ce dernier terme est obtenu en décrivant la propagation bien connue des ondes planes de polarisations TE ou TM le long de l'axe perpendiculaire aux stratifications et en prenant en compte les continuités des champs aux interfaces [Chew, 1995]. Une transformation de Fourier appropriée suivant la variable latérale permet un retour au domaine spatial.

Plan du chapitre

La section (§ 3.2) traite en détail de la résolution du problème direct pour deux formulations (en champ H et en champ E) par une méthode des moments. La section (§ 3.3) présente une famille d'algorithmes d'inversion basés sur des techniques de gradient modifié dans le cas d'un obstacle enfoui dans un demi-espace en polarisation TE. La section (§ 3.4) s'intéresse à la reconstruction d'un obstacle impénétrable placé dans un guide d'ondes par une méthode de sources distribuées en acoustique sous-marine puis étendue au cas électromagnétique. Et enfin, la section (§ 3.5) traite de la résolution du problème inverse par une technique d'ensemble de niveaux appliquée à la fois en milieu stratifié et en espace libre en polarisation TM et TE.

3.2 Problème direct : la polarisation Transverse Électrique (TE)

Dans ce chapitre, nous nous intéressons à la modélisation de l'interaction électromagnétique entre un obstacle bidimensionnel enfoui dans le demi-espace inférieur et une source harmonique incidente de polarisation TE placée dans le demi-espace supérieur. Le but est d'obtenir des méthodes rapides et précises de calcul du champ diffracté par l'utilisation d'un schéma de discrétisation adéquate des équations intégrales et par l'utilisation intensive de transformées de Fourier rapide (TFR).

Ce travail a été conduit en collaboration avec B. J. Kooij, Assistant Professor au Centre for Technical Geoscience (CTG) du Laboratory of Electromagnetic Research de l'Université Technologique de l'université de Delft. Il a débuté lors de son séjour sabbatique de mai à juillet 1996 au L2S. Cette collaboration a permis, par la vérification et la validation à chaque étape des équations mises en jeux et de leurs traitements numériques, le développement en parallèle, de deux algorithmes de résolution du problème direct.

Sa résolution est une première étape nécessaire avant d'aborder le développement de méthodes de résolution du problème inverse de diffraction des ondes en polarisation TE dans le domaine microonde. Elle permet non seulement un calcul rapide de données synthétiques à un coût numérique faible mais également, par une étude paramétrique, d'extraire les paramètres prépondérants du problème de diffraction. De plus, les codes développés peuvent être utilisés comme partie intégrante d'un algorithme d'inversion.

Rappelons que les algorithmes présentés ici sont basés sur une formulation intégrale des champs et appartiennent donc à la classe bien connue des formulations intégrales de domaine ou de frontière des champs. Si le cas de l'espace libre — sources, récepteurs et obstacles sont dans un espace homogène d'extension infini — a largement été étudié [Peterson, 1988; Borup *et al.*, 1987; Joachimowicz et Pichot, 1990; Zwamborn et van den Berg, 1991], le cas stratifié a fait l'objet d'un moins grand nombre de publications significatives [Xu et Yan, 1993a; Xu et Yan, 1993b; Ellis et Peden, 1995].

Ainsi que précisé précédemment, la résolution du problème de diffraction en polarisation TE peut se faire à partir du champ électrique (formulation vectorielle en champ E, orienté parallèlement à la section droite de l'obstacle) ou du champ magnétique (formulation scalaire en champ H, orienté parallèlement à l'axe de l'obstacle), les deux approches ayant avantages et inconvénients.

3.2.1 Formulation en champ H

L'unique composante non-nulle du champ magnétique H s'exprime sous la forme d'une équation intégrale de domaine scalaire l'impliquant ainsi que ses dérivées spatiales et que les dérivées spatiales de la fonction de Green. La difficulté d'une telle approche vient justement de la présence de ces dérivées dans la formulation et plusieurs solutions ont été développées pour la traiter. En particulier les travaux de Xu et Yan [Xu et Yan, 1993a; Xu et Yan, 1993b] introduisent une formulation dite *Volume-Surface Integral Equation* pour laquelle des intégrales à la fois de domaine sur la section droite de l'obstacle et de frontière sur son périmètre sont nécessaires. Cette formulation a l'avantage d'éliminer toute contribution des dérivées de H mais au prix d'une augmentation du nombre des inconnues due à la présence du terme intégral supplémentaire. En effet il est alors nécessaire de discrétiser à la fois la surface (à l'aide d'éléments triangulaires) et le contour (à l'aide de segments) de l'obstacle.

À la différence des investigations de Xu et Yan, la formulation en champ H développée au DRÉ traite directement les gradients spatiaux de H et de la fonction de Green du milieu stratifié. C'est une généralisation au cas stratifié de la méthode brièvement décrite dans [Lixin *et al.*, 1995]. Cette méthode a l'avantage de ne nécessiter que la discrétisation de la section droite de l'obstacle.

La résolution numérique du problème n'est possible qu'à l'aide d'une discrétisation des équations intégrales. Elle est basée sur une méthode de moments dans laquelle la section droite de l'obstacle est divisée en pixels rectangulaires dans lesquels les paramètres électromagnétiques (permittivité, conductivité et perméabilité) sont supposés constants, chaque pixel étant lui-même divisé en deux triangles sur chacun duquel la variation du champ H est supposée linéaire. Cette méthode nécessite également l'intégration du gradient de la fonction de Green sur chaque pixel triangulaire. Le terme singulier, dont l'expression analytique est connue dans le domaine spatial, est intégré numériquement par un schéma de Gauss-Legendre, la singularité ayant été extraite au préalable et intégrée analytiquement. Le terme régulier est intégré analytiquement dans le domaine des fréquences spatiales puis calculé dans le domaine spatial par TFR mono-dimensionnelle. Le système linéaire ainsi obtenu est résolu à l'aide d'un gradient conjugué basé sur une large utilisation de TFR permis par la structure de convolution (selon la variable latérale) et de corrélation (selon la variable de profondeur) de la solution intégrale.

L'algorithme a été validé par comparaison des résultats avec ceux fournis par d'autres méthodes.

– Une méthode d'intégrale de contour [Saillard et Toso, 1997] a été considérée dans la configuration suivante : un objet est enfoui dans un demi-espace inférieur, cet objet est éclairé par une source ponctuelle à 300 MHz placée dans le demi-espace supérieur, et le champ H est mesuré sur une ligne horizontale placée également dans le demi-espace supérieur.
– Une méthode d'intégrale de domaine [Pincemin *et al.*, 1994] basée sur une formulation en champ E, a été considérée dans une configuration identique à la précédente à l'exception d'un champ incident en onde plane et de données formées des deux composantes du champ E.

Équations et détails de l'algorithme sont décrits dans [A.3] proposé en annexe (§ A).

3.2.2 Formulation en champ E

Les deux composantes non nulles du champ électrique E peuvent s'exprimer à l'aide d'une équation intégrale de domaine vectorielle, impliquant le champ E et les dérivées spatiales de la fonction de Green. Dans les faits deux équations intégrales de domaine scalaires sont à résoudre simultanément. Ellis et Peden [Ellis et Peden, 1995] ont utilisé une telle approche pour modéliser la réponse d'un tunnel enfoui dans un demi-espace dans une configuration dite puits-à-puits (sources et récepteurs sont enfouis dans le demi-espace contenant le tunnel). L'obstacle et les équations intégrales correspondantes sont simplement discrétisés à l'aide de cellules rectangulaires dans lesquelles le champ électrique et les paramètres électromagnétiques sont pris constants. Il est à noter que dans [Joachimowicz et Pichot, 1990] une telle approche appliquée en espace libre a donné des champs diffractés erronés mais, qu'à ma connaissance, une telle étude n'a jamais été menée dans le cas stratifié.

À la différence des travaux de Ellis et Peden, la formulation choisie au CTG ne fait intervenir dans les équations intégrales que la fonction de Green (et non plus ses dérivées) et le champ vectoriel E, les opérateurs différentiels étant alors appliqués à l'extérieur de l'équation intégrale vectorielle. Ceci a l'avantage de ne pas augmenter artificiellement le degré de la singularité de la fonction de Green mais se paye par un calcule numérique des dérivées spatiales.

La discrétisation des équations intégrales est effectuée par une méthode de moments dans laquelle le domaine est discrétisé en pixels rectangulaires où le contraste est pris constant. Le champ E est, lui, discrétisé à l'aide de fonctions continues de type « rooftop ». La singularité de la fonction de Green est traitée à partir d'une formulation faible de l'équation intégrale.

Équations et détails de l'algorithme sont décrits dans [A.5].

3.2.3 Illustration de la méthode

L'algorithme développé au laboratoire a été validé en comparant ses résultats avec ceux fournis par un algorithme basé sur une formulation intégrale de surface [Saillard et Toso, 1997]. Pour illustrer cette section deux comparaisons (extraites de [A.3]) sont proposées (FIG. 3.2). La configuration stratifiée (FIG. 3.1) est la suivante : un espace est séparé en un demi-espace supérieur de paramètres électromagnétiques ($\epsilon_{r1} = 1$, $\sigma_1 = 0$ S/m) à l'intérieur duquel la longueur d'onde est λ_0, et un demi-espace inférieur de paramètres électromagnétiques ($\epsilon_{r2} = 4$, $\sigma_2 = 10^{-4}$ S/m) à l'intérieur duquel la longueur d'onde est définie par $\lambda_2 = \lambda_0/\sqrt{\epsilon_{r2}}$. Dans le demi-espace inférieur est placé un obstacle axisymétrique de section carrée centré en $(0, -\lambda_2)$, de côté $d = \lambda_2$ et de permittivité relative $\epsilon_{r\Omega}$ et de conductivité σ_Ω. Deux cas ont été étudiés : (a) ($\epsilon_{r\Omega} = 1$, $\sigma_\Omega = 0$ S/m) et (b) ($\epsilon_{r\Omega} = 16$, $\sigma_\Omega = 0.01$ S/m). L'ensemble est illuminé par une ligne source de fréquence 300 MHz, de polarisation TE et d'amplitude unité placée dans le demi-espace supérieur en $(0, \lambda_2)$ et le champ diffracté est collecté sur 37 récepteurs placés dans le demi-espace supérieur à une hauteur $y = \lambda_2/4$, chaque $\lambda_2/6$ entre $x = -3\lambda_2$ et $x = 3\lambda_2$.

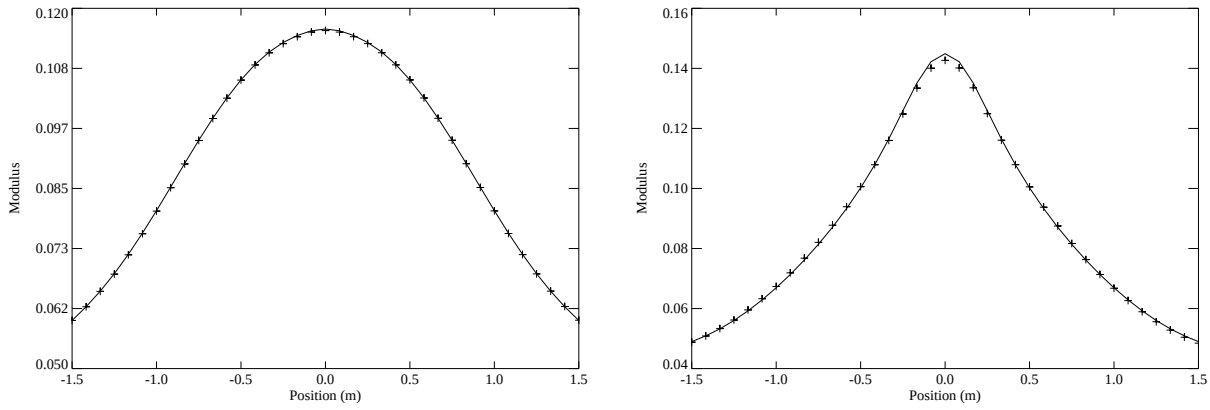

(a) (b)

FIG. 3.2 – Module du champ magnétique total H en fonction de la position des récepteurs. Comparaison entre le résultat fourni dans [Saillard et Toso, 1997] (ligne continue) et celui fourni par l'algorithme développé au DRÉ (croix). En (a) le cas A et en (b) le cas B.

3.3 Problème inverse : gradient modifié et variantes

Dans ce chapitre est abordé la résolution de problèmes inverses à l'aide d'une méthode dite de « gradient modifié » et ses variantes. Ce travail a également bénéficié de la collaboration de B. J. Kooij.

Ainsi qu'illustré dans [Lesselier et Duchêne, 1996], la reconstruction d'un obstacle à partir de l'inversion du champ électromagnétique ou acoustique résultant de l'interaction d'une onde avec un milieu possiblement stratifié contenant un ou plusieurs obstacles est d'un intérêt pratique certain dans de nombreux domaines d'application : évaluation non destructive de tubes, plaques ou autres composants d'équipement industriel, caractérisation de structures géophysiques dans la terre, identification

de mines sur terre ou en mer, mais également de tout autre objet artificiel au sein de milieux naturels, imagerie d'anomalies dans des tissus vivants, etc.

Parmi l'ensemble des méthodes d'inversion existantes, les méthodes appartenant à la famille des méthodes itératives ont été privilégiées et en particulier celles dites « méthodes de gradient » dont les plus couramment utilisées sont décrites dans [van den Berg et Kleinman, 1997a]. Notre choix s'est porté sur des méthodes appartenant à la classe récemment développée des méthodes de « gradient modifié » [Kleinman et van den Berg, 1992a; Kleinman et van den Berg, 1992b]. À la différence des autres méthodes itératives (Newton, Newton-Kantorovich, ...) la résolution par une méthode de gradient modifié se fait sans linéarisation successive des équations et évite la résolution du problème direct à chaque itération.

Dans le cadre de ces travaux, plusieurs extensions de la méthode du gradient modifié ont été développées permettant, avec différentes contraintes sur les solutions, de résoudre un grand nombre de problèmes liés à la reconstruction d'obstacles enfouis en polarisation TE.

3.3.1 Gradient modifié standard

Les premiers travaux ont conduit au développement d'un algorithme de gradient modifié « standard » qui était une extension au cas stratifié des travaux initiaux effectués en espace libre par R. Kleinman et P. van den Berg [Kleinman et van den Berg, 1992b; Kleinman et van den Berg, 1992a]. Le processus est basé sur la recherche de plusieurs[2] fonctions complexes inconnues (décrivant les paramètres physiques et le champ total à l'intérieur d'une zone prédéfinie) par minimisation itérative de deux fonctionnelles coûts mesurant l'écart entre les champs connus (incident et diffracté) et les champs obtenus à partir des paramètres des objets reconstruits. La réécriture de chaque fonction complexe inconnue sous la forme d'une suite de fonctions complexes dont l'élément à l'itération n s'écrit en fonction de l'élément à l'itération $n-1$, d'une direction de projection modifiée à chaque itération et d'une constante complexe permet de transformer le problème de minimisation de fonctionnelles coûts en un problème plus simple de minimisation de fonctions coûts dans lequel les inconnues ne sont plus des fonctions mais des constantes complexes. Deux des clés de ce type d'algorithme sont (i) le choix de la solution initiale à l'itération 0, (ii) le choix des directions de projection à chaque itération (les plus classiques sont une direction du type gradient de la fonction coût ou une direction de type Polak-Ribière).

À la différence de ceux obtenus en espace libre, les résultats des reconstructions se sont montrés décevants, notamment en conduisant à des solutions non-physiques (permittivité inférieure à l'unité, conductivité négative). Ceci nous a conduit à proposer et mettre en œuvre des méthodes de gradients modifiés incorporant de l'information *a priori* sur les solutions recherchées.

3.3.2 Gradient modifié contraint

L'incorporation d'information *a priori* sur les solutions recherchées est l'objet de nombreuses investigations , *e.g.* utilisation de la binarité du contraste pour la reconstruction d'objets homogènes [Souriau *et al.*, 1996; Monebhurrun *et al.*, 1998], contrainte de positivité sur les parties réelles et imaginaires des contrastes reconstruits [Belkebir et Tijhuis, 1996], addition d'un terme de pénalisation dit « de variation totale » dans la fonctionnelle à minimiser [van den Berg et Kleinman, 1995], ou encore utilisation d'une technique de préservation des angles permettant la reconstruction d'obstacles avec

[2] Leur nombre dépend de l'information *a priori* que l'on souhaite incorporer dans le processus.

des discontinuités fortes de contraste [Lobel *et al.*, 1997]. L'un des problèmes majeurs lors de l'addition à la fonctionnelle d'un terme de pénalisation est d'évaluer le poids à donner à cette contrainte. Ce poids, mesuré par un « hyper-paramètre » multiplicatif de la fonctionnelle pénalisatrice, doit être judicieusement choisi : trop grand, la pénalisation domine et le processus n'évolue pas, trop petit, la solution finale n'est pas assez contrainte. Plusieurs méthodes (validation croisée généralisée [Golub *et al.*, 1979], courbe en L [Hansen, 1992; Hansen et O'Leary, 1993]) ont été développées pour trouver une valeur optimale de ce paramètre au prix de calculs numériques parfois coûteux. Récemment une nouvelle technique permettant d'introduire les contraintes par la multiplication de la fonctionnelle coût par un terme de régularisation [Abubakar et van den Berg, 2001] a montré une nouvelle voie intéressante permettant de s'abstraire du problème d'évaluation de cet « hyper-paramètre ».

Contrainte de positivité

Dans un premier temps nous nous sommes intéressés au cas de la reconstruction d'un obstacle inhomogène. Deux algorithmes ont été développés simultanément l'un au CTG, l'autre au DRÉ. L'un et l'autre utilisent les contraintes de positivité sur la partie réelle et imaginaire des contrastes reconstruits. L'idée est de remplacer les inconnues (permittivité et conductivité) par des variables auxiliaires élevées au carré.

- La méthode développée au CTG fait appel à la formulation vectorielle en champ E précédemment introduite (§ 3.2) pour exprimer les équations intégrales de domaine nécessaires au processus.
- Celle développée au DRÉ est basée sur une formulation scalaire en champ H des équations intégrales de domaine utilisées introduite dans la section § 3.2. De mars à juillet 1998, D. Dos Reis, stagiaire du DEA Méthodes Physiques en Télédétection dont j'assurais l'encadrement, a simplifié la formulation générale du gradient modifié en introduisant l'approximation de Born dans les équations intégrales entraînant ainsi une accélération notable des calculs dans le cas de la reconstruction d'obstacles faiblement diffringents.

Les résultats obtenus par ces deux méthodes ont montré la pertinence d'une telle approche pour la reconstruction d'objets purement diélectriques (seule la permittivité est recherchée, la conductivité étant supposée connue et nulle) ou purement conducteurs (seule la conductivité est recherchée, la permittivité étant supposée connue et égale à celle de l'air) mais également ses limites dans la reconstruction simultanée de la permittivité et de la conductivité (cf FIG. 3.3(b)). Ce phénomène, lié non seulement au caractère mal-posé du problème inverse mais également à l'aspect limité des données, montre que, dans le cas d'un obstacle enfoui, les contraintes de positivité ne sont pas nécessairement suffisantes. Ceci nous a conduit à développer une version dite « binaire » du gradient modifié.

Les détails des méthodes ainsi que des résultats numériques ont fait l'objet de plusieurs publications communes [A.4; A.5]. Une copie de [A.4] se trouve en annexe (§ B).

Contrainte de binarité

Ces travaux, extensions de ceux effectués au DRÉ dans le cas de la polarisation TM [Souriau *et al.*, 1996], n'ont été développés que dans le cas d'une formulation en champ H. Ils ont montré que l'incorporation de la binarité dans le processus permettait une amélioration des reconstructions (FIG. 3.3(c)) en particulier dans les cas où l'information de positivité n'était pas suffisante et où la reconstruction échouait.

Ce gradient modifié dit « binaire » ne s'applique qu'à des objets homogènes et a pour but d'obtenir la localisation et la forme de l'objet. Il nécessite une connaissance *a priori* des paramètres électromagnétiques de l'objet (permittivité et conductivité) ou au moins une estimation haute de ces paramètres — l'erreur introduite sur les paramètres, si elle n'est pas trop importante, permettra une bonne reconstruction de l'objet. En pratique, dans une zone de recherche, des pixels noirs (pixel appartenant à l'objet) et des pixels blancs (milieu environnant) sont reconstruits. L'idée est de remplacer la fonction contraste par le produit d'un contraste constant connu et d'une fonction dépendant d'une variable auxiliaire et variant continûment de 0 à 1, fonction dont la pente est gouvernée par un paramètre auxiliaire dont l'évolution au cours du processus permet de faire tendre les pixels plutôt vers le blanc ou plutôt vers le noir. L'introduction d'une telle fonction permet de conserver la différentiabilité des équations intégrales vis-à-vis du contraste tout en permettant la reconstruction d'obstacles binaires.

La théorie ainsi que des résultats numériques ont fait l'objet d'un article [A.8] dont une copie est proposée en annexe (§ C).

3.3.3 Données incomplètes

Jusqu'à présent, l'ensemble des travaux présentés sur le gradient modifié, que ce soit en espace libre ou en milieu stratifié, en polarisation TM ou TE, l'avait été dans le cas de données dite « complètes » pour lesquels le module et la phase du champ diffracté sont mesurés. Or une mesure précise de la phase peut être un challenge difficile ; c'est pourquoi il est utile de s'intéresser à la résolution du problème inverse à partir de données incomplètes (dont seul le module[3] est mesuré). Pour résoudre un tel problème deux chemins sont possibles :

1. le développement d'un algorithme spécifique capable de traiter directement ces données incomplètes [Maleki *et al.*, 1992; Takenata *et al.*, 1997],
2. la résolution de deux problèmes inverses successifs, le premier permettant de reconstruire la phase du champ à partir de la connaissance du module, puis la résolution classique du problème inverse à partir de données complètes [Maleki et Devaney, 1993].

Une comparaison des méthodes dans le cas de la tomographie de diffraction dans le domaine optique a été effectuée [Maleki et Devaney, 1993] et a montré de meilleurs résultats dans le cas de la résolution successive de deux problèmes inverses. Cependant dans [Takenata *et al.*, 1997] un algorithme spécifique appliqué à la reconstruction d'un obstacle cylindrique en espace libre traitant directement les données incomplètes est présenté et les résultats obtenus sont satisfaisants dans nombre de configurations différentes. Aussi, pour notre part, nous avons choisi un chemin identique à celui de [Takenata *et al.*, 1997] permettant de conserver la même structure algorithmique et ne nécessitant que la réécriture d'une partie de la fonctionnelle coût et des gradients correspondants. Un résultat typique est présenté FIG. 3.3(d)

Les équations relatives au gradient modifié binaire à partir de données complètes et incomplètes ainsi que des résultats numériques dans un certain nombre de configurations ont fait l'objet d'un article [A.8] dont une copie est incluse en annexe (§ C).

3.3.4 Illustration des méthodes

Pour illustrer ces différentes méthodes de gradients modifiés une comparaison des résultats fournis par chacune a été extraite de [A.8]. La description de la configuration est la suivante : un espace est

[3] Situation qui limite encore plus les informations contenues dans les mesures.

séparé en un demi-espace supérieur de paramètres électromagnétiques ($\epsilon_{r1} = 1, \sigma_1 = 0$ S/m) à l'intérieur duquel la longueur d'onde est λ_0 et un demi-espace inférieur de paramètres électromagnétiques ($\epsilon_{r2} = 2$, $\sigma_2 = 0$ S/m) à l'intérieur duquel la longueur d'onde est définie par $\lambda_2 = \lambda_0/\sqrt{\epsilon_{r2}}$. Dans le demi-espace inférieur est placé un obstacle axisymétrique de section carrée centré en $(0, -0.50\ \mathrm{m})$, de côté $d = 0.52$ m et de permittivité relative $\epsilon_{r\Omega} = 3$ et de conductivité $\sigma_\Omega = 10^{-2}$ S/m. L'ensemble est illuminé par 15 lignes sources de fréquences 100, 200, 300 et 400 MHz, chacune de polarisation TE et d'amplitude unité, placées dans le demi-espace supérieur à une hauteur $y_S = 0.5$ m et équi-réparties horizontalement entre -5 m et $+5$ m. Le champ diffracté est, quant à lui, collecté, pour chaque fréquence par 47 récepteurs placés dans le demi-espace supérieur à une hauteur $y_R = 0.125$ m et équi-répartis horizontalement entre -10 m et $+10$ m. Le domaine de recherche est un carré centré en $(0, -0.50\ \mathrm{m})$ et de 1 m de côté.

Les résultats obtenus à 400 MHz en utilisant le *frequency hopping*[4] sont présentés FIG. 3.3.

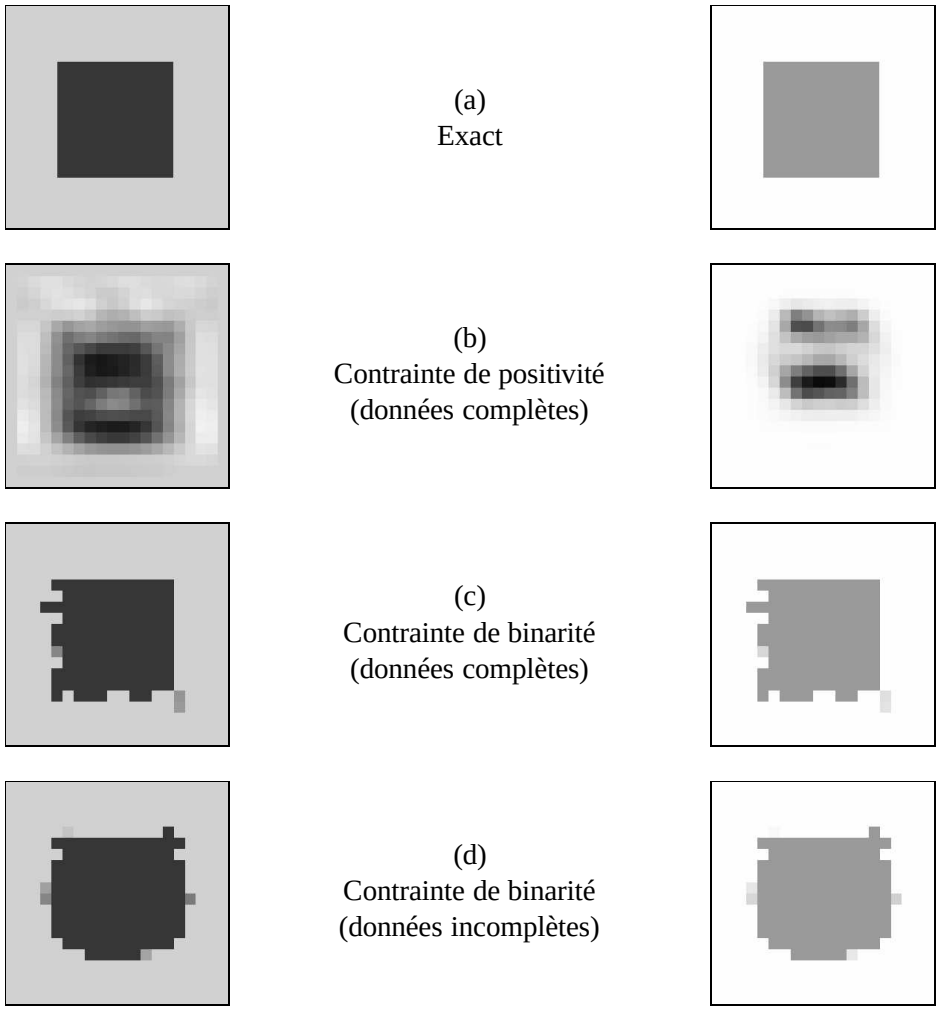

FIG. 3.3 – Comparaison de reconstructions obtenues par les différents gradients modifiés contraints développés au DRÉ. À droite, la carte de permittivité, et à gauche, la carte de conductivité.

[4]En *frequency hopping* les quatre fréquences ne sont pas utilisées simultanément mais l'une après l'autre de la plus basse à la plus haute. À chaque fréquence le processus est initialisé avec la solution obtenue à la fréquence immédiatement inférieure.

3.4 Problème inverse : les sources distribuées

Dans cette section nous nous intéressons à un problème inverse de diffraction des ondes acoustiques avec pour but la reconstruction de la forme d'un obstacle impénétrable immergé dans un chenal sous-marin. Ce travail, initié par C. Rozier [Rozier *et al.*, 1997] lors de sa thèse au L2S, s'est poursuivi notamment dans le cadre d'un Programme de Recherche en Commun CNRS-NSF qui a lié le Center of the Mathematics of Waves de l'Université du Delaware, le Laboratoire de Mécanique et d'Acoustique de Marseille et le L2S de 1998 à 2000.

La caractérisation, au sein d'un environnement marin de faible profondeur, d'un obstacle totalement ou partiellement enfoui dans l'eau ou dans le fond à partir de la mesure du champ de pression résultant de son interaction avec le champ émis par une ou plusieurs sources est un sujet d'intérêt croissant en acoustique sous-marine comme le prouve [Gilbert *et al.*, 1998] et les références qui s'y trouvent. Résoudre un problème inverse de ce type nécessite une bonne connaissance des paramètres non seulement de l'environnement (ceux de la colonne d'eau et du fond marin), ce qui est un problème inverse[5] par lui-même [Collins et Kuperman, 1994], mais également des sources et récepteurs, paramètres auxquels peuvent se rajouter des informations *a priori* sur les objets recherchés.

Le problème inverse de reconstruction de forme dans un environnement confiné tel qu'étudié ici diffère nettement de celui de l'obstacle en espace libre ; problème largement étudié dans la littérature comme le montre [Wirgin et Scotti, 1998] et les références qui y sont incluses ainsi que [Rozier *et al.*, 1997]. Ainsi l'expertise importante acquise dans le cas de l'espace libre n'est que partiellement utilisable dans le cas d'un milieu semi-confiné. La différence de comportement est due à la géométrie et aux particularités physiques qui conduisent non seulement à un problème inverse mal-posé ainsi que déjà précisé mais également à des questions théoriques toujours d'actualité sur la diffraction dans un guide d'onde [Angell *et al.*, 1996; Angell et Kleinman, 1997]. Questions concernant notamment l'unicité du problème aux conditions aux limites sous-jacent (en particulier l'existence de modes propagatifs) ; l'unicité de la solution du problème direct à partir de formulations intégrales spécifiques ; et la « complétude » de la représentation des champs. Bien que nécessitant clairement des investigations plus importantes, ces problèmes théoriques compliqués sortent du cadre des travaux décrits ici.

À ma connaissance, la reconstruction d'un obstacle impénétrable immergé dans un chenal marin de faible profondeur n'a été étudiée que dans dans le cadre d'approximations sur la propagation et la diffraction des ondes, par exemple, (i) la rétropropagation conduisant à la reconstruction de sources équivalentes dont on espère qu'elles se concentreront sur le domaine de l'obstacle [Carrion et Boehm, 1994] ; (ii) la suppression des phénomènes de résonance multiples pour extraire la fonction de diffraction décrivant le comportement de ce même obstacle en espace libre [Yang et Yates, 1994] ; (iii) l'utilisation de techniques de classification à partir de la détection des résonances du diffracteur [Guicking *et al.*, 1998]. À ces travaux s'ajoutent ceux, récents, sur l'ICDA (*Intersecting Canonical Domain approximation*) [Gilbert *et al.*, 1998; Buchanan *et al.*, 2000] sur la reconstruction d'un obstacle 3D « mou » à symétrie de révolution suivant la verticale immergé dans un chenal sous-marin. Sans entrer dans les détails, l'ICDA nécessite une solution canonique du problème direct, solution qui existe en 3D mais n'existe pas, à ma connaissance, dans le cas 2D étudié ici.

La configuration à laquelle nous nous intéressons peut être décrite de la façon suivante :

(i) L'environnement est modélisé par un guide d'onde plan qui consiste en une couche d'eau de hauteur H dont la densité et la célérité des ondes de compression sont constants. L'interface supérieure (air/eau) vérifie une condition de Dirichlet alors que l'interface inférieure (air/socle)

[5] Problème auquel je me suis intéressé lors de ma thèse et de mon séjour à Saclant Centre.

vérifie soit une condition de Neumann (fond dur) soit une condition de transmission (milieu fluide).

(ii) Une source est modélisée par une ligne source idéale. Elle est positionnée à une distance et une profondeur connue dans le guide d'onde et émet à une ou plusieurs fréquences.

(iii) L'obstacle est un obstacle cylindrique impénétrable unique dont le contour a une forme « en étoile » par rapport à un point d'origine et vérifie une condition de Dirichlet (obstacle « mou », pression totale nulle sur le contour) ou de Neumann (obstacle « dur », dérivée normale de la pression totale nulle sur le contour).

(iv) À une fréquence donnée le champ de pression complexe résultant est mesuré sur une ou deux séries de récepteurs verticaux positionnés à une distance connue et couvrant tout ou partie de la hauteur d'eau. Le cas d'un ou plusieurs réseaux placés horizontalement peut également être considéré.

Ce problème peut être vu comme une simplification excessive de la réalité ; il en contient cependant bon nombre d'ingrédients :

(i) Les interactions multiples entre l'obstacle et le guide d'onde ne peuvent être négligées notamment par le fait que nous travaillons dans le domaine de résonance dans lequel la taille de l'obstacle est de l'ordre de grandeur de la longueur d'onde de l'onde incidente se propageant dans l'eau.

(ii) L'aspect limité des données dû au fait que l'obstacle n'est pas vu de tous les côtés est essentiel, même si l'utilisation de plusieurs fréquences permet de combler en partie seulement ce manque d'information. De plus dans le cas d'un fond pénétrable (condition de transmission) une partie de l'énergie est absorbée et n'atteint pas les récepteurs, limitant encore la couverture des données.

(iii) Le problème inverse est résolu de façon exacte (aucune simplification telle que l'approximation de Born ou de l'acoustique physique ou toute autre approximation négligeant en partie ou totalement le couplage entre l'obstacle et les interfaces) et non-linéaire (minimisation d'une fonctionnelle coût mettant en jeu l'équation d'état et l'équation d'observation).

Pour résoudre ce problème notre choix s'est porté sur la méthode des sources distribuées notamment parce qu'elle avait déjà été appliquée avec succès par C. Rozier durant sa thèse dans le cas d'un objet dit « mou » (condition de Dirichlet sur son contour) immergé dans un guide d'ondes dont les parois sont impénétrables (condition limite de Dirichlet à la surface et de Neumann sur le fond) [Rozier *et al.*, 1997]. Plusieurs objectifs ont été poursuivis :

1. la généralisation du travail de C. Rozier au cas d'un objet « dur » (condition de Neumann sur le contour) dans un guide d'onde impénétrable : ce travail a été effectué en 1996 par E. Bocly lors de son stage de DEA. Ces travaux ont fait l'objet d'un article dans des actes de congrès édités [L5.3].
2. une généralisation des travaux précédents au cas d'un objet impénétrable « mou » ou « dur » placé dans un guide d'ondes à parois pénétrables : ce travail a non seulement nécessité une réécriture totale des algorithmes mais également la mise au point d'algorithmes d'accélération des calculs rendue nécessaire par la complexification des formulations. Ces travaux ont fait l'objet de plusieurs communications, d'une partie d'un article dans des actes de congrès édités [L5.4] et d'un article [A.6].
3. une extension de la méthode aux ondes électromagnétiques pour la reconstruction d'un obstacle parfaitement conducteur à partir d'un champ électromagnétique en polarisation TM ou TE.

Ces travaux sont illustrés par l'article [A.6] joint en annexe (§ D), article analysant le cas acoustique.

La méthode des sources distribuées et ses applications

La méthode des « sources distribuées » est basée sur l'hypothèse que les fonctions de Green du guide d'ondes forment une famille complète linéairement indépendante de solutions de l'équation de Helmholtz du guide d'ondes. Tout champ dans le guide peut alors s'écrire sous la forme d'une somme infinie de fonctions de Green du chenal pondérées par des coefficients constants et tout objet présent dans le guide d'ondes peut être remplacé par un ensemble infini dénombrable de sources intérieures ponctuelles dont les positions et les amplitudes complexes sont choisies de telle façon que le champ créé par ces sources vérifie la condition de passage — connue *a priori* (Dirichlet ou Neumann) — sur le contour de l'objet et donnent un champ identique au champ diffracté sur les récepteurs. La démonstration de la complétude des fonctions de Green n'a été effectuée [Angell *et al.*, 1996] que dans le cas d'un objet « mou » de contour « doux », objet placé dans un guide d'ondes vérifiant la condition de Dirichlet à la surface et la condition de Neumann sur le fond. L'extension de la méthode au cas d'un objet « dur » dans un guide à parois impénétrables et d'un objet impénétrable quelconque dans un guide ouvert n'est validée que par expérimentation numérique.

L'idée est la suivante : un obstacle initial (de contour circulaire par exemple) est remplacé par un ensemble fini de sources intérieures d'amplitude complexe dont les positions sont équi-réparties sur un contour intérieur homothétique à la frontière de l'obstacle. L'évolution de la position des sources intérieures et de leurs amplitudes (et par là même la modification de la frontière de l'obstacle) se fait par minimisation de deux fonctionnelles coûts, l'une mesurant l'écart entre le champ créé par ces sources sur les récepteurs et le champ diffracté par l'objet inconnu, l'autre imposant la condition aux limites sur la frontière. Afin de réduire le nombre d'inconnues du problème et de contraindre la frontière de l'obstacle reconstruit à être régulière, il a été choisi de décrire cette frontière sous la forme d'un polynôme trigonométrique à coefficients réels (contour dit en « étoile »), la position équi-répartie des sources intérieures s'en déduisant par un coefficient homothétique. Les inconnues du problème sont alors les coefficients réels décrivant le contour et les amplitudes complexes des sources.

Un algorithme d'inversion permettant la reconstruction de contour d'un objet impénétrable — utilisable tant en acoustique (objet « dur » ou « mou ») qu'en électromagnétisme (objet parfaitement conducteur en polarisation TE ou TM) — faisant appel aux familles complètes a été développé dans le cas d'un guide d'ondes à parois pénétrables. Un résultat typique de reconstruction dans le cas acoustique est présenté FIG. 3.4. Une grande partie des difficultés rencontrées lors du développement numérique s'est concentrée sur le calcul des fonctions de Green. En effet, dans le cas de d'un guide à parois impénétrables les fonctions de Green peuvent se calculer très rapidement — par exemple par une approche rayons/modes [Rozier *et al.*, 1997] — alors que dans le cas d'un guide d'ondes à parois pénétrables leurs calculs nécessitent l'utilisation d'une méthode spectrale beaucoup plus lente ; l'accélération des calculs est alors un point capital. La méthode choisie est basée sur un pré-calcul des fonctions de Green dans une zone pré-définie sur une grille très fine ($\lambda/20$, où λ est la longueur d'onde dans le guide d'ondes), ce qui permet, par interpolation bilinéaire, d'en déduire la valeur en tout point de la zone. Une telle technique a permis de réduire les temps de calcul pour une itération de plusieurs heures à quelques minutes. Le code ainsi développé permet, par ailleurs, de retrouver les résultats obtenus précédemment dans le cas du guide d'ondes impénétrable.

Cet algorithme d'inversion a été confronté à plusieurs types de données :

1. Données synthétiques en acoustique avec des objets impénétrables « mou » ou « dur » (FIG. 3.4). La configuration est la suivante : un objet est plongé dans un guide d'ondes rempli d'eau (modélisant un chenal sous-marin de faible profondeur (≈ 100 m), cet objet est éclairé par une source ponctuelle (fréquences de 30 Hz à 100 Hz), et le champ de pression est mesuré sur une ou deux lignes verticales couvrant tout le chenal.
2. Données réelles obtenues en électromagnétisme basse fréquence par J. M. Geffrin dans le cadre d'un contrat Gesma-DGA/CNRS. La configuration est la suivante : un objet métallique est plongé dans une cuve remplie d'eau (salée ou non), cet objet est illuminé par une source biconique (fréquences de 230 MHz à 810 MHz), et le champ électrique (polarisation TM) est recueilli sur un récepteur biconique se déplaçant horizontalement.
3. Données réelles obtenues en électromagnétisme à l'Institut Fresnel de Marseille (UMR 6133). Dans ce cas l'algorithme a été simplifié pour traiter la reconstruction d'objets en espace libre. La configuration est la suivante : un objet métallique placé en espace libre est illuminé par une antenne cornet (fréquences de 1 GHz à 16 GHz) et le champ électromagnétique (polarisation TM) est mesuré sur un arc de cercle autour de l'objet.

Illustration de la méthode

Pour illustrer cette méthode, des résultats extraits de [A.6] ont été choisis (FIG. 3.4). Nous nous situons dans un cas d'acoustique sous-marine dans une configuration de type guide d'onde (FIG. 3.1). La configuration est la suivante : un espace est divisé en un demi-espace supérieur de paramètres acoustiques ($\rho = 1$ kg/m^3, $c = 330$ m/s) et un demi-espace inférieur modélisant un socle de granit de paramètres acoustiques ($\rho_B = 2200$ kg/m^3, $c_b = 4000$ m/s, $\alpha_B = 0.01$ dB/m/kHz). Entre les deux une lame d'eau de hauteur $H = 100$ m et de paramètres acoustiques constants ($\rho_0 = 1030$ kg/m^3, $c_0 = 1500$ m/s) (l'atténuation étant négligé aux féquences qui nous intéressent). Dans cette lame d'eau est placé un objet « mou » ou « dur » elliptique (de petit axe 7.5 m et de grand axe 15 m) ou en forme de trèfle (d'équation $10 - 3\sin(3\theta)$). L'ensemble est illuminé par une source de fréquence 30 Hz placée à une profondeur de $z_s = 55$ m et à une distance de $x_s = -100$ m à droite de l'obstacle et le champ diffracté est recueilli sur deux réseaux de 41 récepteurs couvrant toute la hauteur d'eau et placés à une distance de 40 m de part et d'autre de l'obstacle.

3.5 Problème inverse : les ensembles de niveaux

Dans ce chapitre nous nous intéressons à la reconstruction d'objets homogènes enfouis dans un demi-espace de paramètres électromagnétiques connus, sources et récepteurs étant positionnés de l'autre côté du demi-plan séparant les deux demi-espaces. Ces travaux sont développés dans le cadre de la thèse de C. Ramananjaona. Ils prolongent et étendent — aux cas des objets enfouis en polarisation TM et TE — les travaux effectués, en polarisation TM, au laboratoire par A. Litman [Litman *et al.*, 1998] sur la reconstruction d'obstacles placés en espace libre à l'aide d'ensemble de niveaux. Ces travaux se font en collaboration avec J.-P. Zolésio de Sophia-Antipolis.

Ainsi qu'indiqué précédemment (§ 3.3) il existe bon nombre de méthodes pour résoudre un tel problème. À la différence du gradient modifié binaire (§ 3.3.2) où le but est la reconstruction d'un domaine à partir de pixels blancs ou noirs [Souriau *et al.*, 1996; A.8], nous nous intéressons ici à la reconstruction de la frontière d'un ou plusieurs obstacles à partir de la mesure du champ diffracté.

Plusieurs méthodes ont été proposées pour résoudre un tel problème que ce soit en espace libre ou en stratifié. Dans la majorité des cas elles sont basées sur l'évolution du contour inconnu ou des

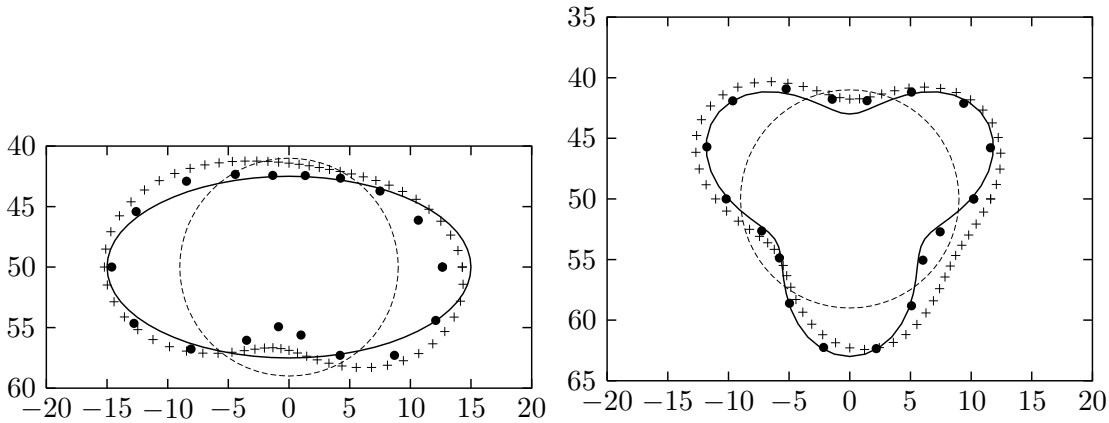

(a) (b)

FIG. 3.4 – Acoustique : reconstruction d'obstacles (ellipse ou trèfle) « dur » ou « mou » à l'aide d'une méthode de sources distribuées : solution exacte (trait épais), initialisation (trait fin), reconstruction pour un objet « mou » (disque noir) et pour un objet « dur » (croix). (a) Ellipse (b) Trèfle

coefficients le décrivant par une succession de petites perturbations. Pour mémoire je rappellerai les travaux effectués en électromagnétisme et en acoustique au laboratoire et présentés dans ce manuscrit (§ 3.4) dans le cas d'un obstacle dans un guide d'onde, travaux qui peuvent s'étendre sans difficulté au cas considéré ici. Notons également les travaux effectués par [Bonnard *et al.*, 1998] qui concernent la reconstruction d'un obstacle parfaitement conducteur au sein d'un milieu homogène à partir d'une formulation intégrale de contour. L'obstacle est décrit par un nombre fini de segments dont les centres sont les inconnues, et le problème inverse est résolu par une méthode de gradient conjugué régularisée. Une extension de la méthode au cas d'un obstacle diélectrique a été proposée [Bonnard *et al.*, 1999]. Cette méthode a l'avantage de ne pas utiliser de représentation polaire du contour permettant ainsi la reconstruction d'obstacles complexes mais nécessite une régularisation de ce contour pour éviter l'obtention de frontières trop chahutées.

Dans [Gosh Roy *et al.*, 1997] les auteurs s'intéressent, en acoustique, à la reconstruction d'un obstacle « dur » placé dans un espace fluide homogène infini. Le problème est résolu en faisant l'hypothèse que la frontière de l'obstacle n'est autre qu'une superposition de petites déformations d'un contour de géométrie simple. En s'appuyant sur une hypothèse de Rayleigh le champ diffracté par l'obstacle est écrit sous la forme d'une série de Taylor fonction d'un réel proportionnel à la déformation du contour (déformation décrite en coordonnées polaires), le rayon de convergence de la série étant étendu par l'utilisation de l'approximation de Padé. L'inversion est menée par une méthode de Gauss-Newton. Le cas de la reconstruction d'un cylindre parfaitement conducteur [Chiu et Kiang, 1991] ou de conductivité finie [Chiu et Kiang, 1992] enfoui dans un demi-espace a également été abordé. Le contour de l'obstacle est décrit en coordonnées polaires sous la forme d'une série de cosinus et sinus dont les coefficients sont les inconnues. L'équation intégrale de contour est discrétisée par une méthode de moments et l'inversion est basée sur une méthode de Newton-Kantorovitch.

Bien que ces méthodes soient efficaces, elles nécessitent la connaissance *a priori* du nombre d'obstacles à reconstruire pour initialiser correctement le processus. Dans [Bonnard *et al.*, 1999] l'opérateur de renversement temporel est utilisé pour estimer, dans la mesure du possible, le nombre de

diffracteurs présents avant d'appliquer l'algorithme d'inversion. Au laboratoire notre choix s'est porté sur une méthode d'ensemble de niveaux qui, bien que dédiée à la reconstruction de la frontière d'un ou plusieurs obstacles, ne nécessite aucune information sur leur nombre. En effet, les changements éventuels de topologie (apparition ou disparition d'un obstacle) sont naturellement pris en compte dans le processus. Bien que ces travaux se poursuivent (la soutenance de thèse de C. Ramananjaona n'aura lieu qu'à l'automne 2002), les avancées par rapport aux travaux d'A. Litman sont déjà nombreuses :

1. Un travail théorique conduisant à une réécriture complète des équations dans le cadre de la théorie du « Min-Max » a été nécessaire pour étendre au cas stratifié et à la polarisation TE les travaux précédents (tout en retrouvant ceux de l'espace libre et de la polarisation TM).
2. Un travail numérique conduisant aux développements de code permettant de résoudre le problème inverse en espace libre ou stratifié, en polarisation TE ou TM.
3. Une validation des algorithmes développés par confrontation avec des données synthétiques et expérimentales.

La théorie et les équations en polarisation TE et TM dans le cas d'objets enfouis ont été présentées dans un article [A.10] inclus en annexe (§ E). Les résultats obtenus par la méthode lorsqu'elle a été confrontée à des données réelles pour la reconstruction d'obstacles en espace libre ont également fait l'objet d'un article [A.11] également inclus en annexe (§ F).

La méthode des « ensembles de niveaux » et ses applications

La méthode des « ensembles de niveaux » développée ici est en fait une combinaison de deux méthodes. La première méthode est basée sur les travaux de J. Sethian [Sethian, 1999] pour la représentation de la forme d'un objet par un ensemble de niveaux — la frontière de l'objet est donnée par le niveau zéro de l'ensemble de niveaux, les valeurs négatives correspondant à des points intérieurs de l'obstacle — et de F. Santosa [Santosa, 1996] pour leurs utilisations dans la résolution de problèmes inverses de diffraction. L'idée est de faire évoluer cet ensemble de niveaux en espace et en temps fictif à l'intérieur d'un domaine fixé *a priori* afin de minimiser une certaine fonctionnelle coût judicieusement choisie. On montre que l'évolution de ces fonctions niveaux est régie par une équation de mouvement de type Hamilton-Jacobi qui prend en compte naturellement les changements éventuels de topologie. Elle lie, par l'intermédiaire d'une vitesse de déformation, la dérivée partielle de l'ensemble de niveaux par rapport au temps fictif à la norme du gradient spatial de cet ensemble de niveaux. Le choix de cette vitesse de déformation est capital car c'est elle qui contrôle l'évolution des ensembles de niveaux et, par là même, la convergence du processus d'optimisation.

La deuxième méthode est basée sur des travaux sur les « méthodes de vitesse » largement utilisées dans la conception optimale de formes [Sokolowski et Zolésio, 1992]. Elle permet de choisir cette vitesse de telle sorte qu'à chaque instant fictif la décroissance de la fonctionnelle coût soit assurée. Pour ce faire il suffit de calculer la dérivée de cette fonctionnelle par rapport au temps fictif et de choisir la vitesse de telle façon que cette dérivée soit toujours négative.

Pour adapter un tel processus aux problèmes inverses de diffraction des ondes qui nous intéressent ici, il est nécessaire de choisir une fonctionnelle coût adaptée. Son expression est classiquement donnée par la norme au carré de l'écart entre le champ diffracté par l'objet inconnu[6] et le champ calculé par le modèle à un certain temps fictif. Un des points clés du processus est de trouver une expression de la dérivée de la fonctionnelle coût. Dans les travaux initiaux en espace libre, son expression a été établie dans le cadre non nécessairement simple de la théorie variationnelle [Litman *et al.*, 1998].

[6] Il est entendu par « objet inconnu » un ou plusieurs obstacles présents dans le domaine de recherche.

L'extension des démonstrations pour le cas de l'objet enfoui en TE et en TM s'est avérée compliquée et une reformulation du problème dans le cadre de la théorie du « Min-Max » [Cuer et Zolésio, 1988] — dans laquelle il est montré que cette dérivée est égale à l'expression, au point selle, de la dérivée partielle par rapport au temps fictif d'une fonctionnelle judicieusement choisie — a permis non seulement de retrouver l'expression établie dans le cas de l'espace libre mais également d'établir, de façon rigoureuse, les expressions en milieux stratifiés. On montre alors que la vitesse de déformation, qui se déduit de la dérivée de la fonction coût, s'écrit en fonction des solutions du problème direct et de son problème adjoint en polarisation TM et en fonction du gradient de ces solutions en polarisation TE. Son calcul ne nécessite que la résolution de deux problèmes directs, le problème adjoint n'étant, classiquement, qu'un problème direct pour lequel les sources sont positionnées en lieu et place des récepteurs et sont d'amplitudes proportionnelles à l'écart entre le champ diffracté et le champ calculé par le modèle à ces emplacements.

Du point de vue pratique, une formulation par intégrale de domaine de la solution de l'équation de Helmholtz scalaire en TE et TM a été choisie. Sa résolution se fait à l'aide d'une méthode de moments pour laquelle le domaine $\mathcal{D}$ supposé contenir l'objet à reconstruire est discrétisé en pixels rectangulaires dans le cas TM et triangulaires dans le cas TE (§ 3.2). Ce travail a nécessité le développement d'un code de résolution du problème direct pour la polarisation TM et l'incorporation de celui déjà développé pour la polarisation TE (§ 3.2). Une des équations clé du processus est l'équation de Hamilton-Jacobi ; sa version discrétisée nécessite l'introduction dans le processus d'un pas de temps discrétisé dont l'importance est cruciale dans la convergence du processus et dont le choix, pour le moment heuristique, est un problème : trop grand, le processus diverge, trop petit, la convergence est lente. Un travail est actuellement mené pour trouver un critère de choix optimal de pas de temps et un schéma de son évolution au cours du processus. En parallèle, des travaux sur l'ajout, dans la fonctionnelle coût, de contraintes de périmètre et de volume se poursuivent et leurs influences sur les reconstructions et sur la convergence du processus sont à l'étude.

Cet algorithme d'inversion a été confronté à plusieurs types de données :

1. Données synthétiques en électromagnétisme (polarisation TM et TE) avec des objets diélectriques. La configuration est la suivante : un objet est plongé un demi-espace, cet objet est éclairé par plusieurs sources ponctuelles (fréquences de 100 MHz à 400 MHz) placées dans l'autre demi-espace et le champ électromagnétique (E ou H) est mesuré sur une ligne horizontale placée également dans cet autre demi-espace.
2. Données réelles obtenues en électromagnétisme à l'Institut Fresnel de Marseille (UMR 6133). Dans ce cas l'algorithme a été simplifié pour traiter la reconstruction d'objets en espace libre. La configuration est la suivante : un ou plusieurs objets diélectriques ou métalliques placés en espace libre sont illuminés par une antenne cornet (fréquences de 1 GHz à 16 GHz) et le champ électromagnétique est mesuré sur un arc de cercle autour de l'objet.

Illustration de la méthode

Ce résultat (FIG. 3.5) est extrait de [A.10] et concerne la reconstruction d'un objet enfoui dans un demi-espace (FIG. 3.1). La configuration est la suivante : un espace est séparé en un demi-espace supérieur de paramètres électromagnétiques ($\epsilon_{r1} = 1$, $\sigma_1 = 0$ S/m) à l'intérieur duquel la longueur d'onde est λ_0 et un demi-espace inférieur de paramètres électromagnétiques ($\epsilon_{r2} = 2$, $\sigma_2 = 0$ S/m) à l'intérieur duquel la longueur d'onde est définie par $\lambda_2 = \lambda_0/\sqrt{\epsilon_{r2}}$. Dans le demi-espace inférieur sont placés deux obstacles axisymétriques de permittivité relative $\epsilon_{r\Omega} = 3$ et de conductivité $\sigma_\Omega = 0$ S/m, l'un de section carrée de côté 0.29 m centré en $(0.28\text{ m}, -0.25\text{ m})$, l'autre de section rectangulaire de

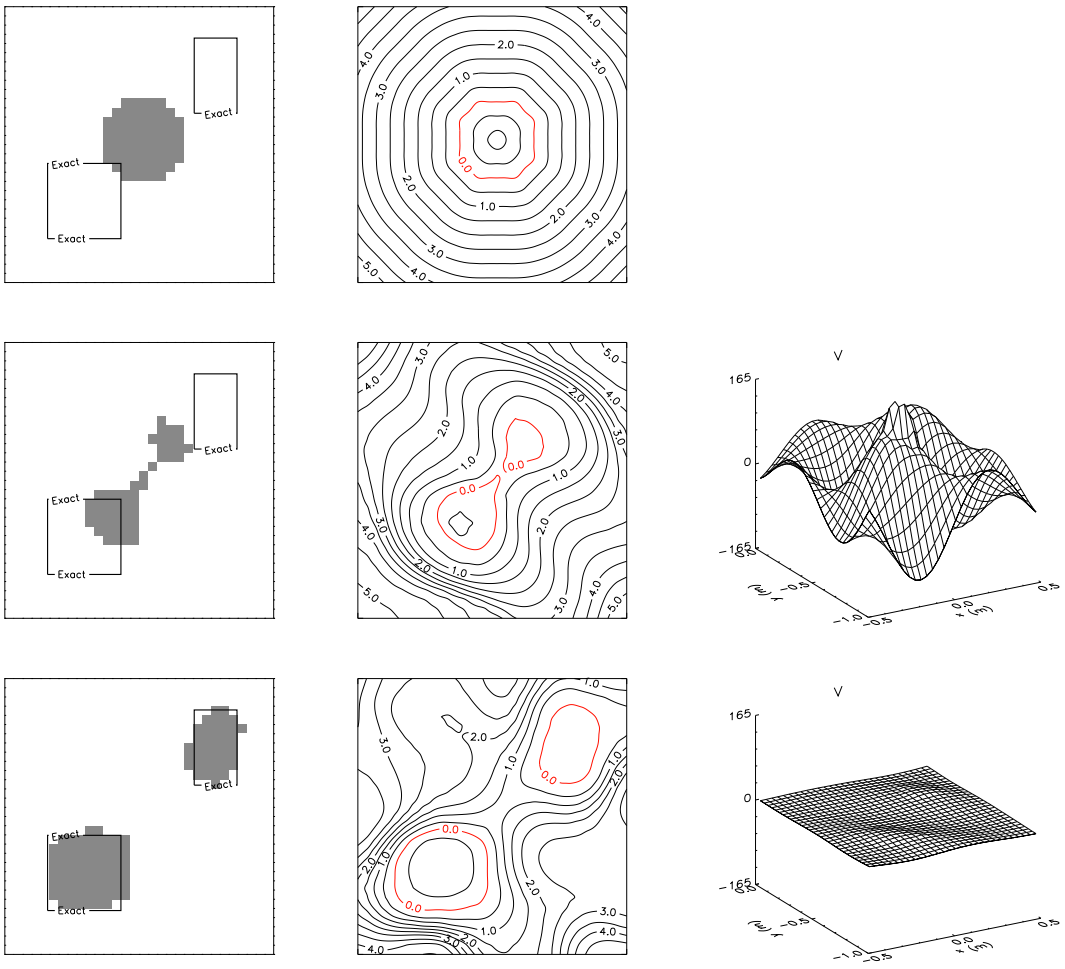

FIG. 3.5 – Évolution du domaine Ω, level set ϕ et de la vitesse V (respectivement à gauche, au centre et à droite). En haut l'initialisation du processus par un disque centré de rayon 0.15 m ; au centre : la 5ième itération ; en bas : le meilleur résultat (obtenu à la 421ième itération). Le pas de temps utilisé est $\Delta t = 3\,10^{-3}$.

côté 0.18 m selon les x et 0.29 m selon les y centré en $(-0.18\text{ m}, -0.68\text{ m})$. L'ensemble est illuminé par 15 lignes sources de fréquence 200 MHz, de polarisation TE et d'amplitude unité placées dans le demi-espace supérieur à une hauteur $y_S = 0.5$ m équi-réparties horizontalement entre -5 m et $+5$ m. Le champ diffracté est collecté par 47 récepteurs placés dans le demi-espace supérieur à une hauteur $y_R = 0.125$ m équi-réparties horizontalement entre -10 m et $+10$ m. Le domaine de recherche est un carré centré en $(0, -0.50\text{ m})$ et de 1 m de côté.

4

Évaluation non destructive d'objets tridimensionnels

Sommaire

4.1 Introduction

Dans ce chapitre nous nous intéressons aux phénomènes électromagnétiques relatifs à des objets tridimensionnels placés dans un environnement complexe avec des préoccupations de détection et de caractérisation de structures dans des milieux naturels (le sous-sol proche ou lointain) ou artificiels (plaque métallique, composite, ...). Les méthodes de détection de ces structures varient selon les applications :

- le sondage d'un sous-sol profond (quelques centaines de mètres) pour la détection de grandes structures (amas minéral de plusieurs dizaines de mètres de longueur caractéristique) nécessite l'utilisation de signaux basse-fréquence (de la dizaine de Hz à quelques kHz).
- le sondage d'un sous-sol proche (quelques mètres à quelques dizaines de mètres) pour la détection de cavités, mines, pièces métalliques ou zones de pollution, requiert des fréquences plus élevées (de l'ordre du MHz) pour une profondeur plus faible.
- la détection de fissures, inclusions dans des plaques métalliques (de conductivité de quelques MS/m) nécessite des fréquences assez basses (quelques centaines de kHz) pour une profondeur de pénétration de quelques millimètres.

Dans la plupart de ces applications les milieux sont conducteurs, nous conduisant à travailler en régime diffusif (les champs électromagnétiques sont atténués), la taille des structures étant soit de l'ordre de grandeur de l'épaisseur de peau caractéristique de l'encaissant (domaine de résonance) soit inférieure (domaine basse-fréquence). Le but de ce travail est le développement de techniques d'inversion adaptées aux applications visées. Il nécessite clairement la modélisation de la réponse d'une structure enfouie dans un milieu complexe soumis à une excitation électromagnétique. L'accent a été

mis sur le cas d'un ou plusieurs obstacles tridimensionnels enfouis dans un milieu stratifié modélisant soit un demi-espace soit une lame d'épaisseur finie, l'ensemble étant illuminé par une ou plusieurs sources généralement placées à la surface et le champ vectoriel diffracté mesuré soit dans l'encaissant (application de géophysique principalement) soit à la surface (application de contrôle non destructif).

Deux applications (FIG. 4.1) ont été privilégiées :

- Le contrôle non destructif par courants de Foucault (FIG. 4.1(a)) dont le but est la détection de défauts (fissures, inclusions, vide, ...) dans des plaques métalliques conductrices. Application pour laquelle la taille caractéristique des défauts est de l'ordre de grandeur de l'épaisseur de peau[1]. Nous sommes dans le domaine de résonance conduisant à utiliser une formulation dite « exacte ».
- La prospection géophysique (FIG. 4.1(b)) dont le but est la détection d'amas minéraux enfouis dans le sous-sol profond. Application pour laquelle la taille caractéristique des amas est très inférieure à l'épaisseur de peau. Nous sommes alors dans le domaine basse-fréquence permettant l'utilisation de développements de type Rayleigh.

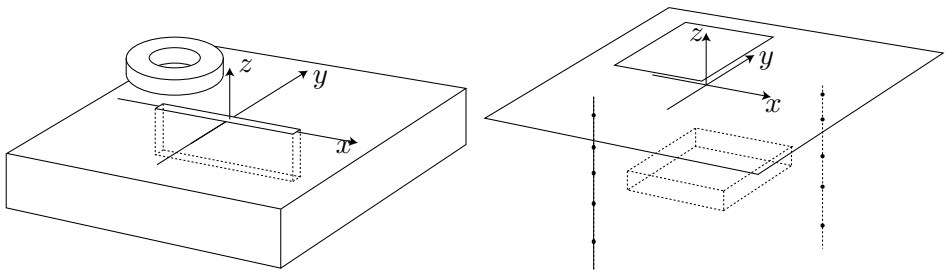

(a) (b)

FIG. 4.1 – Configurations d'intérêt : le contrôle non destructif par courants de Foucault (a) et la détection d'amas minéraux en géophysique de prospection (b).

L'ensemble des travaux présentés dans ce chapitre est basé sur une formulation intégrale de domaine dont les grandes lignes sont rappelées ci-après.

Formulation intégrale

La prise en compte des acquis du laboratoire a tout naturellement conduit à choisir une formulation intégrale de domaine vectorielle —obtenue par application du théorème de Green aux équations gouvernant la propagation des champs— pour résoudre un tel problème. Cette formulation conduit à résoudre deux équations intégrales dans lesquelles interviennent les dyades de Green du milieu stratifié :

- l'équation de couplage relie le champ total dans l'obstacle au champ incident (émis par la source placée dans l'air ou dans le sol) présent dans le milieu en l'absence d'obstacle et à lui-même par l'intermédiaire de la dyade de Green du milieu stratifié et d'une fonction contraste mesurant l'écart entre les paramètres électromagnétiques du milieu stratifié et de l'obstacle.

[1] L'épaisseur de peau (défi nie pour une onde plane) donne une information sur l'atténuation des champs et donc sur la profondeur de pénétration de l'onde.

– l'équation d'observation relie le champ mesuré sur les récepteurs (placés dans l'air ou dans le sol) au champ total dans l'obstacle par l'intermédiaire d'une autre dyade de Green du milieu stratifié et de la fonction contraste.

Au préalable, il s'agit de trouver une expression des dyades de Green ; celles-ci ne sont autres que les solutions élémentaires des équations de propagation des champs pour une source élémentaire modélisée par un petit élément de courant. Chaque dyade se divise en deux termes : un terme singulier modélisant le rayonnement d'un élément de courant électrique ou magnétique dans un espace homogène et dont la formulation est connue analytiquement dans le domaine des fréquences spatiales et le domaine spatial ; un terme régulier prenant en compte les réflexions sur et les transmissions à travers les interfaces et dont la formulation analytique n'est connue que dans le domaine spectral. Ce dernier terme est obtenu par décomposition sur une base de fonctions propres décrivant la propagation bien connue des ondes planes de polarisations TE et TM le long de l'axe perpendiculaire aux stratifications et prenant en compte les continuités des champs aux interfaces [Chew, 1995]. Une transformation de Fourier bidimensionnelle suivant les deux variables latérales permet un retour au domaine spatial.

Une fois connue l'expression des dyades de Green le problème direct est résolu en deux étapes :

1. le calcul du champ total dans l'obstacle à partir de l'équation de couplage : cette étape est la plus coûteuse en temps de calcul même si la structure de convolution suivant les variables latérales des équations intégrales permet l'utilisation de méthodes de type gradient conjugué par TFR. Différentes méthodes ont été proposées pour éviter de la résoudre et permettre d'en obtenir une solution approchée. Ainsi, ont été privilégiées des approximations basées sur l'observation que la dyade de Green, dans l'équation de couplage, présente des pics importants et une décroissance forte (liée à l'atténuation présente dans les matériaux) impliquant que seul le domaine proche d'un point contribue au champ rayonné en ce point. Cette hypothèse, dite de type Born étendu, introduite dans [Habashy *et al.*, 1993] pour un cas de géophysique et étendue dans [Zhdanov et Fang, 1996; Zhdanov et Hursan, 2000], toujours en géophysique, permet d'écrire une relation linéarisée entre le champ total dans l'obstacle et le champ incident par l'intermédiaire d'une dyade[2] dont la formulation, plus ou moins simple suivant les approximations choisies, fait notamment intervenir le produit de la dyade de Green et de la fonction contraste, le tout intégré sur le volume de l'obstacle.
2. le calcul du champ diffracté sur les récepteurs à partir de l'équation d'observation, qui ne pose pas de problème particulier.

Plan du chapitre

Les deux premières sections traitent de la résolution du problème direct par deux approches complémentaires : une (§ 4.2) basée sur l'utilisation d'une méthode de moments est une méthode numérique permettant l'obtention de résultats dits « exacts », car provenant d'une résolution « exacte » des équations impliquées au prix de temps de calcul important ou de résultats approchés impliquant des approximations de type Born et pour un coût numérique réduit ; l'autre (§ 4.3) correspondant à des approches semi-analytiques des équations intégrales dans le cas des basses fréquences (développement de type Rayleigh) pour un objet canonique (ellipsoïde).

Les deux sections suivantes présentent la résolution du problème inverse par deux approches différentes : la première (§ 4.4), appliquée au contrôle non destructif par courants de Foucault, conduit à la reconstruction de cartes de conductivité dans une zone prescrite à l'aide d'une méthode d'inversion

[2]Dans le cas de l'approximation de Born cette dyade n'est autre que la dyade unité

dite « de contraste de source » ; la seconde (§ 4.5), appliquée en basse fréquence, consiste à rechercher des sources équivalentes (ici des dipôles) à la structure diffractante, sources dont la position et les amplitudes donnent des informations sur la position de cette structure, son volume et sa conductivité.

4.2 Problème direct : une méthode de moments

Ces travaux sont développés dans le cadre de la thèse de D. Dos Reis débutée en 1998 et dont la soutenance aura lieu en novembre 2001. Ils prolongent ceux effectués par V. Monebhurrun lors d'un séjour postdoctoral au DRÉ en 1997 [Ruosi *et al.*, 2000].

Nous nous intéressons ici à la modélisation de l'interaction d'une onde électromagnétique émise par une source placée au dessus d'une interface avec un obstacle tridimensionnel enfoui au sein d'un demi-espace ou d'une lame conductrice, champ diffracté ou impédance étant mesuré à la surface. La modélisation choisie permet de traiter à la fois des configurations de type contrôle non destructif par courants de Foucault et de type géophysique de prospection. Cette étude a été conduite pour permettre une bonne compréhension de l'interaction entre l'obstacle et la source, la diversité des géométries et propriétés électriques, la stratification du milieu environnant, les sources de courants localisées et le champ proche devant être pris en compte. Elle permet également de déduire l'influence des différents paramètres géométriques et électromagnétiques sur le champ diffracté afin d'extraire les paramètres prépondérants en vue d'inversions futures. Ont été mis au point des codes généraux de méthodes de moments développés à partir de formulations intégrales vectorielles de volume du champ électromagnétique (en geophysique de prospection [Newman et Hohmann, 1988; Wannamaker *et al.*, 1984; Xiong et Tripp, 1995; Xiong et Tripp, 1997]), en optique [Kottmann et Martin, 2000], en contrôle non destructif par courant de Foucault [Ruosi *et al.*, 2000], en microondes [Gan et Chew, 1995; Zwamborn et van den Berg, 1992]) ou de formulations intégrales vectorielles de surface (en géophysique de prospection [Liu et Lamontagne, 1998; Liu et Lamontagne, 1999], en contrôle non destructif par courants de Foucault, dans le cas particulier de fissures [Bowler, 1994; Yoshida et Bowler, 2000]).

Pour notre part une formulation intégrale de volume vectorielle a été choisie et les équations discrétisées par une méthode de moments. Deux voies de résolution du système linéaire ont été suivies. La première conduit à une résolution exacte des équations intégrales par une méthode de gradient conjugué combinée à des TFR pour bénéficier au mieux de la structure de convolution des équations. Cependant cette résolution exacte du problème direct peut se révéler extrêmement coûteuse en temps CPU notamment en raison de la complexité des interactions mises en jeu et de la taille des problèmes à résoudre. La seconde propose plusieurs types de solutions approchées à un coût numérique moindre. Ces méthodes ont été récemment introduites en géophysique pour obtenir une solution approchée du problème direct lorsque le diffracteur est enfoui au sein d'un milieu atténuant [Habashy *et al.*, 1993; Zhdanov et Fang, 1996; Zhdanov et Hursan, 2000]. Ces approximations, dites de « Born étendu », sont basées sur l'observation que la dyade de Green, solution élémentaire de l'équation de propagation, présente des pics importants et une décroissance forte. Cette observation permet de simplifier la résolution du problème direct en évitant la résolution exacte de l'équation de couplage et en la remplaçant par une relation linéarisée entre le champ incident et le champ total par l'intermédiaire d'une dyade de dépolarisation dont l'expression dépend de l'approximation choisie.

Lors de ce travail un algorithme de résolution du problème direct a été développé et validé par comparaison avec des données synthétiques en géophysique et expérimentales en contrôle non destructif. Les différentes approximations introduites en géophysique ont été utilisées en CND et les résultats validés par comparaison avec une résolution exacte.

Les détails sur la formulation des équations intégrales et des approximations de type Born étendu sont présentés dans un article [A.12] soumis pour publication dans l'*International Journal of Applied Electromagnetics and Mechanics*, publication reproduite en annexe (§ H).

Méthode de moments

La résolution numérique du problème n'est possible qu'à l'aide d'une version discrète de ces équations intégrales. Elle est obtenue par l'utilisation d'une méthode de moments dans laquelle l'obstacle est discrétisé en voxels de forme parallélépipédique rectangle et nécessite l'intégration de la dyade de Green sur chacun de ces voxels. Le terme singulier de la dyade de Green est exprimé analytiquement dans le domaine spatial et intégré numériquement par un schéma de type Gauss-Legendre alors que le terme régulier est intégré analytiquement dans le domaine des fréquences spatiales puis son expression dans le domaine spatial est obtenue par transformée de Fourier bidimensionnelle selon les variables latérales. La solution du système linéaire résultant est obtenue soit de façon exacte (gradient conjugué par TFR) soit de façon approchée.

L'algorithme ainsi développé s'est révélé satisfaisant mais très sensible à la discrétisation et à la forme des voxels utilisés rendant son usage délicat. Sa validation s'est faite par comparaison avec :

- des données synthétiques en géophysique de prospection fournies par M. S. Zhdanov de l'Université de l'Utah. La configuration est la suivante : un obstacle conducteur est enfoui dans un demi-espace faiblement conducteur (quelques mS/m), l'ensemble est illuminé par une source rectangulaire placée à la surface et le champ diffracté est également recueilli à la surface. Les fréquences de travail s'étendent de 10 Hz à 1000 Hz.
- des données réelles en contrôle non destructif par courants de Foucault obtenues soit dans la littérature [Takagi *et al.*, 1995a; Takagi *et al.*, 1995b] soit auprès du Center for Nondestructive Evaluation de l'Université de l'Iowa[3]. La configuration est la suivante : une fissure plane de largeur très inférieure à l'épaisseur de peau affecte une lame très conductrice (quelques MS/m), l'ensemble étant illuminé par une bobine placée à la surface et les récepteurs, mesurant soit une impédance soit un champ magnétique, étant également positionnés en surface. Les fréquences de travail vont de 150 kHz à 300 kHz.

Illustration de la méthode

Pour illustrer ce travail une figure (FIG. 4.2) a été extraite de [A.12]. Elle montre une comparaison entre des mesures obtenues auprès du Center for Nondestructive Evaluation de l'Université de l'Iowa et les modèles développés au DRÉ. La configuration est la suivante : une fissure plane de longueur 5.435 mm selon x de largeur 0.269 mm selon y et de profondeur 0.46 mm selon z affecte une lame d'Inconel de conductivité $\sigma_2 = 0.8$ MS/m et d'épaisseur 1.265 mm. L'impédance d'une sonde de type boucle circulaire épaisse se déplaçant, selon x, à une hauteur de 0.458 mm au dessus de la fissure est mesurée et comparée aux impédances calculées, de façon exacte ou approchée, par le modèle.

4.3 Problème direct : développement basse fréquence

Cette section présente une analyse basse fréquence de la diffraction électromagnétique par un obstacle conducteur quelconque enfoui dans un sol également conducteur pour des applications de type géophysique de prospection. Ces travaux ont été développés par G. Perrusson pendant sa thèse

[3]Consultable à l'adresse suivante http ://www.cnde.iastate.edu/ec/Projects/Projects.html

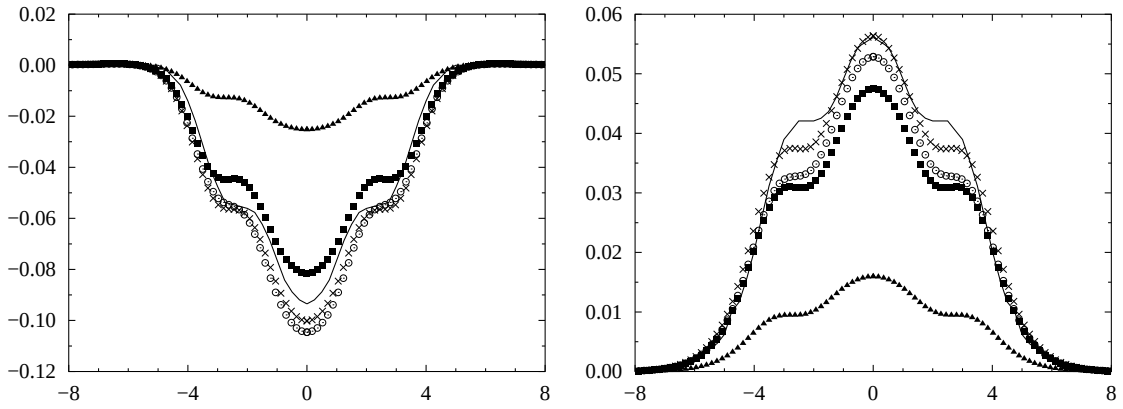

(a) (b)

FIG. 4.2 – 150 kHz, partie réelle (a) et imaginaire (b) de la variation d'impédance de la sonde ΔZ (Ω) selon l'axe x (mm) ; mesure (trait continu), solution exacte (croix), LN (cercle), QLS (triangle), QA (carré)

(soutenue en octobre 1999 et à l'encadrement de laquelle j'ai participé) dans un cadre coopératif comprenant la Division de Mathématiques Appliquées de l'Université de Patras (dans le cadre d'une Action Intégrée franco-grecque PLATON) et le BRGM (dans le cadre d'un contrat de collaboration).

L'introduction de systèmes de mesure des trois composantes de champ dans l'exploration électromagnétique du sous-sol a permis, ces dernières années, d'importants progrès. De tels systèmes permettent d'obtenir les trois composantes complexes du champ magnétique dues à une source de courant opérant à plusieurs fréquences, de quelques dizaines de Hz à plusieurs kHz. La source peut être une boucle de courant à la surface (configuration surface-à-puits), un dipôle magnétique près d'un puits de forage (configuration de tomographie ou puits-à-puits), ou un dipôle magnétique se déplaçant à une distance fixée d'un récepteur dans le même puits (configuration en auto-puits). Le système Slim-Boris [Bourgeois et Alayrac, 1999] et le prototype de sonde tri-axial [L4.1] sont représentatifs de tels instruments.

La mesure des composantes du champ magnétique requiert un traitement approprié ou « réduction » car il contient à la fois le champ primaire[4] (dû à l'interaction de la source avec l'environnement géologique) et le champ secondaire[5] (dû à l'obstacle inconnu ou partiellement connu). C'est ce champ secondaire qui contient les informations sur les paramètres électriques et géométriques de l'obstacle. Suivant la couverture des données, la connaissance géologique, les algorithmes d'inversion et les désirs de l'utilisateur, le but final est la localisation, l'estimation de la taille, l'orientation, la reconstruction de la forme et/ou une évaluation moyenne ou locale des paramètres électriques de l'obstacle. Ainsi que souvent indiqué, toutes nécessitent, dans un premier temps, une bonne compréhension de l'interaction entre l'obstacle et l'environnement (structure du milieu, paramètres électromagnétiques, position des sources et des récepteurs, ...). Pour ce faire, ainsi que résumé dans la section précédente (§ 4.2), de nombreux codes généraux ont été développés ; ils peuvent cependant être coûteux du point de vue numérique et leur utilisation loin d'être simple. C'est pourquoi le développement de codes

[4] Également appelé champ incident
[5] Également appelé champ diffracté

rapides, certes moins généraux et précis, mais basés sur une compréhension fine du comportement des champs électromagnétiques reste nécessaire.

La combinaison de la traditionnelle et rigoureuse théorie de la diffraction basse fréquence [Kleinman et Senior, 1987; Dassios et Kleinman, 2000] et de l'approximation non-linéaire (souvent appelée « approximation de Born étendue » introduite dans [Habashy *et al.*, 1993] et récemment étendue à l'évaluation non destructive par courants de Foucault) permet d'atteindre ce but. Ces travaux ont permis de développer plusieurs approximations basse-fréquence conduisant à la mise au point d'algorithmes de calcul rapide du champ magnétique diffracté par un ellipsoïde placé au sein d'un milieu conducteur.

Ces travaux ont fait l'objet de deux articles [A.7; A.9] dont l'un [A.9] est reproduit en annexe (§ G).

Approximation localisée non-linéaire hybride

Dans ce type d'application la fréquence du signal incident est basse (quelque centaines de Hz) afin de compenser l'atténuation due à la conductivité du milieu environnant et permettre une profondeur d'exploration suffisante. La taille caractéristique de l'obstacle est donc très inférieure à l'épaisseur de peau dans l'encaissant et le champ diffracté n'est alors sensible qu'au volume de cet obstacle et à sa conductivité moyenne, conduisant ainsi à assimiler cet obstacle tridimensionnel à un ellipsoïde homogène, forme canonique la plus générale pour décrire un objet 3D et permettant l'utilisation du système de coordonnées ellipsoïdales pour les calculs analytiques.

La configuration d'intérêt est la suivante (FIG. 4.3) : un ellipsoïde conducteur ($\approx 10^{-3}$ S/m) enfoui au sein d'un demi-espace stratifié homogène conducteur ($\approx 10^{-4}$ S/m) est éclairé par une source électromagnétique localisée, plus ou moins complexe (un dipôle magnétique par exemple), placée soit à la surface soit dans un puits de forage, le champ diffracté résultant étant recueilli sur une série de récepteurs placés en puits de forage.

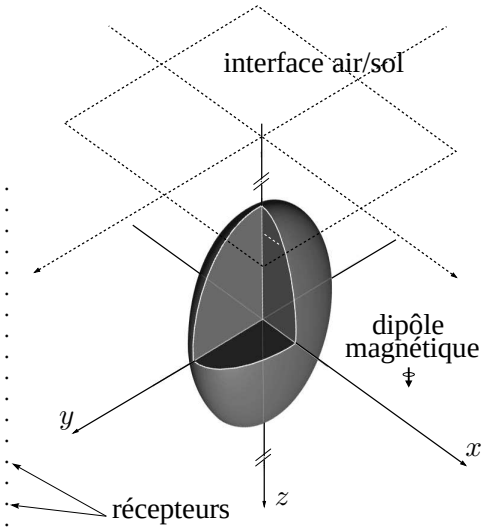

FIG. 4.3 – Configuration type

Les distances objet/source et objet/récepteurs étant petites devant l'épaisseur de peau, nous sommes alors en situation de *champ proche* pour laquelle l'interaction entre l'obstacle et l'interface peut être négligée, la configuration se simplifiant alors au cas d'un ellipsoïde enfoui au sein d'un espace homogène éclairé par une source électromagnétique localisée. Les équations intégrales ne font intervenir que la dyade de Green d'un milieu homogène[6] dont l'expression analytique simple est connue dans le domaine spatial.

De la même façon que précédemment, il s'agit de résoudre l'équation de couplage afin d'en déduire le champ total partout dans l'ellipsoïde puis l'équation d'observation pour obtenir le champ diffracté sur les récepteurs. La méthode dite « hybride » développée ici permet de simplifier la résolution de l'équation de couplage. Elle combine l'*approximation localisée non-linéaire*[7] [Habashy *et al.*,

[6] Cette dyade d'un milieu homogène correspond à la partie singulière de la dyade d'un milieu stratifié.

[7] Également appelé « Born étendu ».

1993] — qui permet d'approximer le champ total dans l'objet par la projection du champ incident sur un tenseur de « dépolarisation » qui fait intervenir l'intégrale de la dyade de Green sur le volume de l'ellipsoïde — et un développement basse-fréquence de type Rayleigh — qui consiste à développer les grandeurs d'intérêt (champ, dyade de Green, contraste, ...) du problème en puissances entières de $\mathrm{j}\,k$ à coefficients réels où k est le nombre d'onde dans le milieu encaissant. La combinaison de ces deux approches et l'utilisation des coordonnées ellipsoïdales a permis d'obtenir une expression analytique des trois premiers termes du développement en puissance de $(\mathrm{j}\,k)$ du tenseur de « dépolarisation ».

L'approximation du champ diffracté est obtenue par remplacement à l'intérieur de l'équation intégrale d'observation du champ total par le résultat de la projection du champ incident sur le développement basse-fréquence de la dyade de « dépolarisation ». Deux chemins s'offrent pour une poursuite des approximations :

- l'équation intégrale d'observation est calculée numériquement, c'est l'« approximation *partielle* du champ diffracté ».
- un développement basse-fréquence du champ diffracté est effectué, c'est l'« approximation *totale* du champ diffracté ». Elle est obtenue grâce au développement basse-fréquence des termes présents dans l'équation intégrale d'observation (dyade de Green, fonction contraste, dyade de « dépolarisation » et champ incident).

Jusqu'à présent source et ellipsoïde sont supposés être enfouis au sein d'un espace homogène ; cependant la prise en compte partielle de l'interface peut être faite en remplaçant le champ incident rayonné en espace libre par celui rayonné dans un demi-espace. Ceci revient à négliger l'influence de l'interface sur l'expression de la dyade de « dépolarisation » — ce qui peut se justifier par le fait que la profondeur de l'ellipsoïde est beaucoup plus grande que sa dimension la plus grande — et les interactions multiples entre l'ellipsoïde et la surface —ce qui peut se justifier par le fait que la distance objet/récepteurs est très inférieure à la distance ellipsoïde/interface. Les deux approximations *partielle* et *totale* sont également applicables.

La validation des approximations a été faite par comparaison avec des codes « exacts » :

- un code par série de Mie (fourni par T. Habashy, Schlumberger-Doll Research) pour le cas d'une sphère pénétrable éclairée par un dipôle magnétique dans un milieu homogène, étant entendu que la sphère n'est autre qu'un ellipsoïde dégénéré.
- Le code EM3D (mis à disposition par B. Bourgeois du BRGM) réalisé à l'université de l'Utah. Ce code, basé sur une méthode de moments, fournit le champ diffracté par un parallélépipède rectangle. Pour effectuer les comparaisons, les objets ont été pris de même volume et de même rapport d'élongation.

Illustration de la méthode

Pour illustrer la méthode (FIG. 4.4) j'ai choisi une comparaison (extraite de [A.9]) entre les champs diffractés calculés par une méthode de moments (EM3D) et par l'approximation *partielle* avec l'expression exacte du champ incident en espace libre ou en milieu stratifié permettant ainsi de faire apparaître l'influence de l'interface. La configuration est la suivante : un ellipsoïde de dimension 62 m selon l'axe z, 31 m selon l'axe y, 15.5 m selon l'axe x, centré en $(0\ \mathrm{m}, 0\ \mathrm{m}, 75\ \mathrm{m})$ et de conductivité $\sigma_e = 2 \times 10^{-2}$ S/m est enfoui dans une terre de conductivité $\sigma = 2 \times 10^{-3}$ S/m. L'ensemble est illuminé par un dipôle magnétique vertical placé en $(100\ \mathrm{m}, 0\ \mathrm{m}, 75\ \mathrm{m})$ émettant à 500 Hz, le champ secondaire est calculé sur une ligne verticale placée en $(x = -50\ \mathrm{m}, y = 90\ \mathrm{m})$.

4.4 Problème inverse : une méthode de contraste de source

Ce travail est effectué dans le cadre de la thèse de D. Dos Reis (thèse dont j'assure le co-encadrement avec D. Lesselier). Il fait suite aux travaux préliminaires effectués par V. Monebhurrun lors de son post-doctorat au L2S en 1997. Le but est la reconstruction d'un ou plusieurs obstacles tridimensionnels enfouis dans un milieu stratifié à partir de mesures effectuées au dessus du milieu stratifié. C'est une extension au cas tridimensionnel des travaux présentés au chapitre précédent § 3.

L'augmentation importante des ressources informatiques ces dernières années a rendu possible le développement d'algorithmes de résolution des problèmes inverses tridimensionnels. Ainsi une section spéciale [Inverse Problems, **16**, octobre 2000] dédiée à l'imagerie et à l'inversion électromagnétique du sous-sol terrestre permet de se faire une bonne idée des avancées dans le domaine de la géophysique de prospection. Un des problèmes majeurs rencontrés dans la résolution du problème inverse est lié à la nécessité, dans la plupart des algorithmes (Newton, Newton-Kantorovitch, gradient conjugué, ...), de résoudre le problème direct à chaque itération. Des méthodes ont été proposées pour utiliser une solution approchée [Zhdanov et Hursan, 2000] ou éviter sa résolution [Kleinman et van den Berg, 1992a; van den Berg et Kleinman, 1997a]. Ainsi dans [Zhdanov et Hursan, 2000] les auteurs utilisent une solution approchée de type Born étendu (cf § 4.2) et une méthode de gradient conjugué pondéré pour la reconstruction d'une anomalie de conductivité enfouie au sein d'un espace homogène conducteur pour une application géophysique. En parallèle, une version vectorielle du gradient modifié standard (présentée § 3.3) a été introduite [L5.2] et une version combinant là fois une contrainte de binarité (telle qu'introduite § 3.3) et une approximation de type Born étendu a été implémenté au laboratoire par V. Monebhurrun avec pour application la reconstruction de défauts dans des plaques conductrices en contrôle non-destructif [Ruosi *et al.*, 2000].

Pour notre part il a été décidé d'utiliser une méthode dite de contraste de source récemment introduite [van den Berg et Kleinman, 1997a] ou plus exactement sa version étendue [van den Berg *et al.*, 1999] combinée à la contrainte de binarité introduite au laboratoire dans le cas bidimensionnel. La méthode de contraste de source et sa version étendue, comme le gradient modifié, permettent de résoudre le problème inverse non linéaire sans résolution du problème direct, mais avec une vitesse de convergence du processus beaucoup plus rapide. Elles ont été appliquées dans le cas de la reconstruction d'une anomalie de conductivité en géophysique [Abubakar et van den Berg, 2000] en les combinant avec des contraintes de type variation totale sur la solution.

Bien que préliminaires les résultats obtenus dans la reconstruction d'un ou plusieurs défauts affectant soit une lame conductrice soit un demi-espace conducteur sont encourageants. Ils font l'objet d'une soumission à publication dans des actes de congrès édités d'une version étendue [L5.5] reproduite en annexe (§ I) d'une présentation ([C.26]) faite dans un congrès.

Méthode de contraste de source

La configuration est celle décrite (FIG. 4.1(a)) : un champ magnétique — créé par une source (ici une bobine) placée à la surface d'un demi-espace conducteur ou d'une lame conductrice — est perturbé par un ou plusieurs défauts affectant ce demi-espace ou cette lame et est recueilli également à la surface. L'objectif est de développer un algorithme permettant de localiser et de caractériser ce ou ces défauts à partir de la mesure du champ diffracté (ou d'une variation d'impédance) sur une surface au dessus de la lame.

La méthode utilisée est une méthode de gradient modifié à contraste de source. Les détails sur la théorie du gradient modifié ont été rappelés (§ 3.3) et seules les différences sont présentées dans la

suite.

La différence principale vient d'une modification du choix de ces fonctions inconnues ; ce ne sont plus le champ total dans le domaine et la fonction contraste qui sont recherchés simultanément mais la fonction contraste et des courants équivalents résultant du produit de cette fonction contraste et du champ total qui sont recherchés alternativement. Les deux étapes de la résolution sont les suivantes :

1. Utilisant le contraste obtenu à l'itération $n-1$, les courants équivalents à l'itération n sont obtenus par minimisation d'une fonctionnelle mesurant l'écart entre des grandeurs connues (champ diffracté sur les récepteurs et les courants incidents équivalent résultant du produit de la fonction contraste et du champ incident) et les grandeurs équivalentes obtenues à partir des paramètres reconstruits.
2. Utilisant les courants équivalents à l'itération n, une nouvelle fonction contraste est obtenue par minimisation d'une fonctionnelle mesurant l'écart entre les courants équivalents et le produit de la fonction contraste et du champ total calculé également à l'itération n.

Cette résolution successive a l'avantage de n'avoir, dans chaque minimisation, qu'une seule inconnue (soit les courants équivalents, soit la fonction contraste) permettant ainsi de calculer analytiquement les solutions minimales des fonctionnelles.

La méthode développée ici combine le gradient modifié à contraste de source appliqué au cas d'obstacles tridimensionnels enfouis et les contraintes de binarité (§ 3.3) introduites au laboratoire. Des résultats préliminaires ont été obtenus à partir de données synthétiques acquises à l'aide du code de résolution du problème direct considéré précédemment (§ 4.2).

4.4.1 Illustration de la méthode

Pour illustrer la méthode, des résultats extraits de [L5.5] ont été choisis. Ces résultats concernent la reconstruction de deux inclusions débouchantes de profondeur différente dans une lame de métal à partir de la mesure soit des trois composantes du champ magnétique soit de sa seule composante H_z sur une surface. La configuration est la suivante : une lame de métal de conductivité $\sigma = 1$ MS/m et d'une épaisseur de 2 mm est affectée de deux inclusions de section carrée (de côté 1.1 mm), la première, centrée en ($x = 1.1$ mm, $y = 1.1$ mm) est de profondeur 0.5 mm, la seconde, centrée en ($x = -1.1$ mm, $y = -1.1$ mm) est de profondeur 1 mm. L'ensemble est soumis au rayonnement d'une boucle de courant épaisse (rayon intérieur 0.6 mm, rayon extérieur 1.6 mm et épaisseur 0.8 mm) centrée en ($x = -0.75$ mm, $y = 0$ mm) à une hauteur de 0.9 mm de la surface du métal. Le champ mesuré correspond à une ou plusieurs composantes du champ diffracté sur une surface centrée de 10 mm^2 située à une hauteur de 1.55 mm au dessus de l'interface.

4.5 Problème inverse : dipôles équivalents

Cette section traite de la localisation et de la caractérisation d'obstacles tridimensionnels enfouis en régime d'induction avec pour application la géophysique de prospection. Ce travail, commencé lors de mon séjour post-doctoral au BRGM de janvier à octobre 1995, a été poursuivi par G. Perrusson pendant son stage de DEA (mai-juin 1996) et sa thèse (octobre 1996 - octobre 1999). L'approche qui a été suivie ici est très pragmatique, elle fait appel à des hypothèses extrêmement simplificatrices conduisant à un code d'inversion rapide, donc utilisable sur le terrain, mais limité dans les informations qu'il procure. Il est en effet possible de montrer que, en basse fréquence, l'expression analytique du champ diffracté par des objets de forme simple est équivalente à celle de dipôles magnétique et/ou

électrique ; les moments de ces dipôles, également appelés dipôles équivalents, dépendent à la fois des propriétés physiques de l'obstacle et de son environnement et du champ incident.

En régime harmonique, les développements basse-fréquences permettent de remonter aux expressions de ces dipôles équivalents. Ainsi, dans [Kleinman et Senior, 1987], les auteurs obtiennent des expressions du champ diffracté statique faisant apparaître les moments de dipôles équivalents dans le cas d'un objet ellipsoïdal éclairé par une onde plane ou un point source. Dans [Kaufman et Keller, 1985] les auteurs s'intéressent à l'expression du champ diffracté par une sphère conductrice illuminée par une onde plane ou un dipôle magnétique ; l'expression analytique des dipôles équivalents est obtenue à partir du développement basse fréquence de la série de Mie du champ diffracté.

L'utilisation, en basse fréquence, de dipôles équivalents pour remonter à des informations sur le diffracteur permet de traiter un certain nombre d'obstacles différents. Ainsi dans [Das *et al.*, 1990] le cas d'un obstacle sphérique métallique est traité, puis dans [Das et Mc Fee, 1991] le cas de l'ellipsoïde de révolution parfaitement conducteur et perméable et ce pour étudier l'influence de la profondeur, de l'orientation et du rapport des propriétés électriques et magnétiques de l'obstacle et de l'environnement. Dans [Angell et Kleinman, 1987] les auteurs s'intéressent au cas d'un ellipsoïde éclairé par une onde plane et cherchent à remonter à ses dimensions et son orientation.

Méthode des dipôles équivalents

L'idée est de remplacer la recherche d'un obstacle volumique, recherche coûteuse du point de vue numérique, par la recherche de sources équivalentes par minimisation d'une fonction coût mesurant l'écart entre le champ diffracté mesuré et le champ rayonné par ces sources. Les inconnues sont alors leurs positions et leurs amplitudes, avec l'espoir que ces données permettent de remonter à des informations sur l'obstacle.

De la même façon que dans la section (§ 4.3) nous nous plaçons dans une hypothèse de basse fréquence et l'interaction entre l'obstacle et la surface est négligée, assimilant ainsi le milieu encaissant à un espace homogène de conductivité constante. La configuration est la suivante : un obstacle tridimensionnel de faible contraste par rapport à l'encaissant est enfoui dans un milieu homogène et est éclairé par un dipôle magnétique. Le champ secondaire est recueilli sur une ou plusieurs lignes de récepteurs modélisant des mesures effectuées en puits de forage.

Dans les premiers travaux effectués au BRGM lors de mon postdoctorat la source équivalente choisie était une boucle de courant rectangulaire dont la position, l'élongation et l'orientation étaient choisies par ajustement manuel. Des résultats encourageants [L4.1] obtenus sur des données réelles acquises en Espagne par le BRGM nous ont convaincus de poursuivre dans cette voie. Par la suite, la recherche de plusieurs dipôles équivalents dont les inconnues sont leurs directions, leur position commune et leurs amplitudes a été privilégiée. Un des avantages est que, dans un certain nombre de cas, ces dipôles équivalents permettent de remonter à des formes volumiques équivalentes et ainsi d'obtenir des informations supplémentaires telles que le volume, la conductivité moyenne et parfois l'orientation principale. Deux voies ont été explorées :

- une sphère équivalente : les expressions analytiques de trois dipôles (deux magnétiques et un électrique) équivalents à une sphère peuvent être établies [Kaufman et Keller, 1985], leurs amplitudes étant fonction du rayon de la sphère et de la fonction contraste mesurant l'écart entre la conductivité de la sphère et celle de l'encaissant.
- un ellipsoïde équivalent : dans sa thèse, G. Perrusson a montré que, à partir du développement basse fréquence *partiel* qu'elle a introduit (§ 4.3), il est possible d'assimiler, en première

approximation, la diffraction d'un ellipsoïde au rayonnement de trois dipôles électriques perpendiculaires dont les directions coïncident avec celles des demi-axes et dont les amplitudes contiennent des informations sur les proportions des ces demi-axes.

Ces travaux ont fait l'objet d'un chapitre de livre [L4.1] et de plusieurs communications dont une [C.20] a été reproduite ci-après.

Illustration de la méthode

Pour illustrer ce chapitre j'ai choisi de présenter des résultats obtenus lors de mon séjour post-doctoral au BRGM. Ces résultats, extrait de [L4.1], concernent la localisation d'un amas conducteur dans un site minier test du BRGM en Espagne (Herrerias). Le but était de chercher une boucle de courant (position et intensité) créant un champ secondaire identique à celui mesuré dans le puits de forage H12. L'ajustement, bien que manuel, des paramètres permet de localiser cette boucle de courant dans l'amas (FIG. 4.6(a)) dont les contours sont estimés grâce à la connaissance fine de la géologie de la région. La comparaison entre le champ simulé dû à la boucle de courant et les champs réduits mesurés dans le puits de forage (FIG. 4.6(b)) montre un bon accord.

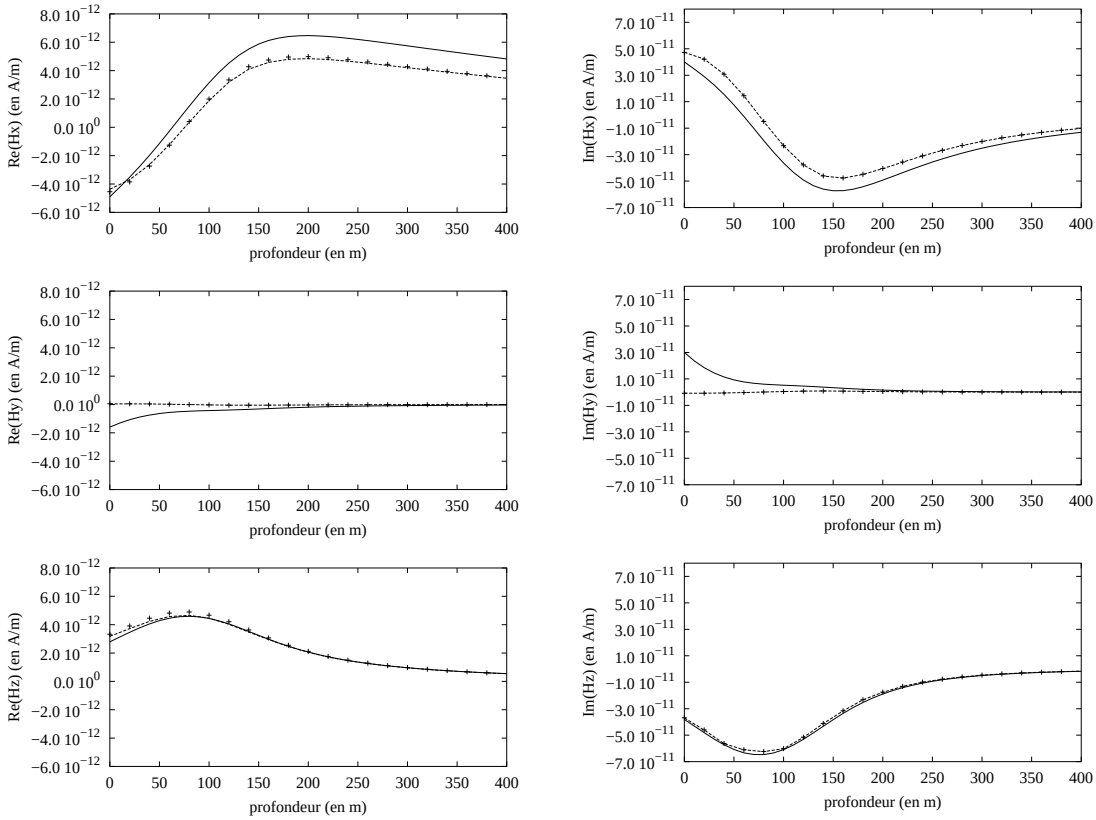

FIG. 4.4 – Champ magétique secondaire diffracté par un ellipsoïde vertical placé dans un demi-espace conducteur illuminé par un dipôle magnétique vertical. Colonne de gauche, partie réelle et colonne de droite, partie imaginaire des 3 composantes. Cas de l'espace infini (croix), cas du demi-espace (tiret) et résultat de la méthode des moments (trait continu).

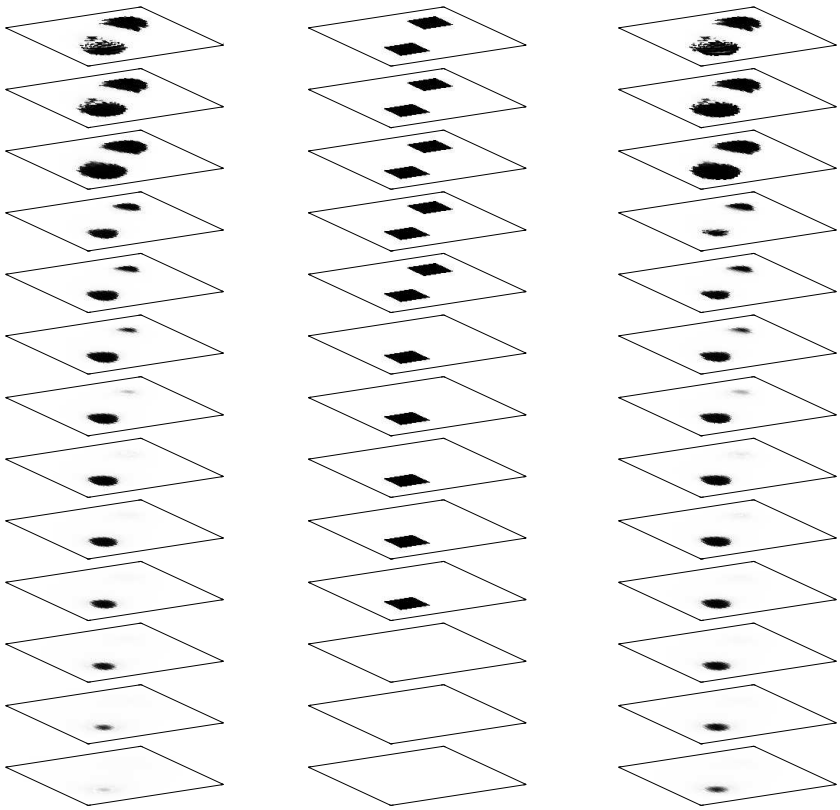

(a) (b) (c)

FIG. 4.5 – Reconstruction de deux inclusions d'air de différentes profondeurs dans une lame métallique. (a) reconstruction à partir des trois composantes du champ magnétique, (b) solution exacte et (c) reconstruction à partir de la seule composante H_z du champ magnétique.

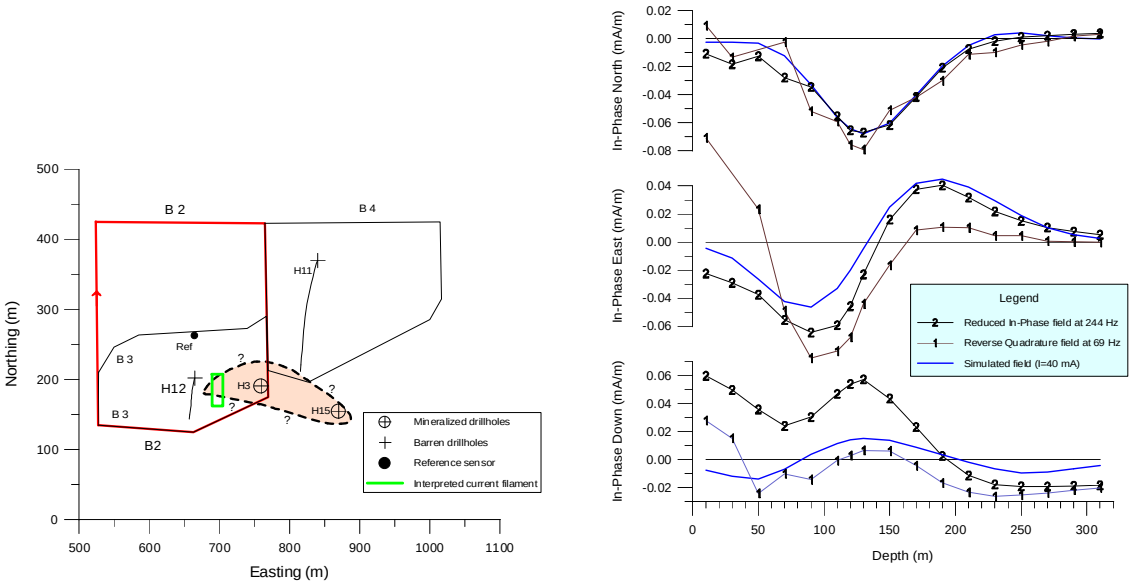

(a) (b)

FIG. 4.6 – Site test du BRGM à Herrerias. (a) configuration de mesure et projection sur la surface de la position de la boucle de courant et du contour estimé de l'amas minéral. (b) comparaison entre les champs simulés et ceux mesurés dans le puits H12.

5

Conclusion et perspectives

Les travaux que j'ai effectués ces dernières années ont été consacrés à la résolution de problèmes inverses de diffraction des ondes et du problème direct qui lui est associé, avec pour application visée la reconstruction d'obstacles enfouis au sein d'un milieu stratifié. Ils ont été marqués majoritairement par le désir de proposer, développer, d'adapter et/ou de combiner diverses approches pour parvenir à des méthodes d'inversion efficaces, bien établies du point de vue théorique et validées du point de vue numérique. Les applications industrielles n'ont, pour autant, pas été négligées, notamment par la prise en compte, lorsque c'était possible, des contraintes ou limitations techniques qu'elles imposent sans toutefois s'y limiter.

Les configurations d'étude choisies (milieu stratifié plan, strates homogènes ou milieux homogènes) peuvent sembler d'une simplicité excessive par rapport à la réalité. Elle sont pourtant riches de difficultés théoriques (unicité des solutions du problème direct et du problème inverse, aspect limité des données, incorporation d'informations *a priori*) et numériques (stabilité des solutions, convergence des algorithmes) conduisant à résoudre des problèmes non nécessairement simples et sont une première étape indispensable avant de prendre en compte une réalité plus complexe.

La majorité des solutions proposées ici est basée sur une formulation intégrale scalaire ou vectorielle de domaine ou de frontière des champs électromagnétiques ou acoustiques. Ce choix, principalement dû à une prise en compte globale des interactions onde/structure (que ce soit en champ proche ou en champ lointain) et à la possibilité de développer des codes numériques rapides, permet une compacité certaine de la formulation — qui cache cependant des difficultés théoriques et numériques — mais n'est pas limitatif. En effet les méthodes d'inversion présentées dans ce manuscrit peuvent aisément être adaptées à d'autres types de formulations des champs, les éléments finis par exemple, ou étendues au domaine temporel.

Plusieurs objectifs ont été poursuivis, et tout d'abord le développement d'algorithmes de résolution du problème direct dans le cas bidimensionnel et tridimensionnel qui permettent (i) de valider les choix de formulations des champs par comparaison avec d'autres algorithmes, (ii) de proposer des approximations accélérant sa résolution, (iii) de mener une étude paramétrique de l'influence des grandeurs physiques et (iv) de développer et valider des modules algorithmiques directement utilisables dans les codes d'inversion. Puis des méthodes d'inversions ont été proposées. Ont été considérées soit des approches pragmatiques dans lesquelles les hypothèses simplificatrices conduisent à des informations rapides mais limitées sur les obstacles, soit des approches plus sophistiquées dans lesquelles

l'ensemble des interactions est pris en compte et qui conduisent à des reconstructions plus ou moins fidèles des obstacles suivant la quantité d'information contenue dans le signal au prix d'une complexité théorique et algorithmique plus importante et à un coût numérique plus grand.

Ces travaux ont également montré l'importance de l'information *a priori* à introduire dans les inversions notamment dans le cas d'obstacles enfouis pour lesquels les données sont limitées par les configurations (pas de possibilité de « voir » l'objet sous tous les angles, perte d'information lorsque l'objet est dans un guide d'onde, ...) et la diversité fréquentielle pas nécessairement suffisante pour combler ce manque. Ceci nous a conduit à spécialiser la plupart des méthodes présentées à la reconstruction d'objets homogènes sans pour autant nous y restreindre.

Les équations relatives à la résolution du problème direct ont été traitées de deux manières différentes.

- Dans le domaine de résonance une résolution exacte est obtenue par discrétisation des équations à l'aide une méthode de moments dans laquelle l'obstacle diffractant est divisé en domaines — rectangulaires en 2D ou parallélépipédiques en 3D. Le système linéaire résultant est résolu soit de façon exacte (méthodes de type Gauss ou gradient conjugué) soit approchée (approximation de type « Born étendue »).
- Dans le domaine des basses fréquences un développement de type Rayleigh appliqué au champ diffracté par un ellipsoïde a été proposé.

Plusieurs algorithmes, basés sur différentes formulations des champs ont été développés et leurs résultats comparés à ceux de la littérature ou à des données expérimentales directement obtenues au laboratoire ou fournies par des laboratoires extérieurs.

Les méthodes d'inversion choisies font partie de la famille des méthodes itératives déterministes non-linéaires. Plusieurs méthodes ont été développées et, lorsque c'était possible, comparées entre elles.

- Le gradient modifié contraint : plusieurs versions du gradient modifié ont été présentées. La première incorpore des contraintes de positivité sur les solutions afin d'éviter l'obtention de solutions non physiques ; elle a été testée sur des données synthétiques et a montré son efficacité sur des obstacles où l'un des deux paramètres (permittivité ou conductivité) est connu. La seconde, une version binaire, s'intéresse à la reconstruction d'un obstacle dont une borne supérieure des paramètres est prescrite par l'utilisateur et dont seul le domaine est recherché. Cette méthode a montré une amélioration des résultats dans les configurations où les contraintes de positivité n'étaient pas suffisantes ; une version permettant une inversion à partir de données incomplètes (la phase du champ diffracté n'est pas connue) a été proposée.
- Les sources distribuées : cette méthode, s'appliquant à la fois en acoustique et en électromagnétisme, s'intéresse à la reconstruction de la frontière d'un obstacle impénétrable enfoui au sein d'un guide d'onde à parois pénétrables, une version simplifiée étant, quand à elle, dédiée à la reconstruction d'un obstacle en milieu homogène. Les algorithmes développés ont été testés non seulement à l'aide de données synthétiques (en acoustique sous-marine) mais également de données expérimentales obtenues au laboratoire (électromagnétisme basse-fréquence) ou à l'extérieur (électromagnétisme microonde)
- Les ensembles de niveaux : cette méthode traite la reconstruction d'obstacles homogènes enfouis au sein d'un milieu homogène ou stratifié, en polarisation TE ou TM. Le but est la reconstruction du contour d'un ou plusieurs obstacles de paramètres électromagnétiques connus. La méthode a été confrontée, dans plusieurs configurations et dans les deux polarisations, à des données synthétiques et expérimentales. Les résultats obtenus se sont montrés très intéressants, que ce soit en espace libre ou en espace stratifié.

– La méthode du contraste de source : cette méthode, qui fait partie de la famille des gradients modifiés, a été combinée avec une contrainte de binarité dans le but de reconstruire des défauts tridimensionnels affectant une plaque ou un demi-plan conducteur pour des applications de contrôle non-destructif. Les résultats obtenus, bien que préliminaires, illustrent les possibilités de la méthode pour des problèmes d'inversion d'obstacles tridimensionnels au sein d'un environnement stratifié encore rarement étudiés dans la littérature.
– Les sources équivalentes : l'obstacle inconnu est remplacé par un ensemble de sources rayonnantes (dans notre cas des combinaisons de dipôles électriques et/ou magnétiques) dont les positions et les amplitudes permettent de remonter à des informations sur cet objet. La méthode a également été confrontée à des données synthétiques et expérimentales.

Perspectives

La synthèse des travaux présentée ici permet, je crois, de mettre en évidence certaines directions de recherche à approfondir sur le thème des problèmes inverses en diffraction des ondes. Je commencerai par présenter les perspectives à court et moyen terme car s'appuyant sur des travaux déjà initiés et que les résultats, prometteurs, encouragent à poursuivre. Puis seront abordées les perspectives à plus long terme sur des sujets peu ou pas abordés au laboratoire et dont les intérêts théoriques et pratiques sont importants.

En premier lieu, les travaux sur le cas bidimensionnel seront poursuivis. Bien que très simpliste par rapport à la réalité cette configuration a l'avantage de permettre des études théoriques plus simples par la forme des équations mises en jeu et des calculs numériques plus rapides conduisant à des études paramétriques plus faciles à mettre en œuvre. De plus la capacité de ce modèle 2D à rendre compte correctement des champs électromagnétiques dans le cas d'obstacles dont une des dimensions est beaucoup plus grande que les autres — comme l'illustrent les résultats obtenus, en espace libre, sur les données expérimentales fournies par l'Institut Fresnel à Marseille — montre tout son intérêt. L'une des premières étapes concerne la méthode des ensembles de niveaux et son extension à la reconstruction d'obstacles homogènes dont les paramètres électromagnétiques sont à déterminer, puis à la reconstruction d'obstacles inhomogènes.

En parallèle, les travaux sur le cas tridimensionnel seront également poursuivis. Une des priorités sera le développement d'un algorithme de résolution du problème direct plus stable que celui déjà développé au laboratoire, notamment dans le cas de la modélisation de fissure. La poursuite des travaux sur l'inversion par une méthode de contraste de source binaire et l'extension de la méthode des ensembles de niveaux au cas tridimensionnel, dans une configuration d'espace libre ou stratifié, font également partie des priorités. Le développement basse-fréquence des champs, avec pour application la géophysique de prospection, ne sera pas pour autant abandonné et ce grâce au recrutement de G. Perrusson en tant que Maître de conférence à l'Université Paris Sud en octobre 2001.

En second lieu une nouvelle voie de recherche sur la reconstruction de fissures dans des matériaux est actuellement à l'étude. Ce problème, important dans l'industrie pour la détection d'amorces de rupture, ne peut pas être traité de façon simple par les méthodes développées au laboratoire en raison de l'extrême finesse des obstacles, finesse mal prise en compte par les intégrales de domaine utilisées jusqu'à présent. Une des difficultés provient de la forme de ces fissures qui peuvent se propager en se divisant sous forme de rameau ; la méthode de reconstruction doit donc être à même de faire apparaître ou disparaître ces fissures pendant le processus itératif. Ce problème est encore peu abordé dans la littérature.

Bien qu'à plus long terme, le problème concernant les milieux anisotropes reste une suite logique aux travaux effectués sur les milieux isotropes au laboratoire. Les objectifs sont le développement de modèles d'interaction d'une onde électromagnétique avec des matériaux composites complexes (quelques kHz à quelques MHz) permettant une prédiction de leurs comportements et une meilleure compréhension des résultats obtenus par caractérisation expérimentale et de techniques de contrôle et d'évaluation de ces structures et ce afin de caractériser tout défaut pouvant en affecter le comportement mécanique. En effet, les matériaux composites sont de plus en plus utilisés par l'industrie tant pour leurs propriétés électromagnétiques que mécaniques, et rares sont encore les modèles d'interaction permettant de prédire leur réponse à une onde électromagnétique incidente.

Troisième partie

Quelques publications illustratives

A

Diffraction par un obstacle bidimensionnel : méthode de moments

[A.3] TE scattering by cylindrical dielectric obstacle buried in half-space : a H-field-based solution method
Marc Lambert
J. Electromagn. Waves Applic. **12** 1217-1239 1998

Journal of Electromagnetic Waves and Applications, Vol. 12, 1217–1239, 1998

TE SCATTERING BY A CYLINDRICAL DIELECTRIC OBSTACLE BURIED IN A HALF-SPACE: A H-FIELD-BASED SOLUTION METHOD

M. Lambert

Laboratoire des Signaux et Systèmes (LSS)
CNRS/SUPÉLEC
Plateau de Moulon
F-91192 Gif-sur-Yvette Cedex
France

Abstract–Scattering of a transverse electric (TE) wavefield by an inhomogeneous lossy dielectric cylindrical obstacle embedded in a lossy dielectric half-space is investigated. The cylinder is of arbitrary cross-section, and its axis lies parallel to the interface. The formulation involves a domain integral equation of the field obtained by applying the Green's theorem to the appropriate Helmholtz wave equations. The convolution-correlation structure of the formulation is such that the discretized counterpart of the integral equation (provided by the application of a Method of Moments where the obstacle is divided into triangular patches and where the contrast and the H-field are expanded using two different basis functions) can be efficiently handled using a FFT-based conjugate gradient solver. The validity of the approach is illustrated by comparison with results found in the literature.

1. INTRODUCTION

A modeling method of the electromagnetic interaction between a 2-D linear non-magnetic obstacle embedded in a (lower) half-space and a time-harmonic H-polarized (TE) incident wave generated above in the upper half-space is proposed herein. The aim is to obtain an accurate and fast method as allowed by clever discretization schemes of the wave equation and the intensive use of Fast Fourier Transforms (FFT).

This may be viewed as a first and necessary step toward the inversion of H-polarized wavefields in the microwave domain due to a buried cylindrical structure. Such a direct algorithm indeed enables us to calculate sound synthetic data at a low computational cost, and to illustrate the influence

of such or such parameter of the scattering problem at hand. Furthermore it could be used as a building block of an inversion algorithm applied to TE-field data.

Let us emphasize that this algorithm is based on an integral formulation of the wavefield and then belongs to the well-known class of boundary and domain integral formulations, which we will henceforth focus on, leaving aside FD-TD and like techniques. The free-space case — sources, receivers and scatterers are in a homogeneous infinite space — has been extensively studied, e.g., [1–4]. The stratified case as the one considered herein has also seen a number of significant contributions [5–7] but at a much lesser extent.

To solve the TE-case it appears that one can start either from the electric field, whose direction is parallel with the cross-section (x, y) of the obstacle, or from the magnetic field, which is oriented parallel to the axis (z) of the obstacle. Both approaches have their pros and cons, as one can summarize below:

1. The H-field formulation: the single non-zero component of the magnetic field (H) is expressed by means of a Scalar Domain Integral Equation (SDIE) derived from the application of the Green's theorem to the Helmholtz wave equations and which involves this component and its derivatives versus (x, y) (in addition with the Green's function and/or its space derivatives). In so doing the main difficulty comes from the presence of the derivatives of the H-field in the SDIE. Several solutions can be developed so as to overcome this difficulty. Particularly interesting appears to be Xu and Yan's contribution [5, 6] where the SDIE has been rewritten as a so-called *Volume-Surface Integral Equation* (see p. 576 in [8]), integrals both along the contour of the obstacle cross-section and upon the cross-section itself being required. This has the advantage of cancelling out the contribution of any derivative of H. However the resulting integral equation suffers from an increase in the number of unknowns due to the contour integral term. Indeed one has to discretize both the cross-section (using triangular patches) and the contour (using line segments). Notice that this approach is valid for a permeable obstacle, as well as for a non-magnetic one.
2. The E-field formulation: the two non-zero components of the electric field (E) can be expressed by means of a Vector Domain Integral Equation (VDIE) again derived from the application of the Green's theorem and which now only involves the field E itself and the derivatives versus (x, y) of the Green's function. In effect one has to solve a couple of two simple scalar domain integral equations (SDIE). Ellis and Peden [7] have used such an approach in order to model the response of a tun-

nel embedded in a semi-infinite earth in a borehole-to-borehole probing configuration. Here the VDIE is simply discretized from a description of the obstacle cross-section as a distribution of square patches. Notice that in free-space, it has been shown [3] that this technique may provide us with an inaccurate scattered field, but a similar analysis has not been carried out onto the stratified case.

In contrast with Xu and Yan's investigation, the H-field formulation developed in the following does only involve the gradient of H versus (x, y) and the one of the Green's function. It is a generalization to the stratified case of the method briefly described by Lixin et al. in [9]. The obstacle cross-section is again divided into triangular patches (which are organized differently from those of Xu and Yan) while the field gradient in the integral equation is handled by using a set of linear basis functions.

The paper develops as follows. In section 2 the integral formulation is established and its peculiar convolution-correlation structure is pointed out. Then, in section 3, its discretized counterpart is considered, and a FFT-based conjugate-gradient solver adapted to this structure is developed in section 4. In section 5 typical synthetic results are shown and compared with those obtained with other existing techniques. Further work is sketched in the Conclusion (section 6). Appendices A and B provide some technical details of the derivation of the integral formulation and of its numerical treatment.

2. FIELD FORMULATION

As said above we are interested in the time-harmonic scattering of a cylindrical obstacle (with axis parallel to z) buried in the lower homogeneous half-space of a two half-space medium — numbered 1 and 2 — (see Fig. 1), the horizontal planar interface being the x-z plane. The time convention $e^{-j\omega t}$ — $\omega = 2\pi f$ where f is the frequency — is omitted from now on.

The obstacle cross-section Ω is of the dimension of the wavelength in the lower half-space, or somewhat larger (resonance domain). Its relative permittivity and its conductivity may vary arbitrarily with position (x, y). All materials are assumed to be linear, isotropic and non-magnetic dielectrics that are fully characterized by their relative permittivity ε_{rm} and conductivity (in S/m) σ_m, $m = 1, 2, \Omega$. The complex permittivity is defined as $\varepsilon_m = \varepsilon_0 \varepsilon_{rm} + j\sigma_m/\omega$ and the corresponding complex wave number k_m is such that $k_m^2 = \omega^2 \mu_0 \varepsilon_m, \Im(k_m) \geq 0$ where ε_0 and μ_0 are the vacuum permittivity and permeability, respectively.

A finite number of line sources which radiate a H_z-polarized magnetic field are placed on a horizontal line above the interface at some height y_S

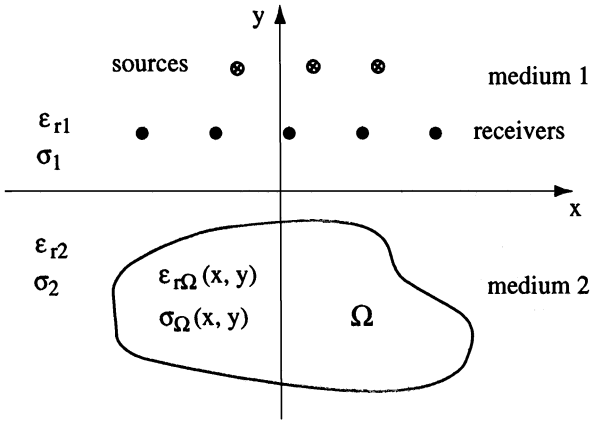

Figure 1. Configuration of study.

and one looks at the scattered field observed along an other horizontal (probing) line $\mathcal{L}$ also placed above the interface at arbitrary height y_R. Notice that the approach is not restricted to a line source illumination and could be easily extended to other H-polarized sources (planar, distributed, etc.).

For simplicity the single z-component of the magnetic field H_z in half-space m ($m = 1, 2$) will be denoted below as H_m.

The domain integral equation satisfied by the magnetic field H_m follows from the application of the Green's theorem to the partial differential wave equations that are valid in the several materials, with accounting for appropriate boundary conditions (see Appendix A). It reads:

$$H_m(x,y) = H_m^i(x,y) + \int_\Omega dx'dy'\chi\left(x',y'\right)\left[\nabla' G_{m2}(x,y,x',y')\cdot\nabla' H_2(x',y')\right] \tag{1}$$

where the two-component ∇' operator is taken with respect to the primed variables, where $H_m^i(x,y)$ is the incident field in the half-space m, and where $\chi(x,y)$ is the complex contrast function given by:

$$\chi(x,y) = 1 - \frac{\varepsilon_2}{\varepsilon_\Omega(x,y)} \tag{2}$$

The Green's function $G_{mn}(x,y,x',y')$ of the two half-space configuration is solution of:

$$\Delta G_{mn}\left(x,y,x',y'\right) + k_m^2 G_{mn}\left(x,y,x',y'\right) = \delta\left(x-x',y-y'\right)\delta_{mn} \tag{3}$$

$$(x,y)\in D_m, \text{ and } \left(x',y'\right)\in D_n, \text{ with } m=1,2,\ n=1,2$$

where $G_{mn}(x,y,x',y')$ is the field at the observation point (x,y) (in the half-space numbered m) due to a line source at (x',y') (in the half-space numbered n).

As is well-known [10, 11] the exact expression of $G_{mn}(x,y,x',y')$ is given in the α spatial-frequency domain (α associated to x) by the following expression:

$$G_{mn}(x,y,x',y') = \frac{1}{2\pi}\int_{-\infty}^{+\infty} d\alpha g_{mn}(\alpha,y,x',y')\, e^{j\alpha x} \tag{4}$$

The spectral component $g_{mn}(\alpha,y,x',y')$ is written in closed-form using two terms, a singular one (with superscript s) and a non-singular one (with superscript ns), as :

$$g_{mn}(\alpha,y,x',y') = g^s_{mm}(\alpha,y,x',y')\,\delta_{mn} + g^{ns}_{mn}(\alpha,y,x',y') \tag{5}$$

Equation (5) shows that the singular part of the Green's function is to be accounted for only when the source point (x,y) and the observation point (x',y') are considered in the same half-space, and it corresponds to the direct trajectory of the wave between these two points. The non-singular part takes into account either the reflection on, or the transmission through, the interface depending upon the respective location of the source point and of the observation point. Introducing the propagation factor β given by $\beta_m = \sqrt{k_m^2 - \alpha^2}$ with $\Im(\beta_m) > 0, m = 1,2$, one gets

$$g^s_{mm}(\alpha,y,x',y') = \frac{j}{2\beta_m} e^{j\beta_m|y-y'|} e^{-j\alpha x'} \tag{6}$$

$$g^{ns}_{mn}(\alpha,y,x',y') = \frac{j}{2\beta_n}\Gamma e^{j(\beta_m|y|+\beta_n|y'|)} e^{-j\alpha x'} \tag{7}$$

where Γ is a spectral-domain H-field reflection or transmission coefficient such that

$$\Gamma = \begin{cases} r = \frac{k_1^2\beta_2 - k_2^2\beta_1}{k_1^2\beta_2 + k_2^2\beta_1}, & \text{if } m = 2, n = 2 \\ t = \frac{2k_2^2\beta_1}{k_1^2\beta_2 + k_2^2\beta_1}, & \text{if } m = 2, n = 1 \end{cases} \tag{8}$$

The singular part of the Green's function in the spatial domain is known in closed-form:

$$\begin{aligned} G_{mn}(x,y,x',y') &= \frac{1}{2\pi}\int_{-\infty}^{+\infty} d\alpha \frac{j}{2\beta_m} e^{j\beta_m|y-y'|} e^{-j\alpha(x'-x)} \\ &= \frac{j}{4}\mathrm{H}_0^{(1)}(k_m r), \quad r = \sqrt{(x-x')^2 + (y-y')^2} \end{aligned} \tag{9}$$

Let us point out the resulting convolution-correlation structure in terms of the lateral variable x and the depth y of the integral equation (1). Indeed the gradient of $G_{mn}(x,y,x',y')$ at (x',y') is given by:

$$\nabla' G_{mn}(x,y,x',y') = \nabla' G^s_{mn}(x,y,x',y')\,\delta_{mn} + \nabla' G^{ns}_{mn}(x,y,x',y') \quad (10)$$

with

$$\nabla' G^s_{mm}(x,y,x',y') = \frac{jk_m}{4r} \mathrm{H}_1^{(1)}(k_m r) \begin{pmatrix} x-x' \\ y-y' \end{pmatrix} \quad (11)$$

and with

$$\nabla' G^{ns}_{mn}(x,y,x',y') = \frac{1}{4\pi} \int_{-\infty}^{+\infty} d\alpha\, \Gamma e^{j(\beta_m|y|+\beta_n|y'|)} e^{-j\alpha(x'-x)} \begin{pmatrix} \frac{\alpha}{\beta_n} \\ -\mathrm{sgn}(y') \end{pmatrix} \quad (12)$$

For $m=n=2$ the right-hand side of equation (11) depend on $x-x'$ and on $y-y'$, which enables us to write $\nabla' G^s_{22}(x,y,x',y')$ as $\nabla' G^s_{22}(x-x',y-y')$; while in (12) it depends both on $x-x'$ and on $y+y'$, which is such that $\nabla' G^{ns}_{22}(x,y,x',y')$ reads $\nabla' G^{ns}_{22}(x-x',y+y')$. Thus equation (1) becomes

$$\begin{aligned} H_2(x,y) = H_2^i(x,y) + \int_\Omega dx'dy'\chi(x',y') \Big\{ &[\nabla' G^s_{22}(x-x',y-y') \\ &+ \nabla' G^{ns}_{22}(x-x',y+y')] \cdot \nabla' H_2(x',y') \Big\}, \quad (x,y) \in \Omega \end{aligned} \quad (13)$$

The above equation is the so-called coupling or state equation satisfied by the magnetic field.

For $m=2, n=1$ the interface breaks the correlation structure along the y-direction but preserves the convolution along the x-direction. The scattered field H_1^d follows as

$$\begin{aligned} H_1^d(x,y) = \int_\Omega dx'dy'\chi(x',y') \left[\nabla' G^{ns}_{12}(x-x',y,y') \cdot \nabla' H_2(x',y')\right], \\ (x,y) \in \mathcal{L} \end{aligned} \quad (14)$$

which is the so-called observation or data equation.

3. DISCRETISATION

In order to solve the direct problem a method of moments is used [12, 13]. The obstacle cross-section is divided into square pixels of side Δ in which the contrast χ is taken to be constant; each pixel is divided again into two

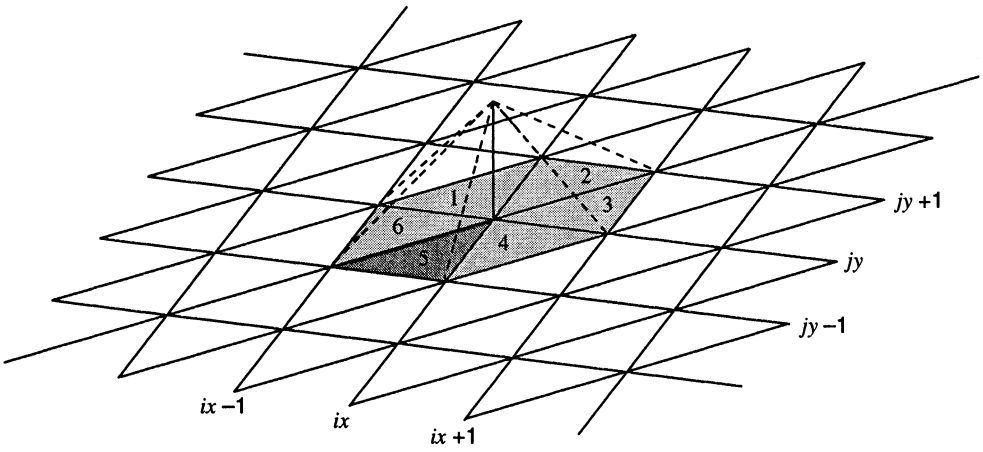

Figure 2. The discretisation of the cross-section of the obstacle is performed in two steps: (1) division into square pixels of constant electromagnetic parameters. (2) division of each such pixel into two rectangular triangles in which the magnetic field is assumed to vary linearly. Then, the field is determined at each node of the mesh referred as (ix, iy). The basis function used to described the magnetic field is made of six triangular basis functions of triangle supports — having a common vertex with the node (ix, iy) and numbered 1–6 — e.g., the support of the triangular basis numbered 5 is displayed in dark grey.

rectangular triangles in which the magnetic field is assumed to vary linearly [14], while the testing functions are simply chosen as Dirac δ-functions. The field is thus determined at each node of the mesh referred as (ix, iy), $N_x \times N_y$ such nodes being accounted for (see Fig. 2). One has

$$H_2(x,y) = \sum_{ix=1}^{Nx} \sum_{iy=1}^{Ny} H_2(ix \times \Delta, iy \times \Delta)\, B_{ix,iy}(x,y), \quad (x,y) \in \Omega \tag{15}$$

$$B_{ix,iy}(x,y) = \sum_{it=1}^{Nt_{ix,iy}} t_{it}(x,y), \quad t_{it}(x,y) = (a_{it} + b_{it}x + c_{it}y)\, \mathbf{1}_{it}(x,y)$$

$$\mathbf{1}_{it}(x,y) = \begin{cases} 1 \text{ if } (x,y) \in \Omega^t_{it} \\ 0 \text{ elsewhere} \end{cases}, \quad \Omega^B_{ix,iy} = \sum_{it=1}^{Nt_{ix,iy}} \Omega^t_{it} \tag{16}$$

where $Nt_{ix,iy}$ is the number of triangles which have a vertex in common with the node (ix, iy), and where $B_{ix,iy}(x,y)$ is the basis function associated to

the same node. The basis function $B_{ix,iy}(x,y)$ of support $\Omega^B_{ix,iy}$ (depicted with pale and dark grey in Fig. 2) is the sum of, at most, six triangular basis functions $t_{it}(x,y)$ with a triangular support Ω^t_{it} (one of them, $it = 5$, is shown in dark grey).

In so doing the total magnetic field in the obstacle is given by:

$$H_2(x,y) = \sum_{ix=1}^{Nx}\sum_{iy=1}^{Ny} H_2(ix\times\Delta, iy\times\Delta) \sum_{it=1}^{Nt_{ix,iy}} t_{it}(x,y) \tag{17}$$

and its gradient by:

$$\nabla H_2(x,y) = \sum_{ix=1}^{Nx}\sum_{iy=1}^{Ny} H_2(ix\times\Delta, iy\times\Delta) \sum_{it=1}^{Nt_{ix,iy}} \begin{pmatrix} b_{it} \\ c_{it} \end{pmatrix} \mathbf{1}_{it}(x,y) \tag{18}$$

letting

$$\chi(x,y) = \sum_{it=1}^{Nt} \chi_{it}\mathbf{1}_{it}(x,y) \tag{19}$$

where Nt is the total number of triangles used to describe the obstacle.

Enforcing (18) and (19) in (13) yields the discretized state equation:

$$\begin{aligned} H_2(jx,jy) = H_2^i(jx,jy) + \sum_{ix=1}^{Nx}\sum_{iy=1}^{Ny}\Bigg\{ H_2(ix,iy) \sum_{it=1}^{Nt_{ix,iy}} \Big[\chi_{it}(ix,iy) \\ h_{it}^s(jx-ix, jy-iy) + h_{it}^{ns}(jx-ix, jy+iy)\Big]\Bigg\} \\ jx = 1,...,Nx; jy = 1,...,Ny \end{aligned} \tag{20}$$

where we have implied the Δ factor in the space coordinates. Similarly, enforcing (18) and (19) in (14) yields the discretized observation equation:

$$H_1^d(kx, y_R) = \sum_{ix=1}^{Nx}\sum_{iy=1}^{Ny}\Bigg\{ H_2(ix,iy) \sum_{it=1}^{Nt_{ix,iy}} \Big[\chi_{it}(ix,iy)\, f_{it}^{ns}(kx-ix, y_R, iy)\Big]\Bigg\} \tag{21}$$

where the scattered field is calculated along the line at a step Δ. In the two equations above, one has introduced the integrated Green's elements

$$h_{it}^s(x-x', y-y') = b_{it}\int_{\Omega^t_{it}} dx'dy' \frac{\partial}{\partial x'} G_{22}^s(x-x', y-y')$$

$$+ c_{it} \int_{\Omega_{it}^t} dx'dy' \frac{\partial}{\partial y'} G_{22}^s (x - x', y - y') \qquad (22)$$

$$h_{it}^{ns} (x - x', y + y') = b_{it} \int_{\Omega_{it}^t} dx'dy' \frac{\partial}{\partial x'} G_{22}^{ns} (x - x', y + y')$$

$$+ c_{it} \int_{\Omega_{it}^t} dx'dy' \frac{\partial}{\partial y'} G_{22}^{ns} (x - x', y + y') \qquad (23)$$

the corresponding $f_{it}^{ns}(x - x', y, y')$ being obtained by replacing $G_{22}^{ns}(x - x', y + y')$ with $G_{12}^{ns}(x - x', y, y')$ in (23).

4. FFT-BASED SOLUTION OF THE DISCRETIZED EQUATIONS

4.1 State Equation

When solving for (20) two techniques are available. One may use brute force and in effect sum over all the discrete indices; or one may resort to Fast Fourier Transforms so as to deal suitably with the convolution-correlation structure of the equation [15, 16], as we do now. Different steps are to be considered:

1. $Mx \times My$ elements h_{it}^s and h_{it}^{ns} should be calculated, with $Mx \geq 2Nx$ and $My \geq 2Ny$ to avoid overlapping. Usually Mx or My is equated to the closest integer of power 2 greater than $2Nx$ or $2Ny$ for taking advantage of the most efficient FFT algorithms. h_{it}^s is calculated numerically using a Gauss-Legendre scheme except at the singular point — $(x, y) = (x', y')$. The self-term must be treated differently to take into account the singularity; in (9) it is obtained from a small argument expansion of the Green's function, the resulting integration being made analytically. Here the singularity is extracted and is, after tedious calculations, analytically integrated over the full triangle; the remaining part is numerically calculated (Appendix B). h_{it}^{ns} is calculated using a FFT for nonequispaced data [17].
2. χ_{it} is extended from $Nx \times Ny$ to $Mx \times My$ by zero-padding, with keeping the same $Nx \times Ny$ central points.
3. H_2 is then made of $Mx \times My$ elements where the only ones which will be kept at the end of the calculation are the $Nx \times Ny$ central ones.

Let us define Nt_{max} the maximum number of triangles which have a common vertex with a given node — in our discretisation procedure $Nt_{max} = 6$. Any node located inside the obstacle cross-section belongs to Nt_{max} triangles except those on the border. So what we do here is to add an appropriate

number of triangles with zero contrast to get also Nt_{max} triangles associated to the border nodes. This allows us to write the FFT-based version of the state equation:

$$H_2 = H_2^i + \sum_{it=1}^{Nt_{max}} \left\{ \mathrm{FFT}_{XY}^{-1} \left[\mathrm{FFT}_{XY}\left(H_2 \chi_{it}\right) \times \mathrm{FFT}_{XY}\left(h_{it}^s\right) \right. \right. \\ \left. \left. \overline{\mathrm{FFT}_X\left(\overline{\mathrm{FFT}_Y\left(H_2\chi_{it}\right)}\right)} \times \mathrm{FFT}_{XY}\left(h_{it}^s\right) \right] \right\} \tag{24}$$

with introducing the appropriate field, contrast and integrated Green's element matrices, and where overbar means complex conjugate. In the above the FFT are enforced on the matrices in between parentheses, the X and/or Y subscripts indicating the directions along which the FFT is carried out.

Now, solving the direct problem is to find H_2 satisfying the equation $\mathcal{A}H_2 = H_2^i$ where $\mathcal{A}$ is a direct operator defined by :

$$\mathcal{A}H_2 = H_2 - \sum_{it=1}^{Nt_{max}} \left\{ \mathrm{FFT}_{XY}^{-1} \left[\mathrm{FFT}_{XY}\left(H_2 \chi_{it}\right) \times \mathrm{FFT}_{XY}\left(h_{it}^s\right) \right. \right. \\ \left. \left. \overline{\mathrm{FFT}_X\left(\overline{\mathrm{FFT}_Y\left(H_2\chi_{it}\right)}\right)} \times \mathrm{FFT}_{XY}\left(h_{it}^s\right) \right] \right\} \tag{25}$$

A standard conjugate-gradient algorithm which minimizes the solution error has been used to solve this equation. A good review of the applications of this technique in electromagnetics and in acoustics can be found in [18], whereas various algorithms are presented in [19].

4.2 Observation Equation

The computation of the scattered field H_1^d at the receiver points on the line $\mathcal{L}$ is performed in two steps: (i) the scattered field is computed every Δ, (ii) a linear interpolation is done to get the field at the chosen lateral locations. The FFT-formulation of the scattered field is simply:

$$H_1^d = \sum_{it=1}^{Nt_{max}} \sum_{iy=1}^{Ny} \left\{ \mathrm{FFT}_X^{-1} \left[\mathrm{FFT}_X\left(H_2|_{iy} \chi_{it}|_{iy}\right) \times \mathrm{FFT}_X\left(f_{it}^{ns}|_{iy}\right) \right] \right\} \tag{26}$$

In the above the FFT are enforced only on each line, denoted as $\cdot|_{iy}$, of the matrices in between parentheses due to the non-correlation structure of (21)

along y, and the discrete summation is then performed over each such line to obtain the scattered field on the probing line.

5. NUMERICAL RESULTS

The first step of our validation was to verify the reciprocity theorem and the convergence of the scheme when increasing the number of discretisation elements. Then, three procedures have been attempted to validate from the literature the numerical results provided by the scheme presented in this paper: comparing with total H-fields inside the obstacle, comparing with scattered or total H-fields on the probing line, and comparing with scattered E-fields on the probing line. However we did not find any numerical results concerning the total H-field in an obstacle embedded in a half-space, and this part of the validation has been in effect made for an obstacle in free-space, where an exact calculation of the H-field can be carried out (numerical results are compared with those of [14]). For the total H-field on the receivers, numerical results are directly comparable with those of [20], while some work has to be done before comparing our results with the scattered E-field on the probing line provided to us by A. Sentenac with using the technique described in [21].

5.1 Total H-Field in the Obstacle

In [14] the integral equation is based on (A.6) and it involves $H(x,y)$ and $\mathbf{J}(x,y)$ where $\mathbf{J}(x,y) = (1-\varepsilon_0/\varepsilon(x,y))\,\nabla' H_z(x,y)$. The object is divided in triangular patches, in which the permittivity is taken to be constant and the magnetic field is varied linearly. Numerical results on homogeneous or layered circular cylinders are provided and compared with eigenfunction results. Among these results two sets have been chosen to validate the method presented in this paper.

1. The frequency of the incident wave is $f = 100$ MHz, the cylinder's circumference is λ_0 where λ_0 is the wavelength in air, its relative permittivity $\epsilon_{r\Omega} = 2.56$ and its conductivity $\sigma_\Omega = 0\,\mathrm{S/m}$. The $Nx \times Ny$ discretization is of 21×21 points. The results are presented in Fig. 3.
2. The frequency of the incident wave is $f = 3$ GHz, the cylinder circumference is π, its relative permittivity $\epsilon_{r\Omega} = 4$ and its conductivity $\sigma_\Omega = 16.69\,\mathrm{S/m}$. The $Nx \times Ny$ discretisation is of 25×25 points. The results are presented in Fig. 4.

These two comparisons show a fair agreement between the exact solutions and those provided by our scheme.

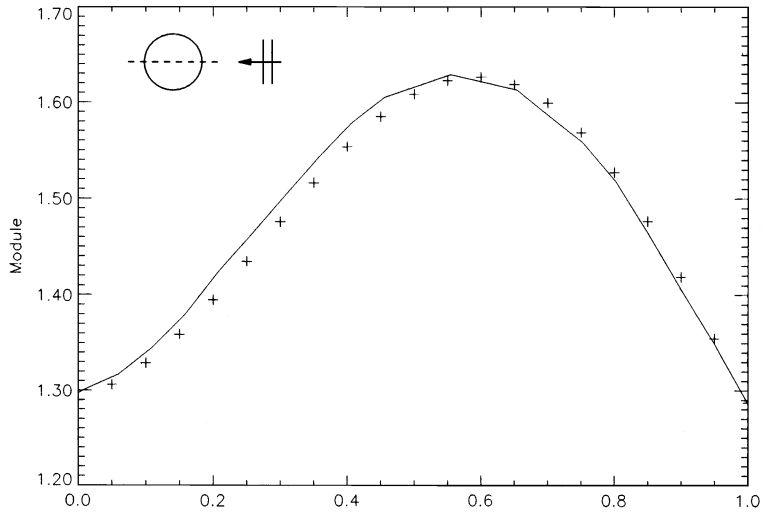

Figure 3. Field scattered by a circular cylinder of circumference λ_0 — the wavelength in air — of relative permittivity $\varepsilon_{r\Omega} = 2.56$ and of conductivity $\sigma_\Omega = 0\,\mathrm{S/m}$ placed in the air and illuminated by an incident plane wave of frequency $f = 100\,\mathrm{MHz}$. Here is represented the ratio of the total field to the incident field $|H|/|H^i|$ versus the normalized distance along the diameter of the cylinder: solid line the exact solution, with crosses the solution obtained by the scheme herein (with a 21×21 discretisation).

5.2 Total H-Field on the Receiver Line

In [20] the direct scattering problem of a homogeneous buried obstacle with a rough half-space interface is studied. The problem is solved using a single boundary integral equation discretized using a boundary finite-element method. Among the numerical results presented in this paper, two simulations are of interest to validate our code:

1. Frequency: $f = 300$ MHz (wavelength in air $\lambda_0 = 1$ m)
2. Half-space 1: $\epsilon_{r1} = 1$, $\sigma_1 = 0\,\mathrm{S/m}$, half-space 2: $\epsilon_{r2} = 4$, $\sigma_2 = 10^{-4}\,\mathrm{S/m}$, wavelength $\lambda_2 = \lambda_0/\sqrt{\epsilon_{r2}}$
3. Cylindrical object of square section centered at $(0, -\lambda_2)$, of side $d = \lambda_2$ and of relative permittivity $\epsilon_{r\Omega}$ and conductivity σ_Ω. Two cases have been studied: case A ($\epsilon_{r\Omega} = 1, \sigma_\Omega = 0$ S/m); and case B ($\epsilon_{r\Omega} = 16, \sigma_\Omega = 0.01$ S/m).
4. A line source of unit amplitude at $(0, \lambda_2)$.
5. A line of 37 receivers placed at $y = \lambda_2/4$, every $\lambda_2/6$ between $x = -3\lambda_2$ and $x = 3\lambda_2$.

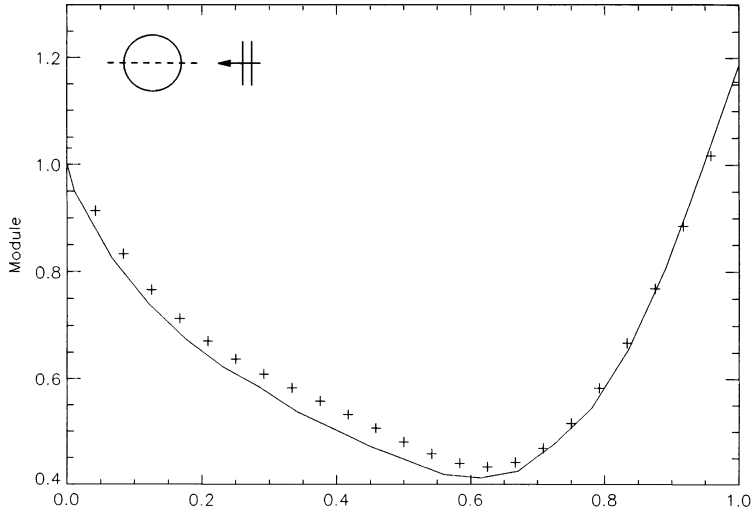

Figure 4. Field scattered by a circular cylinder of circumference π — the wavelength in air — of relative permittivity $\varepsilon_{r\Omega} = 4$ and of conductivity $\sigma_\Omega = 16.69\,\mathrm{S/m}$ placed in the air and illuminated by a incident plane wave of frequency $f = 3\,\mathrm{GHz}$. Here is represented the ratio of the total field to the incident field $|H|/|H^i|$ versus the normalized distance along the diameter of the cylinder: solid line the exact solution, with crosses the solution obtained by the scheme herein (with a 25×25 discretisation).

The results are presented in Fig. 5 and in Fig. 6. An excellent agreement is observed between both sets of results. Notice that the obstacle has been discretized differently in case A — (15×15) — and in case B — (21×21) — due to the fact that the permittivity in case B is much higher than in case A and convergence is observed to require a much finer mesh.

5.3 Scattered E-Field on the Receiver Line

In [21] the direct scattering problem of an inhomogeneous buried obstacle with a flat half-space interface is studied. The problem is solved using a E-field formulation and the linear system of equations is obtained by applying a standard Method of Moments — the obstacle is a distribution of rectangular cells in which the electric field and the complex permittivity are assumed to be constant. The system is solved by using standard routines of matrix inversion.

This technique has been applied to the obstacles A and B presented in 5. 2. except that the incident field is now a plane wave perpendicularly impinging

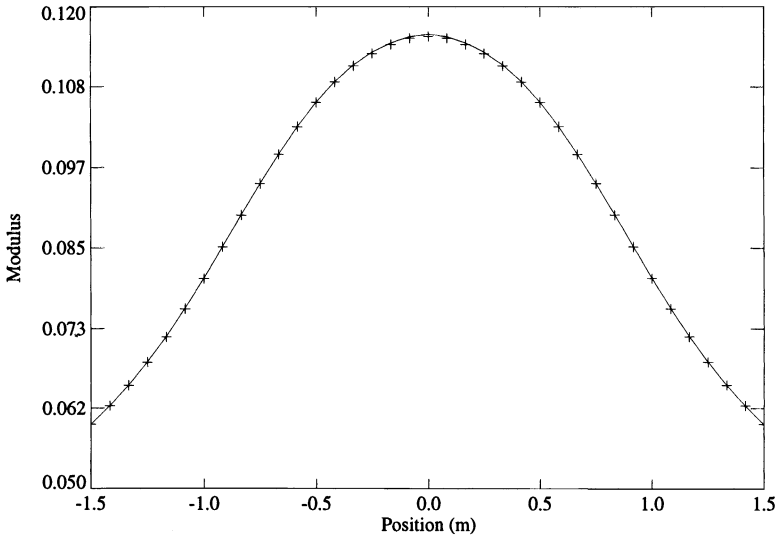

Figure 5. Case A: The configuration is introduced §5.2. The total magnetic field $|H|$ versus the receiver position is shown here (in solid line the field as found in [20], with crosses the solution obtained by the scheme herein).

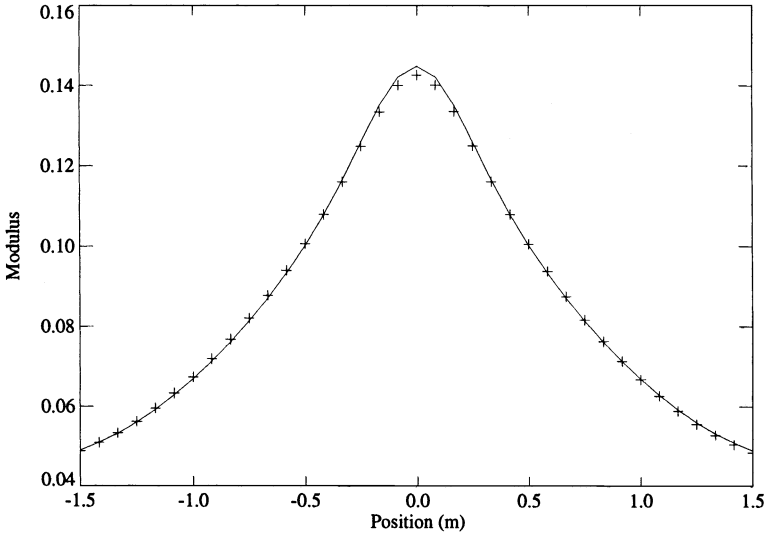

Figure 6. Case B: The configuration is introduced §5.2. The total magnetic field $|H|$ versus the receiver position is shown here (in solid line the field as found in [20], with crosses the solution obtained by the scheme herein).

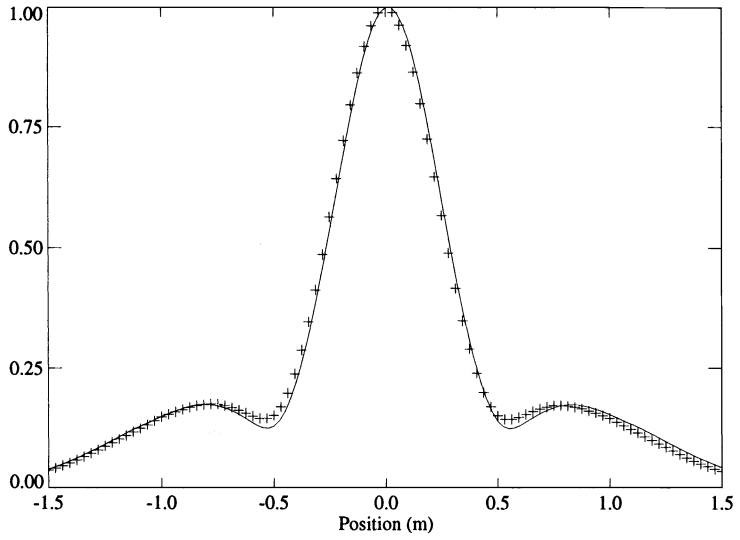

Figure 7. Case A: The configuration is presented §5.3. except that the incident field is now a plane wave impinging perpendicularly to the interface. The scattered electric $|E_y|$ — in arbitrary unit — versus the receiver position is shown here (in solid line the field as found in [21], with crosses the solution obtained by the scheme herein).

on the interface. Fig. 7 shows the comparison between the E_x components of the electric field in case A and Fig. 8 shows the comparison between the E_y components — in our case the electric field is calculated from the magnetic field by centred finite-difference from the magnetic field values just above and just below the assumed probing line. A good agreement can be observed between the two sets of data. It has to be noted that, with cells of size $\lambda_0/40$, the E-field code has not yet completely converged to the stable solution but a higher discretisation has not been possible due to the limitation of the computer memory. The latter comment may explain the discrepancy between both curves in Fig. 8.

5.4 Scattered field H-Field on the Receiver Line

The case of multiple obstacles can also be treated the same way. The configuration is the following:

1. Frequency: $f = 300\,\text{MHz}$ (wavelength in air $\lambda_0 = 1\,\text{m}$)
2. Half-space 1: $\epsilon_{r1} = 1$, $\sigma_1 = 0\,\text{S/m}$, half-space 2: $\epsilon_{r2} = 4$, $\sigma_2 =$

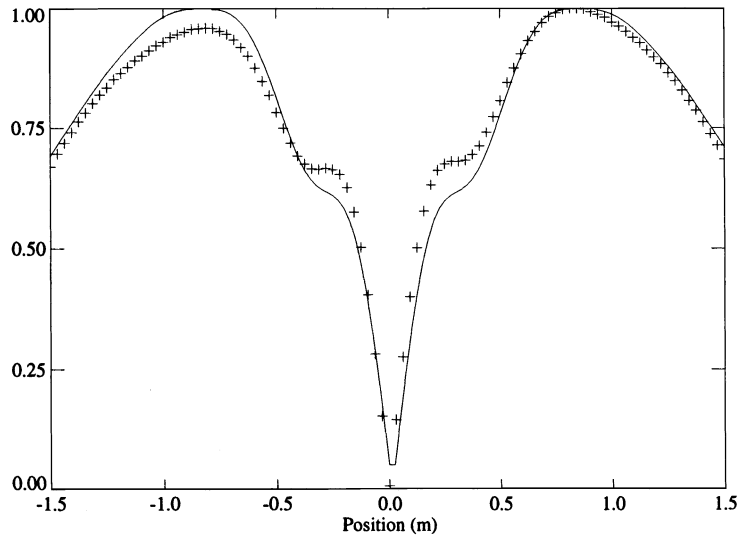

Figure 8. Case B: The configuration is presented §5.3. except that the incident field is now a plane wave impinging perpendicularly to the interface. The scattered electric $|E_y|$ — in arbitrary unit — versus the receiver position is shown here (in solid line the field as found in [21], with crosses the solution obtained by the scheme herein).

10^{-4} S/m, wavelength $\lambda_2 = \lambda_o/\sqrt{\epsilon_{r2}}$

3. Two cylindrical objects of square section respectively centered at $(-5\lambda_2/4,\ -3\lambda_2/2)$ and at $(-5\lambda_2/4,\ -3\lambda_2/4)$, of side $d = \lambda_2$ and of relative permittivity $\epsilon_{r\Omega} = 8$ and conductivity $\sigma\Omega = 0$ S/m.
4. A line source of unit amplitude at $(0, \lambda_2)$.
5. A line of 50 receivers equally spaced between $(-3\lambda_2, \lambda_2/2)$ and $(3\lambda_2, \lambda_2/2)$

In contrast with the case of one obstacle, we need to discretize the cross-section of the smaller rectangular zone including the two obstacles and not only their cross-sections. In our case this zone is of size $(5\lambda_2/2 \times 2\lambda_2)$ centered at $(0, -5\lambda_2/4)$ and discretized with 51×41 points. Fig. 9 shows the scattered H-field H^d measured on the probing line.

6. CONCLUSION

An algorithm to calculate the magnetic field observed in the TE polarisation case has been developed for a buried cylindrical obstacle. The formulation is

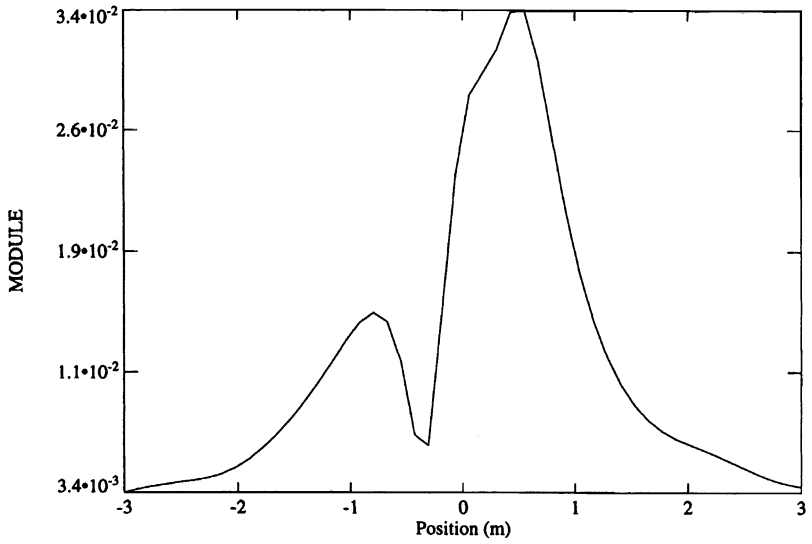

Figure 9. The configuration is presented §5.4. The scattered magnetic field $|H^d|$ versus the receiver position in the case of two obstacles is shown here.

based on a scalar domain integral formulation of the magnetic field which is discretized using a Method of Moments. The convolution-correlation structure of the resulting integral equations has been emphasized and a appropriate FFT-based solver developed and validated with results available in the literature.

This method can directly be applied to the calculation of the field scattered by several disjoint obstacles embedded in a half-space.Also it can easily be extended to provide the scattered field for :

1. more complicated sources than the line source or plane wave source, such as extended sources;
2. different configurations, such as the so-called borehole-to-borehole configurations, and surface-to-borehole configurations; an obstacle above the interface; a stratified half-space if the obstacle is entirely contained in a given layer.

Present works are now devoted to the reconstruction of a similarly buried obstacle from a limited observation of the scattered field. The method presented here provides synthetic data as input data for the inversion, and is a building part of the inversion itself (first results have been presented in [22]).

ACKNOWLEDGEMENTS

The author acknowledges the contribution of M. Saillard, Laboratoire d'Optique Électromagnétique, Marseille, and A. Sentenac, Laboratoire d'Optique des Surfaces et des Couches Minces, Marseille, who have provided numerical results for comparison. The help of B. J. Kooij, Laboratory of Electromagnetic Research, Delft University, was also quite useful. The many and lively discussions with D. Lesselier, Laboratoire des Signaux et Systèmes, Gif-sur-Yvette, have been very fruitful.

APPENDIX A.

For the sake of simplicity the demonstration is in free-space. One starts from the Maxwell's equations outside the sources:

$$\nabla \times \mathbf{H}(\mathbf{r}) + j\omega\varepsilon\mathbf{E}(\mathbf{r}) = 0, \text{ with } \varepsilon = \begin{cases} \varepsilon(\mathbf{r}), \text{if } \mathbf{r} \in \Omega \\ \varepsilon_0, \text{otherwise} \end{cases} \tag{A.1}$$

$$\nabla \times \mathbf{E}(\mathbf{r}) - j\omega\mu_0\mathbf{H}(\mathbf{r}) = 0 \tag{A.2}$$

where $\mathbf{r}$ is only dependent on x and y, where ε_0 and μ_0 are respectively the permittivity and permeability of the vacuum, where $\varepsilon(\mathbf{r})$ is the complex permittivity of the obstacle of bounded cross-section Ω, where $\mathbf{H}(\mathbf{r})$ is the magnetic field (A/m) and where $\mathbf{E}(\mathbf{r})$ is the electric field (V/m).

Dividing both sides of (A.1) by $\varepsilon(\mathbf{r})$, taking the curl of this new equation, using (A.2) to eliminate $\mathbf{E}(\mathbf{r})$, taking in account that $\nabla\nabla \cdot \mathbf{H}(\mathbf{r}) = \mathbf{0}$ and that $\nabla \times \mathbf{H}(\mathbf{r}) = \nabla H_z(\mathbf{r}) \times \mathbf{e_z}$ because of the assumed TE polarization ($\mathbf{H}(\mathbf{r}) = H_z(\mathbf{r})\mathbf{e_z}$) and re-arranging the different terms, gives the scalar Helmholtz wave equation:

$$\Delta H_z(\mathbf{r}) + \omega^2\varepsilon_0\mu_0 H_z(\mathbf{r}) = \nabla \times \left[\left(\frac{\varepsilon_0}{\varepsilon(\mathbf{r})} - 1\right)\nabla H_z(\mathbf{r}) \times \mathbf{e_z}\right] \tag{A.3}$$

Let us introduce the free-space Green's function $G(\mathbf{r}, \mathbf{r}')$ such that:

$$\Delta G(\mathbf{r}, \mathbf{r}') + k_0^2 G(\mathbf{r}, \mathbf{r}') = -\delta(\mathbf{r} - \mathbf{r}'), \quad k_0^2 = \omega^2\varepsilon_0\mu_0 \tag{A.4}$$

with the 2-D Sommerfeld radiation condition:

$$\lim_{r\to\infty} \sqrt{r}\left[\frac{\partial G(\mathbf{r}, \mathbf{r}')}{\partial r} - jk_m G(\mathbf{r}, \mathbf{r}')\right] = 0, \quad r = |\mathbf{r}|, m = 1, 2 \tag{A.5}$$

Using the Green's theorem yields the domain integral equation satisfied by $H_z(\mathbf{r})$:

$$H_z(\mathbf{r}) = H_z^i(\mathbf{r}) + \int_\Omega \nabla' \times \left[\left(1 - \frac{\varepsilon_0}{\varepsilon(\mathbf{r}')}\right)\nabla' H_z(\mathbf{r}') \times \mathbf{e_z}\right] G(\mathbf{r}, \mathbf{r}')d\mathbf{r}' \tag{A.6}$$

where $H_z^i(\mathbf{r})$ is the incident field and ∇' acts on the primed variable.

This equation can be rewritten. Since $\nabla \times (\phi \mathbf{A}) = \phi \nabla \mathbf{A} - \mathbf{A} \times \nabla \phi$ one has :

$$\begin{aligned} &\int_\Omega \nabla' \times \left[\chi(\mathbf{r}') \nabla' H_z(\mathbf{r}') \times \mathbf{e_z}\right] G(\mathbf{r}, \mathbf{r}') d\mathbf{r}' \\ &= \int_\Omega \nabla' \times \left[\chi(\mathbf{r}') \nabla' H_z(\mathbf{r}') \times \mathbf{e_z} G(\mathbf{r}, \mathbf{r}')\right] d\mathbf{r}' \\ &+ \int_\Omega \chi(\mathbf{r}') \left[\nabla' H_z(\mathbf{r}') \times \mathbf{e_z} \times \nabla' G(\mathbf{r}, \mathbf{r}')\right] d\mathbf{r}' \end{aligned} \tag{A.7}$$

where $\chi(\mathbf{r}) = \mathbf{1} - \varepsilon_0 / \varepsilon(\mathbf{r})$. Let us write that

$$\begin{aligned} &\int_S \nabla' \times \left[\chi(\mathbf{r}') \nabla' H_z(\mathbf{r}') \times \mathbf{e_z} G(\mathbf{r}, \mathbf{r}')\right] d\mathbf{r}' \\ &= \oint_C \chi(\mathbf{r}') \left[\nabla' H_z(\mathbf{r}') \times \mathbf{e_z}\right] G(\mathbf{r}, \mathbf{r}') d\mathbf{r}' \end{aligned}$$

where S is a 2-D bounded domain and C its contour. S can be chosen including Ω such that the integral over C is null — since $\chi(\mathbf{r})$ is of bounded support. So:

$$\int_\Omega \nabla' \times \left[\chi(\mathbf{r}') \nabla' H_z(\mathbf{r}') \times \mathbf{e_z} G(\mathbf{r}, \mathbf{r}')\right] d\mathbf{r}' = \mathbf{0}$$

which allows us to simplify (A.7)

$$\begin{aligned} &\int_\Omega \nabla' \times \left[\chi(\mathbf{r}') \nabla' H_z(\mathbf{r}') \times \mathbf{e_z}\right] G(\mathbf{r}, \mathbf{r}') d\mathbf{r}' \\ &= \int_\Omega \chi(\mathbf{r}') \left[\nabla' H_z(\mathbf{r}') \times \mathbf{e_z} \times \nabla' G(\mathbf{r}, \mathbf{r}')\right] d\mathbf{r}' \\ &H_z(\mathbf{r}) = H_z^i(\mathbf{r}) + \int_\Omega \chi(\mathbf{r}') \left[\nabla' H_z(\mathbf{r}') \times \mathbf{e_z} \times \nabla' G(\mathbf{r}, \mathbf{r}')\right] d\mathbf{r}' \end{aligned} \tag{A.8}$$

In fine, knowing that

$$\begin{aligned} \nabla H_z(\mathbf{r}) \times \mathbf{e_z} \times \nabla G(\mathbf{r}, \mathbf{r}') &= \left[\nabla G(\mathbf{r}, \mathbf{r}') \cdot \nabla H_z(\mathbf{r}')\right] \mathbf{e_z} \\ - \left[\nabla G(\mathbf{r}, \mathbf{r}') \cdot \mathbf{e_z}\right] \nabla H_z(\mathbf{r}') &= \left[\nabla G(\mathbf{r}, \mathbf{r}') \cdot \nabla H_z(\mathbf{r}')\right] \mathbf{e_z} \end{aligned} \tag{A.9}$$

because the z-component of $\nabla G(\mathbf{r}, \mathbf{r}')$ is null, the H-field integral equation is obtained:

$$H_z(\mathbf{r}) = H_z^i(\mathbf{r}) + \int_\Omega \chi(\mathbf{r}') \nabla' G(\mathbf{r}, \mathbf{r}') \cdot \nabla' H_z(\mathbf{r}') d\mathbf{r}' \tag{A.10}$$

APPENDIX B. SINGULARITY INTEGRATION

Numerical integration of

$$\iint_{\Omega^t} \nabla' \mathrm{H}_0^{(1)}(kr)dx'dy', \quad r = \sqrt{(x-x')^2 + (y-y')^2} \tag{B.1}$$

where Ω^t is the surface of a triangle and $\nabla' \mathrm{H}_0^{(1)}(kr)$ is given by

$$\nabla' \mathrm{H}_0^{(1)}(kr) = \frac{jk}{4r} \mathrm{H}_1^{(1)}(kr) \begin{pmatrix} x-x' \\ y-y' \end{pmatrix} \tag{B.2}$$

fails when $\mathbf{X} \to \mathbf{X}'$ where $\mathbf{X} = (x, y)$ and $\mathbf{X}' = (x', y')$ due to the logarithmic singularity of $\nabla' \mathrm{H}_0^{(1)}(kr)$ at $r = 0$. To solve this numerical problem the extraction of the singularity is to be performed. For brevity only the x-component of $\nabla' \mathrm{H}_0^{(1)}(kr)$ will be studied.

Taking into account that $\mathrm{H}_1^{(1)}(kr) = \mathrm{J}_1(kr) + j\mathrm{Y}_1(kr)$,

$$\lim_{\mathbf{X}\to\mathbf{X}'} \frac{x-x'}{r} \mathrm{H}_1^{(1)}(kr) = \lim_{\mathbf{X}\to\mathbf{X}'} j\frac{x-x'}{r} \mathrm{Y}_1(kr) \tag{B.3}$$

where $\mathrm{Y}_1(kr)$ is singular at $\mathbf{X} = \mathbf{X}'$.

A second-order expansion of $\mathrm{Y}_1(kr)$ versus kr and a first-order one of $\mathrm{J}_1(kr)$ is needed,

$$\left.\begin{aligned} \mathrm{Y}_1(kr) &\approx -\frac{2}{\pi kr} + \frac{2}{\pi} \ln\left(\frac{kr}{2}\right) \mathrm{J}_1(kr) \\ \mathrm{J}_1(kr) &\approx \frac{kr}{2} \end{aligned}\right\} \Leftrightarrow \mathrm{Y}_1(kr) \approx -\frac{2}{\pi kr} + \frac{kr}{\pi} \ln\left(\frac{kr}{2}\right) \tag{B.4}$$

In so doing we obtain:

$$\lim_{\mathbf{X}\to\mathbf{X}'} \frac{jk(x-x')}{4r} \mathrm{H}_1^{(1)}(kr) = \lim_{\mathbf{X}\to\mathbf{X}'} \left[\frac{x-x'}{2\pi r^2} - \frac{k^2(x-x')}{4\pi} \ln\left(\frac{kr}{2}\right)\right] \tag{B.5}$$

A higher-order expansion of $\mathrm{Y}_1(kr)$ and of $\mathrm{J}_1(kr)$ will provide terms in $r^n, n \geq 1$, which are not singular.

Now that the singularity has been determined, the integral can be divided in two terms:

$$\frac{j}{4}\iint_{\Omega^t}\frac{x-x'}{r}\mathrm{H}_1^{(1)}(kr)dx'dy' = \iint_{\Omega^t} h(x,x',y,y')dx'dy' + \iint_{\Omega^t} f(x,x',y,y')dx'dy'$$

$$h(x,x',y,y') = \frac{x-x'}{2\pi kr^2} - \frac{k^2(x-x')}{4\pi}\ln\left(\frac{kr}{2}\right) \tag{B.6}$$

$$f(x,x',y,y') = \frac{jk(x-x')}{4r}\mathrm{H}_1^{(1)}(kr) - \left[\frac{x-x'}{2\pi kr^2} - \frac{k^2(x-x')}{4\pi}\ln\left(\frac{kr}{2}\right)\right]$$

- The first part takes into account the singularity and it can be, after tedious developments, analytically determined.
- The second part is now regular and it can be numerically calculated using a Gauss-Legendre scheme.

REFERENCES

1. Peterson, A. F., "A comparison of integral, differential and hybrid methods for TE-wave scattering from inhomogeneous dielectric cylinder," *J. Electromagn. Waves Applic.*, Vol. 3, No. 2, 87–106, 1988.
2. Borup, D. T., D. M. Sullivan, and O. P. Gandhi, "Comparison of the FFT conjugate gradient method and the finite-difference time-domain method for the 2-D absorption problem," *IEEE Trans. Microwave Theory Tech.*, Vol. MTT-35, No. 4, 383–395, 1987.
3. Joachimowicz, N., and C. Pichot, "Comparison of three integral formulations for the 2-D TE scattering problem," *IEEE Trans. Microwave Theory Tech.*, Vol. MTT-38, No. 2, 178–185, 1990.
4. Zwamborn, P., and P. M. van den Berg, "A weak form of the conjugate gradient FFT method for two-dimensional TE scattering problems," *IEEE Trans. Microwave Theory Tech.*, Vol. MTT-39, No. 6, 953–960, 1991.
5. Xu, X. B., and W. Yan, "A hybrid integral equation solution of scattering of TE excitation by inhomogeneous cylinder near a medium interface," *J. Electromagn. Waves Applic.*, Vol. 7, No. 7, 919–942, 1993.
6. Xu, X. B., and W. Yan,"Modification of hybrid integral equation for determining scattering by an inhomogeneous cylinder of discontinuous electromagnetic parameters near a media interface," *J. Electromagn. Waves Applic.*, Vol. 7, No. 10, 1389–1394, 1993.
7. Ellis, G. A., and I. C. Peden, "An analysis technique for buried inhomogeneous dielectric object in the presence of an air-earth interface," *IEEE Trans. Geosci. Remote Sensing*, Vol. 33, No. 3, 535–540, 1995.

8 Jin, J. M., V. V. Liepa, and C. T. Tai, "A volume-surface integral equation for electromagnetic scattering by inhomogeneous cylinders," *J. Electromagn. Waves Applic.*, Vol. 2, No. 5–6, 573–588, 1988.

9. Lixin, W., R. E. Kleinman, and P. M. van den Berg,"Modified gradient profile inversion using H-polarized waves," *Proc. IEEE Antennas and Propagation Society International Symposium*, Vol. 3, 1598–1601, Newport Beach, California, 18-23 June, 1995.
10. Frisk, G. V., and J. F. Lynch, "Shallow water wave guide characterization using the Hankel transform," *J. Acoust. Soc. Am.*,Vol. 76, No. 1, 205–216, 1984.
11. DeSanto, J. A., *Scalar Wave Theory*, Vol. 12 of *Wave Phenomena*, Berlin: Springer-Verlag, 1992.
12. Harrington, R. F., "The method of moments in electromagnetics," *J. Electromagn. Waves Applic.*, Vol. 1, No. 3, 181–200, 1987.
13. Harrington, R. F., *Field Computation by Moment Method*, New York, The Macmillan Company, 1968.
14. Peterson, A. F., and P. W. Klock, "An improved MFIE formulation for TE-wave scattering from lossy, inhomogeneous dielectric cylinder," *IEEE Trans. Antennas Propagat.*, Vol. AP-36, No. 1, 45–49, 1988.
15. Brigham, E. O., *The Fast Fourier Transform*, Englewoods Cliffs, Prentice-Hall, 1974.
16. Lesselier, D., and B. Duchêne, "Buried, 2-D penetrable objects illuminated by line sources: FFT-based iterative computations of the anomalous field," *Application of Conjugate Gradient Methods to Electromagnetics and Signal Analysis* (Sarkar, T. P., ed.), Progress in Electromagnetics Research, Vol. 5, 400–438, New York, Elsevier, 1991.
17. Dutt, A., and V. Rokhlin, "Fast Fourier transforms for nonequispaced data," *SIAM J. Sci. Comput.*, Vol. 14, No. 6, 1368–1393, 1993.
18. Sarkar, T. K., *Application of Conjugate Gradient Methods to Electromagnetics and Signal Analysis*, Progress in Electromagnetics Research, Vol. 5, New York, Elsevier, 1991.
19. Sarkar, T. K., X. Yang, and E. Arvas, "A limited survey of various conjugate gradient methods for solving complex matrix equations arising in electromagnetic wave interaction," *Wave Motion*,Vol. 10, No. 6, 527–546, 1988.
20. Saillard, M., and G. Toso, "Electromagnetic scattering from bounded or infinite subsurface bodies," *Radio Sci.*, Vol. 32, No. 4, 1347–1360, 1997.
21. Pincemin, F., A. Sentenac, and J. -J. Greffet, "Near field scattered by a dielectric rod below a metallic surface," *J. Opt. Soc. Am. A*, Vol. 11, No. 3, 1117–1125, 1994.

22. Lambert, M., B. J. Kooij, and B. Duchêne, "Reconstruction of a buried 2-D penetrable object: the TE-case," *Proc. Progress In Electromagnetic Research Symposium*, 554, Cambridge, Massachusetts, USA, 7–11 July, 1997.

Marc Lambert, born in Grenoble, France, in October 1966, received the degree of *Maître es Sciences* in 1989, and *Docteur en Sciences* from the *Université de Paris-Sud– Orsay* in 1994. Since 1995, he is with the *Laboratoire des Signaux et Systèmes* (CNRS-SUPÉLEC). He is presently *Chargé de Recherche* at CNRS. His research interests include radiation, scattering and propagation of electromagnetic and acoustic waves, particularly in the so-called inverse problem domain applied to electromagnetic and acoustic characterization of buried obstacle; and geophysical and medical imaging applications.

B

Gradient modifié contraint

[A.4] The retrieval of a buried cylindrical obstacle by a constrained modified gradient method in the H-polarization case and for Maxwellian materials
Marc Lambert, Dominique Lesselier et Bert Jan Kooij
Inverse Problems **14** 1265-1283 1998
Featured article (for a semester, in the Journal Information Page for Inverse Problems of the WWW site of t he Institute of Physics)

Inverse Problems **14** (1998) 1265–1283. Printed in the UK PII: S0266-5611(98)93808-4

The retrieval of a buried cylindrical obstacle by a constrained modified gradient method in the *H*-polarization case and for Maxwellian materials

M Lambert†§, D Lesselier†‖ and B J Kooij‡¶

† Département de Recherche en Électromagnétisme, Laboratoire des Signaux et Systèmes (CNRS/SUPÉLEC), Plateau de Moulon, F-91192 Gif-sur-Yvette, France

‡ Centre for Technical Geoscience, Laboratory of Electromagnetic Research, Department of Electrical Engineering, Delft University of Technology, The Netherlands

Received 1 May 1998

Abstract. The retrieval of an unknown, possibly inhomogeneous, penetrable cylindrical obstacle buried entirely in a known homogeneous half-space—the constitutive material parameters of the obstacle and of its embedding obey a Maxwell model—is considered from single- or multiple-frequency aspect-limited data collected by ideal sensors located in air above the embedding half-space, when a small number of time-harmonic transverse electric (TE)-polarized line sources—the magnetic field H is directed along the axis of the cylinder—is also placed in air. The wavefield is modelled from a rigorous H-field domain integral-differential formulation which involves the dot product of the gradients of the single component of H and of the Green function of the stratified environment times a scalar-valued contrast function which contains the obstacle parameters (the frequency-independent, position-dependent relative permittivity and conductivity). A modified gradient method is developed in order to reconstruct the maps of such parameters within a prescribed search domain from the iterative minimization of a cost functional which incorporates both the error in reproducing the data and the error on the field built inside this domain. Non-physical values are excluded and convergence reached by incorporating in the solution algorithm, from a proper choice of unknowns, the condition that the relative permittivity be larger than or equal to 1, and the conductivity be non-negative. The efficiency of the constrained method is illustrated from noiseless and noisy synthetic data acquired independently. The importance of the choice of the initial values of the sought quantities, the need for a periodic refreshment of the constitutive parameters to avoid the algorithm providing inconsistent results, and the interest of a frequency-hopping strategy to obtain finer and finer features of the obstacle when the frequency is raised, are underlined. It is also shown that though either the permittivity map or the conductivity map can be obtained for a fair variety of cases, retrieving both of them may be difficult unless further information is made available.

1. Introduction

As is illustrated in Lesselier and Duchêne (1996), the retrieval of a buried obstacle from the inversion of the electromagnetic (or acoustic) wavefield, which is resulting outside its (possibly stratified) embedding from the illumination by a known probing signal also generated outside the embedding, is of practical interest in various application domains:

§ E-mail address: marc.lambert@lss.supelec.fr
‖ E-mail address: lesselier@supelec.fr
¶ E-mail address: b.j.kooij@et.tudelft.nl

0266-5611/98/051265+19$19.50

non-destructive evaluation of tubes, plates and other components of industrial equipment and airplanes, mapping of geophysical structures in the earth, identification of land and sea mines or other artificial objects in natural media, characterization of civil engineering constructions, imaging of anomalies in living tissues, etc.

However, this retrieval often remains quite challenging in theoretical, computational, and/or experimental terms. This paper intends to contribute to the ongoing investigation of such wavefield inversion problems, with a clear emphasis on algorithmic issues, and it tackles the rather rarely studied nonlinearized electromagnetic mapping of a buried, possibly inhomogeneous, penetrable obstacle in the transverse electric (TE) or H-polarization case—the magnetic field is assumed to be parallel to the axis of the cylinder—when the obstacle and its embedding both obey a Maxwell material model.

The solution method of choice belongs to the class of the recently developed modified gradient methods (Kleinman and van den Berg 1992a, b). It is developed from a rigorous wavefield domain integral formulation deduced from the Green theorem, and it is such that the incorporation of proper constraints within the iterative scheme ensures that the retrieval of non-physical electrical parameters is prohibited. A suitable initial choice of the sought quantities, their periodic refreshment in order both not to get stuck too early within a plateau of the minimized cost functional and to avoid the retrieval of an inconsistent couple of solutions (fields, material parameters), and the use of a marching-on-in-frequency procedure when frequency-diverse data are available, also contribute to improve—or are prerequisites to—the convergence of the iterates towards stable and satisfactory values.

Once reminded of the well known nonlinearity and ill-posedness of the retrieval of a buried obstacle from inversion of a wavefield, this ill-posedness being clearly worsened with respect to free-space configurations by the limited aspect of the data (one obviously cannot illuminate the obstacle from all around), one should observe the following.

(i) It has been evidenced that the modelling of the electromagnetic interaction of the probing wave with a penetrable obstacle in the H-polarization case is much more prone to inaccuracy, and computationally demanding, than in the corresponding E-polarization case (see as an early example Zwamborn and van den Berg (1991)). This may forbid, or greatly complicate, the solution of the corresponding inversion problem although E-polarization and H-polarization field data should be of equal concern if one wishes to further the development of, say, ground probing electromagnetic systems. Here one starts from an H-field integral formulation (the operator is, in effect, of integral-differential type (Kleinman and van den Berg 1997)) and one takes inspiration from the corresponding mathematical and numerical analysis of the direct scattering problem (Lambert 1998).

(ii) In close relation with observation (i), it is still far from clear nowadays whether the nonlinearized inversion methods, such as the modified gradient ones that are demonstrated to be rather effective for the retrieval of buried penetrable obstacles in the E-polarization case (Kleinman *et al* 1997a), will perform as well in the H-polarization case for the same configurations; in particular there is an evident lack of results to go back to—Lixin *et al* (1995a, b) consider a free-space embedding only and we do not know of results concerning the buried case.

(iii) It is of practical interest to consider embedding and obstacle materials which are both obeying a Maxwell model. Indeed, in many materials—as soon as the frequency is large enough—polarization and conduction phenomena occur with like importance. Here they are modelled in a first step from the permittivity and conductivity which are taken as frequency-independent parameters—this is still idealized particularly for some natural media whose dispersion law is often complicated, for example a compound Debye medium, even though the range of frequencies is strongly band-limited.

(iv) It is useful to see how the ability of an inversion method to retrieve the permittivity map and/or the conductivity map of such an obstacle then relies on *a priori* information, and to show under which conditions effectiveness may be reached: size and electrical parameters of the obstacle, sources and sensors location, discretization of the search domain, initialization of the algorithm, use of frequency-diversity, for example by *frequency-hopping* (Chew and Lin 1995, Belkebir and Tijhuis 1996, Litman *et al* 1998). Notice that one should also appraise the consequences of the fact that the obstacle may now be either a weaker or a stronger electromagnetic scatterer with respect to its embedding, which is in obvious contrast with free-space configurations.

(v) In close relation with observation (iv), properly incorporating the *a priori* information is a matter of current investigation, for example Souriau *et al* (1996) and Monebhurrun *et al* (1998) make use of the binarity of a contrast function, Belkebir and Tijhuis (1996) enforce the positivity of its real and imaginary parts, van den Berg and Kleinman (1995) regularize the inversion by means of a total variation term added to the cost functional, Lobel *et al* (1997) use an edge-preserving technique to retrieve large plateaux with sharp edges. Here the choice of non-negative real-valued unknowns, excluding obvious non-physical cases (the permittivity is greater than or equal to 1, and the conductivity is non-negative), leads to an inversion strategy which is performing fairly well, although the complication of the solution method is considerably increased.

The paper is organized as follows. In section 2 the H-field formulation is introduced and the modified gradient solution scheme is developed with particular attention devoted to the introduction of constraints on the constitutive material parameters and to the resulting changes of the scheme with respect to the usual ones. In section 3 results of inversion led from single-frequency or multiple-frequency, multiple-source synthetic data acquired in typical configurations—and generated with meshes appropriately finer than those used in the inversion so as not to suffer from the *inverse crime*—are displayed. Emphasis is on the choice of the initial values of the unknowns within the test domain and the necessity of their periodic refreshment, while the interest of the frequency-hopping technique is confirmed. It is also shown that the retrieval of either a permittivity map or a conductivity map is possible for a fair variety of cases, but retrieving both of them together is difficult unless complementary *a priori* information is made available. A short conclusion follows which outlines further work, such as imposing the binarity of the contrast function as an alternate regularization technique.

2. The theoretical machinery

2.1. The field formulation

The geometry and the electrical configuration are as follows (see figure 1).

A small number, N_s, of time-harmonic H-polarized line sources is located at the same given height y_s above the planar interface x–z between a homogeneous upper air half-space—numbered 1—and a homogeneous lower half-space—numbered 2—where a possibly inhomogeneous, penetrable cylindrical obstacle of z-axis is entirely embedded and whose cross section is assumed to lie within a prescribed search domain $\mathcal{D}$ (as a matter of fact this hypothesis is the main topological information introduced on the obstacle). The resulting single H_z component of the scattered magnetic field is collected along a probing line $\mathcal{L}$ also placed at fixed height y_r above and close to the interface by a number N_r of (equally distributed) ideal receivers. For simplicity, the z-component of the total magnetic field H_z

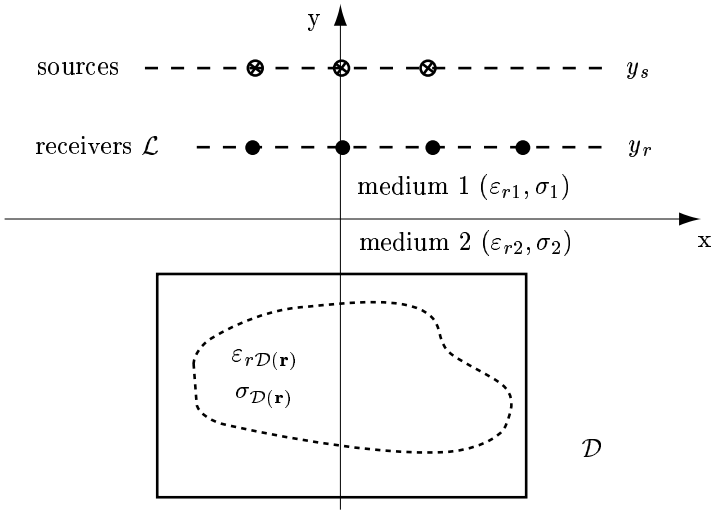

Figure 1. The geometrical and electrical configurationof study.

will be denoted from now on as H and its scattered part as H^{scat}. The data fieldwill be denoted as ζ.

The circular frequency, $\omega = 2\pi f$ where f is the frequency (the time dependence $\mathrm{e}^{-\mathrm{j}\omega t}$ is omitted from now on) may take several values in a given band so as to partially offset the consequences of the limited aspect of the data, but the characteristic dimensions of the obstacle cross section always remain of the order of the mean wavelength of the probing wave in the embedding—we focus onto the resonance domain, and numerical applications will be carried out at a few hundred MHz frequencies for a sand-like embedding.

All materials are assumed to be linear, isotropic and non-magnetic, and to obey a Maxwell model. Thus they are fully specified by their frequency-independent relative permittivity ε_{rm} and conductivity (in S m^{-1}) σ_m, $m = 1, 2, \mathcal{D}$. $\varepsilon_{r\mathcal{D}}$ and $\sigma_{\mathcal{D}}$ are allowed to vary with position $\boldsymbol{r} = (x, y)$ within $\mathcal{D}$. The complex permittivity of each medium is defined as $\varepsilon_m = \varepsilon_0\varepsilon_{rm} + \mathrm{j}\sigma_m/\omega$, the corresponding complex wavenumbers k_m with non-negative imaginary parts being such that $k_m^2 = \omega^2\mu_0\varepsilon_m$, where ε_0 and μ_0 are the vacuum permittivity and permeability, respectively. In the numerical applications we limit ourselves to an air upper half-space, i.e. $\varepsilon_{r1} = 1$, $\sigma_1 = 0$, and $k_1 = k_0$.

The wavefield modelling is based on a rigorous scalar H-field domain integral formulation which is deduced by application of the Green theorem to the Helmholtz wave equations satisfiedby the electromagnetic fieldin either medium and with using the proper transmission and radiation conditions. This formulation yields the single component H of the magnetic field at the location $\boldsymbol{r} = (x, y)$ anywhere in space from the integration of the dot product of the transverse gradients of the Green function of the two-half-space environment and of the H-fieldcomponent, times a complex-valued contrast function $\mathcal{M}$ which is representative of the space variations of the obstacle parameters and per extension of those of the search domain $\mathcal{D}$.

For a given obstacle, and a given source numbered as j, $j = 1, \ldots, N_s$, which is operating at a fixed frequency ω (implied), the total magnetic field H_j in $\mathcal{D}$ and the scattered magnetic field H_j^{scat} along $\mathcal{L}$ satisfy the state (coupling) equation (2) and the data (observation) equation (3). Letting the incident fieldin the half-space 2 be $H_j^{\text{inc}}(\boldsymbol{r})$ and

the contrast function be

$$\mathcal{M}(\boldsymbol{r}) = 1 - \frac{\varepsilon_2}{\varepsilon_{\mathcal{D}}(\boldsymbol{r})} \tag{1}$$

these two equations read

$$H_j(\boldsymbol{r}) = H_j^{\text{inc}}(\boldsymbol{r}) + \int_{\mathcal{D}} \mathrm{d}\boldsymbol{r}'\, \mathcal{M}(\boldsymbol{r}')[\nabla' G_{\mathcal{D}}(\boldsymbol{r}, \boldsymbol{r}') \cdot \nabla' H_j(\boldsymbol{r}')] \qquad \boldsymbol{r} \in \mathcal{D} \tag{2}$$

and

$$H_j^{\text{scat}}(\boldsymbol{r}) = \int_{\mathcal{D}} \mathrm{d}\boldsymbol{r}'\, \mathcal{M}(\boldsymbol{r}')[\nabla' G_{\mathcal{L}}(\boldsymbol{r}, \boldsymbol{r}') \cdot \nabla' H_j(\boldsymbol{r}')] \qquad \boldsymbol{r} \in \mathcal{L}. \tag{3}$$

The two-component ∇' operator is taken with respect to the primed variables. $G_{\mathcal{D}}(\boldsymbol{r}, \boldsymbol{r}')$ is the Green function of the stratified environment when (in the absence of the obstacle) an ideal line source oriented along z is set at point $\boldsymbol{r}$ and the resulting field is observed at the location $\boldsymbol{r}'$, both source and observation points being in the half-space 2. $G_{\mathcal{L}}(\boldsymbol{r}, \boldsymbol{r}')$ is the corresponding Green function when the source point $\boldsymbol{r}$ is in the half-space 2 and the observation point $\boldsymbol{r}'$ is in the half-space 1.

The formulation, its discrete counterpart, and the numerical testing thereof is detailed in Lambert (1998)—we emphasize that one may use a vector integral formulation of the two-component transverse electric field instead of this scalar formulation of the axially oriented magnetic field, at the price of the manipulation of a higher-dimension unknown manifold and with the benefit of dealing with a purely integral operator instead of the above integral-differential one (the inversion cast in this framework is briefly analysed in Kooij and Lambert (1997)).

2.2. The constrained nonlinearized inversion scheme

As already indicated, the inversion method developed here belongs to the now well known class of modified gradient iterative solution methods (one may refer to Kleinman and van der Berg (1997), Kleinman *et al* (1997a), as well as to a recent overview of Kleinman *et al* (1997b) where a number of specialized papers are referenced and three-dimensional (3D) inversion cases are also introduced).

Such methods make good use of the bilinear aspect of the scattering problem with respect to the wavefield and to the contrast function, and in practice they operate by minimizing a cost functional (*joint criterion* in a Bayesian framework, see, e.g. Carfantan and Mohammed-Djafari (1997)) which is made of the least-square norms of two residuals:

(i) the residual of the state equation measures how well a field iterate, for a given iterate of the contrast function, satisfies the correct wavefield equations and boundary conditions inside $\mathcal{D}$;

(ii) the residual of the data equation weighs the discrepancy at the sensor locations between the data and the predicted field values which are associated to given iterates of both field and contrast functions.

For simplicity, equations (2) and (3) are written in operator form

$$H_j(\boldsymbol{r}) = H_j^{\text{inc}}(\boldsymbol{r}) + \mathcal{G}_{\mathcal{D}}\mathcal{M}H_j(\boldsymbol{r}) \qquad \boldsymbol{r} \in \mathcal{D} \tag{4}$$

$$H_j^{\text{scat}}(\boldsymbol{r}) = \mathcal{G}_{\mathcal{L}}\mathcal{M}H_j(\boldsymbol{r}) \qquad \boldsymbol{r} \in \mathcal{L}. \tag{5}$$

We do not intend here to dwell on the mathematical properties of the above integral-differential operators $\mathcal{G}_{\mathcal{D}}$ and $\mathcal{G}_{\mathcal{L}}$, and of those of the field and material parameters involved (one may consult, e.g. Kleinman *et al* (1997a)). Let us only keep in mind that the field and the data are at least square integrable over $\mathcal{D}$ and/or $\mathcal{L}$, and usually much smoother, and

that the contrast function is of bounded support included within $\mathcal{D}$ and smooth enough (at least continuously differentiable with respect to x and y), and emphasize that in practice we only tackle a finite number of bounded, real- and/or complex-valued fields and material parameters within a discrete counterpart (obtained via a method of moments) of the formulation developed in this section.

Then the modified gradient method usually involves the construction of two complex-valued, position-dependent sequences of iterates $H_{j,n}$ and $\mathcal{M}_n$ which are such that they should reduce at every step a positive real-valued cost functional as mentioned before. The data and state residuals read

$$r_{j,n}(\boldsymbol{r}) = H_j^{\text{inc}}(\boldsymbol{r}) - H_{j,n}(\boldsymbol{r}) + \mathcal{G}_{\mathcal{D}}\mathcal{M}H_{j,n}(\boldsymbol{r}) \qquad \boldsymbol{r} \in \mathcal{D} \tag{6}$$

$$\rho_{j,n}(\boldsymbol{r}) = \zeta_j(\boldsymbol{r}) - \mathcal{G}_{\mathcal{L}}\mathcal{M}H_{j,n}(\boldsymbol{r}) \qquad \boldsymbol{r} \in \mathcal{L} \tag{7}$$

when data ζ_j are collected on $\mathcal{L}$. The cost functional is

$$F_n(\boldsymbol{H}_n, \mathcal{M}_n) = \omega_{\mathcal{D}} \sum_{j=1}^{N_s} \|r_{j,n}\|_{\mathcal{D}}^2 + \omega_{\mathcal{L}} \sum_{j=1}^{N_s} \|\rho_{j,n}\|_{\mathcal{L}}^2 \tag{8}$$

where one denotes $\boldsymbol{H}_n = (H_{1,n}, H_{2,n}, \ldots, H_{N_s,n})$, the normalization constants $\omega_{\mathcal{D}}$ and $\omega_{\mathcal{L}}$ being such that

$$\omega_{\mathcal{D}} = \left(\sum_{j=1}^{N_s} \|H_j^{\text{inc}}\|_{\mathcal{D}}^2 \right)^{-1} \qquad \omega_{\mathcal{L}} = \left(\sum_{j=1}^{N_s} \|\zeta_j\|_{\mathcal{L}}^2 \right)^{-1} \tag{9}$$

with $\|\cdot\|_{\mathcal{A}}$ as the norm associated to the inner product $\langle \cdot, \cdot \rangle_{\mathcal{A}}$ in $L^2(\mathcal{A})$, $\mathcal{A} = \mathcal{D}, \mathcal{L}$. (Notice that the above normalization in effect gives the same weight to the error on the field in the search domain and to the error on the data in the measurement domain; whether or not this choice is the most pertinent remains an open question.)

At step $n \geqslant 1$, the iterates $H_{j,n}$ and $\mathcal{M}_n$ are updated from those at $n-1$ along well chosen directions. In a free-space H-polarization case (Lixin *et al* 1995a, b) proceed as follows:

$$\mathcal{M}_n = \mathcal{M}_{n-1} + \beta_n d_n \tag{10}$$

$$H_{j,n} = H_{j,n-1} + \alpha_n v_{j,n} \tag{11}$$

where the two complex-valued constants β_n and α_n are line minimizers of the cost functional along the position-dependent, Polak–Ribière conjugate-gradient directions d_n and $v_{j,n}$.

However, preliminary numerical experimentation showed us that the above scheme applied to the buried configuration did not converge in many cases and was plagued by non-physical solutions (notably, but not only, a negative conductivity arising after a few iterations) whereas since the real and imaginary parts of the contrast function $\mathcal{M}_n$ are not necessarily non-negative one cannot extend to the H case the previous analysis of Belkebir and Tijhuis (1996). (Other choices, such as imposing the binarity of the contrast function (Souriau *et al* 1996, Monebhurrun *et al* 1998), deserve investigation.)

So one resorts to two new real-valued unknowns ξ and η chosen such that they incorporate the minimal though most obvious amount of *a priori* information, i.e. the fact that $\varepsilon_{r\mathcal{D}} \geqslant 1$, $\sigma_{\mathcal{D}} \geqslant 0$, by letting $\varepsilon_{r\mathcal{D}} = 1 + \xi^2$ and $\sigma_{\mathcal{D}}/(\omega\varepsilon_0) = \eta^2$. The complex-valued sequence $\{\mathcal{M}_n\}$ is now replaced by two real-valued sequences $\{\xi_n\}$ and $\{\eta_n\}$ such that

$$\mathcal{M}_n = 1 - \frac{\varepsilon_2}{\varepsilon_0(1 + \xi_n^2 + \mathrm{j}\eta_n^2)} \tag{12}$$

while the updating strategy from $n = 1$ becomes

$$\xi_n = \xi_{n-1} + \beta_n d_n \tag{13}$$

$$\eta_n = \eta_{n-1} + \gamma_n w_n \tag{14}$$

$$H_{j,n} = H_{j,n-1} + \alpha_n v_{j,n} \tag{15}$$

for a proper set of initial guesses ξ_0, η_0, and $H_{j,0}$.

In the above expressions the real-valued constants β_n and γ_n, and the complex-valued constant α_n, are calculated by minimizing F via a Fletcher–Reeves version of the conjugate gradient method, the position-dependent directions d_n, w_n, and $v_{j,n}$ being of the Polak–Ribière conjugate-gradient type and definedas

$$d_n = g_n^d + \frac{\langle g_n^d, g_n^d - g_{n-1}^d \rangle}{\langle g_{n-1}^d, g_{n-1}^d \rangle} d_{n-1} \tag{16}$$

$$w_n = g_n^w + \frac{\langle g_n^w, g_n^w - g_{n-1}^w \rangle}{\langle g_{n-1}^w, g_{n-1}^w \rangle} w_{n-1} \tag{17}$$

$$v_{j,n} = g_{j,n}^v + \frac{\sum_{j=1}^{N_s} \langle g_{j,n}^v, g_{j,n}^v - g_{j,n-1}^v \rangle}{\sum_{j=1}^{N_s} \langle g_{j,n-1}^v, g_{j,n-1}^v \rangle} v_{n-1} \tag{18}$$

with restriction of the directions to those of the gradients g_n^d, g_n^w and $g_{j,n}^v$ when $n = 1$. Such gradients are those of F evaluated at the $(n-1)$th step and they are taken with respect to ξ, η, and H_j, respectively, the other variables being kept constant during the evaluation (see the appendix).

2.3. Some key ingredients: initialization, refreshment, and frequency-hopping

To our knowledge no proof of uniqueness of the solution of the inversion problem in the buried configurationat hand exists, and in practice we shall cope with a limited number of sources and sensors, a band-limited frequency coverage, inaccurate data, and use a peculiar discretization (whose meshes should be neither too large since the reproduction of the obstacle and the accuracy of the wavefieldwould be poor, neither too small for fear of calculation errors and prohibitive CPU times), which would reduce the interest of a proof if any.

More interesting maybe is the fact that, although the sequence of iterates above is to decrease the cost functional, one cannot expect in computational terms to reach something better than a plateau (a local minimum, associated to stable iterates) of this functional with a more or less high magnitude (commensurate with the noise level when noisy data are input). So one usually concludes that the lower the plateau the closer the solution to the sought obstacle, with no certainty that a lower plateau cannot be reached from another choice of initial values, or by a cleverer calculation of the iterates.

In section 3 one will illustrate from a number of numerical examples three somewhat *ad hoc* procedures (introduced later) which contribute to fair performances of the inversion scheme.

First, the set of initial values, ξ_0, η_0, and $H_{j,0}$, has to be chosen properly. However, one cannot directly apply the back-propagation technique which has been successfully employed for modifiedgradient methods, for example Kleinman *et al* (1997a), and whose intent is to take us from the measurement domain $\mathcal{L}$ onto the search domain $\mathcal{D}$ via the data equation (5) and to provide us with an initial wavefield(and a contrast function via the state equation (4)). Indeed, back-propagation should produce not only values of H within $\mathcal{D}$ but also consistent values of ∇H, and we observed from preliminary numerical experimentation that deducing

from back-propagated H fields useful values of the needed gradient did not work. Also from equations (23) and (24), it is not possible to start with the easiest guess available, i.e. $\xi_0 = 0$ and $\eta_0 = 0$ (in effect from the corresponding contrast function $\mathcal{M}_0$).

So at the present time the initial material parameters ξ_0 and η_0 are rather arbitrarily set such that the relative permittivity and/or conductivity vary smoothly over $\mathcal{D}$ (henceforth assumed to be rectangular for simplicity) and peak at its centre. Letting q be either a relative permittivity $\varepsilon_{r\mathcal{D}}$ or a conductivity $\sigma_{\mathcal{D}}$, one thus assumes

$$q(x, y) = q_i \left\{ \sin\left[\frac{\pi}{L_x}\left(x - \frac{L_x}{2}\right)\right] \sin\left[\frac{\pi}{L_y}\left(y - \frac{L_y}{2}\right)\right] \right\}^2 \tag{19}$$

where L_x and L_y are the x and y side lengths of $\mathcal{D}$, and where the value of q_i is chosen to be close to the corresponding one in the embedding—although one may fear that the mapping of an obstacle when located at the centre of the test domain will be favoured, this was not confirmed by numerical results for, say, off-centre obstacles. As for the initial field $H_{j,0}$, it is taken as the field calculated inside $\mathcal{D}$ when it is characterized by the just chosen ξ_0 and/or η_0.

Second, once initialized as above, the sequence of iterates ξ_n and η_n and the sequence of iterates $H_{j,n}$ follow after the calculations described in the above. However, although the cost functional F decreases gradually, which means that one may expect that the $2 \times N_s$ norms of the state and data residuals $r_{j,n}$ and $\rho_{j,n}$ decrease together (nothing in the theoretical machinery of modified gradient methods so far provides for the fact that the increase of several residuals might not compensate for a time the decrease of several others), the values of the field iterate $H_{j,n}$ may still differ to a rather large extent from those of the field obtained within $\mathcal{D}$ by solving the associated direct problem for given material parameters ξ_n and η_n due to the ill-posedness of the inversion.

In effect, this is remedied as follows. At one (or more) given step(s) m, which can be decided upon in an adaptive fashion from, say, some plateauing of the cost functional F, or which can be chosen in advance with a fixed periodicity, one derives from the parameters ξ_m and η_m the exact solution of the state equation (4), and one takes as a new $H_{j,m}$ this solution; the cost functional—which may increase on the spot—and all other quantities of interest are calculated accordingly thereupon, and the procedure is started again.

This periodic refreshment procedure in some respect is parallel with the refreshment procedure enforced in the binary-specialized modified gradient versions (Souriau *et al* 1996, Monebhurrun *et al* 1998) (the contrast function is updated via a nonlinear transformation at a number of steps), and obviously both enable us to escape from certain local minima. However, in the binary case the main goal is to get a sharper map of the search domain, and the consistency of the set of iterates (the field in the obstacle and the obstacle parameters) is more of a by-product.

Third, so far we have considered that the N_s sources are operating at a single, fixed frequency. However, frequency-diverse data do compensate for the lack of viewing of the obstacle. Then, two paths may be followed once it is assumed that M frequencies in a given band are input for each of the N_s sources.

The first one is to aggregate all data together (the j index now runs from 1 to $N_s \times M$) and in short to simultaneously calculate M times more fields—and M times more material losses (if one keeps the frequency inside the loss parameter as in $\sigma_{\mathcal{D}}/(\omega\varepsilon_0)$)—the discretization strategy being adapted to the highest frequency for keeping the accuracy.

The second one, whose benefit is already illustrated in Chew and Lin (1995), Belkebir and Tijhuis (1996) and Litman *et al* (1998), is to march on in frequency (frequency-hopping), from the lowest frequency—one simply aims at a gross reproduction of the obstacle—up

to the highest frequency—one is keen to map fine details—while using each previously retrieved solution as the first guess of the new search, and with the immediate advantage that each problem is attacked with a commensurate discretization strategy. True, solving M smaller-sized independent problems instead of one large one may not be faster when measured in pure CPU time, but this is not our major concern at this stage of the study.

3. Some illustrative numerical results

3.1. The discrete formulation

The corresponding direct scattering problem can be solved by means of an iterative algorithm which takes careful account of the convolution and correlation structure of the field equations and then makes intensive use of fast Fourier transforms in order to maintain the accuracy while avoiding prohibitive computation times (Lambert 1998).

Here it is only worthwhile mentioning that this solver is based on a method of moments with triangular basis functions—the domain $\mathcal{D}$ is divided into square pixels of side Δ where the contrast $\mathcal{M}$ is taken to be constant, and each pixel is again divided into two rectangular triangles where the magnetic field is assumed to vary linearly—and with point-matching—the testing functions are Dirac δ-functions set at every centre of the square pixel—and that the same line of reasoning directly yields the discrete counterpart of each functional equation introduced in the above (e.g. the adjoint operators are equivalent to conjugate transpose matrices).

As for the data of the inversion problem they are computed by solving the associated direct problem by using an appropriately finer mesh, the nodes of which are never placed at the same location as those used in the inversion. So *inverse crime* is avoided. Consequently one cannot retrieve a perfect copy of the obstacle—which has a price, i.e. the global minimum of the cost functional is unknown, and it may be far from zero.

In terms of the numerical burden, if one assumes that $\mathcal{D}$ is made of $n_x \times n_y$ square pixels, which corresponds to $(n_x + 1) \times (n_y + 1)$ nodes, the number of unknown field and material real-valued samples is $a \times (n_x \times n_y) + 2 \times [(n_x + 1) \times (n_y + 1)] \times N_s$—where $a = 1$ if either $\varepsilon_{r\mathcal{D}}$ or $\sigma_{\mathcal{D}}$ is unknown, and $a = 2$ if both are unknown—while the number of known samples, which consist of the scattered field data collected by the sensors and of the incident fields at the nodes of $\mathcal{D}$, is $2 \times [(n_x + 1) \times (n_y + 1)] \times N_s + 2 \times N_s \times N_r$ since there are N_s sources and N_r receivers. This usually leads to a ratio (number of unknowns)/(number of data) close to 1.

3.2. The key parameters of the simulations

The numerical study assumes a 1 m sided square test domain $\mathcal{D}$ centred at a 0.5 m depth, and a homogeneous 0.52 m sided square obstacle. The measurement configuration comprises $N_s = 15$ line sources regularly spaced between -5 m and $+5$ m at height $y_S = 0.5$ m, and radiating at most at four frequencies 100, 200, 300, and 400 MHz, and $N_r = 47$ receivers regularly spaced between -10 m and $+10$ m at height $y_r = 0.125$ m.

We emphasize that the chosen length of the probing line is such that most of the scattered signal is collected for almost all assumed source locations (see figures 10 and 13), the sampling rate being of the order of half a wavelength in air at the highest frequency, and that these locations are such that the view angle of the obstacle is as large as feasible; the number of sources itself is not a determining factor—15 sources appeared to us as a good compromise, using more of them was costlier without real gain in terms of the accuracy of the reproduction of the obstacle, and using less of them reduced this accuracy too much.

In all examples the embedding is lossless and is characterized by a relative permittivity $\varepsilon_{r2} = 2$ and conductivity $\sigma_{r2} = 0$ S m^{-1}, and the obstacle then only differs by its relative permittivity ($\varepsilon_{r\mathcal{D}} = 1$, 3 or 4) and/or its conductivity (set to 10^{-2} S m^{-1}).

Accurate data ζ are generated with a 44×44-pixel discretization of $\mathcal{D}$, which corresponds with a sampling step always less than about $\lambda/23$ where $\lambda = 0.53$ m is the smallest wavelength of the probing signal to be propagated in the embedding. The modelling is illustrated in figure2 which shows a 3D piecewise representation of the obstacle (here it is purely dielectric with a relative permittivity equal to 3). As for $\mathcal{D}$, when carrying out the inversion algorithm, it is save exception definedby 20×20 pixels. Correspondingly at a given frequency the number of unknowns is 13 630 if one looks for either the permittivity map or the conductivity map, and 14 030 if one looks for both, whereas the number of data is 14 640. Notice that in every situation the number of iterations performed is 100 and the maps displayed are those found at this number.

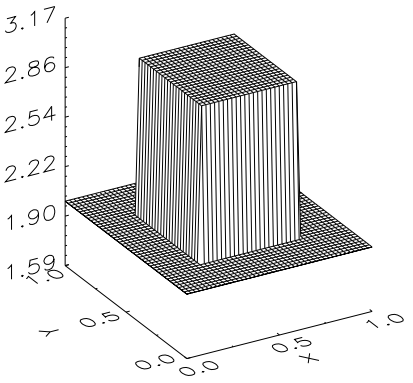

Figure 2. The square obstacle in the search domain modelled with a 44×44-pixel mesh.

3.3. The retrieval of the permittivity map or of the conductivity map

3.3.1. Influence of the discretization. The influence of the discretization on the results of the inversion (one looks for the permittivity map only) is exemplified in figure 3. The sources are at the 200 MHz frequency and the search domain is described by either 20×20 or 30×30 pixels. The initialization is the simple one (refer to (19)) where ξ_0 is such as the peak value, the assumed virtual permittivity is $\epsilon_i = 2.2$, and no refreshment is made. One observes no improvement with the finerdiscretization mesh and, therefore, the 20×20-pixel mesh is used from now on.

3.3.2. Influence of the periodic refreshment. As emphasized, the solution algorithm is based on the evolution of sequences $H_{j,n}$, and ξ_n and/or η_n. To assure that the total field $H_{j,n}$ corresponds to the obstacle represented by, say, ξ_n, $H_{j,n}$ is regularly refreshed by solving the state equation every mth step.

Figure 4 shows that the periodic refreshment procedure yields a much better map of the relative permittivity of the obstacle (compare with figure3). As for the cost functional, although it sharply raises after each refreshment, the lowest values that are obtained at the term of each period decrease monotonically and the plateau they finallytend to reach is

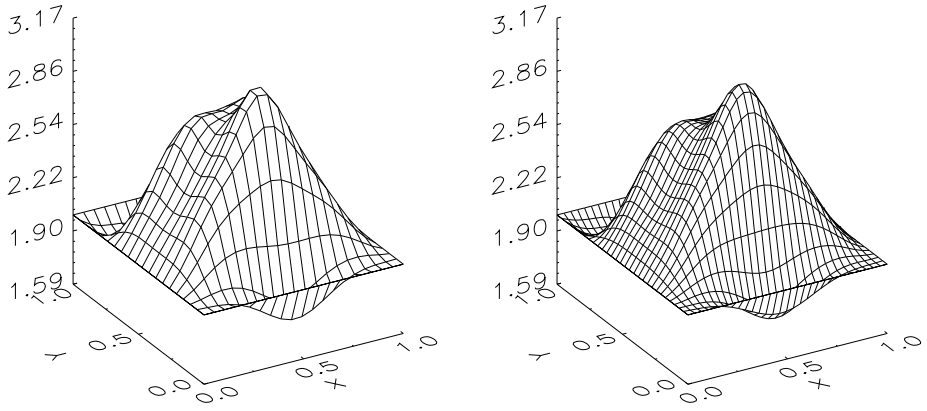

Figure 3. Reconstruction of the square obstacle displayed in figure2 when the search domain is made of 20×20 pixels (left) and a 30×30 pixels (right). No refreshment is made.

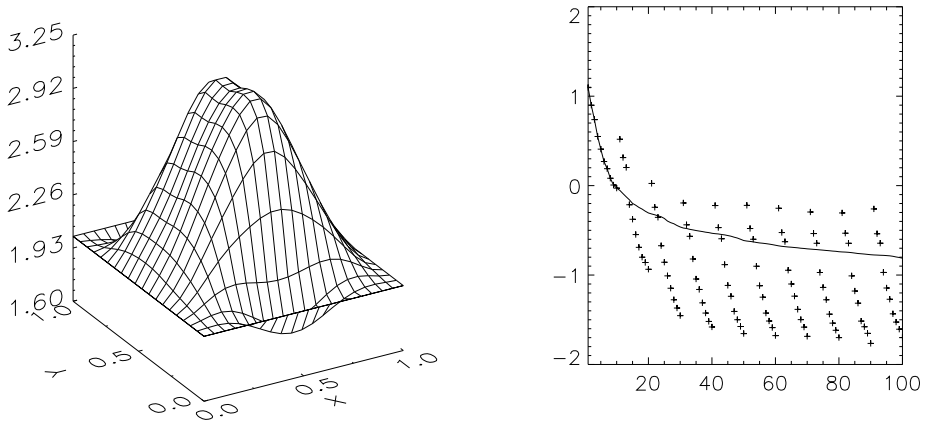

Figure 4. Reconstruction of the square obstacle displayed in figure2 with a 20×20-pixel mesh and refreshment each 10 iterations. The retrieved obstacle with refreshment (compared with figure 3) and the evolution of the log of the cost functional F_n against the iteration number (with (+) and without (——) refreshment) are shown.

about 10 times lower than without refreshment. Less tight refreshment schedules have also been tried out, but if the overall data fit,as then manifested by the cost functional, remains of the same order, the reproduction of the obstacle itself gets poorer, which confirmsthat the main interest of the refreshment procedure is to favour the most consistent solutions.

3.3.3. Influence of the initialization. The choice of the first element ξ_0 of the sequence appears to be very important. In figure5 one compares the results obtained at a 300 MHz frequency with the simple initialization (see (19)) where ξ_0 is such as $\epsilon_i = 2.2$, and using as firstguess the solution obtained by the inversion of the same obstacle at 200 MHz (figure4).

It is obvious that the closer to the exact obstacle is the initial map the closer the solution, and in effect even a slight amount of frequency-diversity (the data are taken at two rather close frequencies) in a frequency-hopping strategy (the lowest frequency is used first,and so on) may considerably improve the reconstruction of the obstacle. (With periodic refreshment the results with the simple initial guess will be somewhat better.)

3.3.4. Influence of noise. In this section the synthetic data are corrupted with an additive noise. It is generated by adding to each data point a random complex number τ whose real and imaginary part are uniformly drawn between prescribed limits. The chosen signal-to-noise ratio SNR $= 20\log(\|\zeta\|/\|\tau\|)$ is 10 dB. The reconstruction is obtained with both refreshment (every 15 iterations) and frequency-hopping (two frequencies are available, 200 and 300 MHz). The results are displayed in figure6. One observes a good reconstruction which is globally similar to that observed without noise (compare with figure5). Note that the refreshment procedure does not imply large increases of the cost functional as was the case before.

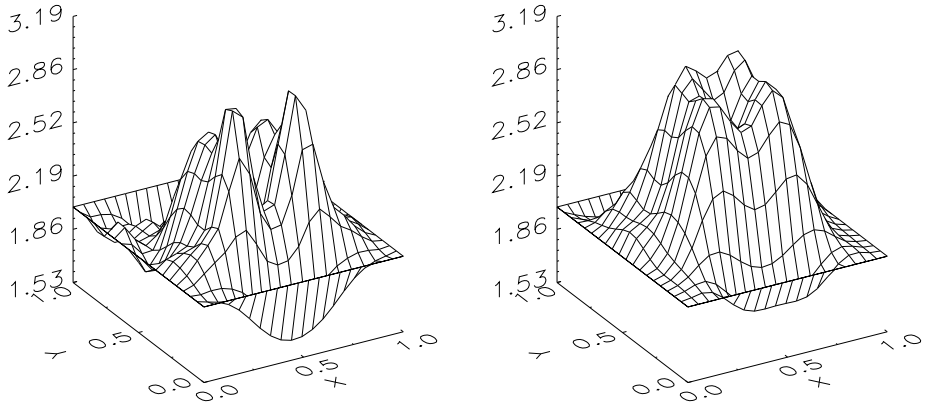

Figure 5. Reconstruction of the square obstacle displayed in figure2 with a 20×20-pixel mesh. The inversion is started either from a simple smoothly varying guess of the relative permittivity and goes on without refreshment (left) or from the map obtained by a previous inversion led at 200 MHz (the one in figure4) with refreshment each 15 iterations (right).

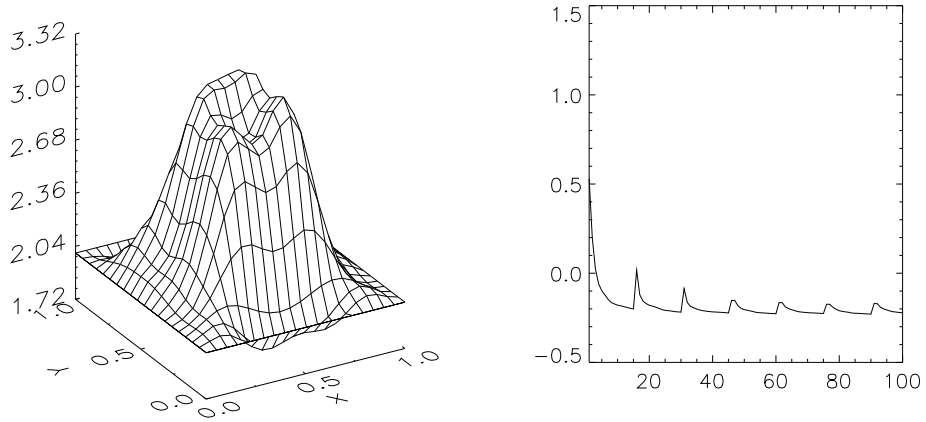

Figure 6. Reconstruction at 300 MHz of the square obstacle displayed in figure 2 with a 20×20-pixel mesh and refreshment each 15 iterations (left) and evolution of the log of the cost functional F_n against the iteration number (right). The inversion is started from the map obtained by a previous inversion led at 200 MHz. The data are corrupted with a 10 dB noise.

3.3.5. Influence of the contrast. The obstacle now has a relative permittivity of 4 and the inversion is performed as indicated before (20×20 pixels, refreshment each 15 iterations, and frequency-hopping). The results obtained at 400 MHz (figure 7) show a good localization of the obstacle but only a fair reconstruction of the overall shape with the presence of spurious features.

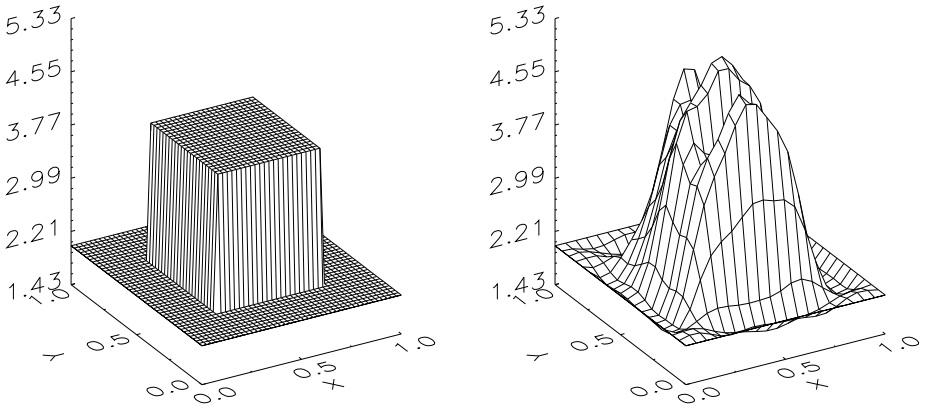

Figure 7. Reconstruction at 400 MHz and by frequency-hopping (four frequencies are used: 100, 200, 300, 400 MHz) of the higher-contrast square obstacle (relative permittivity equal to 4) with a 20×20-pixel mesh and refreshment each 15 iterations.

3.3.6. Retrieving an air void. The obstacle now has a relative permittivity of 1 (this is an air void) and the inversion is performed as indicated before (20×20 pixels, refreshment each 15 iterations, and frequency-hopping). The results obtained at 400 MHz (figure 8) show a good localization of the obstacle and a good reconstruction of the shape, although again erroneous features show up near the boundary of the obstacle.

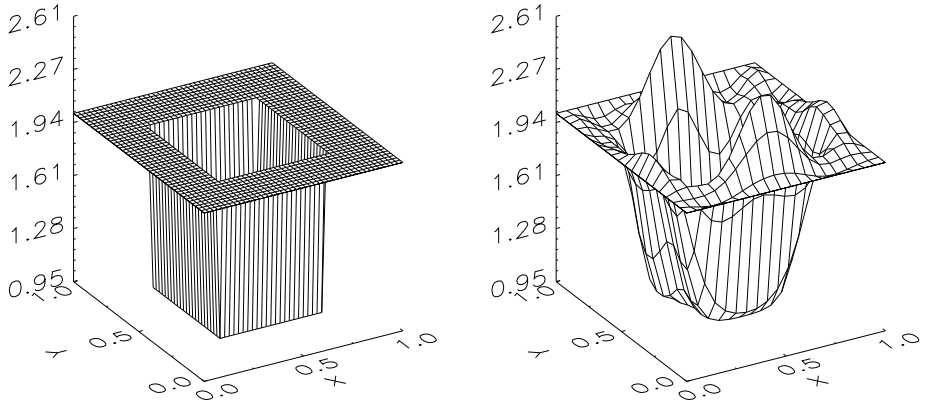

Figure 8. Reconstruction at 400 MHz and by frequency-hopping (four frequencies are used: 100, 200, 300, 400 MHz) of the lower-contrast square obstacle (relative permittivity equal to 1) with a 20×20-pixel mesh and refreshment each 15 iterations.

3.3.7. Retrieving the conductivity. The conductivity of the obstacle (10^{-2} S m^{-1}) now differs from that (0 S m^{-1}) of its embedding, the relative permittivity being kept the same (equal to 2). The initial guess is made according to (19) where η_i is such that the peak value of the assumed initial conductivity is $\sigma_i = 10^{-4}$ (figure9).

The obstacle is correctly localized, although the conductivity map differs to a large extent and obviously lacks the expected smoothness. However, as is illustrated in figure10, the corresponding scattered fielditerates (the $\mathcal{G}_{\mathcal{L}}\mathcal{M}H_{j,100}(\boldsymbol{r})$ that are produced by the inversion algorithm, not those which could be derived from the retrieved conductivity map by solving the direct problem independently) are almost indistinguishable from the data ζ, which confirmsthe strong ill-posedness of the inversion.

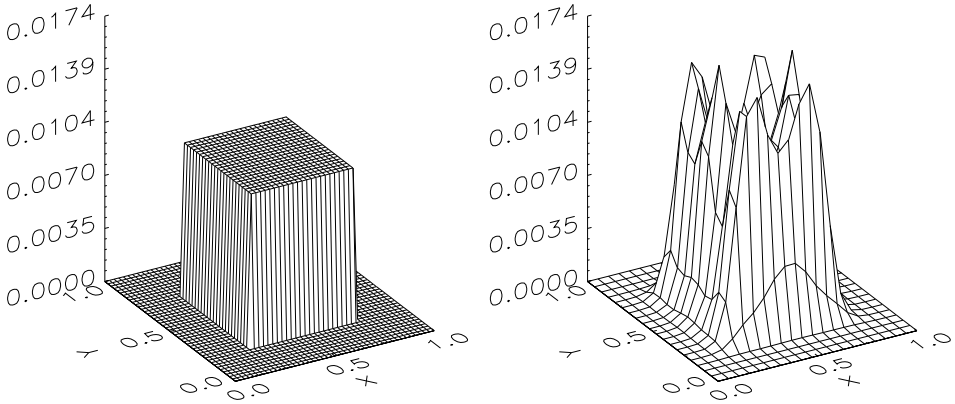

Figure 9. Reconstruction at 400 MHz and by frequency-hopping (four frequencies are used: 100, 200, 300, 400 MHz) of a conductive square obstacle (conductivity equal to 10^{-2} S m^{-1}) with a 20×20-pixel mesh and refreshment each 15 iterations. The inversion is started from a simple smoothly varying guess of the conductivity, letting $\sigma_i = 10^{-4}$ S m^{-1}.

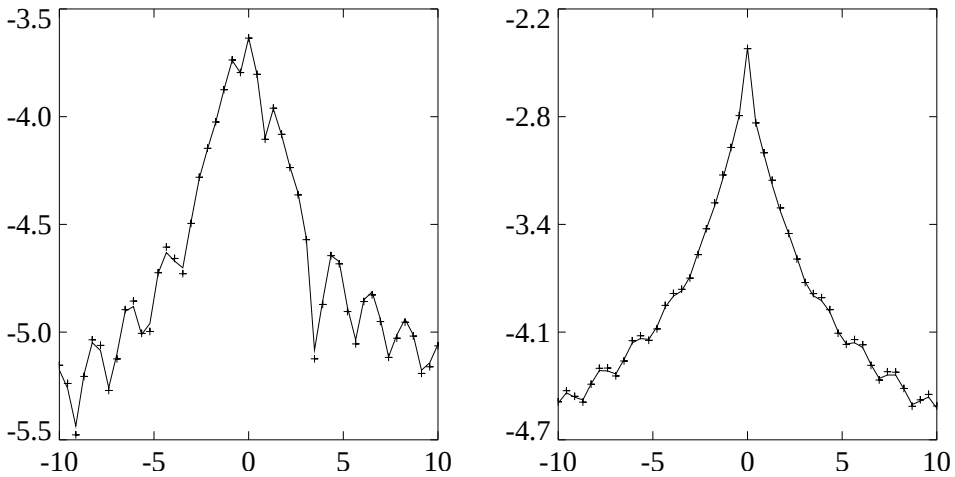

Figure 10. The 400 MHz scattered field(in dB) yielded by the inversion after 100 iterations and corresponding to the retrieved obstacle displayed in figure9 (crosses) is compared with the data field ζ (full curve) for the first and most eccentric line source (left) and the eighth and central line source (right).

3.4. The simultaneous retrieval of the permittivity and conductivity maps

The obstacle is now of relative permittivity 3 and of conductivity 10^{-2} S m^{-1} in the $\varepsilon_{r2} = 2$ and $\sigma_{r2} = 0$ S m^{-1} embedding. Both permittivity and conductivity maps are sought. To achieve this goal one uses the full frequency-hopping scheme from 100 MHz to 400 MHz, using each time the usual 15-iteration periodic refreshment. Results are displayed in figure 11 (the permittivity map), figure 12 (the conductivity map), and figure 13 (the scattered field). One observes that the permittivity map is retrieved fairly well while the conductivity map is poorer, which is in accord with what has been observed previously. Also the fields provided by the algorithm are very close to the exact one which confirms the ill-posedness of the inversion.

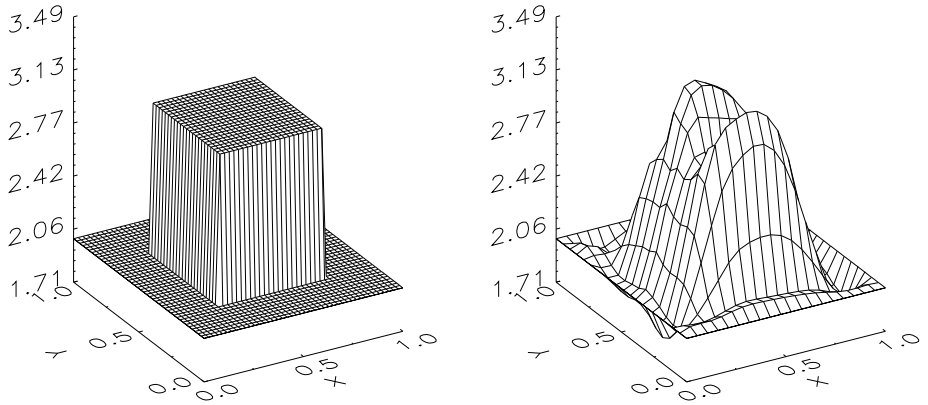

Figure 11. Reconstruction at 400 MHz and by frequency-hopping (four frequencies are used: 100, 200, 300, 400 MHz) of the relative permittivity map of a square obstacle (relative permittivity, 3; conductivity, 10^{-2} S m^{-1}) with a 20 × 20-pixel mesh and refreshment each 15 iterations.

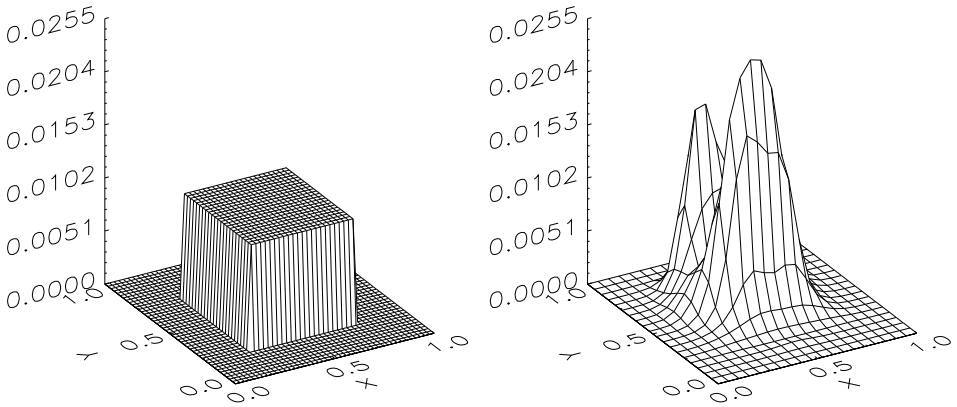

Figure 12. Same as in figure11 with the conductivity map.

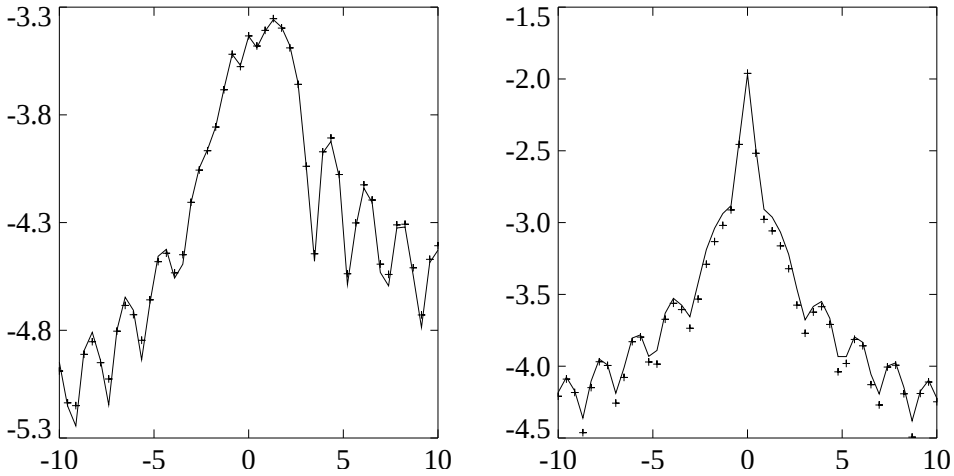

Figure 13. The 400 MHz scattered field(in dB) yielded by the inversion after 100 iterations and corresponding to the retrieved obstacle displayed in figures11 and 12 (crosses) is compared with the exact one (full curve) for the firstand most eccentric line source (left) and the eighth and central line source (right).

4. Conclusion

The reconstruction of a buried penetrable obstacle in the H-polarization case has been investigated herein by means of a constrained modified gradient method and has been shown to succeed to a fair extent even when both the permittivity map and the conductivity maps of the search domain are unknown.

The computational intricacy remains quite high although computation times do not really matter at the present stage of the analysis, and the ill-posedness of the wavefieldinversion problem at hand is strong as manifested by the excellent agreement between scattered field data and fieldsprovided by the solution algorithm, although the corresponding maps may be affected by peaks or other spurious features.

This ill-posedness can only be obviated by further information on the obstacle, such as it being homogeneous. With that assumption, work is presently in progress on a binary version of the method which will parallel what has been already demonstrated to be of interest in the E-case (Souriau *et al* 1996) and even applied to full 3D cases (Monebhurrun *et al* 1998).

As for the computational burden, results recently obtained by a contrast-source version of the modifiedgradient method in the E-case for a free-space configuration(van den Berg and Kleinman 1997) show that looking for electric Huygens sources instead of electric fields outperforms the usual version in terms of complexity while maintaining the same versatility and robustness. This substitution can readily be made with the vector electric field formulation already considered (Kooij and Lambert 1997), but the scalar magnetic fieldformulation itself is not directly amenable to a similar treatment due to the different operator involved. (Along the same line of thought, the two-step approach promoted in Caorsi and Gragnani (1998) may be of interest.)

Clearly, alternative solution methods also exist whose extension to the configuration dealt with herein deserves further investigation, again in the hypothesis of a buried obstacle of known material properties.

If the obstacle is penetrable, i.e. if transmission conditions apply, the alliance (Litman *et al* 1998) of the level-set representation—to describe the obstacle cross section—and of the speed method—to evolve the level set—is highly effective in the E-polarization case in the free-space configuration and has the key advantage of allowing merging or splitting of the retrieved structure during its evolution; it is to face a critical test in the much more demanding H-polarization case in the buried configuration. Notice that the main theoretical complexity should lie in the calculation of the shape gradient of the cost functional within the appropriate variational formulation of the problem. Notice also that no topological information, other than the fact the obstacle is contained in a given search domain, is effectively required with this controlled evolution of a level-set, this is also the case with the binary-specialized modified gradient method.

If the obstacle is impenetrable, and in electromagnetics we should usually deal with a perfectly conducting structure the electric field boundary condition being of the Dirichlet or Neumann type depending upon the polarization (E or H), the complete family approach is an obvious candidate and work is presently in progress on it; with reference to the retrieval of an obstacle in a shallow water waveguide developed in Rozier *et al* (1997), using it mainly requires us to change the Green function representation and replace acoustic quantities by electromagnetic ones. However, this approach may only be applied when the number of disjoint parts that may characterize the sought obstacle is prescribed beforehand, and an interior point for each part given. (Its extension to a penetrable obstacle will require us to handle both interior and exterior sets of equivalent sources which will not be an easy task.)

To conclude, we acknowledge that we have not gone into a detailed analysis of the behaviour of the integral-differential operator faced with, and in effect we have mostly relied upon numerical experimentation to devise the best solution strategy. Nevertheless, it would be interesting to see whether the highly nonlinear problem considered here is amenable to a quadratic approximation like that developed in Pierri and Tamburrino (1997) and to the subsequent analysis of pertinent geometrical properties—although the E-field vector formulation may present less of a challenge in the first stage since the operator at hand is much simpler.

Acknowledgments

Part of the study has been conducted with the support of a CNRS-NSF International Cooperation grant No INT-9415493. The authors are grateful to P M van den Berg for his contribution to the cooperation between their two laboratories. They wish to pay their respects to the memory of R E Kleinman, recently deceased, who showed great interest in the investigation developed here.

Appendix. Expression of the gradients g_n^d, g_n^w, and $g_{j,n}^v$

They read

$$g_n^v = \frac{\partial}{\partial H_j} F(\boldsymbol{H}, \xi, \eta)|_{H_{j,n-1}, \xi_{n-1}, \eta_{n-1}}$$
$$= -\omega_{\mathcal{D}}[r_{j,n-1} - \overline{\mathcal{M}}_{n-1}\mathcal{G}_{\mathcal{D}}^{\star} r_{j,n-1}] - \omega_{\mathcal{L}}\overline{\mathcal{M}}_{n-1}\mathcal{G}_{\mathcal{L}}^{\star}\rho_{j,n-1} \quad (20)$$

$$g_n^d = \frac{\partial}{\partial \xi} F(\boldsymbol{H}, \xi, \eta)|_{H_{j,n-1}, \xi_{n-1}, \eta_{n-1}}$$
$$= 2\omega_{\mathcal{D}} \sum_{j=1}^{Ns} \Re[\overline{\mathcal{M}}_{n-1}^{\xi} \overline{H}_{j,n-1} \mathcal{G}_{\mathcal{D}}^{\star} r_{j,n-1}] + 2\omega_{\mathcal{L}} \sum_{j=1}^{Ns} \Re[\overline{\mathcal{M}}_{n-1}^{\xi} \overline{H}_{j,n-1} \mathcal{G}_{\mathcal{L}}^{\star} \rho_{j,n-1}] \quad (21)$$

$$g_n^w = \frac{\partial}{\partial \eta} F(\boldsymbol{H}, \xi, \eta)|_{H_{j,n-1}, \xi_{n-1}, \eta_{n-1}}$$
$$= 2\omega_{\mathcal{D}} \sum_{j=1}^{Ns} \Re[\overline{\mathcal{M}}_{n-1}^{\eta} \overline{H}_{j,n-1} \mathcal{G}_{\mathcal{D}}^{\star} r_{j,n-1}] + 2\omega_{\mathcal{L}} \sum_{j=1}^{Ns} \Re[\overline{\mathcal{M}}_{n-1}^{\eta} \overline{H}_{j,n-1} \mathcal{G}_{\mathcal{L}}^{\star} \rho_{j,n-1}] \quad (22)$$

where overbar means complex conjugate, $\mathcal{G}_{\mathcal{D}}^{\star}$ and $\mathcal{G}_{\mathcal{L}}^{\star}$ are the adjoint operators of $\mathcal{G}_{\mathcal{D}}$ and $\mathcal{G}_{\mathcal{L}}$, respectively, and $\mathcal{M}_{n-1}^{\xi}$ and $\mathcal{M}_{n-1}^{\eta}$ are definedby

$$\mathcal{M}_{n-1}^{\xi} = \frac{\partial}{\partial \xi} \mathcal{M}\bigg|_{\xi_{n-1}, \eta_{n-1}} = \frac{2\varepsilon_2 \xi_{n-1}}{[(1 + \xi_{n-1}^2) + \mathrm{j}\eta_{n-1}^2]^2} \quad (23)$$

$$\mathcal{M}_{n-1}^{\eta} = \frac{\partial}{\partial \eta} \mathcal{M}\bigg|_{\xi_{n-1}, \eta_{n-1}} = \frac{2\mathrm{j}\varepsilon_2 \eta_{n-1}}{[(1 + \xi_{n-1}^2) + \mathrm{j}\eta_{n-1}^2]^2}. \quad (24)$$

References

Belkebir K, Kleinman R E and Pichot C 1997 Microwave imaging—location and shape reconstruction from multifrequency scattering data *IEEE Trans. Microwave Theory Tech.* **45** 469–76

Belkebir K and Tijhuis A G 1996 Using multiple frequency information in the iterative solution of a two-dimensional nonlinear inverse problem *Proc. Progress in Electromagnetic Research Symp. (Innsbruck)* p 353

Caorsi S and Gragnani G L 1998 A novel inverse-scattering method for dielectric objects based on the reconstruction of the nonmeasurable equivalent current density *Radio Sci.* submitted

Carfantan H and Mohammad-Djafari A 1997 An overview of nonlinear diffraction tomography within the Bayesian estimation framework *Inverse Problems of Wave Propagation and Diffraction* ed G Chavent and P C Sabatier (Berlin: Springer) pp 107–24

Chew W C and Lin J H 1995 A frequency-hopping approach for microwave imaging of large inhomogeneous bodies *IEEE Microwave Guided Wave Lett.* **5** 439–41

Kleinman R E and van den Berg P M 1992a A modified gradient method for two-dimensional problems in tomography *J. Comput. Appl. Math.* **42** 17–35

——1992b An extended range modified gradient technique for profile inversion *Radio Sci.* **29** 877–84

——1997 Gradient methods in inverse acoustic and electromagnetic scattering *Large-Scale Optimization with Applications* ed L T Biegler *et al* (Berlin: Springer) pp 173–94

Kleinman R E, van den Berg P M, Duchêne B and Lesselier D 1997a Location and reconstruction of objects using a modified gradient approach *Inverse Problems of Wave Propagation and Diffraction* ed G Chavent and P C Sabatier (Berlin: Springer) pp 143–58

Kleinman R E, van den Berg P M, Kooij B J, Duchêne B, Lesselier D, Lambert M and Monebhurrun V 1997b Multifrequency version of the modified gradient algorithm for reconstruction of complex refractive indices *Computational, Experimental, and Numerical Methods for Solving Ill-Posed Inverse Imaging Problems: Medical and Nonmedical Applications (SPIE 3171)* ed R L Barbour *et al* (Bellingham, WA: SPIE) pp 76–87

Kooij B J and Lambert M 1997 Nonlinear inversion of a buried object in TE-scattering *IEEE Antennas and Propagation Society Int. Symp. (Montréal)* vol 4, pp 2617–20

Lambert M 1998 TE-scattering by a cylindrical dielectric obstacle buried in a half-space: a H-field-based solution method *J. Electromagn. Waves Appl.* **12** 1817–39

Lesselier D and Duchêne B 1996 Wavefield inversion of objects in stratified environments. From backpropagation schemes to full solutions *Review of Radio Science 1993–1996* ed W R Stone (Oxford: Oxford University Press) pp 235–68

Litman A, Lesselier D and Santosa F 1998 Reconstruction of a two-dimensional binary obstacle by controlled evolution of a level set *Inverse Problems* **14** 685–706

Lixin W, Kleinman R E and van den Berg P 1995a Two-dimensional profile inversion—the TE case *Proc. URSI Int. Symp. Electromagn. Theory (Saint Petersburg)* pp 160–2

——1995 Modified gradient profile inversion using H-polarized waves *Proc. IEEE Antennas and Propagation Society International Symposium (Newport Beach)* vol 3, pp 598–601

Lobel P, Blanc-Féraud L, Pichot C and Barlaud M 1997 A new regularization scheme for inverse scattering *Inverse Problems* **13** 403–10

Monebhurrun V, Duchêne B and Lesselier D 1998 3-D inversion of eddy current data for Nondestructive Evaluation of steam generator tubes *Inverse Problems* **14** 707–24

Pierri R and Tamburrino A 1997 On the local minima problem in conductivity imaging via a quadratic approach *Inverse Problems* **13** 1547–68

Rozier C, Lesselier D, Angell T S and Kleinman R E 1997 Shape retrievial of an obstacle immersed in shallow water from single frequency farfieldsusing a complete family method *Inverse Problems* **13** 487–508

Souriau L, Duchêne B, Lesselier D and Kleinman R E 1996 Modifiedgradient approach to inverse scattering for binary objects in stratifiedmedia *Inverse Problems* **12** 463–81

van den Berg P M and Kleinman R E 1995 A total variation enhanced modifiedgradient algorithm for profile reconstruction *Inverse Problems* **11** L5–10

——1997 A contrast-source inversion method *Inverse Problems* **13** 1607–20

Zwamborn P and van den Berg P M 1991 A weak form of the conjugate gradient FFT method for two-dimensional TE scattering problems *IEEE Trans. Microwave Theory Tech.* **39** 953–60

C

Gradient conjugué binaire

[A.8] Binary-constrained inversion of a buried cylindrical obstacle from complete and phaseless magnetic field
Marc Lambert, Dominique Lesselier
Inverse Problems **16** 563-576 2000

Inverse Problems **16** (2000) 563–576. Printed in the UK PII: S0266-5611(00)05424-1

Binary-constrained inversion of a buried cylindrical obstacle from complete and phaseless magnetic fields

M Lambert and D Lesselier

Département de Recherche en Électromagnétisme—Laboratoire des Signaux et Systèmes (CNRS-SUPÉLEC-UPS), Plateau de Moulon, F-91192 Gif-sur-Yvette, France

E-mail: marc.lambert@supelec.fr and dominique.lesselier@supelec.fr

Received 24 June 1999, in final form 21 January 2000

Abstract. The investigation herein is two-fold: specialization to a homogeneous obstacle of recent work (Lambert M *et al* 1998 *Inverse Problems* **14** 1265–83) carried on the retrieval of an inhomogeneous cylindrical obstacle buried in a half-space in the transverse electric (or H) polarization case; extension from the usual case of complete wavefield data (known amplitude and phase) to the more severe case of amplitude-only data (absent phase). The developed inversion method belongs to the class of modified gradient methods. The field distribution (here, the magnetic field) and the distribution of the obstacle parameters (here, the permittivity and conductivity) are simultaneously sought in a search domain $\mathcal{D}$. This is done by minimizing a two-component objective function, one of which is characterizing the satisfaction of the wave equations within $\mathcal{D}$, the other the data fit. But now the electrical parameters of the sought obstacle are prescribed beforehand; this allows one to equate an appropriate complex-valued contrast function either to 0 (outside the obstacle) or to a known constant $\mathcal{M}_{\mathcal{D}}$ (inside). Two variants of a binary-constrained modified gradient algorithm are developed accordingly, tailored to either complete or phaseless data. Numerical experimentation illustrates how they behave in a variety of obstacle configurations, for both exact and erroneous prescribed contrasts.

1. Introduction

In this paper, we consider the retrieval of the unknown geometry of a homogeneous, possibly multi-connected cross-section of a penetrable cylindrical obstacle which is entirely buried in a known homogeneous half-space and which is illuminated and viewed from sources and sensors placed in the other, homogeneous, half-space. The chosen polarization is transverse electric (TE), i.e., the magnetic field is orientated parallel to the cylinder axis, and the electric field is correspondingly contained within the cross-section. All materials are Maxwellian, i.e., they are characterized by their frequency-independent permittivity and static conductivity (a more complicated but known frequency dependence could be accounted for) and assumed linear, isotropic and non-magnetic. Data consist in a finite number of samples of the scattered magnetic (near-)fields collected along a line of sensors in the exterior half-space. These fields result from interrogation of the obstacle by a finite number of time-harmonic line sources orientated parallel to its axis and placed along a line parallel to and near the sensor line, this operation being carried out at one or at best at a few discrete frequencies of operation. One hypothesizes that the sensors enable us either to collect, as is usually considered, both the amplitude and phase of the field (the data are said to be complete), or to collect only its amplitude (the data are said to be phaseless).

0266-5611/00/030563+14$30.00

It is well known that the probed obstacle features are included in a coded manner within the measured wavefields, and that the goal of the inversion is to extract from the latter pertinent information on the former, with the least of prior information and the most faithfulness. The subject of the inversion of an object buried in a layered environment (here, reduced for simplicity to the two half-spaces) is of increasing importance in many applications while being rather challenging in particular due to the severe ill-posedness which is caused by the availability of aspect-limited data only (the obstacle is not viewed from all around); one may refer to a recent survey by Lesselier and Duchêne (1996). There correspondingly exist many solution methods, increasingly nonlinearized ones, and the particular family of such methods which we are concerned herein with is the one of modified gradient methods (MGM); one may refer to their in-depth discussion and comparative analysis in van den Berg and Kleinman (1997).

In a recent investigation (Lambert *et al* 1998), the reconstruction of the permittivity and conductivity maps of an inhomogeneous buried obstacle has been attempted from an exact scalar Green representation of the single component of the magnetic field, by means of a so-called constrained MGM, which is such that realizability constraints are enforced (non-negative conductivity, relative permittivity no less than 1). If the retrieval of either map has then been proved feasible in many cases of interest, their simultaneous retrieval mainly failed, as further confirmation via numerical experimentation (in the absence of theoretical proofs) of the ill-posedness.

The assumption of a homogeneous obstacle whose—then uniform—material parameters may be prescribed beforehand by the user at least to a certain degree of accuracy but whose geometry (the distribution of this material in a certain search domain assumed to contain the obstacle) is unknown, has led us to the development of a binary-constrained MGM. In that effort we have been inspired by earlier works (Souriau *et al* 1996) which were carried out in the dual but simpler transverse magnetic (TM) polarization case (the electric field is orientated along the cylinder axis). The prior knowledge of the obstacle means that any interior (resp., exterior) point should have an electrical contrast valued at 1 (resp., to 0), after suitable normalization. The resulting iterative algorithm is thus built in order to yield a distribution of contrasts that get closer and closer to either 1 or 0 while ensuring that an appropriate cost functional—which measures both the data fit on the sensors and the satisfaction of the wave equations inside the search domain—is suitably decreased.

In that frame, complete data can be dealt with in a rather classical manner, and in effect the solution algorithm is the direct counterpart of the solution algorithm developed in the TM case, the main difficulty now coming from the peculiarities of the domain integral–differential wavefield formulation dealt with (in contrast with the more standard and purely integral formulation of the TM case).

However, the phaseless, incomplete data problem is a challenge *per se*. Two paths appear to be followed in the literature: (i) an amplitude-only reconstruction algorithm is directly applied onto the data without any preprocessing (Maleki *et al* 1992, Takenata *et al* 1997). (ii) Two nonlinear ill-posed inverse problems are solved in succession, the phase retrieval problem which gets us the phase of the amplitude-only data, and the classical reconstruction from the now complete data (calculated from the measured amplitude and the just retrieved phase) (Maleki and Devaney 1993).

A comparison in the context of optical diffraction tomography is found in Maleki and Devaney (1993); better results are shown for the second two-step approach. However, the discussion of respective pros and cons is still open in our opinion; indeed, Takenata *et al* (1997) describe an amplitude-only solution algorithm in the case of a cylindrical obstacle in free space which yields rather good results for a number of different configurations. So, we

choose to follow the same path, which has the clear advantage of enabling us to keep the same algorithmic structure: in practice the only change is within the cost functional, and the corresponding, somewhat more complicated but still manageable, calculation of its gradient.

This paper is organized as follows. The theoretical analysis of the field formulation and of the nonlinearized binary inversion is sketched in section 2 (which is completed in the appendix where the calculation of the gradients is outlined). In section 3 numerical inversion results are presented, for both exact and erroneous prescribed contrasts, and complete data as well as amplitude-only data. A short conclusion follows.

Let us emphasize that some complementary material is found in previous publications—the discrete counterpart of the formulation and the numerical validation of the direct problem solution are detailed in Lambert (1998), the realizability-constrained MGM is discussed at length in Lambert *et al* (1998) wherein a large amount of references is also introduced—but this paper may still be read independently from them.

Let us also note that the formulation employed, as stated in the above, describes the behaviour of the scalar magnetic field, but a two-component vector electric field formulation could likewise be started from Kooij *et al* (1998); both formulations are equivalent in the sense that they rigorously describe the same electromagnetic wavefield due to a penetrable obstacle buried in the half-space, but their numerical implementation differs to a large extent. However, no attempts are made here to carry out a comparative study of both approaches though well deserved it may be. Finally, we take for granted that the direct scattering problem is well-posed whichever be the employed formulation; our confidence in this aspect comes from several noteworthy theoretical investigations of the buried obstacle case (Petry 1995, Kleinman and Angell 1996, Liukkonen 1999) though we recognize that none of them specifically considers the peculiar TE configuration in either magnetic or electric forms.

2. The theoretical analysis

2.1. The field formulation

Let us refer to figure 1. We consider two homogeneous half-spaces (an upper one and a lower one, respectively numbered 1 and 2) separated by a planar interface x–z. A possibly inhomogeneous, penetrable cylindrical z-axis obstacle is fully embedded in the lower half-space, and contained inside a prescribed domain $\mathcal{D}$.

All materials are linear, isotropic and non-magnetic, and obey a Maxwell model: their complex permittivity reads $\varepsilon_m = \varepsilon_0\varepsilon_{rm} + \mathrm{j}\sigma_m/\omega$, $m = 1, 2, \mathcal{D}$, where ε_{rm} is the frequency-independent relative permittivity and σ_m the conductivity in S m^{-1}, omitting from now the time-dependence $\mathrm{e}^{-\mathrm{j}\omega t}$, at circular frequency ω. The corresponding complex wavenumbers k_m with non-negative imaginary parts are such that $k_m^2 = \omega^2\mu_0\varepsilon_m$, where ε_0 and μ_0 are the vacuum permittivity and permeability, respectively. In the numerical applications we limit ourselves to an air upper half-space, i.e., $\varepsilon_{r1} = 1$, $\sigma_1 = 0$, and $k_1 = k_0$.

N_s H-polarized line sources S_j ($j = 1, \ldots, N_s$) are placed in half-space 1 at height y_s and the resulting single component, H_z^{scat}, of the scattered magnetic field is collected by N_r (equally distributed) ideal receivers along a probing line $\mathcal{L}$ also placed in that half-space at height y_r. For simplicity the single z-component of the total magnetic field H_z is henceforth denoted as H, and its scattered part as H^{scat}. The data field is denoted as ζ.

For a given obstacle and a given source S_j radiating at ω, the total magnetic field H_j in $\mathcal{D}$ and the scattered magnetic field H_j^{scat} along $\mathcal{L}$ satisfy the state (coupling) equation (2) and the data (observation) equation (3)—which are deduced by application of the Green theorem to the Helmholtz wave equation satisfied by the electromagnetic field and by accounting for

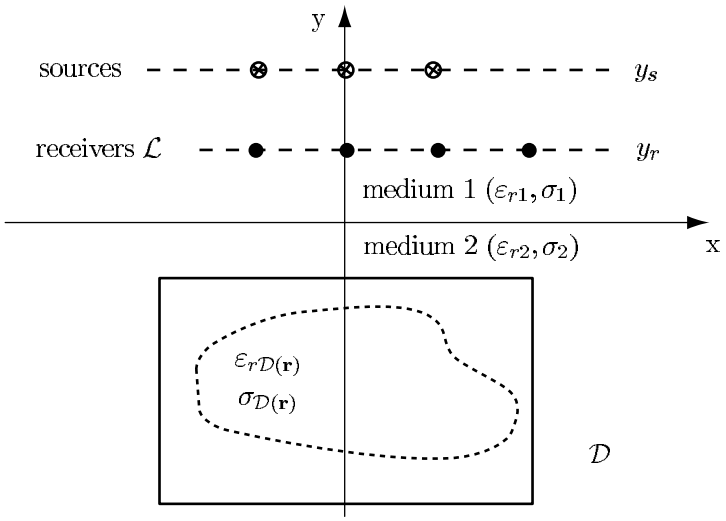

Figure 1. The geometrical and electrical configuration of the study (same figure as figure 1 in Lambert *et al* (1998)).

the appropriate transmission and radiation conditions. (As already stated in the introduction, an integral representation of the electric field could be set forth as an alternative, from which a vector state equation yielding the electric field in $\mathcal{D}$ and a scalar observation equation yielding the magnetic field along $\mathcal{L}$ would emerge.)

Letting the incident field in the half-space 2 be $H_j^{\text{inc}}(\boldsymbol{r})$ and the contrast function be

$$\mathcal{M}(\boldsymbol{r}) = 1 - \frac{\varepsilon_2}{\varepsilon_{\mathcal{D}}(\boldsymbol{r})}, \tag{1}$$

these two equations read

$$H_j(\boldsymbol{r}) = H_j^{\text{inc}}(\boldsymbol{r}) + \int_{\mathcal{D}} \mathrm{d}\boldsymbol{r}' \mathcal{M}(\boldsymbol{r}')[\nabla' G_{\mathcal{D}}(\boldsymbol{r}, \boldsymbol{r}') \cdot \nabla' H_j(\boldsymbol{r}')], \qquad \boldsymbol{r} \in \mathcal{D}, \tag{2}$$

and

$$H_j^{\text{scat}}(\boldsymbol{r}) = \int_{\mathcal{D}} \mathrm{d}\boldsymbol{r}' \mathcal{M}(\boldsymbol{r}')[\nabla' G_{\mathcal{L}}(\boldsymbol{r}, \boldsymbol{r}') \cdot \nabla' H_j(\boldsymbol{r}')], \qquad \boldsymbol{r} \in \mathcal{L}. \tag{3}$$

The two-component ∇' operator is taken with respect to the primed variables. $G_{\mathcal{D}}(\boldsymbol{r}, \boldsymbol{r}')$ is the Green function of the two half-space environment when (in the absence of obstacle) an ideal line source orientated along z is set at point $\boldsymbol{r}'$ and the resulting field is observed at location $\boldsymbol{r}$, both source and observation points being in the half-space 2. $G_{\mathcal{L}}(\boldsymbol{r}, \boldsymbol{r}')$ is the corresponding Green function when the source point $\boldsymbol{r}'$ is in the half-space 2 and the observation point $\boldsymbol{r}$ in the half-space 1.

2.2. Binary-constrained inversion

As already mentioned, the (binary) specialization of the MGM to the retrieval of a buried homogeneous obstacle was originally introduced in Souriau *et al* (1996), TM polarization cases in electromagnetics and corresponding cases in acoustics being investigated therein. Here we generalize the approach to TE-polarized wavefields for both complete and amplitude-only (phaseless) frequency-diverse magnetic field data.

In a binary-constrained inversion, it is known that the obstacle is homogeneous; thus, it is characterized by a fixed electrical contrast taken with respect to the embedding, but the map of the obstacle (the contrast distribution as a function of space in the search domain) remains unknown. So, $\mathcal{M}(\boldsymbol{r})$ is written as

$$\mathcal{M}(\boldsymbol{r}) = \mathcal{M}_{\mathcal{D}}\Psi_\theta(\tau(\boldsymbol{r})) \qquad \text{with} \quad \mathcal{M}_{\mathcal{D}} = 1 - \frac{\varepsilon_2}{\varepsilon_{\mathcal{D}}}, \tag{4}$$

where $\Psi_\theta(\tau(\boldsymbol{r})) : \mathbb{R} \to [0, 1]$, is a real-valued, strictly monotonous function smoothly varying from 0 to 1. Henceforth, it is given by

$$\Psi_\theta(\tau(\boldsymbol{r})) = [1 + \exp(-\tau(\boldsymbol{r})/\theta)]^{-1} \tag{5}$$

where the real and strictly positive parameter θ is a tuning parameter which is controlling the slope of Ψ_θ between 0 and 1; θ plays the role of a regularization parameter that can be evolved whenever necessary.

In practice, at a given point $\boldsymbol{r}$, decreasing θ moves the corresponding contrast value $\mathcal{M}(\boldsymbol{r})$ to a higher value if $\Psi_\theta(\tau(\boldsymbol{r}))$ was larger than 0.5 and to a lesser value if not. The problem is to choose an evolution law which avoids being stuck too early at a local minimum of the objective function, and which ends up with clearly visible zones of contrast values as close to 0 or as close to $\mathcal{M}_{\mathcal{D}}$ as possible (in view of the necessary discretization those bounds are never reached, τ being always finite valued); then, the exterior and the interior of the singly or multiply connected obstacle would be reproduced while ensuring us a good data fit (through a low magnitude of the objective function). Let us emphasize two points:

- The prescribed value of the contrast may not be the exact one; if it should be no smaller than the exact contrast value $\mathcal{M}_{\mathcal{D}}$ since convergence to this exact value could never be expected otherwise, it may be larger, the obstacle interior then being associated with values of τ somewhat smaller than with the exact prescription.
- The functional derivatives with respect to the contrast that are needed in the inversion exist because of the derivability of Ψ_θ.

The major steps of the method are as follows. For notational simplicity, and with the benefit of being in close accord with the discrete representation (Lambert 1998) for the gradients of the field at any sampling node of $\mathcal{D}$ show up in this representation as linear combinations of the field at this node and at the neighbouring nodes, (2) and (3) are written in operator form:

$$H_j(\boldsymbol{r}) = H_j^{\text{inc}}(\boldsymbol{r}) + \mathcal{G}_{\mathcal{D}}[\mathcal{M}_{\mathcal{D}}\Psi_\theta(\tau)H_j](\boldsymbol{r}), \qquad \boldsymbol{r} \in \mathcal{D}, \tag{6}$$

$$H_j^{\text{scat}}(\boldsymbol{r}) = \mathcal{G}_{\mathcal{L}}[\mathcal{M}_{\mathcal{D}}\Psi_\theta(\tau)H_j](\boldsymbol{r}), \qquad \boldsymbol{r} \in \mathcal{L}. \tag{7}$$

The MGM involves the construction of two position-dependent sequences of iterates, a complex-valued one $\{H_{j,n}\}$ and a real-valued one $\{\tau_n\}$. This is intended to reduce the cost or objective functional, which involves a data residual and a state residual at each source position. The state residual reads

$$r_{j,n}(\boldsymbol{r}) = H_j^{\text{inc}}(\boldsymbol{r}) - H_{j,n}(\boldsymbol{r}) + \mathcal{G}_{\mathcal{D}}[\mathcal{M}_{\mathcal{D}}\Psi_\theta(\tau_n)H_{j,n}](\boldsymbol{r}), \qquad \boldsymbol{r} \in \mathcal{D}. \tag{8}$$

The data residual (respectively for complete data and for amplitude-only data, the same notation being kept for simplicity though physical dimensions are not the same) reads

$$\rho_{j,n}(\boldsymbol{r}) = \left\{ \begin{array}{c} \zeta_j(\boldsymbol{r}) - \mathcal{G}_{\mathcal{L}}[\mathcal{M}_{\mathcal{D}}\Psi_\theta(\tau_n)H_{j,n}](\boldsymbol{r}), \\ |\zeta_j(\boldsymbol{r})|^2 - |\mathcal{G}_{\mathcal{L}}[\mathcal{M}_{\mathcal{D}}\Psi_\theta(\tau_n)H_{j,n}](\boldsymbol{r})|^2, \end{array} \right\} \qquad \boldsymbol{r} \in \mathcal{L}, \tag{9}$$

when data ζ_j are collected on $\mathcal{L}$. Other expressions for the phaseless data residual might be proposed as well—notably one could use a difference of amplitudes instead of this difference of squared amplitudes—and different normalizations (see below) employed accordingly.

However, the choice made here has the advantage to allow quite simple—both formal and numerical—calculations of the gradient (e.g., the difference of amplitudes would need somewhat tedious calculations and also lead to computationally more demanding expressions) while being easily interpreted in terms of scattered power fits.

The cost functional is made of the two residuals after proper normalization. It reads

$$F_n(\boldsymbol{H_n}, \mathcal{M}_n) = \omega_{\mathcal{D}} \sum_{j=1}^{N_s} ||r_{j,n}||^2_{\mathcal{D}} + \omega_{\mathcal{L}} \sum_{j=1}^{N_s} ||\rho_{j,n}||^2_{\mathcal{L}} \tag{10}$$

where one denotes $\boldsymbol{H_n} = (H_{1,n}, H_{2,n}, \ldots, H_{N_s,n})$, the weights $\omega_{\mathcal{D}}$ and $\omega_{\mathcal{L}}$ being such that

$$\omega_{\mathcal{D}} = \left(\sum_{j=1}^{N_s} ||H_j^{\text{inc}}||^2_{\mathcal{D}} \right)^{-1}, \tag{11}$$

$$\omega_{\mathcal{L}} = \begin{cases} \left(\sum_{j=1}^{N_s} ||\zeta_j||^2_{\mathcal{L}} \right)^{-1}, & \text{for complete data,} \\ \left(\sum_{j=1}^{N_s} ||\zeta_j||^4_{\mathcal{L}} \right)^{-1}, & \text{for amplitude-only data,} \end{cases} \tag{12}$$

with $||\cdot||_{\mathcal{A}}$ as the norm associated with the inner product $\langle \cdot, \cdot \rangle_{\mathcal{A}}$ in $L^2(\mathcal{A})$, $\mathcal{A} = \mathcal{D}, \mathcal{L}$.

Let us assume that the scheme is initialized (see the next section) by a set of fields and contrasts indexed by $n = 0$. At step $n \geqslant 1$, the iterates $H_{j,n}$ and τ_n are updated from those at iteration $n - 1$ according to

$$\tau_n = \tau_{n-1} + \beta_n d_n, \tag{13}$$

$$H_{j,n} = H_{j,n-1} + \alpha_n v_{j,n}. \tag{14}$$

The position-dependent, real-valued weight β_n and complex-valued one α_n are line minimizers of the cost functional varied along the Polak–Ribière conjugate-gradient directions d_n and $v_{j,n}$. The gradients g_1^d and $g_{j,1}^v$ are those of F calculated at the $(n-1)$th step with respect to τ (assuming fixed fields $H_l, l = 1, \ldots, N_s$) and to each of the H_j (assuming fixed contrast variable τ, and fixed fields $H_l, l \neq j, l = 1, \ldots, N_s$). At $n = 1$ initial update directions are simply reduced to gradients g_1^d and $g_{j,1}^v$. All such quantities are given in the appendix in a highly concatenated fashion; less formal derivations may be given, notably from the Fréchet directional derivative point-of-view, but the material relative to like calculations of gradients and descent directions in gradient methods is ample, and in one way or another most references given in this paper consider them in this fashion.

3. Numerical results

3.1. Some key ingredients of the inversion

Detailed coverage of the numerical discretization of the integral equations is found in Lambert (1998) and Lambert *et al* (1998); this will not be repeated here. Three key ingredients of the inversion: initialization, refreshment and frequency hopping, will also not be dwelled upon unnecessarily. A few elements should however be emphasized:

- The initial guess of the obstacle electrical parameters is such that

$$p(x, y) = p_i \left\{ \sin\left[\frac{\pi}{L_x} \left(x - \frac{L_x}{2} \right) \right] \sin\left[\frac{\pi}{L_y} \left(y + \frac{L_y}{2} \right) \right] \right\}^2 \tag{15}$$

where L_x and L_y are the x and y side lengths of (henceforth rectangular) $\mathcal{D}$, and where p_i is either the relative permittivity or the conductivity. The initial distribution of $\tau_0(x, y)$ follows from (5) and the one of the contrast $\mathcal{M}_0(x, y)$ follows from (4), the initial field distribution $H_{j,0}$ for each source $j = 1, \ldots, N_s$, then being taken as the solution of the corresponding state equation (2). (Note that the box $\mathcal{D}$ is in practice divided into pixels, and the contrast of the most exterior pixels is slightly larger than 0, and associated to a very low value of τ_0.)

- The refreshment ensures that the total field $H_{j,n}$ effectively corresponds to the obstacle as is represented by $\mathcal{M}_n$; this is enforced by solving the state equation for this contrast every mth step, and using the field solution as the new starting value of the scheme.
- The law governing the θ parameter (the so-called cooling scheme) has to be determined from numerical experimentation; setting $\theta_{\text{new}} = 0.8 \times \theta_{\text{old}}$ if the cost function does not decrease by more than 1% during ten iterations leads to a good compromise between speed of convergence and computational burden.
- Frequency-diverse data partially alleviate the availability of aspect-limited data only. A frequency-hopping scheme is then operated upon: assume one is working with P frequencies (from the lowest one to the highest one), the inversion is performed with frequency 1; then with frequency 2, the just retrieved contrast solution being chosen as the initial guess; and so on, until the Pth frequency.

In effect, the numerical simulations have shown that good results require combining the above frequency-hopping, periodic refreshment and cooling scheme procedures: for the $P - 1$ first frequencies, the inversion is performed with refreshment each 15 iterations then, for the Pth frequency, cooling is a substitute to refreshment.

An additional constraint is added to the binary MGM. A filter is enforced onto the contrast update direction d_n in order that $d_n = 0$ on the boundary of $\mathcal{D}$, i.e., the parameters that are characteristic of the pixels located along the boundary remain those of the embedding at each iteration, and they are allowed to vary more and more freely when the pixels move farther and farther away. So one multiplies d_n by

$$q(x, y) = \left\{ \sin\left[\frac{\pi}{L_x}\left(x - \frac{L_x}{2}\right)\right] \sin\left[\frac{\pi}{L_y}\left(y + \frac{L_y}{2}\right)\right] \right\}^{\frac{1}{10}}. \tag{16}$$

3.2. The parameters of the simulations

The numerical experimentation assumes a 1 m sided square test domain $\mathcal{D}$ centred at a 0.5 m depth. The measurement configuration comprises $N_s = 15$ line sources regularly spaced between -5 and +5 m at height $y_S = 0.5$ m, and radiating at most at four frequencies, 100, 200, 300 and 400 MHz; and $N_r = 47$ receivers regularly spaced between -10 and +10 m at height $y_r = 0.125$ m.

Note that the inversion of phaseless data is performed with the same number of sources and receivers as the one of complete data, which leads to a much lesser coverage. Data are always acquired independently from the solution of the direct scattering problem using a significantly higher number of pixels in order to describe the search domain $\mathcal{D}$ and to avoid committing the *inverse crime* to a fair extent (more comments on this aspect are found in Lambert *et al* (1998)).

The results displayed are grey-level maps of the distribution in space of a pertinent characteristic parameter of the probed configuration, the blackest tone being usually associated with the highest retrieved value of this parameter for each separated figure, unless mentioned otherwise. Such maps are those found at the end of the iterative reconstruction procedure,

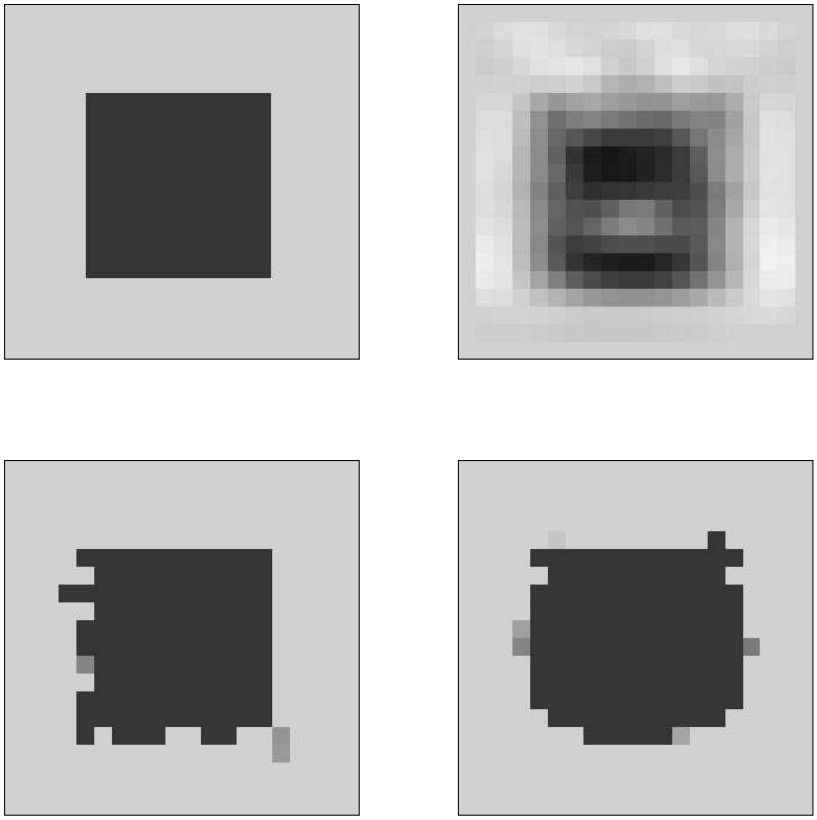

Figure 2. Permittivity maps corresponding to the case of a square obstacle centred in the (44×44)-pixel search domain $\mathcal{D}$: the exact map (top left) and those retrieved by the constrained MGM from complete data (top right) and by the binary MGM from either complete data (bottom left) or amplitude-only data (bottom right) are displayed.

this being manifested by the reaching of a stable plateau of the cost functional (and stable distributions of the unknown(s)), from which neither refreshment nor cooling enable us to leave, the four frequencies having been accounted for. Note also that, unless mentioned otherwise, the update directions have been filtered as seen previously.

3.3. A single, centred square obstacle

In this section, the obstacle is a centred, 0.52 m sided square obstacle. The embedding (respectively the obstacle) is of relative permittivity $\varepsilon_{2r} = 2$ ($\varepsilon_{\mathcal{D}} = 3$) and of conductivity $\sigma_2 = 0$ S m^{-1} ($\sigma_{\mathcal{D}} = 10^{-2}$ S m^{-1}). The initialization is carried out accordingly with (15), letting p_i equal to 2.2 for the relative permittivity and 10^{-4} for the conductivity, respectively.

The results provided by the binary-constrained modified gradient method are displayed in figure 2 (maps of the relative permittivity) and in figure 3 (maps of the conductivity) for both complete and amplitude-only data; and they are compared (for complete data only) with those provided by the modified gradient method investigated in Lambert *et al* (1998).

The latter, as already stated, is constrained by realizability conditions, and is set to simultaneously construct one complex-valued sequence of magnetic fields and two independent,

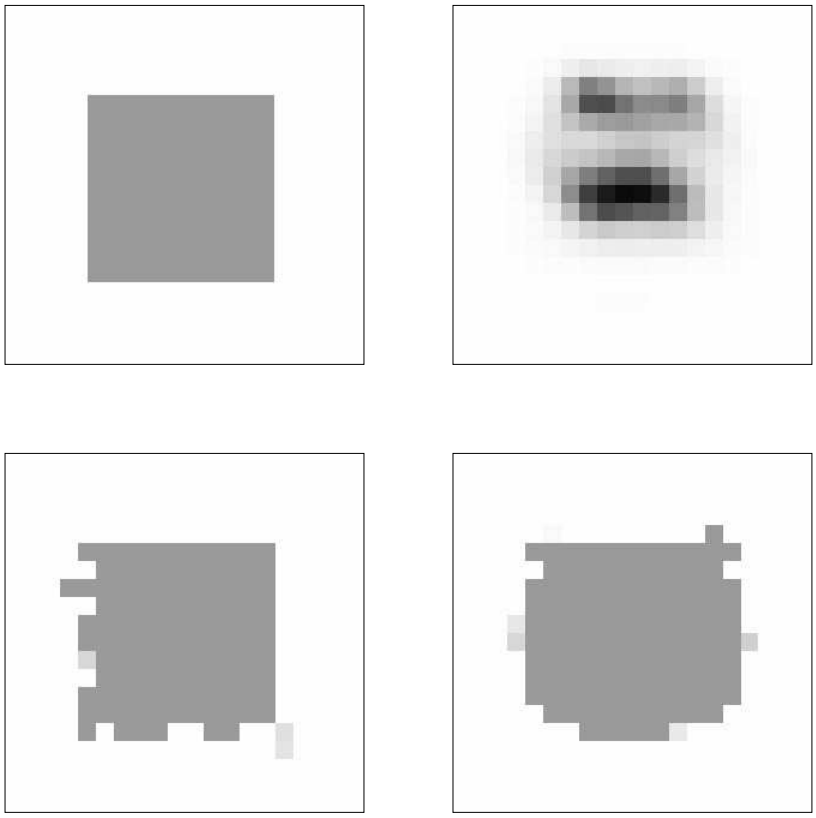

Figure 3. Same as in figure 2: the conductivity maps are now shown.

real-valued sequences of electrical parameters where permittivity and conductivity are mixed in, and are extracted upon completion. That is, both permittivity and conductivity maps contain specific, complementary, information on the obstacle. This is in contrast with the binary MGM which constructs one complex-valued sequence of fields and one real-valued sequence of the contrast variable τ, from which permittivity and conductivity directly proceed in a one-to-one correspondence, since their prescribed bounds have been input into $\mathcal{M}_{\mathcal{D}}$. That is, the conductivity map is no more informative than the permittivity map and vice versa.

The obstacle appears fairly well retrieved by the binary MGM, be this reconstruction led with or without the phase information. As for the constrained MGM (input by complete data only), it succeeds to a good extent with the reconstruction of the permittivity map but it yields a high-pass filtered and blurred version of the conductivity map.

3.4. A two-component, non-symmetric obstacle

In this section, the obstacle is made of two identical rectangular components, which are 36.25×18.75 cm^2 sized and are buried at different depths and lateral ranges, their centres being $(x, y) = (-29.5\text{ cm}, -70.5\text{ cm})$ and $(24.5\text{ cm}, -37.5\text{ cm})$. The embedding parameters are $\varepsilon_{2r} = 2.55$ and $\sigma_2 = 4 \times 10^{-3}$ S m^{-1} and those of the obstacle are $\varepsilon_{\mathcal{D}} = 3.5$ and $\sigma_{\mathcal{D}} = 10^{-2}$ S m^{-1}. The initialization is made accordingly with (15), letting p_i equal 3 for the relative permittivity and 5×10^{-3} for the conductivity, respectively.

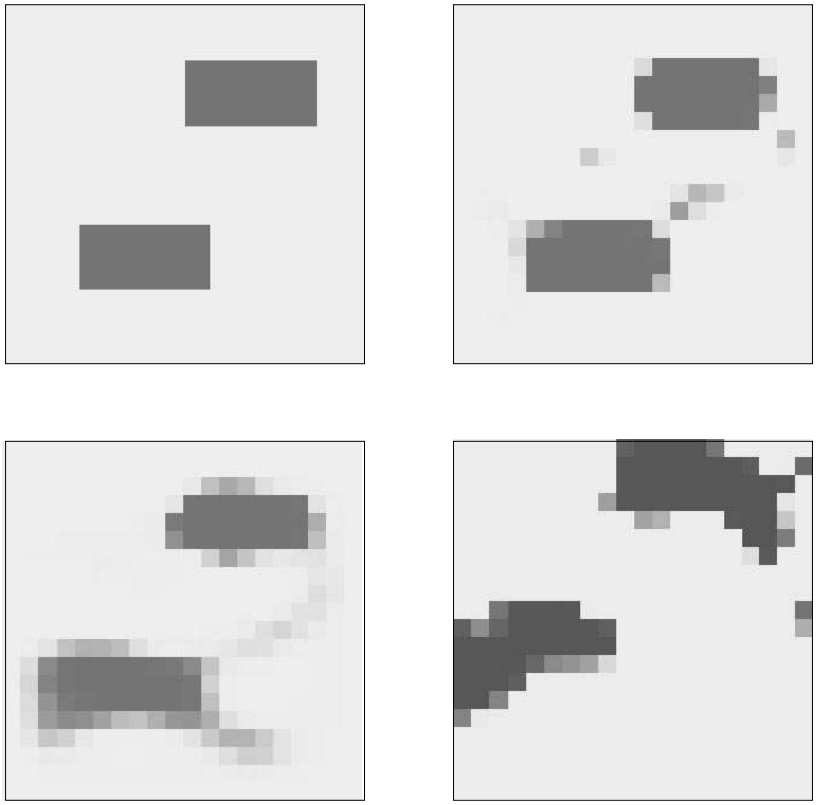

Figure 4. Permittivity maps corresponding to the case of two off-axis rectangular obstacles (a shallow one and a deep one) in the (44 × 44)-pixel search domain $\mathcal{D}$: the exact map (top left) and those retrieved by the binary MGM either from complete data (top right) or from amplitude-only data, without filtering (bottom left) or with filtering (bottom right), are displayed.

Retrieved permittivity maps are shown in figure 4, the inversion being carried out using the exact value of $\mathcal{M}_\mathcal{D}$; and in figure 5, the inversion being carried out using either an underestimated value of $\mathcal{M}_\mathcal{D}$ (correspondingly, of the permittivity and conductivity) or an overestimated value. In practice, instead of the exact values of $\varepsilon_\mathcal{D} = 3.5$ and $\sigma_\mathcal{D} = 1 \times 10^{-2}$ S m^{-1} the inversion is performed with 10% underestimated parameters—$\varepsilon_\mathcal{D} = 3.15$ and $\sigma_\mathcal{D} = 9 \times 10^{-3}$ S m^{-1}—and with 20% overestimated parameters—$\varepsilon_\mathcal{D} = 4.2$ and $\sigma_\mathcal{D} = 1.2 \times 10^{-2}$ S m^{-1}. Notice that the reference maximum permittivity is the same for both figures (so black pixels show up only in figure 5 and the exact obstacle looks grey-like in figure 4) and is equated to the overestimated value of 4.2.

The above figures illustrate that the binary MGM with phase information (complete data) enables both a good location and shape retrieval of the two components of the sought obstacle (refer to figure 4, top right) whereas the binary MGM without this phase information tends to provide black (obstacle) pixels that lie outside the search domain if one does not properly filter the contrast update directions (refer to figure 4, bottom left). As hoped for, filtering these update directions significantly improves the grouping and location of the obstacle components (refer to figure 4, bottom right), which also exemplifies that phaseless but frequency-diverse data, properly processed, may ensure suitable depth (and range) discrimination.

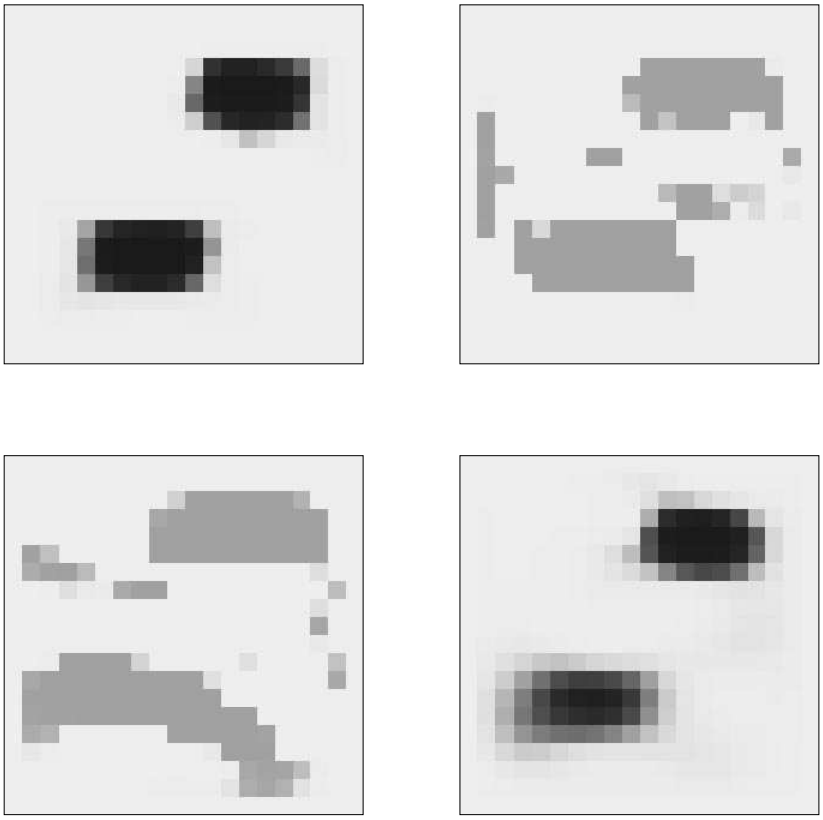

Figure 5. Same as in figure 5: the permittivity maps retrieved from complete data (top) and amplitude-only data (bottom) by assuming either overestimated (left) electrical parameters $\varepsilon_{\mathcal{D}}$ and $\sigma_{\mathcal{D}}$ or underestimated (right) ones, are now displayed.

These figures also illustrate that an incorrect contrast choice may still be bearable. That is, maps retrieved with an overestimated contrast (refer to figure 5, left) are fairly good with complete data as well as with amplitude-only data; the only inaccuracy comes from the fact that the contrast converges toward a higher value (close to the one prescribed) than the exact one, while—as if the algorithm was to keep the scattering strength of the obstacle of the same magnitude—the size of each component is slightly reduced. In contrast, underestimating this contrast results in a number of spurious peaks in the search domain while also degrading the shape of the deepest obstacle component particularly when the phase information is absent (compare figure 4, bottom right, to figure 5, bottom).

3.5. A deeply buried, off-centre rectangular obstacle

In this section the obstacle is the deepest component of the two-component obstacle dealt with in section 3.4. Retrieved permittivity maps are shown in figure 6, the inversion being carried out using the exact value of $\mathcal{M}_{\mathcal{D}}$. The binary MGM with complete data yields fairly good results, as is expected from the previous results. However, using phaseless data now leads to a rather poor map, in contradistinction with what was exhibited in figure 4 (left).

However, neither increasing the number of receivers along the probing line, nor adding an second line of receivers at a different height, nor starting from a higher frequency, nor using

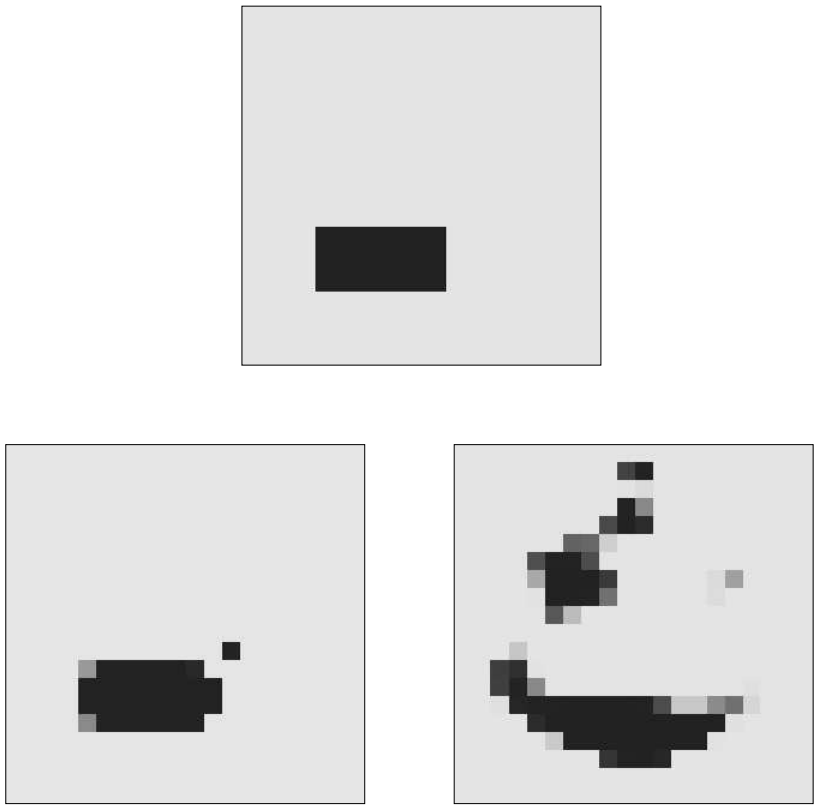

Figure 6. Permittivity maps corresponding to the case of an off-axis rectangular obstacle (the deeper of the two considered in figures 4 and 5): the exact map (top) and those retrieved by the binary MGM from complete data (bottom left) and from amplitude-only data (bottom right) are displayed.

the four frequencies simultaneously instead of one by one, improved the reconstruction. The reason is not obvious so far, but it seems to be linked with the choice of the initial guess; this comment is substantiated by our observation that a much better initial guess of the inversion—here, using for the sake of the experimentation the contrast map retrieved at 100 MHz by the binary MGM when it is input by complete data—does greatly improve the reconstruction of this deep obstacle from the phaseless data.

4. Conclusion

The research described herein intends to contribute to the demonstration that modified gradient methods are versatile tools of rigorous nonlinearized inversion, and that they may be tailored to rather severe data configurations—this being paid for by further complexity in the theoretical and numerical machinery.

The proposed binary-constrained modified gradient method aims to the retrieval of a buried obstacle of known electrical contrast with its half-space embedding and of unknown topology. This is performed in the TE polarization case—for which far less work has been done (again, we refer the reader to the discussion in van den Berg and Kleinman (1997)) save, e.g., the

recent parallel investigations of Kooij and van den Berg (1998) and Kooij *et al* (1998)—within the framework of a rigorous formulation of the scalar magnetic field involving a integral–differential operator on the search domain, which is in some contrast with the use of the vector electric field formulation in the last two references. The investigation takes its inspiration from previous research (Lambert *et al* 1998) which has shown that a modified gradient method, obeying realizability constraints, succeeds in reconstructing either the permittivity map or the conductivity map of the buried obstacle from magnetic field data but usually fails to get accurate maps of both of them in a simultaneous fashion.

Here, one addresses this ill-posedness problem by assuming that the obstacle is constituted by an uniform material which is characterized by a constant complex-valued contrast, prescribed to a certain accuracy; and one goes one step further in the analysis since it is shown that both complete and amplitude-only H-field data are amenable to processing by the resulting binary-constrained method.

Overall numerical results appear fairly good, and in practice are much better than those obtained by the previously derived algorithm, on condition that the numerical tuning of the chosen method is careful. This observation is true for complete data, but remains also as such with phaseless data at least in some challenging cases, e.g., a two-component obstacle, where both components are well discriminated from one another and accurately shaped.

In other cases, the amplitude-only variant of the algorithm may not succeed as well. Evidently, much less information on the obstacle is contained in the phaseless data (how much is a question which deserves further investigation) but the limited numerical experimentation conducted here shows that this lack of information does not hinder the reconstruction to too high a degree; this is exemplified *a contrario* by the fact that probing the field with two lines of receivers, one above and at some distance from the other, did not improve the results at all if those were not already satisfactory with one line.

The strong influence of initialization in these cases is also a reminder that backpropagation of complete data is a well-understood tool for the derivation of a first contrast guess, but that to do the same with phaseless data is yet to be proved successful (preliminary results—not considered herein—show that this appears to be restricted to the case of an obstacle small with respect to the probing wavelength).

Finally, it remains to be studied in more detail whether our choice of the H-field formulation is equivalent to the one of the E-field formulation, or if one may be preferable to the other. The only results available appear to be those of Kooij and van den Berg (1998) which show that in free space the E-field formulation may perform better in some cases—in the absence of results on the respective behaviour of the operator equations, this may simply arise from the numerical implementations. However, nothing of that kind has been documented yet in the more demanding buried obstacle configuration and *a fortiori* with amplitude-only data.

Appendix. Expression of the gradients g_n^d and $g_{j,n}^v$ †

The gradient with respect to the field reads

$$g_{j,n}^v = \frac{\partial}{\partial H_j} F(\boldsymbol{H}, \tau)\bigg|_{\boldsymbol{H}_{n-1}, \tau_{n-1}} . \tag{17}$$

For either complete data or amplitude-only data, one has

$$g_{j,n}^v = -\omega_{\mathcal{D}}[r_{j,n-1} - \overline{\mathcal{M}}_{n-1}\mathcal{G}_{\mathcal{D}}^{\star} r_{j,n-1}] - \begin{cases} \omega_{\mathcal{L}}\overline{\mathcal{M}}_{n-1}\mathcal{G}_{\mathcal{L}}^{\star}\rho_{j,n-1} \\ 2\omega_{\mathcal{L}}\overline{\mathcal{M}}_{n-1}\mathcal{G}_{\mathcal{L}}^{\star}[H_{j,n-1}^{\text{scat}}\rho_{j,n-1}] \end{cases} \tag{18}$$

† Unfortunately the $+\omega_{\mathcal{L}}$ in equations (21) and (22) in Lambert *et al* (1998) should read $-\omega_{\mathcal{L}}$.

with $\mathcal{M}_{n-1} = \mathcal{M}_{\mathcal{D}}\Psi_\theta(\tau_{n-1})$ and $H^{\text{scat}}_{j,n-1} = \mathcal{G}_{\mathcal{L}}\mathcal{M}_{n-1}H_{j,n-1}$.

The gradient with respect to the contrast reads

$$g^d_n = \frac{\partial}{\partial\tau}F(\boldsymbol{H},\tau)\bigg|_{\boldsymbol{H}_{n-1},\tau_{n-1}} \tag{19}$$

$$g^d_n = 2\omega_{\mathcal{D}}\sum_{j=1}^{N_s}\text{Re}\,[\overline{\mathcal{M}}^{\tau}_{n-1}\overline{H}_{j,n-1}\mathcal{G}^{\star}_{\mathcal{D}}r_{j,n-1}] - \begin{cases} 2\omega_{\mathcal{L}}\displaystyle\sum_{j=1}^{N_s}\text{Re}\,[\overline{\mathcal{M}}^{\tau}_{n-1}\overline{H}_{j,n-1}\mathcal{G}^{\star}_{\mathcal{L}}\rho_{j,n-1}] \\ 4\omega_{\mathcal{L}}\displaystyle\sum_{j=1}^{N_s}\text{Re}\,[\overline{\mathcal{M}}^{\tau}_{n-1}\overline{H}_{j,n-1}\mathcal{G}^{\star}_{\mathcal{L}}[H^{\text{scat}}_{j,n-1}\rho_{j,n-1}]] \end{cases} \tag{20}$$

where Re stands for real part and the overbar stands for complex conjugation, where $\mathcal{G}^{\star}_{\mathcal{D}}$ and $\mathcal{G}^{\star}_{\mathcal{L}}$ are the adjoint operators of $\mathcal{G}_{\mathcal{D}}$ and $\mathcal{G}_{\mathcal{L}}$, respectively, and where $\mathcal{M}^{\tau}_{n-1}$ is defined by

$$\mathcal{M}^{\tau}_{n-1} = \frac{\partial}{\partial\tau}\mathcal{M}\bigg|_{\tau_{n-1}} = \frac{\mathcal{M}_{\mathcal{D}}}{\theta}\exp(-\tau_{n-1}/\theta)\Psi^2_\theta(\tau_{n-1}). \tag{21}$$

The descent directions are correspondingly chosen as

$$d_n = g^d_n + \frac{\langle g^d_n, g^d_n - g^d_{n-1}\rangle}{\langle g^d_{n-1}, g^d_{n-1}\rangle}d_{n-1}, \tag{22}$$

$$v_{j,n} = g^v_{j,n} + \frac{\sum_{l=1}^{N_s}\langle g^v_{l,n}, g^v_{l,n} - g^v_{l,n-1}\rangle}{\sum_{l=1}^{N_s}\langle g^v_{l,n-1}, g^v_{l,n-1}\rangle}v_{j,n-1}. \tag{23}$$

References

Kleinman R E and Angell T S 1996 Reciprocity, Radiation Conditions and Uniqueness *Center for the Mathematics of Waves Report 96-11* (University of Delaware, Newark)

Kooij B J and van den Berg P M 1998 Nonlinear inversion in TE scattering *IEEE Trans. Microw. Theory Tech.* **46** 1704–12

Kooij B J, Lambert M and Lesselier D 1999 Nonlinear inversion of a buried object in transverse electric scattering *Radio Sci.* **34** 1361–71

Lambert M 1998 TE-scattering by a cylindrical dielectric obstacle buried in a half-space: a H-field-based solution method *J. Electromagn. Waves Appl.* **12** 1217–39

Lambert M, Lesselier D and Kooij B J 1998 The retrieval of a buried cylindrical obstacle by a constrained modified gradient method in the H-polarization case and for Maxwellian materials *Inverse Problems* **14** 1265–83

Lesselier D and Duchêne B 1996 Wavefield inversion of objects in stratified environments: from backpropagation schemes to full solutions *Review of Radio Science 1993* ed W R Stone (Oxford: Oxford University Press) pp 235–68

Liukkonen J 1999 Uniqueness of electromagnetic inversion by local surface measurements *Inverse Problems* **15** 265–80

Maleki M H, Devaney A J and Schatzberg A 1992 Tomographic reconstruction from optical scattered intensities *J. Opt. Soc. Am.* A **9** 1356–63

Maleki M H and Devaney A J 1993 Phase-retrieval and intensity-only reconstruction algorithms for optical diffraction tomography *J. Opt. Soc. Am.* **10** 1086–92

Petry M 1995 Acoustic scattering in a layered medium *Inverse Scattering and Potential Problems in Mathematical Physics* ed R E Kleinman *et al* (Frankfurt am Main: Peter Lang) pp 140–56

Souriau L, Duchêne B, Lesselier D and Kleinman R E 1996 Modified gradient approach to inverse scattering for binary objects in stratified media *Inverse Problems* **12** 463–81

Takenata T, Wall D J N, Harada H and Tanaka M 1997 Reconstruction algorithm of the refractive index of cylindrical object from the intensity measurements of the total field *Microw. Opt. Technol. Lett.* **14** 182–8

van den Berg P and Kleinman R E 1997 Gradient methods in inverse acoustic and electromagnetic scattering *Large-Scale Optimization with Applications* ed L T Biegler *et al* (Berlin: Springer) pp 173–94

D

Sources distribuées

[A.6] Distributed source method for retrieval of the cross-sectional contour of an impenetrable cylindrical obstacle immersed in a shallow water waveguide
Marc Lambert et Dominique Lesselier
ACUSTICA - Acustica united with Acta Acustica **86** 15-24 2000

ACUSTICA · acta acustica
Vol. 86 (2000) 15–24

Distributed Source Method for Retrieval of the Cross-Sectional Contour of an Impenetrable Cylindrical Obstacle Immersed in a Shallow Water Waveguide

M. Lambert, D. Lesselier
Département de Recherche en Électromagnétisme - Laboratoire des Signaux et Systèmes (CNRS-SUPÉLEC-UPS), Plateau de Moulon, 91192 Gif-sur-Yvette Cedex, France, E-mails: Marc.Lambert@supelec.fr, Dominique.Lesselier@supelec.fr

Summary
The nonlinear retrieval of the cross-sectional contour of a sound-soft or sound-hard, closed cylindrical obstacle which is fully immersed in the water column of a shallow water waveguide is investigated. Time-harmonic pressure field data are acquired on two nearby vertical arrays when the obstacle is illuminated by a line source operated at one or at best two discrete frequencies. These data are inverted by a distributed source method. This involves the minimization of a two-term cost functional which is characteristic of the fit between data and wavefield associated to a test obstacle, and of the satisfaction of the boundary condition on the contour of this test obstacle. The method relies on the modeling of the acoustic wavefields as a superposition of elementary waves (the Green's functions of the waveguide) and uses the smoothness of the sought contour as a main constraint. Numerical experimentation shows that it yields good shape reconstructions for soft, and at a lesser extent hard, obstacles above a sedimentary fluid-like sea bottom of low as well as of high contrast using a fairly limited dataset (with some substantial improvement using the two frequencies), whereas it has the potential for generalization to elastic bottom layers as well as to obstacles fully buried in the bottom.

PACS no. 43.30.Pc, 43.30.Xm

1. Introduction

In a shallow sea water environment, the characterization of a passive obstacle which may be fully immersed in the water column, or fully buried in the bottom, or even partially emerging in water or in air, from an observation of the acoustic pressure field which results from its interaction with a given source or set of sources located in water, is a topic of increasing concern in underwater acoustics, e.g., [1] and references therein.

Solving this inverse scattering problem requires a precise knowledge of the environmental parameters (those of the water column and of the bottom), which is an inverse problem *per se* [2], and of the illuminating source and receiving sensor parameters, plus a number of *a priori* assumptions on the sought obstacle itself.

Here we shall assume the following "prototype" problem (refer to Figure 1 for a sketch of the configuration under investigation):
(i) The environment is modeled as a range-independent, planar-layered waveguide which is consisting of an isovelocity, iso-density water column (wavenumber k_0 at circular frequency ω) of known height H comprised between a pressure-release air/water flat interface (the (x, y) plane in a Cartesian coordinate setting) and a homogeneous linear isotropic half-space with flat interface (the sea floor) at $z = H$.
(ii) The source is modeled as an ideal time-harmonic line source which is orientated parallel to the y axis. It is placed at given range and depth in the water column, and it is operated at one discrete frequency, or, at best, at two successive discrete frequencies.

Received 26 July 1999,
accepted 18 October 1999.

(iii) The obstacle is an infinitely long, singly-connected cylindrical obstacle whose axis is also parallel to the y axis and whose smooth cross-sectional contour, star-shaped with respect to a prescribed interior point, is satisfying either a Dirichlet boundary condition (sound-soft: the total pressure field should be zero on the contour) or a Neumann boundary condition (sound-hard: the normal derivative of this pressure field should be zero on the contour).
(iv) At a given frequency, the resulting complex-valued pressure field is collected by two vertical arrays of sensors; they are placed at given range on either side of the obstacle and span with a fixed sampling step the full water column —long enough horizontal arrays or other sensor arrangements could be considered likewise.

This problem can be seen as somewhat simple with respect to those commonly encountered in a real sea environment, but it has already many of their ingredients:
(i) Multiple interaction occurs between the obstacle and the waveguide walls (and waveguiding within the environment itself), and this phenomenon cannot easily be left aside, notably but not only due to the fact that we focus onto the so-called resonance domain, where key dimensions of the obstacle are of the same order or somewhat larger as a typical wavelength of the probing wave.
(ii) Aspect-limited data are the only ones available since source and sensors illuminate and/or see only a limited part of the obstacle, while the source itself is kept at fixed location and is not moved within the water column. The resulting lack of information is only partially alleviated for when frequency-diverse data are processed. In addition, part of the acoustic signal goes away into the sea bottom and it cannot be accessed to by the sensor arrays, which further limits the data coverage.
(iii) Exact inversion with respect to the unknown (the contour of the obstacle) is targeted, implying that no approxi-

ACUSTICA · acta acustica
Vol. 86 (2000)

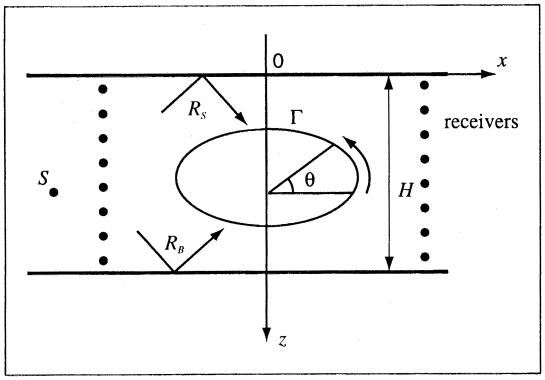

Figure 1. The geometrical configuration.

mation of the wavefield is used, like the Born or Physical Acoustics approximations, or other approximations such as neglecting part of or all coupling of the obstacle to the two interfaces.

(iv) The full non-linear problem is dealt with, in the sense that not only the pressure field samples associated to a test obstacle must be "fitted" to the data collected by the sensors —which is understood in practice as "the mean square norm of their discrepancy should be minimized"— but that the field equations must be simultaneously satisfied —which is now understood as "the mean square norm of samples of the pressure field or of its normal derivative computed along the retrieved contour should be minimized". (Let us however notice that the phase of the signal on the receivers is assumed to be available and accurate, which is a frequent but not necessarily minor assumption, e.g., [3] where both complete and phaseless data are handled.)

Furthermore, the shape inversion problem in semi-confined environments (this is the case here) is markedly different from the one extensively considered for obstacles in free-space in the literature, e.g., [4] and references therein, as is already underlined by [5]. So the considerable expertise acquired in free space is only partially relevant in the semi-confined case.

This difference of behavior is due to the above geometrical and physical peculiarities, which, as such, are already leading to a severely ill-posed inverse problem, but also to a number of still pending theoretical questions on the general question of scattering in waveguides [6, 7]. Those include the uniqueness of the underlying boundary value problems (notably the existence of trapped modes); the introduction of a global radiation condition as a substitute to the traditional imposition of separate conditions on each propagated mode; the unique solvability of the direct scattering problem using specific integral formulations; and the completeness of wavefield representations.

All such theoretical issues are rather difficult and they clearly deserve more investigation. However, they will be for the most part left aside in this paper. That is, from the aforementioned theoretical material, we infer —and henceforth keep in mind— that certain restrictions on the obstacle contour are/should be needed, such as a convex or at best a mildly concave contour as is already shown in the Dirichlet case. And we definitely focus onto more pragmatic questions like the trade-off between complexity and reliability of the inversion method, the amount of needed assumptions, the actual computational burden, and potential generalizations.

Let us emphasize that, to the best of our knowledge, the "full-fledged" retrieval of an impenetrable obstacle immersed in shallow water is not attacked so far without resorting to some approximation of the propagation and scattering phenomena: backpropagation so as to build equivalent sources hoped to concentrate upon the obstacle domain [8]; suppression of multiple scattering so as to extract the scattering function which describes the behavior of the same scatterer in free space [9]; or via involved classification techniques that are implemented from the resonance scattering technique [10].

This is also the case to some extent with the pioneering investigations of the so-called Intersecting Canonical Domain Approximation or ICDA, *e.g.* [1] (rigid bottom), [11] (fluid-like sediment layer above a rigid bottom), though the direct scattering problem therein is modeled from a known canonical solution. A 3-D soft obstacle is retrieved by assuming that the field measured at a given point is the same as the one which would be due to a vertically orientated, truncated cylinder (the same boundary condition holding) whose radius is determined accordingly.

Let us notice that in contrast to these rotationally symmetric 3-D configurations, no canonical solution for an extended obstacle seems available for the cylindrically symmetric, 2-D configuration which is treated here.

The paper is organized as follows. In section 2 the distributed source inversion method is described and some necessary material (the Green's function) provided. In section 3 the numerical experimentation is discussed with emphasis on the geometrical and acoustical parameters of the tested configurations; on the calculation of proper input data acquired independently by solving the direct scattering problem; on the key parameters of the inversion itself; and on the corresponding numerical results and their dependence upon the obstacle and environment properties. In section 4, lessons directly drawn from the investigation are outlined; then, it is briefly discussed, in a more subjective fashion, whether the distributed source approach is promising for tackling more complex obstacles within more complex environments.

2. The distributed source inversion method

The distributed source inversion method considered herein owes its origin to the so-called complete family approach which has been investigated earlier in great detail [5] for the reconstruction of soft (Dirichlet) obstacles placed in a homogeneous waveguide with perfectly reflecting walls (pressure-release sea surface, rigid bottom) from monochromatic data. Preliminary results for a hard obstacle with the same perfect reflection and data monochromaticity assumptions are found in [12].

Here, for both the soft obstacle and the hard obstacle, we extend the investigation to the case of a homogeneous fluid bottom half-space, which intends to model a thick enough sediment layer, and to multiple frequency data (some results have already been discussed in [13]).

Let us emphasize that a more complicated solid elastic layering may be considered in the same terms: only its plane wave reflection coefficient as a function of the horizontal wavenumber k_x (the Fourier counterpart of the range x), e.g., [14], plays a role as it will be reminded later on.

So let us assume that in a given sea configuration (refer again to Figure 1) there exists a time-harmonic line source S which is radiating at a circular frequency ω — the $\exp(-\mathrm{j}\omega t)$ dependence is henceforth implied— and which is set at given range x_S and depth z_S in the water column. And let us take for granted that L_R equidistant samples, $p_S^{mes}(l_R)$, $l_R = 1, \cdots, L_R$, of the scattered pressure resulting from the interaction of the probing source with the probed obstacle have been acquired along a certain set of sensor arrays in water —one on each side of the obstacle— globally denoted as R.

From past investigation in the case of a perfect waveguide (soft air/water interface and hard sea floor) when a soft obstacle is embedded in between [6], the resulting waveguide Green's functions whose source points are located on a closed curve placed within the cross-section of the obstacle, constitute a so-called Dirichlet complete family.

In practice it means that the scattered pressure field can be represented as the sum of an infinite series made of Green's functions with position-independent weighting coefficients. Which leads to assume that a finite number of them is sufficient to get a good estimate of the pressure field, this assumption having been validated from comprehensive numerical experimentation in [5].

No similar body of knowledge, however, exists for a penetrable bottom and/or a hard obstacle so far. Nonetheless, the simplest choice —which we recognize as heuristic— is to assume that a finite subset of the waveguide Green's functions enables us to approximate the pressure field in a well-behaved and accurate fashion, leaving open the question whether other representations might be more appropriate. (Refer also to the discussion of a free space scattering case in [4] and to several references quoted therein.)

Assuming a test obstacle with a certain contour Γ, its scattered pressure field is henceforth equated to a weighted sum of M exact Green's functions of the waveguide $G(\mathbf{r}, \mathbf{r}_m^\Gamma)$; their source locations $\mathbf{r}_m^\Gamma, m = 1, \cdots, M$, are located on a closed curve $\hat{\Gamma}$ which is kept inside the domain encircled by Γ and homothetic with it, via the imposition of $|\, \mathbf{r}_m^\Gamma(\theta) \,| = \alpha\gamma(\theta)$, α constant real multiplicative factor less than 1. One has

$$p_S(\Gamma, \mathbf{r}) = \sum_{m=1}^{M} c_m G(\mathbf{r}, \mathbf{r}_m^\Gamma). \quad (1)$$

The Green's function G represents the wavefield at point $\mathbf{r} = (x, z)$ which would be due to a Dirac line source located at $\mathbf{r}' = (x', z')$. It is a sum of two terms, $G = G_D + G_M$. The first term, G_D, of singular behavior, is associated to the direct wave radiated by the line source (this is a first-kind, zero-order Hankel function). The second term, G_M, of regular behavior, is only known in closed form in the k_x spectral domain and it accounts for the presence of multiple reflection of the wavefield between the waveguide walls. In the spectral domain its Fourier transform is

$$g_D(k_x, z, x', z') = -\frac{\exp(\mathrm{j}\beta\,|z' - z|)}{2\mathrm{j}\beta} \exp(\mathrm{j}k_x x'), \quad (2)$$

$$g_M(k_x, z, x', z') = \frac{\mathrm{j}}{2\beta}\left[\frac{R_S + R_B \exp\left[2\mathrm{j}\beta(H - z - z')\right]}{1 - R_S R_B \exp(2\mathrm{j}\beta H)} \exp\left[\mathrm{j}\beta(z + z')\right] + \frac{2R_S R_B \cos\left(\beta|z - z'|\right)}{1 - R_S R_B \exp\left(2\mathrm{j}\beta H\right)}\right] \exp\left(\mathrm{j}k_x x'\right). \quad (3)$$

In the above $\beta = \sqrt{{k_x}^2 - {k_0}^2}$ with positive or null imaginary part. R_B is the reflection coefficient of the sea bottom when it is illuminated by a plane wave propagated in a water half-space, and is its appropriate extension into the evanescent spectrum when $k_x \geq k_0$. Similar analysis yields the R_S reflection coefficient of the air half-space whenever illuminated from water. $R_B = 1$ for a hard bottom, whereas it can be derived for a general (solid elastic) layered bottom via, e.g., a chain matrix technique. $R_S = -1$ for a pressure-release sea surface, and in that case a term radiated by the image of the line source may be exhibited in the space domain [15]. However, for more generality, the numerical code which has been developed is valid for any fluid upper half-space, which is including air, and R_S is thus equated to its exact value.

Notice that formulations of the Green's function are available for a point-source in a general multi-layered sea channel as it was investigated in [16] and the formulation herein can be seen as a specialization.

What we need now is the definition of a proper cost functional which reflects both the fit between data and wavefield associated to the test obstacle and the satisfaction of the field equations, and which also integrates in some sense the user's priors.

In practice one always works within an appropriate discrete setting in L_2. So we iteratively solves a penalized, discrete optimization problem whose cost functional, henceforth denoted as $F = f_1 + \sigma f_2$, σ being a penalty parameter, is the weighted sum of two appropriate residuals f_1 and f_2 (they are defined below) at the chosen operation frequency. If L frequencies were to be available, results of the problem at the lowest frequency $l = 1$ would be used to initialize the problem at the next frequency $l = 2$, and so forth, by *frequency-hopping*.

ACUSTICA · acta acustica
Vol. 86 (2000)

The simplest definition of the so-called observation cost, or residual f_1, is the discrete mean square norm of the discrepancy between the collected data $p_S^{mes}(l_R)$ and the pressure $p_S(\Gamma, l_R)$ at same point l_R which would be due to the test obstacle, appropriately normalized with respect to the discrete mean square norm of the data. It reads:

$$f_1 = \frac{\sum_{l_R=1}^{L_R} |p_S(\Gamma, l_R) - p_S^{mes}(l_R)|^2}{\sum_{l_R=1}^{L_R} |p_S^{mes}(l_R)|^2}. \quad (4)$$

Correspondingly, the boundary cost, or residual f_2, simply is the normalized discrete mean square norm of the error along Γ in canceling out either the total pressure (Dirichlet) or its normal derivative (Neumann); the normalization is now effected with respect to the norm of the incident pressure p_0 existing in the unperturbed waveguide at same location, or of its normal derivative, accordingly.

Let us introduce for simplicity a set of polar coordinates $\mathbf{r} = (r, \theta)$, letting $r = \gamma(\theta)$ be the radial coordinate characteristic of Γ. If we assume that the boundary condition is enforced at Q discrete nodes chosen at regularly spaced polar angles θ_q, the Dirichlet hypothesis leads to

$$f_2 = \frac{\sum_{q=1}^{Q} |p(\Gamma, \theta_q)|^2 J_\Gamma(\theta_q)}{\sum_{q=1}^{Q} |p_0(\Gamma, \theta_q)|^2 J_\Gamma(\theta_q)}. \quad (5)$$

In the above, $p(\Gamma, \theta_q)$ (respectively, $p_0(\Gamma, \theta_q)$) is the total (respectively, incident) pressure field at point (r_q, θ_q), $r_q = \gamma(\theta_q)$, and $J(\theta_q)$ is the corresponding discrete value of the Jacobian $J_\Gamma(\theta) = \sqrt{r^2 + \left(\frac{dr}{d\theta}\right)^2}$. This Jacobian transformation enables us to calculate the boundary cost on the fixed unit circle and not on the evolved contour [17]. As for the Neumann hypothesis, it is readily dealt with by replacing p by $\partial_n p$ in the above Dirichlet-type equation.

No specific assumption on the obstacle contour has yet been introduced, at least explicitly. As in previous studies, Γ is easily described by means of a $2N$ sine-cosine expansion of $\gamma(\theta)$:

$$\gamma(\theta) = a_0 + \sum_{n=1}^{N} a_n \cos(n\theta) + \sum_{n=1}^{N-1} a_{N+n} \sin(n\theta), \quad (6)$$

that is, the contour is assumed to be smooth and star-shaped with respect to the origin of coordinates (this is the prescribed interior point mentioned earlier).

The unknowns are the $2N$ real coefficients a_n (describing the contour Γ) and the M complex coefficients c_m (amplitudes of the interior sources) whereas the data are the pressure fields on the L_R receivers, the boundary condition being enforced at the Q nodes on Γ.

3. Numerical experimentation

3.1. Geometry and acoustics

A $H = 100$ m deep acoustic channel is considered. Water density ρ_0 and velocity of sound in water c_0 are 1030 kg/m^3 and 1500 m/s, respectively; losses in water are neglected. The sea bottom is considered as a fluid-like sediment with density ρ_B, sound velocity c_B, and attenuation α_B proportional to the frequency corresponding to the wavenumber $k_B = \omega/c_B + j\alpha_B$.

Two cases are investigated in the following: a slow, clay-like bottom, $\rho_B = 1800$ kg/m^3, $c_B = 1650$ m/s, $\alpha_B = 0.3$ dB/m/kHz; a fast, granit-like bottom, $\rho_B = 2200$ kg/m^3, $c_B = 4000$ m/s, $\alpha_B = 0.01$ dB/m/kHz. The first type of bottom will be said to correspond with a low-contrast environment, the second one with a high-contrast environment.

Probing frequencies are 30 Hz (the wavelength in water is 50 m, 4 modes are propagated if the attenuation is neglected in the bottom), and 100 Hz (wavelength in water 15 m, 13 such propagated modes).

The source is placed at depth $z_S = 55$ m and range $|x_S| = 100$ m on the right of the obstacle (the incident field is but the Green's function $G(x, z, x_S, z_S)$). The two sensor arrays (41 samples each 2.5 m) are placed at range $|x_R| = 40$ m on either side of the obstacle.

Contour reconstructions of a sound-soft and of a sound-hard elliptic obstacle with respective vertical and horizontal semi-axes 15 m and 7.5 m, and of a three-leaf clover $\gamma(\theta) = 10 - 3\sin(3\theta)$ m are carried out from the resulting two sets of data using either the single low frequency, 30 Hz, or the 30 Hz and 100 Hz frequencies in succession within the frequency-hopping scheme. (Using more frequencies was observed not to yield significantly improved results.)

3.2. Input data

In the absence yet of satisfactory experimental data, and in order to test the method, appropriate sets of synthetic data have to be generated. This has to be made independently from the solution algorithms used in the inversion to avoid at best the "inverse crime".

A computer code implementing the discrete counterpart (derived by means of the Nyström method) of a system of exact contour integral equations is used. One should refer to [5] for the derivation of the integral formulation, once noticed that in this reference one considers a rigid bottom and the corresponding hybrid ray-mode estimate of the Green's function. The complementary material needed for the calculation of the Green's function in the presence of a semi-infinite fluid bottom using fast Fourier transforms for nonequispaced data [18], as well as the intricate analytical calculations of the Green's terms which are required by the Nyström method, is discussed in [15].

As for the regular parts G_M of the Green's functions or their normal derivatives (produced from the partial derivatives with respect to depth and to range) which are used to expand the pressure field or its normal derivative during the course of the inversion (see (1)), they are estimated differently, as follows.

For simplicity, let us denote as X such a function. A regular space mesh covering the rectangular water column from the source to the sensors is defined, at the nodes U_n

of which all further calculation is restricted, values at intermediate locations being linearly interpolated from the nodal values $X(U_n)$.

To calculate these nodal values $X(U_n)$, Dutt's and Rokhlin's fast Fourier transforms are applied to discrete values of the known, closed-form k_x spectrum of X. However, this spectrum peaks on the real spectral axis, near the propagation constants of the waveguide modes in the spectral complex plane; in short, direct calculation may not be reliable.

So, we follow the analysis developed earlier by [19] (it was in an other context, the calculation of radar cross-sections): we do it by *complexification*.

First, three fictitious wavenumbers in water $k_{0i}, i = 1, \cdots, 3$, are chosen. Each has the same real part (the one of the real water wavenumber k_0) and a smaller and smaller imaginary part. Second, the corresponding fictitious nodal values $X(U_{ni}), i = 1, \cdots, 3$, associated to the k_{0i}, are calculated. Third, parabolic extrapolation onto the real axis —to get $X(U_n)$ associated to k_0— is performed from the quadratic Lagrange interpolation polynomial which is easily determined from these three nodal values.

The procedure is in practice of similar accuracy and of much lesser computational cost than the alternate means of using high-precision integration routines in order to calculate the nodal values $X(U_n)$ from their spectral values at k_0.

As for carrying out the calculation of the Green's functions and/or their normal derivatives only at the space points in the water column needed at a given iteration, it was seen as considerably costlier than this two-step interpolation-complexification procedure, and of no better accuracy —in average at least— provided that the sampling step in the water column is small enough (a step size of $\lambda_0/33$ was observed to be necessary).

3.3. Parameters of the inversion

The initial contour is either a circle of radius $a_0 = 9$ m or the contour which has been derived from the data at the lower frequency (when the two frequencies are used). The homothetic contour where the equivalent sources will be distributed is such that $\alpha = 0.75$ (which choice was shown in [5] by numerical experimentation to lead to good results) and the penalty parameters such that $\sigma = 1$. As for the retrieved contour itself, it is described by $2N = 8$ polynomial coefficients.

The initial sources are either "off" ($c_m = 0$ for all m) or "on". The first choice (extinguished sources) is the easiest one, the initial guess for the total field simply being the incident field. The other involves already some preliminary calculation: the contour is set to a fixed value, i.e., the above circle or the retrieved contour from the study carried out at the immediatly lower frequency, and the distribution of sources which induces a zero field (Dirichlet) or a zero field derivative (Neumann) at the sampling points along the contour is the first guess.

The chosen sets of unknown contour and source coefficients, $\{a_n\}$ and $\{c_m\}$, are calculated by an iterative non-linear minimization routine applied to the two-term cost functional F, and which employs a Levenberg-Marquardt algorithm (DNLS1 from the package SLATEC freely available from http://www.netlib.org). The whole procedure is repeated twice when the two frequencies are used.

Both sets of coefficients are sought simultaneously. Variants, where at each iteration, one seeks the contour coefficients by using the previously estimated source coefficients as fixed inputs, and then one seeks the source ones by using the newly found contour ones as fixed inputs, might be considered [17].

The inversion itself assumes $M = Q = 18$ Green's functions in the Dirichlet case and $M = Q = 64$ in the Neumann case. These —rather different— numbers of sources have been chosen from careful numerical experimentation with the solution of the direct scattering problem as follows. For a known contour satisfying a Dirichlet condition, a distribution of the complex amplitudes of M interior sources such that the pressure on the contour is zero at $M = Q$ observation points is solution of a square linear system of Q equations which results from equating at these points the scattered pressure field as developed in the right-hand side of equation (1) to minus the incident pressure field —we may or may not multiply the coefficients of the system by the Jacobian values but this does not matter in that case. And we do the same in the Neumann case by simply operating upon the normal derivative instead.

But any such calculated distribution is valid, i.e., is a suitable solution of the Boundary Value Problem (BVP) which one is faced with, only if the exterior field is numerically accurate, since, in particular, we know (Dirichlet) or expect (Neumann) that an infinitely denumberable set of sources should theoretically be needed.

Comparison of the pressure field on the sensor arrays calculated by summing up the contributions of the just retrieved source distribution with the pressure field calculated independently from the previously analyzed exact integral formulation has been led. In a variety of representative cases excellent agreement is reached (refer to Figure 2 and to Figure 3 for an illustration in the high-contrast environment) somewhat below, at, and beyond values of $M = Q = 18$ (Dirichlet) and 64 (Neumann). And the results remain good fairly below this bound in the Dirichlet case, which is not true with the Neumann case where the agreement quickly worsens at lesser values.

Furthermore, the boundary condition should also be satisfied in between the samples, and a good test is at the Q mid-points, the polar angles of which are the arithmetic means of the angles of the samples used to calculate the above source distribution.

In the same representative cases (again refer to the results displayed in Figures 2–3) the pressure field or its normal derivative on the contour is effectively 0 somewhat below, at, and beyond values of $M = Q = 64$ (Dirichlet) and 128 (Neumann); nonetheless, fair results are already observed at about $M = Q = 18$ (Dirichlet) and 64 (Neu-

ACUSTICA · acta acustica
Vol. 86 (2000)

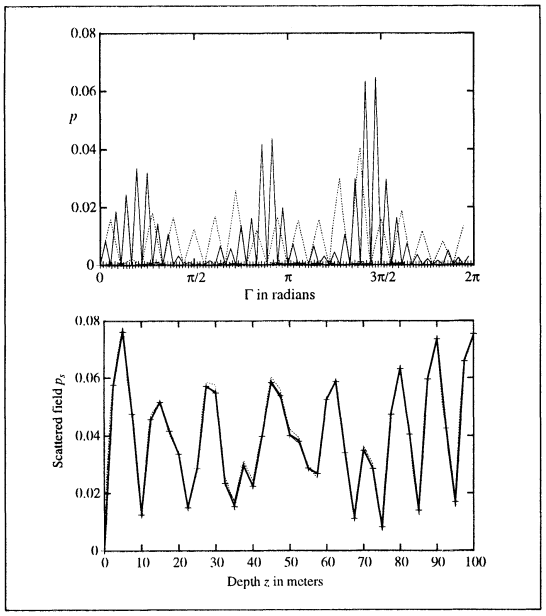

Figure 2. Sound-soft three-leaf clover obstacle in the high-contrast environment at 100 Hz: (top) satisfaction of the boundary condition (the value of the total pressure on the contour Γ) at $Q = 2M$ nodes from M interior sources; (bottom) comparison of the exact scattered mesure (bold plain line) along the $x_R = 40$ m receiver array with the one calculated by solving the BVP with M interior sources; $M = 18$ (dotted line), $M = 36$ (plain line) and $M = 64$ (cross symbol). Notice that the boundary condition is perfectly fulfilled in the $M = 64$ case (the crosses are on the horizontal axis).

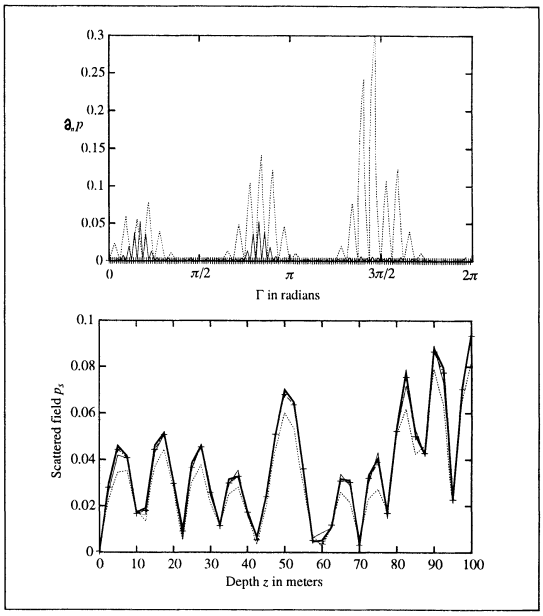

Figure 3. Same as Figure 2 for the sound-hard three-leaf clover obstacle with now $M = 32$ (dotted line), $M = 64$ (plain line) and $M = 128$ (cross symbol) whereas the boundary condition concerns the normal derivative of the total pressure.

mann) —going to lower values in the Neumann case leads to unacceptable differences.

In short the choice of $M = Q = 18$ Green's functions in the Dirichlet case is quite effective. As for the choice of $M = Q = 64$ in the Neumann case, it is the result of a compromise between the stringent conditions that would enable us to closely satisfy the boundary condition on the entire contour, and the more relaxed conditions that already enable us to reach a good data fit at some distance of the obstacle. Let us emphasize that too high a number of unknown source coefficients would also lead to a very slow evolution of the Levenberg-Marquardt solution.

3.4. A few examples

In accord with the previous elements a number of examples are displayed in Figures 4–9. Notice that the retrieved contours, in order to emphasize the impact of the numerical implementation, are displayed via $M = Q$ markers at the same angles as the equivalent source or the observation point locations used to retrieve them, even though these contours could be represented by continuous lines (since we know their polynomial representation).

In Figures 4–5 the soft Dirichlet case is considered for both the ellipse and the clover inside the low-contrast environment. Figure 4 exemplifies the weak influence of the choice of the initial guess of the sources ("on" or "off")

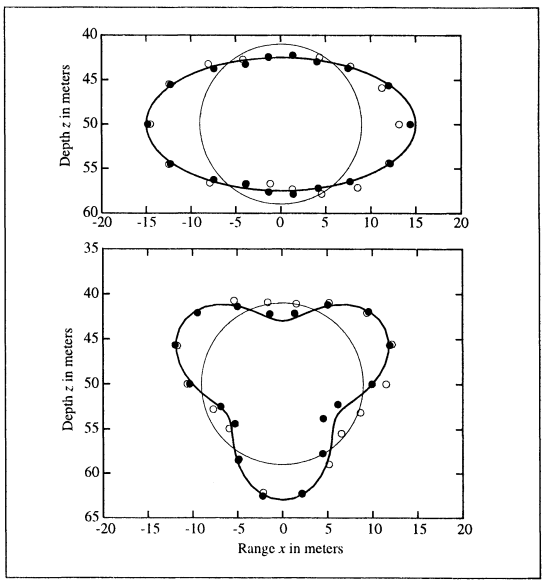

Figure 4. Sound-soft obstacle in the low-contrast environment: comparison of the exact contour (plain line) with the reconstructed ones obtained at 30 Hz from the initial circular contour (dotted line) with "off" (black dot) and "on" (white dot) initial interior sources.

at the 30 Hz frequency, though a slightly better contour reconstruction is reached with the extinguished ones. Figure 5 indicates how from the 30 Hz result one derives from

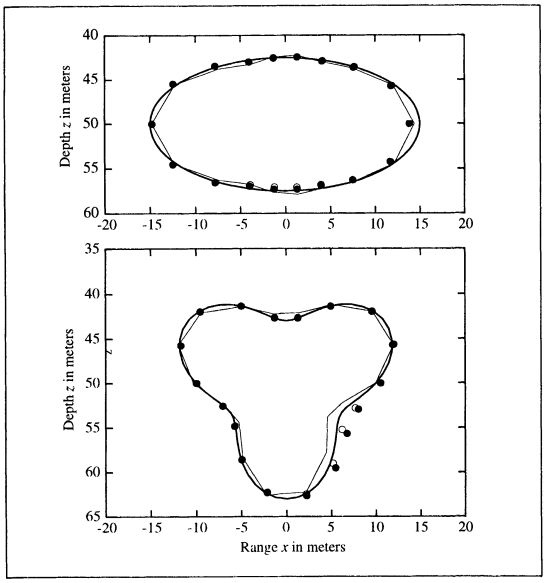

Figure 5. Sound-soft obstacle in the low-contrast environment: comparison of the exact contour (plain line) with the reconstructed ones obtained at 100 Hz with "off" (black dot) and "on" (white dot) initial interior sources, the initial circular contour (dotted line) being obtained by solving the inverse problem at 30 Hz initialized by "off" interior sources.

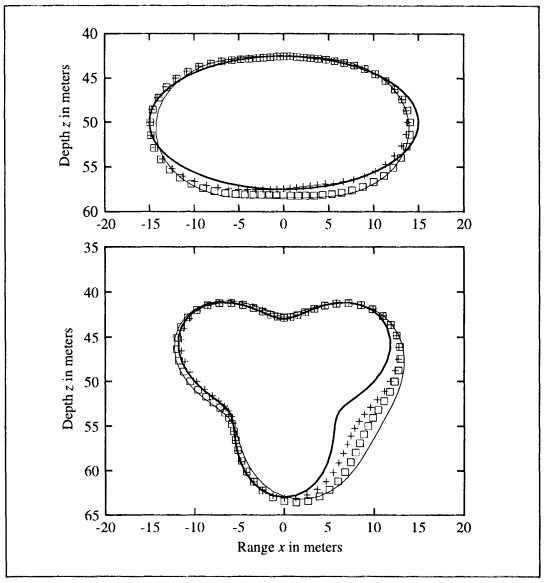

Figure 6. Sound-hard obstacle in the low-contrast environment: comparison of the exact contour (plain line) with the reconstructed ones obtained at 100 Hz with "off" (cross) and "on" (white square) initial interior sources, the initial contour (dotted line) being obtained by solving the inverse problem at 30 Hz initialized by "off" interior sources.

the 100 Hz dataset a somewhat better reconstruction of the clover —this is manifested by the evolution of the geometry of the two shadowed concave parts— but one benefits only from a slight improvement of the contour of the ellipse; notice also that the influence of the sources' first guess is quite minor, as was to be hoped from the rather good initial contour (the 30 Hz solution) input into the algorithm.

The Dirichlet case had been studied at length for a hard bottom and it is not too surprising that the results remain fair with a penetrable bottom. The Neumann case is more challenging as is expected from the fact that one already needs about four times more equivalent sources to suitably solve the BVP than in the Dirichlet case, and gets at that price no better and even worst results.

This observation is confirmed by the results displayed in Figure 6 for the same two-frequency case as in Figure 5 with the Neumann condition. They show that inversion of the single 30 Hz dataset leads to a poor reconstruction of the concave part of the clover in deep shadow (the one on its right side, the source being on the left side), which improves though still lacks good quality when the 100 Hz dataset is input.

The same is true but to a much lesser extent with the ellipse. For the extinguished sources the mapping of the lower part (the one near the bottom) and the tail part (with respect to the source) of the obstacle improves when using the two frequencies, but the results still differ somewhat from the exact solution. For the non-extinguished ones results appear worst.

In short, the frequency-hopping scheme is needed while the use of extinguished sources is the most appropriate. Nonetheless, a concave part in the deep shadow with respect to the source should not be expected to be well retrieved.

The environment is of obvious consequence on the inversion. This is confirmed by the results presented in Figures 7–9. The high-contrast environment is now assumed, since a number of numerical experiments has revealed this environment to be more critical a benchmark environment than the low-contrast one for both Dirichlet and Neumann cases.

In Figure 7 the displayed contours are derived from the 30 Hz dataset and in Figure 8 they are derived from the 30 Hz and 100 Hz datasets —always from extinguished sources as the first guess. In Figure 9 the scattered pressure field at 100 Hz associated to the retrieved contour of the ellipse obstacle is compared to the input data along the receiver array on the same size of the source, and the variations of the global cost function, F, are displayed.

Such results confirm that, overall, the Dirichlet case is less difficult to tackle than the Neumann case, the retrieved contour being significantly better and the final value of the cost functional significantly lower (correspondingly the data fit is improved) though this functional is plateauing rather quickly in terms of the number of iterations in both cases.

But there may be exceptions; this occurs when using the 30 Hz dataset for the ellipse, the contour of the hard ellipse and the one of the soft ellipse being not very accurately

ACUSTICA · acta acustica
Vol. 86 (2000)

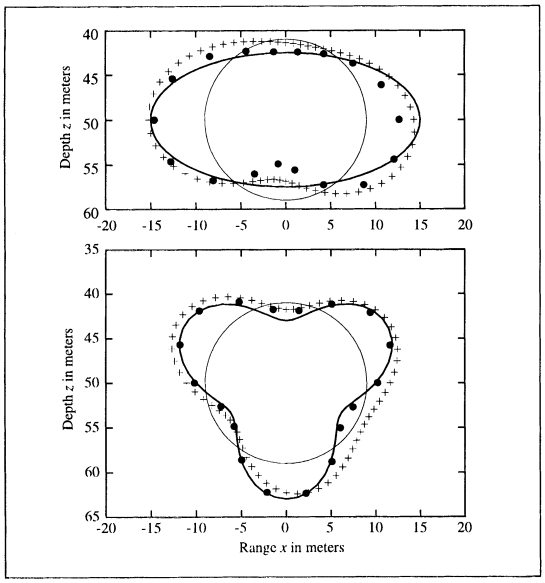

Figure 7. Sound-hard and sound-soft obstacles in the high-contrast environment: comparison of the exact contour (plain line) with the reconstructed ones obtained at 30 Hz from the initial circular contour (dotted line) for a sound-hard obstacle (cross) and a sound-soft one (black dot). Initial interior sources are always "off".

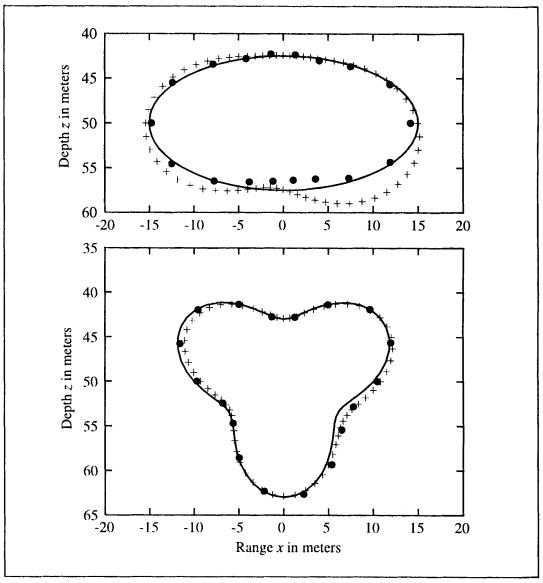

Figure 8. Sound-hard and sound-soft obstacles in the high-contrast environment: comparison of the exact contour (plain line) with the reconstructed ones obtained at 100 Hz from the contour calculated at 30 Hz (cf. Figure 7) for a sound-hard obstacle (cross) and sound-soft one (black dot). Initial interior sources are always "off".

reproduced; and when using the 30 and 100 Hz datasets for the clover, the contour of the clover remaining much the same (and excellent) in both hard and soft cases.

Also as a general observation, the reconstructions improve when the two frequencies are used in succession, though this is certainly truer with the clover than with the ellipse. In effect, the shadowed concave parts of the clover are indeed strongly improved in the Neumann case (the ones in the Dirichlet case are already quite close to the exact contours), but the retrieval of the ellipse —fairly improved in the Dirichlet case for which the 30 Hz reconstruction was poor— still shows some errors, notably regarding the lower and tail parts of the hard ellipse.

Finally, let us indicate that the inversions take what can be seen as a large amount of computation time, particularly in the Neumann case. For example, considering that all nodal values of the Green's functions and their normal derivatives are available beforehand, the retrievals of the sound-soft ellipse and of the sound-hard ellipse from 100 Hz datasets, the results of which are displayed in Figures 7 and 8, has taken 1.5 mn and 17 mn per 10 iterations, respectively, on a 168 MHz Sun Ultra II equipped with Solaris 2.5.1 and Sun f90.

4. Conclusion

4.1. Present-day results

Involved theoretical questions remain, as mentioned in the Introduction, but the efficacy of the method as is exemplified from a number of numerical results, appears fairly good in most cases of interest. The method is also somewhat more effective for a sound-soft obstacle than for a sound-hard one, which is numerically much more involved, whereas noticeable improvement generally comes from successively using two input frequencies.

As is already known, the obvious limitation of the method is that the contour must be star-like with respect to an inner point acquired (or prescribed) beforehand, but this knowledge is a prior for most techniques based on the search of a contour and not of a distribution of pixels, even in free space —[20] is, in electromagnetics, one of the noteworthy exceptions.

In practice, the most feared bottleneck was the calculation tool of the Green's functions and/or of their normal derivatives, since it requires the handling of source points (on the homothetic contour $\hat{\Gamma}$) and/or observation points (on the contour Γ itself) which are moved at each iteration in *a priori* arbitrary fashion.

The hybrid ray-mode technique is very fast but applicable as such only to a rigid bottom. For a penetrable bottom as considered here, complexity is notably increased; a two-step procedure (calculation of nodal values from an array of spectral expansions at several fictitious water wavenumbers with smaller and smaller imaginary parts, and extrapolation to accommodate the zero imaginary part, interpolation to intermediate locations from the nodal values) has been developed, and its success demonstrated for a fluid bottom even for multiply-peaked spectra.

As for the Levenberg-Marquardt solution method, its efficacy will be improved if the derivatives of the cost function with respect to the contour and source coeffi-

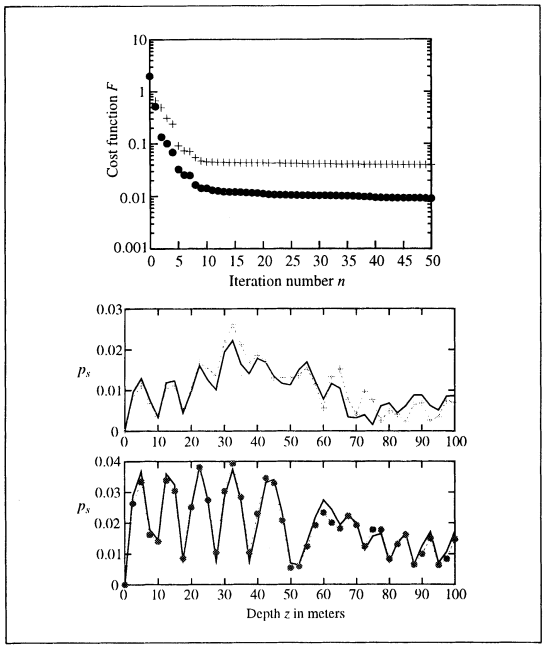

Figure 9. Same configuration as Figure 8 but for the elliptic obstacle only: (i) decrease of the cost function F versus the iteration number for a sound-hard (cross) and a sound-soft (black dot) obstacle (top); (ii) comparison of the exact scattered pressure (plain line) along the $x_R = -40$ m receiver array with those obtained after convergence of the inversion procedure for a sound-hard (middle) and for a sound-soft (bottom) obstacle.

cients were calculated. As of today the analytical calculation has been completed but no numerical implementation has been attempted yet, in particular due to the fact that the second-order derivatives of the Green's function are needed in the Neumann case.

4.2. Perspectives

Difficult problems still need to be addressed. They result either from a more precise modeling of the unperturbed shallow water channel (keeping the hypothesis of range-independent environments), or from a higher material and geometrical complexity of the perturbing obstacle (assumed to be located in full within the water column), or from both.

For example, if the modeling of the sea bottom should not be the present-day main challenge —a layered solid (visco-)elastic bottom will be accommodated via its planar reflection coefficient—, a depth-varying water column would greatly complicate the calculation of the Green's function and its derivatives.

As for the retrieval of the contour of a penetrable fluid-like obstacle in water, we believe it is feasible: it would mean finding out sets of equivalent line sources both inside the obstacle domain (to model the outer wavefield) and outside it (to model the inner wavefield), the continuity of the pressure being the enforced boundary condition. One should refer to [21] for a direct modeling of a simpler electromagnetic case. But we do not know of further example of inversion along this line of thought, e.g., [22] only addresses the retrieval of impenetrable cylinders in free space. But generalization to a solid elastic shell is expected to face both strong theoretical challenges (such as which equivalent sources do we use?) and heavy computational burden.

Other situations are further challenging: Partial burial in a sedimentary layer is a source of evident theoretical difficulties that are linked to the wavefield representation, but the case of an obstacle completely buried in a known superficial layer of the sea bottom should be doable. As for three-dimensional bodies in the water waveguide or in the bottom, the first case to study would be a body of revolution with axis perpendicular to the waveguide walls; one would directly extend in that matter successful free space investigations [17], the cleverest probably being a two-pronged attack, the distributed source method being started from an approximated shape retrieved by the ICDA method [11].

In short, we believe this distributed source approach is promising (provided that a great amount of computer power is available). It has the key advantage to be independent of the wavefield formulation in contrast with many approaches which require explicit boundary integral or domain integral operators to describe the wavefield. It needs, however, a pertinent choice of equivalent sources, which choice can only be partially inferred from theoretical examination in the absence of the proper mathematical machinery in the waveguides; and *de facto* the more complicated the tested configuration, the more this choice is to rely on numerical experimentation and ground truth.

References

[1] R. P. Gilbert, T. Scotti, A. Wirgin, Y. S. Xu: The unidentified object problem in a shallow ocean. Journal of the Acoustical Society of America **103** (1998) 1320–1328.

[2] M. D. Collins, W. A. Kuperman: Inverse problems in ocean acoustics. Inverse Problems **10** (1994) 1023–1040.

[3] P. Gerstoft: Inversion of acoustic data using a combination of genetic algorithms and the Gauss-Newton approach. Journal of the Acoustical Society of America **97** (1995) 2181–2190.

[4] A. Wirgin, T. D. Scotti: Complete family of functions methods, based on the Rayleigh hypothesis and on the extinction theorem, for inverse acoustic wave scattering problems. ACUSTICA - acta acustica **84** (1998) 1083–1090.

[5] C. Rozier, D. Lesselier, T. S. Angell, R. E. Kleinman: Shape retrieval of a cylindrical obstacle immersed in shallow water from single-frequency farfields using a complete family method. Inverse Problems **13** (1997) 487–508.

[6] T. S. Angell, R. E. Kleinman, C. Rozier, D. Lesselier: Uniqueness and complete families for an acoustic waveguide problem. Technical Report 96-4, Center for the Mathematics of Waves, University of Delaware, Newark, 1996.

[7] T. S. Angell, R. E. Kleinman: Radiation condition and uniqueness. Technical Report 97-2, Center for the Mathematics of Waves, University of Delaware, Newark, 1997.

[8] P. Carrion, G. Boehm: Tomographic imaging of opaque and low-contrast objects in range-independent waveguides. Journal of the Acoustical Society of America **91** (1992) 1440–1446.

[9] T. C. Yang, T.-W. Yates: Scattering from an object in a stratified medium. II Extraction of scattering signature. Journal of the Acoustical Society of America **96** (1994) 1020–1031.

[10] D. Guicking, K. Gork, H. Peine: Classification of underwater objects using resonance scattering and neural networks. – In: Underwater Acoustics. A. Alippi, G. B. Canelli (eds.). CNR-IDAC, Rome, 1998, 567–570.

[11] J. L. Buchanan, R. P. Gilbert, A. Wirgin, Y. S. Xu: The unidentified object problem in a shallow ocean with a fluid-like sediment layer overlying a rigid seabed. preprint, LMA, Marseille, 1999.

[12] M. Bocly, M. Lambert, C. Rozier, D. Lesselier: Optimal contour reconstruction of a sound-hard obstacle in a shallow water acoustic waveguide. – In: Underwater Acoustics. A. Alippi, G. B. Canelli (eds.). CNR-IDAC, Rome, 1998, 643–648.

[13] M. Lambert, D. Lesselier, B. Duchêne: On the characterization of obstacles in shallow water using rigorous inversion methods. 1st Workshop on Inverse Problems in Underwater Acoustics, Heraklion, 17-19 May, 1999.

[14] M. Lambert, D. Lesselier: On the retrieval of the plane wave reflection coefficient of a seabed in shallow water. acta acustica **3** (1995) 243–249.

[15] C. Rozier, D. Lesselier: Inversion of a cylindrical vibrating body in shallow water from aspect-limited data using filtered SVD and the L-curve. ACUSTICA - acta acustica **82** (1996) 717–728.

[16] G. V. Frisk, A. V. Oppenheim, D. R. Martinez: A technique for measuring the plane-wave reflection coefficient of the ocean bottom. Journal of the Acoustical Society of America **68** (1980) 602–612.

[17] T. S. Angell, J. Jiang, R. E. Kleinman: A distributed source method for inverse acoustic scattering. Inverse Problems **13** (1997) 531–546.

[18] A. Dutt, V. Rokhlin: Fast Fourier transforms for nonequispaced data. SIAM Journal on Scientific Computing **14** (1993) 1368–1393.

[19] W. D. Murphy, V. Rokhlin, M. S. Vassiliou: Acceleration methods for the iterative solution of electromagnetic scattering problems. Radio Science **28** (1993) 1–12.

[20] S. Bonnard, P. Vincent, M. Saillard: Cross-borehole inverse scattering using a boundary finite-element method. Inverse Problems **14** (1998) 521–534.

[21] Y. Leviatan, Y. Meyouhas: Analysis of electromagnetic scattering from buried cylinders using a multifilament current model. Radio Science **25** (1990) 1231–1244.

[22] J. Tal, Y. Leviatan: Inverse scattering analysis for perfectly conducting cylinders using a multifilament current model. Inverse Problems **6** (1990) 1065–1074.

E

Ensemble de niveaux

[A.10] Shape reconstruction of buried obstacles by controlled evolution of a level set : from a Min Max formulation to numerical experimentation
Christophe Ramananjaona, Marc Lambert, Dominique Lesselier et Jean-Paul Zolésio
Inverse Problems (Special Issue to celebrate Pierre Sabatier's 65th Birthday) **17** 1087-1111 2001

INSTITUTE OF PHYSICS PUBLISHING INVERSE PROBLEMS

Inverse Problems **17** (2001) 1087–1111 www.iop.org/Journals/ip PII: S0266-5611(01)17834-2

Shape reconstruction of buried obstacles by controlled evolution of a level set: from a min–max formulation to numerical experimentation

C Ramananjaona[1], M Lambert[1], D Lesselier[1] and J-P Zolésio[2]

[1] Département de Recherche en Électromagnétisme—Laboratoire des Signaux et Systèmes (CNRS-SUPÉLEC-UPS), Plateau de Moulon, 3, rue Joliot-Curie, 91192 Gif-sur-Yvette Cedex, France

[2] Centre de Mathématiques Appliquées, École des Mines, 2004, Route des Lucioles, BP 93, 06902 Sophia Antipolis Cedex, France

E-mail: christophe.ramananjaona@lss.supelec.fr, marc.lambert@lss.supelec.fr, dominique.lesselier@lss.supelec.fr and jpzoles@cma.inria.fr

Received 6 October 2000, in final form 9 April 2001

Abstract

The nonlinearized reconstruction of the cross-sectional contour of a homogeneous, possibly multiply connected obstacle buried in a half-space from time-harmonic wave field data collected above this half-space in both transverse magnetic (TM) and transverse electric (TE) polarization cases is investigated. The reconstruction is performed via controlled evolution of a level set that was pioneered by Litman *et al* (Litman A, Lesselier D and Santosa F 1998 *Inverse Problems* **14** 685–706) but at this time restricted to free space for TM data collected all around the sought obstacle. The main novelty of the investigation lies in the following points: from the rigorous contrast-source domain integral formulation (TM) and integral–differential formulation (TE) of the direct scattering problems in the buried obstacle configuration, and from appropriately cast adjoint scattering problems, we demonstrate, by processing min–max formulations of an objective functional J made of the data error to be minimized, that its derivatives with respect to the evolution time t are given in closed form. They are contour integrals involving the normal component of the velocity field of evolution times the product of direct and adjoint fields (TM), or of the scalar product of gradients of such fields (TE) at t. This approach only calls for the analysis of the well posed direct and adjoint scattering problems formulated from the TM and TE Green systems of the unperturbed layered environment and, unusually, it avoids the differentiation of state fields. Other contributions of the paper come from exhibiting and analysing via comprehensive numerical experimentation how and under which conditions evolutions of level sets involving velocities opposite to shape gradients perform in demanding configurations including two disjoint obstacles, constitutive materials strongly less or more refractive than the embedding material, aspect-limited and noisy monochromatic data, in the severe TE case as well as in the more menial TM case. A comparison with a binary-specialized modified-

0266-5611/01/041087+25$30.00

gradient solution method is also led for several, more and more lossy embedding half-spaces. Rules of thumb for effectiveness of the inversions and pending theoretical and computational questions are outlined in conclusion.

(Some figures in this article are in colour only in the electronic version; see `www.iop.org`)

1. Introduction

Our general problem is the nonlinearized reconstruction of the two-dimensional cross-sectional shape of a cylindrical obstacle, denoted as Ω, buried in a given (lower) half-space, using a finite number of monochromatic electric or magnetic current line sources (they radiate known primary wave fields with transverse electric (TE) or transverse magnetic (TM) polarization) and a finite number of sensors (they collect discrete values of the scattered field resulting from the interaction of the perturbed environment with the primary signals: for example, along a certain probing line), all sources and sensors being placed in the other (upper) half-space.

Further simplification comes from the assumption that this obstacle is homogeneous (a so-called binary obstacle) and is made of a known material: this enables us to prescribe its electric contrast with respect to the host half-space beforehand (all materials being assumed to be of linear, isotropic and non-magnetic behaviour for simplification). However, the cross section Ω is arbitrary save some smoothness of its contour Γ to be hypothesized in order to carry out some formal calculations, and, more importantly, might be singly connected as well as multiply connected. That is, one single isolated obstacle as well as several isolated ones (possibly hollow) might be buried in the half-space, whilst no interior point is prescribed beforehand (to construct, for example, star-shaped contours). Therefore, most of the topological information available in the shape reconstruction is reduced to that Ω be located inside some known box $\mathcal{D}$ which itself is fully included in the lower half-space, and is from now on taken as a fixed search domain.

Stated as such, the scenario remains somewhat ideal with respect to real-world situations of which it only intends to be a preliminary model, those including Earth subsurface imaging, radar ground probing, non-destructive and evaluation of man-made structures, and underwater acoustics also by paralleling electromagnetic and acoustic investigations (although our scenario is canonical enough not to be too dependent on particular geometries and material parameters).

However, finding a proper solution, even without any linearization of forward and inverse scattering problems, as done here—which is in itself challenging due to the severe ill posedness resulting from the availability of only aspect-limited data and lack of crucial topological information—is believed to be worthwhile to the theoretician and the practitioner alike, while the challenges to be overcome are illustrative of those to be faced at any application stage. More on the topic of reconstruction of buried obstacles is available in recent research contributions by the authors and colleagues: see, for example, (Souriau *et al* 1996, Lambert *et al* 1998, Lambert and Lesselier 2000a) and references therein.

The above three papers are focused on modified-gradient solution methods and binary-constrained versions, which all belong to the replete family of gradient methods (see the thoughtful analysis in van den Berg and Kleinman (1997)) and are intended to build up maps of the distribution of constitutive parameters (permittivity and/or conductivity, or speed of sound, in practice) throughout the search domain $\mathcal{D}$ without explicit design of the contour of the obstacles' cross sections.

Here, we take a different point of view and focus on the so-called controlled evolution of level sets that was proposed in Litman *et al* (1998) in order to solve an inverse scattering

problem posed in free space and in the TM polarization case only. This method is a combination of two methods: (i) a level set representation of shapes (for a general overview of powerful level set representations and their ever-growing range of applications, see Sethian (1999)) inside an inversion algorithm as was pioneered in Santosa (1996), which is to be evolved in pseudo-time t at a certain velocity according to a Hamilton–Jacobi-type equation; (ii) the speed or velocity method for shape optimal design and control (for a comprehensive investigation see Sokołowski and Zolésio (1992)) that aims at a monotonic decrease of an objective functional J in time t from the flow of a certain velocity of deformation of the shape contour (which for us will be the level set 0). The purpose of our investigation is then twofold.

Firstly, we demonstrate that mathematically sound processing of a min–max formulation of an objective functional J made of the data error to be minimized directly yields closed form expressions of its derivatives with respect to the evolution time t. These derivatives are given as contour integrals whose integrands involve the normal component of the velocity field times the normal component of a 'shape gradient' which is equal to the product of direct and adjoint fields (TM), or to the scalar product of their gradients (TE) at this t.

The analysis—which calls for involved theoretical material concerning min–max differentiability described, for example, in Cuer and Zolésio (1988)—makes good use of the fact that well posed direct and adjoint scattering problems can be cast from the TM and TE Green systems of the unperturbed layered environment using rigorous integral (TM) or integral–differential (TE) formulations; and, unusually, it avoids differentiation of the state fields—and as was done inside a rather cumbersome variational framework in Litman *et al* (1998).

As such, the analysis holds true in the buried configuration (and evidently in free space) and for both TM and TE polarization cases. It naturally retrieves the earlier TM free-space results while providing wholly new results in the TE case. And it is believed to be of good novelty in applications to scattering—in addition to having much potential for generalization to three-dimensional configurations (Monebhurrun *et al* 1999), since those enjoy exact Green-based (dyadic) formulations that can be treated similarly through a min–max.

Secondly, we show and analyse via comprehensive numerical experimentation how and under which conditions evolutions of level sets involving velocities that are simply opposite to the shape gradients perform in the complicated TE case as well as in the more menial TM case—without a specific regularization apparatus, in contrast to Dorn *et al* (2000)—and in rather demanding configurations. The latter include two disjoint obstacles, constitutive materials strongly less (voids) or more refractive (up to relative permittivities of 8, this value not being an upper bound) than the host material, aspect-limited and noisy monochromatic data, the influence of frequency hopping (i.e. the successive use of data at several frequencies) being considered in addition. A comparison with the binary-specialized modified-gradient method developed earlier (Lambert and Lesselier 2000a) is also carried out for several, more and more embedding half-spaces in the TE case; this highlights the ability of the approach to retrieve inclusions in conductive media where the field decays with depth, and illustrates the effectiveness of two methods that both use, though in their distinctive ways, the binary aspect of the sought obstacles.

The paper is organized as follows. The theoretical analysis is focused upon in section 2, most of the work being on the proper introduction and subsequent manipulation of the min–max formulation. In section 3 the discrete implementation of the method (in particular, caring for the peculiarities of the TE case) and the illustrative numerical results are discussed in some detail. Rules of thumb for effectiveness of the inversions and pending theoretical and computational questions are outlined in section 4.

Complementary material is found in Ramananjaona *et al* (2000), where it is illustrated

how laboratory-controlled experimental data in the microwave regime are inverted by the level set method and provide the shape of dielectric and conductive objects placed in an anechoic chamber and illuminated and seen by linearly polarized horn antennas in the far field (in particular, this shows that non-ideal sources and sensors and far fields can easily be dealt with); more on that demanding issue (Ramananjaona *et al* 2001a) will appear in a forthcoming special section on real data of *Inverse Problems* devoted to an international confrontation of inversion methods. The short contribution of Zolésio *et al* (1998) points out how merging and splitting during the evolution, which naturally occurs in the discrete setting as is exhibited here in a novel situation, requires generalization of the usual flow mapping theory. As for the necessary issue of regularization of the level set evolution from prior information, this is dealt with in Ramananjaona *et al* (2001b). In addition, one should certainly consider the considerable work recently reported by Dorn *et al* (2000) from a similar starting point (level set representation of shapes and optimal deformation of them) on cross-borehole 2D electromagnetic tomography (in a TM case only); the retrieval of perfectly conducting targets (in a free-space TM case only) proposed by Ferrayé *et al* (2000) is also a valuable contribution.

Finally, let us note that no attempt has been made herein to cover the several solution methods that amount to finding the contour of a generally singly connected and star-shaped obstacle with known acoustic or electromagnetic boundary condition by a proper optimization within some prescribed class of admissible contours. Numerical experimentation to highlight the advantages and disadvantages of such methods with respect to those of the *topology-free* method of retrieval proposed here has not been attempted either as it is similarly felt to be beyond the scope of our paper—but the aforementioned special section should provide the wave field inversion community with a rare opportunity to compare methods on common data sets. Nevertheless, such a contour identification method, involving a complete family representation of the field, is detailed in Lambert and Lesselier (2000b) for an impenetrable obstacle immersed in a semi-confined embedding space (a shallow-water waveguide with penetrable bottom), and appropriate references can be found therein—the method has not yet been extended to a penetrable obstacle. Also, the insightful coverage of direct and inverse scattering by obstacles made by Kress (2001) provides much needed theoretical material whilst pointing to many other references on inversion (mostly in that framework).

2. The theoretical analysis

2.1. TM and TE formulations of the direct wave field

The geometrical and electric configuration of interest is illustrated in figure 1. A homogeneous dielectric cylindrical obstacle of axis parallel to the z axis, having possibly multiply connected cross-sectional shape Ω, and whose any constitutive parts should be of smooth enough contour and remain strictly contained within the prescribed box $\mathcal{D}$, is fully buried in a homogeneous dielectric lower half-space (numbered 2). The latter is separated by a planar interface x–z from the upper half-space (numbered 1).

All constitutive materials are assumed linear, isotropic and non-magnetic (permeability μ_0). Their known permittivities read as $\varepsilon_m = \varepsilon_0 \varepsilon_{rm}$, $m = 1, 2, \Omega$, at implied circular frequency ω—omitting the time dependence $\exp(-\mathrm{j}\omega t)$—where ε_0 is the permittivity of the upper half-space assumed to be air (i.e. $\varepsilon_{r1} = 1$), and where both ε_{r2} and $\varepsilon_{r\Omega}$ might take frequency-dependent, complex values with positive or null imaginary parts (for example, via a conductivity contribution). Corresponding propagation constants k_m are such that $k_m^2 = \omega^2 \mu_0 \varepsilon_m$ with positive or null imaginary parts. The electrical contrast function $\chi(\boldsymbol{r})$ defined in $\mathcal{D}$ and whose value depends upon the polarization of the wave field is also introduced.

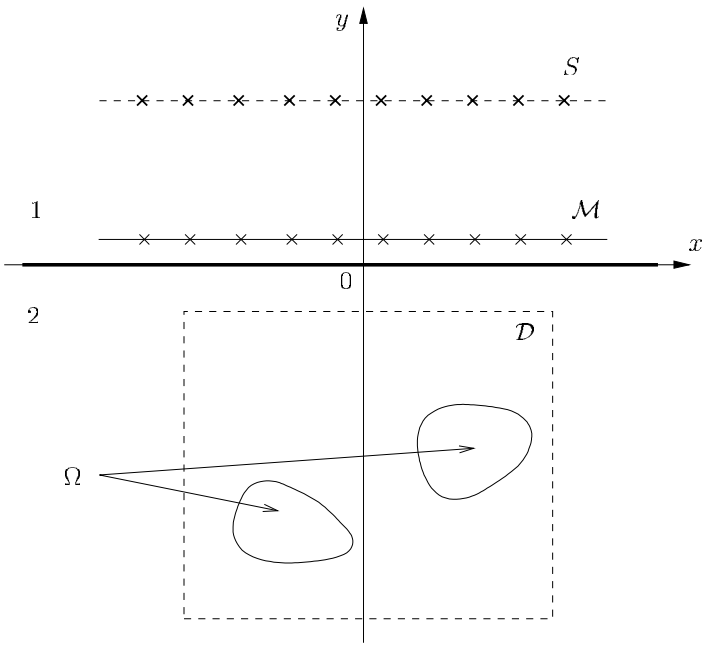

Figure 1. Geometrical and electrical configuration under study. All the following figures display the results within the search domain $\mathcal{D}$ only, the global orientation—interface at the top—being retained.

For any $\boldsymbol{r}$ in Ω, $\chi(\boldsymbol{r})$ is constant-valued and is set equal to $\eta = \frac{\varepsilon_\Omega}{\varepsilon_2} - 1$ in the TM case, and to $\eta = 1 - \frac{\varepsilon_2}{\varepsilon_\Omega}$ in the TE case; in the exterior domain the contrast function is simply reduced to 0 in both cases.

Ideal time-harmonic electric current line sources S_j ($j = 1, \ldots, N_s$) set parallel to the z axis (TM polarization case) or their magnetic counterparts (TE polarization case) are placed strictly above the interface x–z. Similarly ideal sensors are also placed above the interface and they collect the single z component of the scattered electric field E^{scat} or magnetic field H^{scat} at N_r locations. For simplicity—this does not restrict the scope of the forthcoming theoretical analysis—we henceforth assume the existence of a certain probing line $\mathcal{M}$ at constant height y_r along which the sensors are equally distributed, while the sources are also taken to be equally distributed at constant height y_s.

For notational simplicity we denote as u, u^{inc} and u^{scat} the single z components of the total, incident and scattered field, be they of electric nature (TM case) or of magnetic nature (TE case); recall that the incident field is due to the chosen source radiating at ω in the unperturbed environment—no obstacle within the lower half-space—and accounts for the layering. The data field collected in the measurement domain $\mathcal{M}$ will be denoted as ζ. Subscript j will emphasize, if necessary, that the corresponding source is S_j.

By application of the Green theorem to the Helmholtz wave equations that are satisfied by the field u and by accounting for the appropriate TM and TE transmission conditions at the flat interface and at the contour(s) of the obstacle, and Sommerfeld radiation conditions at infinity in both half-spaces, rigorous state equations (1) and (3), and their companion data equations, (2) and (4), are obtained. They read in the TM case as

$$u(\boldsymbol{r}) = u^{\text{inc}}(\boldsymbol{r}) + \int_{\mathcal{D}} \mathrm{d}\boldsymbol{r}'\, \chi(\boldsymbol{r}')\, G_{22}(\boldsymbol{r}, \boldsymbol{r}')\, u(\boldsymbol{r}'), \qquad \boldsymbol{r} \in \mathcal{D}, \tag{1}$$

and

$$u^{\text{scat}}(\boldsymbol{r}) = \int_{\mathcal{D}} \mathrm{d}\boldsymbol{r}'\, \chi(\boldsymbol{r}')\, G_{12}(\boldsymbol{r}, \boldsymbol{r}')\, u(\boldsymbol{r}'), \qquad \boldsymbol{r} \in \mathcal{M}. \tag{2}$$

In the TE case (see, for example, Lambert *et al* (1998)) they retain a somewhat more complicated form:

$$u(\boldsymbol{r}) = u^{\text{inc}}(\boldsymbol{r}) + \int_{\mathcal{D}} \mathrm{d}\boldsymbol{r}'\, \chi(\boldsymbol{r}') \left[\nabla' G_{22}(\boldsymbol{r}, \boldsymbol{r}') \cdot \nabla' u(\boldsymbol{r}')\right], \qquad \boldsymbol{r} \in \mathcal{D}, \tag{3}$$

and

$$u^{\text{scat}}(\boldsymbol{r}) = \int_{\mathcal{D}} \mathrm{d}\boldsymbol{r}'\, \chi(\boldsymbol{r}') \left[\nabla' G_{12}(\boldsymbol{r}, \boldsymbol{r}') \cdot \nabla' u(\boldsymbol{r}')\right], \qquad \boldsymbol{r} \in \mathcal{M} \tag{4}$$

where the two-component ∇' operator is taken with respect to the primed variables.

The domain integral formulation (TM case) and the domain integral–differential formulation (TE case) both correspond to well posed direct scattering problems whose fields are in $H^1(\mathcal{D})$ due to assumptions of finite energy. Concerning wellposedness, see Colton and Kress (1983) in free space or Petry (1995) in a planar-layered host medium, the demonstration in the TE case, using the particular scalar field formulation used here, not being developed as such in the literature, as noted earlier (Lambert and Lesselier 2000a). Let us mention that proofs appear to require that the contour of the obstacle (as has already been said, there may be several parts) satisfies a Lyapunov condition, which is in practice far from restrictive, whilst (see Petry (1995)) the assumption of a scatterer embedded fully inside one single layer (here, this is the lower half-space) is standard simplification.

A key but canonical step of the proofs is the definition of well behaved systems of Green functions G of the plane-layered environment. These systems, which are polarization dependent, take different values as a function of the respective locations of source point and observation points in either half-space: in effect four Green functions $G_{mn}(\boldsymbol{r}, \boldsymbol{r}')$ are of interest for each polarization case, which model the radiation of a source at $\boldsymbol{r}'$ in the half-space n and the observation of the field at $\boldsymbol{r}$ in the half-space m, where $m = 1, 2$, $n = 1, 2$. Among other properties they satisfy reciprocity (Tai 1993), of which much use will be made in the forthcoming theoretical analysis: $G_{mn}(\boldsymbol{r}, \boldsymbol{r}') = G_{nm}(\boldsymbol{r}', \boldsymbol{r})$ and $\frac{1}{\varepsilon_m} G_{mn}(\boldsymbol{r}, \boldsymbol{r}') = \frac{1}{\varepsilon_n} G_{nm}(\boldsymbol{r}', \boldsymbol{r})$ in the TM and TE cases, respectively. (The above involves that (1) and (3) have unique solutions u in $H^1(\mathcal{D})$; this will be used below.)

2.2. Controlled evolution and min–max formulation: preliminary elements

As already mentioned, the level set representation (Sethian 1999) puts emphasis on the evolution as a function of a (pseudo-)time t of a level set function ϕ. The latter is valued everywhere in time $t \geqslant 0$ and space $\boldsymbol{r}$ within $\mathcal{D}$ (taking a user's prescribed value ϕ_0 at $t = 0$). Its zero level at time t is but the contour of the homogeneous (multiply connected) obstacle retrieved at this t, negative values of the level set function then corresponding to interior points of the obstacle. To evolve the level set, a certain velocity field $\boldsymbol{V}$ is defined throughout $\mathcal{D}$, the evolution then proceeding from the satisfaction of a Hamilton–Jacobi-type equation

$$\frac{\partial}{\partial t}\phi(t, \boldsymbol{r}) + \boldsymbol{V}(t, \boldsymbol{r}) \cdot \boldsymbol{n}\, |\nabla \phi(t, \boldsymbol{r})| = 0, \qquad \boldsymbol{r} \in \mathcal{D}, \tag{5}$$

which readily follows from differentiating the equation of the level contour $\phi = \text{cte}$ using the relationships $\frac{\partial}{\partial t}\boldsymbol{r} = \boldsymbol{V}(t, \boldsymbol{r})$ and $\boldsymbol{n} = \nabla\phi/|\nabla\phi|$, where $\boldsymbol{n}$ is the unit normal to the said contour.

Any such evolution, to be effective in terms of the solution of the inverse scattering problem at hand, should ensure the decrease at increasing time, by making a suitable choice of the velocity field $\boldsymbol{V}$, of a certain objective functional $J\,(t)$, the latter being characteristic in some sense of the discrepancy of the true obstacle with the one retrieved at time t (Santosa 1996).

On the other hand, the speed or velocity method (Sokołowski and Zolésio 1992) states that a domain Ω can be optimized under some mild conditions from an initial domain Ω_0 if one is able to build up a transformation T_t from $t = 0$ to ∞, which is one-to-one mapping $\mathcal{D}$ onto $\mathcal{D}$—leaving the boundary of $\mathcal{D}$ unchanged—such that $\Omega_t = T_t(\Omega_0)$, and ensuring that $\frac{\mathrm{d}J}{\mathrm{d}t}$ is negative or null. This transformation of domains T_t, which can be seen also as yielding the characteristic function χ_t (valued to η inside and 0 outside) of Ω_t, is equivalently defined from the flow of a velocity field of deformation $\boldsymbol{V}(t, \boldsymbol{r})$, $\boldsymbol{r} \in \mathcal{D}$. Its choice relies on the calculation of the derivative with respect to the parameter t of the objective functional J, or equivalently on the calculation of a shape gradient $\boldsymbol{G}$ at Ω_t. (In effect, only normal components $V = \boldsymbol{V} \cdot \boldsymbol{n}$ and $g = \boldsymbol{G} \cdot \boldsymbol{n}$ valued on Γ_t ($\Gamma_t = \partial\Omega_t$) will matter.)

Combining both methods, as proposed by Litman *et al* (1998), boils down to enforcing a velocity field orthogonal to the level contours of ϕ in the evolution equation (5) that ensures a decrease of J, which velocity field the above speed method yields along the boundary of Ω_t, i.e. along the zero level set. It suffices to heuristically extend this velocity field throughout $\mathcal{D}$ to be able to evolve the whole level set (accordingly to (5)) and get (in principle) a fitter obstacle contour on which to apply the speed method again, and so on until some criterion is met (for example, small or plateauing J).

How to perform the evolution in the numerical practice on a fixed space grid at successive discrete time steps is considered in the next section somewhat briefly, since most of that analysis parallels the one carried out in Litman *et al* (1998) once the peculiarities of the geometry (buried obstacle) and polarization state (notably the involved TE case) are accounted for.

The focus below is mostly on the calculation of the time derivative, $\frac{\mathrm{d}J}{\mathrm{d}t}$, of the objective function via a min–max formulation. The crucial point here is that the latter allows us to avoid having to differentiate the state field, and to introduce material derivatives and the like, as is usually done in design problems and as was done within a rather cumbersome variational analysis in Litman *et al* (1998) in the simpler TM free-space situation. There are two main steps:

(i) We cast the objective functional J as a min–max functional $\mathcal{L}$ parametrized by t whose saddle points will be shown to consist of the unique pair of solutions of the state problem and its corresponding adjoint problem.

(ii) We make good use of rich differentiability analysis (Cuer and Zolésio 1988) which, in particular, states that $\frac{\mathrm{d}J}{\mathrm{d}t}$ under mild conditions is simply equal to the partial time derivative $\frac{\partial \mathcal{L}}{\partial t}$ of the min–max functional at the saddle point, so as to arrive at a closed-form expression of $\frac{\mathrm{d}J}{\mathrm{d}t}$—that reduces in the TM free-space situation to the one given earlier (Litman *et al* 1998)—and provide the shape gradients, as is necessary.

The starting point is the objective functional J. The simplest choice (constraints in terms of shape or of field variations might be added to it) is to consider the discrepancy between the collected data ζ and the field u^{scat} that would be scattered by the evolved obstacle: one uses the square norm of the residual of the data equation—for one implied source S_j of given polarization—the discrete value of which will be made of the corresponding field discrepancies at the N_r sensors. (When the whole set of N_s sources is employed the objective function becomes the sum of N_s individual objective functionals.) J reads as

$$J = \tfrac{1}{2} \| u^{\mathrm{scat}}\,(\boldsymbol{r}) - \zeta\,(\boldsymbol{r}) \|^2_{L^2(\mathcal{M})}. \tag{6}$$

Casting that functional J as the min–max of a Lagrangian functional $\mathcal{L}$, one has

$$J = \min_{w_r \in H^1(D)} \min_{w_i \in H^1(D)} \max_{\varphi_r \in H^1(D)} \max_{\varphi_i \in H^1(D)} \mathcal{L}, \tag{7}$$

where $w_r + \mathrm{j}w_i$ is the complex-valued state field and $\varphi = \varphi_r + \mathrm{j}\varphi_\mathrm{i}$ is the complex-valued adjoint field, the functional being convex with respect to w and concave with respect to φ. It remains to construct the saddle points of $\mathcal{L}$, i.e. the set of real-valued functions of space $(w_r, w_i, \varphi_r, \varphi_i) \in (H^1(\mathcal{D}))^4$ such that

$$\frac{\partial \mathcal{L}}{\partial w_r} = 0, \qquad \frac{\partial \mathcal{L}}{\partial w_i} = 0, \qquad \frac{\partial \mathcal{L}}{\partial \varphi_r} = 0, \qquad \frac{\partial \mathcal{L}}{\partial \varphi_i} = 0. \tag{8}$$

However, any complex field, say, $z = z_r + \mathrm{j}z_i$, is written versus z and its conjugate $\bar{z}$ as well (Brandwood 1983). So, letting the complex partial derivative of a real-valued functional $(\mathcal{L})$ with respect to the complex-valued variable (z) be

$$\frac{\partial \mathcal{L}}{\partial z} = \frac{1}{2}\left(\frac{\partial \mathcal{L}}{\partial z_r} - \mathrm{j}\frac{\partial \mathcal{L}}{\partial z_i}\right), \tag{9}$$

the following equivalences hold true:

$$\frac{\partial \mathcal{L}}{\partial w} = 0 \quad \Longleftrightarrow \begin{cases} \dfrac{\partial \mathcal{L}}{\partial w_r} = 0, \\ \dfrac{\partial \mathcal{L}}{\partial w_i} = 0; \end{cases} \tag{10}$$

$$\frac{\partial \mathcal{L}}{\partial \varphi} = 0 \quad \Longleftrightarrow \begin{cases} \dfrac{\partial \mathcal{L}}{\partial \varphi_r} = 0, \\ \dfrac{\partial \mathcal{L}}{\partial \varphi_i} = 0. \end{cases} \tag{11}$$

This enables us to study the variations of $\mathcal{L}$ as a function of the variations of the pair of complex-valued fields w and φ only, since it would easily be proven that working with the pair of conjugates $\bar{w}$ and $\bar{\varphi}$—assumed to be independent from the original pair—yields the same results as the ones obtained below.

2.3. Calculation of the derivative of the objective function in the TM case

Let us now investigate the TM case more closely. The chosen Lagrangian $\mathcal{L}$ in (7) which one is associating to the objective functional (6) in the TM polarization reads as

$$\begin{aligned} \mathcal{L}(t, w, \bar{w}, \varphi, \bar{\varphi}) = {} & \tfrac{1}{2}\int_{\mathcal{M}} \left| \int_{\mathcal{D}} \chi_t(\boldsymbol{r}') G_{12}(\boldsymbol{r}, \boldsymbol{r}') w(\boldsymbol{r}')\, \mathrm{d}\boldsymbol{r}' - \zeta(\boldsymbol{r}) \right|^2 \mathrm{d}\boldsymbol{r} \\ & + \mathrm{Re} \int_{\mathcal{D}} \left(w(\boldsymbol{r}) - u^{\mathrm{inc}}(\boldsymbol{r}) - \int_{\mathcal{D}} \chi_t(\boldsymbol{r}') G_{22}(\boldsymbol{r}, \boldsymbol{r}') w(\boldsymbol{r}')\, \mathrm{d}\boldsymbol{r}' \right) \varphi(\boldsymbol{r})\, \mathrm{d}\boldsymbol{r}. \end{aligned} \tag{12}$$

The following proposition holds.

Proposition. *The Lagrangian $\mathcal{L}$ given by (12) has a unique saddle point* $(t, u, \bar{u}, \psi, \bar{\psi})$.

Indeed, the saddle point is characterized by an optimality condition that holds with respect to the four variables $w, \bar{w}, \varphi, \bar{\varphi}$. It is unique if and only if the equations derived from the optimality condition have unique solutions.

Let us consider first the solution of the equation relevant to w. Making use of the aforementioned reciprocity relationships, one easily arrives at

$$\left\langle \frac{\partial \mathcal{L}}{\partial w}, v \right\rangle = 0 \iff \frac{1}{2}\int_{\mathcal{D}} v(\boldsymbol{r})\Bigg[\chi_t(\boldsymbol{r})\int_{\mathcal{M}} \Theta(\boldsymbol{r}')G_{21}(\boldsymbol{r},\boldsymbol{r}')\,\mathrm{d}\boldsymbol{r}' + \varphi(\boldsymbol{r}) - \chi_t(\boldsymbol{r})\int_{\mathcal{D}} G_{22}(\boldsymbol{r},\boldsymbol{r}')\varphi(\boldsymbol{r}')\,\mathrm{d}\boldsymbol{r}'\Bigg]\mathrm{d}\boldsymbol{r} = 0, \qquad \forall\, v \in H^1(\mathcal{D}), \tag{13}$$

where one has denoted the conjugated difference between the scattered field and the data, $\overline{u^{\mathrm{scat}}(\boldsymbol{r}) - \zeta(\boldsymbol{r})}$, as $\Theta(\boldsymbol{r})$ for brevity. Thus, $\forall \boldsymbol{r} \in \mathcal{D}$, the saddle point should be such that

$$\chi_t(\boldsymbol{r})\int_{\mathcal{M}} \Theta(\boldsymbol{r}')G_{21}(\boldsymbol{r},\boldsymbol{r}')\,\mathrm{d}\boldsymbol{r}' + \psi(\boldsymbol{r}) - \chi_t(\boldsymbol{r})\int_{\mathcal{D}} G_{22}(\boldsymbol{r},\boldsymbol{r}')\psi(\boldsymbol{r}')\,\mathrm{d}\boldsymbol{r}' = 0. \tag{14}$$

From the binary definition of χ_t this equation involves $\psi = 0, \forall \boldsymbol{r} \in \mathcal{D} \setminus \bar{\Omega}_t$. Proceeding with the change of variable $\psi = -\chi_t p$ in (14) yields, $\forall \boldsymbol{r} \in \Omega_t$,

$$\int_{\mathcal{M}} \Theta(\boldsymbol{r}')G_{21}(\boldsymbol{r},\boldsymbol{r}')\,\mathrm{d}\boldsymbol{r}' - p(\boldsymbol{r}) + \int_{\mathcal{D}} G_{22}(\boldsymbol{r},\boldsymbol{r}')\chi_t(\boldsymbol{r}')p(\boldsymbol{r}')\,\mathrm{d}\boldsymbol{r}' = 0. \tag{15}$$

The domain integral equation (15) satisfied by p would actually be the same as the state equation (1) satisfied by the field u, if the impinging wave was generated by a Dirac distribution of sources, $\Theta\delta_M$. The underlying adjoint scattering problem is, therefore, similarly well posed and the adjoint field $p \in H^1(\mathcal{D})$ is unique—it is as usual generated by a (electrical density of) source confined to the probing line and its amplitude Θ is the conjugate of the discrepancy between the scattered field, u^{scat}, and the field effectively collected, ζ.

(Writing down the Helmholtz wave equations satisfied by p, using the necessary transmission and radiation conditions, and applying the Green theorem, would demonstrate that p indeed satisfies this domain integral equation but there seems no need to do so in view of the existing material.)

As for φ, one has

$$\left\langle \frac{\partial \mathcal{L}}{\partial \varphi}, v \right\rangle = 0 \iff \frac{1}{2}\int_{\mathcal{D}} v(\boldsymbol{r})\Bigg(w(\boldsymbol{r}) - u^{\mathrm{inc}}(\boldsymbol{r}) - \int_{\mathcal{D}} \chi_t(\boldsymbol{r}')G_{22}(\boldsymbol{r},\boldsymbol{r}')w(\boldsymbol{r}')\,\mathrm{d}\boldsymbol{r}'\Bigg)\mathrm{d}\boldsymbol{r} = 0, \qquad \forall\, v \in H^1(\mathcal{D}). \tag{16}$$

Thus, $\forall \boldsymbol{r} \in \mathcal{D}$,

$$u(\boldsymbol{r}) - u^{\mathrm{inc}}(\boldsymbol{r}) - \int_{\mathcal{D}} \chi_t(\boldsymbol{r}')G_{22}(\boldsymbol{r},\boldsymbol{r}')u(\boldsymbol{r}')\,\mathrm{d}\boldsymbol{r}' = 0, \tag{17}$$

which is the state equation satisfied by the field (1), of known unique solution $u \in H^1(\mathcal{D})$.

Similar results are obtained with the conjugated pair of state and adjoint fields. So the equations that describe the optimality condition of the Lagrangian have unique solutions and the saddle point is unique. Now it remains to validate the following proposition.

Proposition. *The derivative of the objective functional in the TM polarization case is*

$$\frac{\mathrm{d}J}{\mathrm{d}t} = \mathrm{Re}\int_{\Gamma_t} \eta u(s)p(s)\boldsymbol{V}(s)\cdot\boldsymbol{n}\,\mathrm{d}s. \tag{18}$$

$\boldsymbol{V}$ is, as usual, the velocity of deformation. Dependence upon t of the considered field quantities is made implicit for notational simplicity (the relationship holds at any t). Indeed, the results shown in Cuer and Zolésio (1988) lead us to

$$\frac{\mathrm{d}J}{\mathrm{d}t} = \frac{\partial \mathcal{L}}{\partial t}(t, u, \bar{u}, \psi, \bar{\psi}). \tag{19}$$

As the characteristic function χ_t is the only quantity to be differentiated with respect to t in the following formulae, and again making use of reciprocity, this successively yields (with $\Theta = \overline{u^{\text{scat}} - \zeta}$)

$$\frac{\mathrm{d}J}{\mathrm{d}t} = \mathrm{Re}\left[\int_{\mathcal{M}} \overline{\left(\int_{\mathcal{D}} \chi_t(\boldsymbol{r}')G_{12}(\boldsymbol{r},\boldsymbol{r}')u(\boldsymbol{r}')\,\mathrm{d}\boldsymbol{r}' - \zeta(\boldsymbol{r})\right)} \times \frac{\partial}{\partial t}\left(\int_{\mathcal{D}} \chi_t(\boldsymbol{r}')G_{12}(\boldsymbol{r},\boldsymbol{r}')u(\boldsymbol{r}')\,\mathrm{d}\boldsymbol{r}' - \zeta(\boldsymbol{r})\right)\right]\mathrm{d}\boldsymbol{r} - \mathrm{Re}\int_{\mathcal{D}} \frac{\partial}{\partial t}\left(\int_{\mathcal{D}} \chi_t(\boldsymbol{r}')G_{22}(\boldsymbol{r},\boldsymbol{r}')u(\boldsymbol{r}')\,\mathrm{d}\boldsymbol{r}'\right)\psi(\boldsymbol{r})\,\mathrm{d}\boldsymbol{r} \tag{20}$$

$$\frac{\mathrm{d}J}{\mathrm{d}t} = \mathrm{Re}\int_{\mathcal{M}} \Theta(\boldsymbol{r})\int_{\Gamma_t} \eta G_{12}(\boldsymbol{r},s)u(s)\boldsymbol{V}(s)\cdot\boldsymbol{n}\,\mathrm{d}s\,\mathrm{d}\boldsymbol{r} - \mathrm{Re}\int_{\mathcal{D}}\left(\int_{\Gamma_t} \eta G_{22}(\boldsymbol{r},s)u(s)\boldsymbol{V}(s)\cdot\boldsymbol{n}\,\mathrm{d}s\right)\psi(\boldsymbol{r})\,\mathrm{d}\boldsymbol{r} \tag{21}$$

$$\frac{\mathrm{d}J}{\mathrm{d}t} = \mathrm{Re}\int_{\Gamma_t} \eta u(s)\left[\int_{\mathcal{M}} \Theta(\boldsymbol{r})G_{21}(s,\boldsymbol{r})\,\mathrm{d}\boldsymbol{r} - \int_{\mathcal{D}} G_{22}(s,\boldsymbol{r})\psi(\boldsymbol{r})\,\mathrm{d}\boldsymbol{r}\right]\boldsymbol{V}(s)\cdot\boldsymbol{n}\,\mathrm{d}s. \tag{22}$$

However, since $\forall \boldsymbol{r} \in \mathcal{D}$, $\psi = -\chi_t p$,

$$\frac{\mathrm{d}J}{\mathrm{d}t} = \mathrm{Re}\int_{\Gamma_t} \eta u(s)\left[\int_{\mathcal{M}} \Theta(\boldsymbol{r})G_{21}(s,\boldsymbol{r})\,\mathrm{d}\boldsymbol{r} + \int_{\mathcal{D}} G_{22}(s,\boldsymbol{r})\chi_t(\boldsymbol{r})p(\boldsymbol{r})\,\mathrm{d}\boldsymbol{r}\right]\boldsymbol{V}(s)\cdot\boldsymbol{n}\,\mathrm{d}s, \tag{23}$$

and one arrives at the sought relationship.

Let us emphasize that other Lagrangian functionals lead to the same conclusion. Indeed, one can write them (including the one used so far) in a general form as

$$\mathcal{L}(t,w,\bar{w},\varphi,\bar{\varphi}) = \tfrac{1}{2}\int_{\mathcal{M}}\left|\int_{\mathcal{D}} \chi_t(\boldsymbol{r}')G_{12}(\boldsymbol{r},\boldsymbol{r}')w(\boldsymbol{r}')\,\mathrm{d}\boldsymbol{r}' - \zeta(\boldsymbol{r})\right|^2\mathrm{d}\boldsymbol{r} + \alpha\mathrm{Re}\int_{\mathcal{D}}\left(w(\boldsymbol{r}) - u^{\text{inc}}(\boldsymbol{r}) - \int_{\mathcal{D}} \chi_t(\boldsymbol{r}')G_{22}(\boldsymbol{r},\boldsymbol{r}')w(\boldsymbol{r}')\,\mathrm{d}\boldsymbol{r}'\right)\varphi(\boldsymbol{r})\,\mathrm{d}\boldsymbol{r} + \beta\mathrm{Im}\int_{\mathcal{D}}\left(w(\boldsymbol{r}) - u^{\text{inc}}(\boldsymbol{r}) - \int_{\mathcal{D}} \chi_t(\boldsymbol{r}')G_{22}(\boldsymbol{r},\boldsymbol{r}')w(\boldsymbol{r}')\,\mathrm{d}\boldsymbol{r}'\right)\varphi(\boldsymbol{r})\,\mathrm{d}\boldsymbol{r}, \tag{24}$$

letting α and β be arbitrary constants in $\mathbb{R}$. Since

$$\alpha z_r + \beta z_i = \tfrac{1}{2}[\alpha(z+\bar{z}) - \mathrm{j}\beta(z-\bar{z})] = \tfrac{1}{2}[(\alpha-\mathrm{j}\beta)z + (\alpha+\mathrm{j}\beta)\bar{z}], \tag{25}$$

letting $\gamma := \alpha + \mathrm{j}\beta$ yields $\alpha z_r + \beta z_i = \frac{1}{2}(\bar{\gamma}z + \gamma\bar{z}) = \mathrm{Re}\,(\bar{\gamma}z)$. Consequently, it now suffices to perform the change of variable $\psi = -\frac{\chi_t}{\bar{\gamma}}p$ for the saddle point in order to obtain the same expression for the derivative of the cost functional J.

2.4. Calculation of the derivative of the objective function in the TE case

In the TE case, the analysis follows lines which look like those followed in the TM case, but peculiarities and further complexities notably emerge from the occurrence of gradient operators, which requires specific care. Firstly, one introduces the appropriate Lagrangian $\mathcal{L}$ associated to the objective functional (6) in the TE polarization as

$$\mathcal{L}(t,w,\bar{w},\varphi,\bar{\varphi}) = \tfrac{1}{2}\int_{\mathcal{M}}\left|\int_{\mathcal{D}} \chi_t(\boldsymbol{r}')\nabla' G_{12}(\boldsymbol{r},\boldsymbol{r}')\cdot\nabla' w(\boldsymbol{r}')\,\mathrm{d}\boldsymbol{r}' - \zeta(\boldsymbol{r})\right|^2\mathrm{d}\boldsymbol{r} + \mathrm{Re}\int_{\mathcal{D}}\left(w(\boldsymbol{r}) - u^{\text{inc}}(\boldsymbol{r}) - \int_{\mathcal{D}} \chi_t(\boldsymbol{r}')\nabla' G_{22}(\boldsymbol{r},\boldsymbol{r}')\cdot\nabla' w(\boldsymbol{r}')\,\mathrm{d}\boldsymbol{r}'\right)\varphi(\boldsymbol{r})\,\mathrm{d}\boldsymbol{r}. \tag{26}$$

Again, other variants of the Lagrangian functional would lead, as in the TM case, to similar results. Next, we establish the following proposition.

Proposition. *The Lagrangian $\mathcal{L}$ given by (12) has a unique saddle point* $(t, u, \bar{u}, \psi, \bar{\psi})$.

Indeed, the optimality condition in terms of w yields, $\forall v \in H^1(\mathcal{D})$,

$$\begin{aligned}\left\langle \frac{\partial \mathcal{L}}{\partial w}, v \right\rangle &= \frac{1}{2}\int_{\mathcal{M}} \left(\int_{\mathcal{D}} \chi_t(\boldsymbol{r}')\nabla' G_{12}(\boldsymbol{r}, \boldsymbol{r}') \cdot \nabla' v(\boldsymbol{r}')\, \mathrm{d}\boldsymbol{r}' \right) \\ &\quad \times \overline{\left(\int_{\mathcal{D}} \chi_t(\boldsymbol{r}')\nabla' G_{12}(\boldsymbol{r}, \boldsymbol{r}') \cdot \nabla' w(\boldsymbol{r}')\, \mathrm{d}\boldsymbol{r}' - \zeta(\boldsymbol{r}) \right)} \mathrm{d}\boldsymbol{r} \\ &\quad + \tfrac{1}{2}\int_{\mathcal{D}} \left(v(\boldsymbol{r}) - \int_{\mathcal{D}} \chi_t(\boldsymbol{r}')\nabla' G_{22}(\boldsymbol{r}, \boldsymbol{r}') \cdot \nabla' v(\boldsymbol{r}')\, \mathrm{d}\boldsymbol{r}' \right) \varphi(\boldsymbol{r})\, \mathrm{d}\boldsymbol{r}, \\ &= \frac{1}{2}\int_{\mathcal{M}} \left(-\int_{\Omega_t} \Delta' G_{12}(\boldsymbol{r}, \boldsymbol{r}') v(\boldsymbol{r}')\, \mathrm{d}\boldsymbol{r}' + \int_{\Gamma_t} \frac{\partial G_{12}}{\partial n}(\boldsymbol{r}, s) v(s)\, \mathrm{d}s \right) \Theta(\boldsymbol{r})\, \mathrm{d}\boldsymbol{r} \\ &\quad + \frac{1}{2}\int_{\mathcal{D}} \left(v(\boldsymbol{r}) + \int_{\Omega_t} \Delta' G_{22}(\boldsymbol{r}, \boldsymbol{r}') v(\boldsymbol{r}')\, \mathrm{d}\boldsymbol{r}' - \int_{\Gamma_t} \frac{\partial G_{22}}{\partial n}(\boldsymbol{r}, s) v(s)\, \mathrm{d}s \right) \varphi(\boldsymbol{r})\, \mathrm{d}\boldsymbol{r} \\ &= 0. \end{aligned} \tag{27}$$

At the saddle point $(t, u, \bar{u}, \psi, \bar{\psi})$, application of the Fubini theorem and proper account of TE reciprocity provides, $\forall v \in H^1(\mathcal{D})$,

$$\begin{aligned}&\int_{\Omega_t} v(\boldsymbol{r}) \left[-\int_{\mathcal{M}} \frac{\varepsilon_1}{\varepsilon_2} \Delta G_{21}(\boldsymbol{r}, \boldsymbol{r}') \Theta(\boldsymbol{r}')\, \mathrm{d}\boldsymbol{r}' + \int_{\mathcal{D}} \Delta G_{22}(\boldsymbol{r}, \boldsymbol{r}') \psi(\boldsymbol{r}')\, \mathrm{d}\boldsymbol{r}' \right] \mathrm{d}\boldsymbol{r} + \int_{\mathcal{D}} v(\boldsymbol{r}) \psi(\boldsymbol{r})\, \mathrm{d}\boldsymbol{r} \\ &\quad + \int_{\Gamma_t} v(s) \left[\int_{\mathcal{M}} \frac{\varepsilon_1}{\varepsilon_2} \frac{\partial G_{21}}{\partial n}(s, \boldsymbol{r}') \Theta(\boldsymbol{r}')\, \mathrm{d}\boldsymbol{r}' - \int_{\mathcal{D}} \psi(\boldsymbol{r}') \frac{\partial G_{22}}{\partial n}(s, \boldsymbol{r}') \mathrm{d}\boldsymbol{r}' \right] \mathrm{d}s = 0. \end{aligned} \tag{28}$$

Subsequently, $\forall v \in H^1(\mathcal{D})$,

$$\begin{aligned}&\int_{\Omega_t} v(\boldsymbol{r}) \Delta \left[-\int_{\mathcal{M}} \frac{\varepsilon_1}{\varepsilon_2} G_{21}(\boldsymbol{r}, \boldsymbol{r}') \Theta(\boldsymbol{r}')\, \mathrm{d}\boldsymbol{r}' + \int_{\mathcal{D}} G_{22}(\boldsymbol{r}, \boldsymbol{r}') \psi(\boldsymbol{r}')\, \mathrm{d}\boldsymbol{r}' \right] \mathrm{d}\boldsymbol{r} + \int_{\mathcal{D}} v(\boldsymbol{r}) \psi(\boldsymbol{r})\, \mathrm{d}\boldsymbol{r} \\ &\quad + \int_{\Gamma_t} v(s) \frac{\partial}{\partial n} \left[\int_{\mathcal{M}} \frac{\varepsilon_1}{\varepsilon_2} \Theta(\boldsymbol{r}') G_{21}(s, \boldsymbol{r}')\, \mathrm{d}\boldsymbol{r}' - \int_{\mathcal{D}} \psi(\boldsymbol{r}') G_{22}(s, \boldsymbol{r}')\, \mathrm{d}\boldsymbol{r}' \right] \mathrm{d}s = 0. \end{aligned} \tag{29}$$

Upon integration by parts and appropriate simplification, one arrives at, $\forall v \in H^1(\mathcal{D})$,

$$\begin{aligned}&\int_{\Omega_t} \nabla v(\boldsymbol{r}) \cdot \nabla \left[\int_{\mathcal{M}} \frac{\varepsilon_1}{\varepsilon_2} \Theta(\boldsymbol{r}') G_{21}(\boldsymbol{r}, \boldsymbol{r}')\, \mathrm{d}\boldsymbol{r}' - \int_{\mathcal{D}} G_{22}(\boldsymbol{r}, \boldsymbol{r}') \psi(\boldsymbol{r}')\, \mathrm{d}\boldsymbol{r}' \right] \mathrm{d}\boldsymbol{r} \\ &\quad + \int_{\mathcal{D}} v(\boldsymbol{r}) \psi(\boldsymbol{r})\, \mathrm{d}\boldsymbol{r} = 0. \end{aligned} \tag{30}$$

Then, the following change of variables is made: $\forall v \in H^1(\mathcal{D})$,

$$\int_{\mathcal{D}} \psi(\boldsymbol{r}) v(\boldsymbol{r})\, \mathrm{d}\boldsymbol{r} = -\int_{\mathcal{D}} \chi_t(\boldsymbol{r}) \nabla p(\boldsymbol{r}) \cdot \nabla v(\boldsymbol{r})\, \mathrm{d}\boldsymbol{r}, \tag{31}$$

being required that $\psi = 0, \forall \boldsymbol{r} \in \partial D$. Consequently, the observation that $\int_{\mathcal{D}} G_{22}(\boldsymbol{r}, \boldsymbol{r}') \psi(\boldsymbol{r})\, \mathrm{d}\boldsymbol{r} = -\int_{\mathcal{D}} \chi_t(\boldsymbol{r}) \nabla G_{22}(\boldsymbol{r}, \boldsymbol{r}') \cdot \nabla p(\boldsymbol{r})\, \mathrm{d}\boldsymbol{r}$ enables us to rewrite (30) as, $\forall v \in H^1(\mathcal{D})$,

$$\begin{aligned}&\int_{\Omega_t} \nabla v(\boldsymbol{r}) \cdot \nabla \left[\int_{\mathcal{M}} \frac{\varepsilon_1}{\varepsilon_2} \Theta(\boldsymbol{r}') G_{21}(\boldsymbol{r}, \boldsymbol{r}')\, \mathrm{d}\boldsymbol{r}' \right. \\ &\quad \left. + \int_{\mathcal{D}} \chi_t(\boldsymbol{r}') \nabla G_{22}(\boldsymbol{r}, \boldsymbol{r}') \cdot \nabla p(\boldsymbol{r}')\, \mathrm{d}\boldsymbol{r}' - p(\boldsymbol{r}) \right] \mathrm{d}\boldsymbol{r} = 0. \end{aligned} \tag{32}$$

Equation (32) is but the weak formulation of the adjoint scattering problem

$$p(\boldsymbol{r}) = \int_{\mathcal{M}} \frac{\varepsilon_1}{\varepsilon_2}\Theta(\boldsymbol{r}')G_{21}(\boldsymbol{r},\boldsymbol{r}')\,\mathrm{d}\boldsymbol{r}' + \int_{\mathcal{D}} \chi_t(\boldsymbol{r}')\nabla G_{22}(\boldsymbol{r},\boldsymbol{r}')\cdot\nabla p(\boldsymbol{r}')\,\mathrm{d}\boldsymbol{r}', \quad (33)$$

which has a unique solution $p \in H^1(\mathcal{D})$, it being noticed that the impinging wave is generated by a Dirac distribution of sources, $\frac{\varepsilon_1}{\varepsilon_2}\Theta\delta_M$, slightly more complicated than in the TM case since it now involves the ratio between permittivities of the two half-spaces.

As for the derivative of the Lagrangian with respect to φ, one has, $\forall v \in H^1(D)$,

$$\left\langle \frac{\partial \mathcal{L}}{\partial \phi}, v \right\rangle = 0 \Longleftrightarrow \int_{\mathcal{D}} v(\boldsymbol{r})\left(w(\boldsymbol{r}) - u^{\mathrm{inc}}(\boldsymbol{r}) - \int_{\mathcal{D}} \chi_t(\boldsymbol{r}')\nabla' G_{22}(\boldsymbol{r},\boldsymbol{r}')\cdot\nabla' w(\boldsymbol{r}')\,\mathrm{d}\boldsymbol{r}'\right)\mathrm{d}\boldsymbol{r} = 0. \quad (34)$$

Therefore, $\forall \boldsymbol{r} \in \mathcal{D}$,

$$u(\boldsymbol{r}) - u^{\mathrm{inc}}(\boldsymbol{r}) - \int_{\mathcal{D}} \chi_t(\boldsymbol{r}')\nabla' G_{22}(\boldsymbol{r},\boldsymbol{r}')\cdot\nabla' u(\boldsymbol{r}')\,\mathrm{d}\boldsymbol{r}' = 0, \quad (35)$$

which is the state equation to be satisfied by the field u of equation (3) and which has a unique solution in $H^1(\mathcal{D})$.

So, after using the like results obtained with the conjugated pair, the Lagrangian functional is concluded to have a unique saddle point. It then remains to establish the following proposition.

Proposition. *The derivative of the objective functional in the TE polarization case is*

$$\frac{\mathrm{d}J}{\mathrm{d}t} = \mathrm{Re}\int_{\Gamma_t} \eta\nabla u(s)\cdot\nabla p(s)\boldsymbol{V}(s)\cdot\boldsymbol{n}\,\mathrm{d}s. \quad (36)$$

Indeed, from relationship (19), one deduces by proceeding as in the TM case in order to handle χ_t as a function of t, and applying reciprocity as needed, that

$$\begin{aligned}\frac{\mathrm{d}J}{\mathrm{d}t} &= \mathrm{Re}\int_{\mathcal{M}} \Theta(\boldsymbol{r})\int_{\Gamma_t} \eta\nabla G_{12}(\boldsymbol{r},s)\cdot\nabla u(s)\boldsymbol{V}(s)\cdot\boldsymbol{n}\,\mathrm{d}s\,\mathrm{d}\boldsymbol{r}\\ &\quad -\mathrm{Re}\int_{\mathcal{D}}\int_{\Gamma_t} \eta\nabla G_{22}(\boldsymbol{r},s)\cdot\nabla u(s)\boldsymbol{V}(s)\cdot\boldsymbol{n}\,\mathrm{d}s\,\psi(\boldsymbol{r})\,\mathrm{d}\boldsymbol{r}\\ &= \mathrm{Re}\int_{\Gamma_t} \eta\nabla u(s)\cdot\nabla\left[\int_{\mathcal{M}} \frac{\varepsilon_1}{\varepsilon_2}\Theta(\boldsymbol{r})G_{21}(s,\boldsymbol{r})\,\mathrm{d}\boldsymbol{r} - \int_{\mathcal{D}} G_{22}(s,\boldsymbol{r})\psi(\boldsymbol{r})\,\mathrm{d}\boldsymbol{r}\right]\\ &\quad \times\boldsymbol{V}(s)\cdot\boldsymbol{n}\,\mathrm{d}s. \end{aligned} \quad (37)$$

Since $\int_{\mathcal{D}} G_{22}(\boldsymbol{r},\boldsymbol{r}')\psi(\boldsymbol{r})\,\mathrm{d}\boldsymbol{r} = -\int_{\mathcal{D}} \chi_t(\boldsymbol{r})\nabla G_{22}(\boldsymbol{r},\boldsymbol{r}')\cdot\nabla p(\boldsymbol{r})\,\mathrm{d}\boldsymbol{r}$, the sought result immediately follows:

$$\begin{aligned}\frac{\mathrm{d}J}{\mathrm{d}t} &= \mathrm{Re}\int_{\Gamma_t} \eta\nabla u(s)\cdot\nabla\left[\int_{\mathcal{M}} \frac{\varepsilon_1}{\varepsilon_2}\Theta(\boldsymbol{r})G_{21}(s,\boldsymbol{r})\,\mathrm{d}\boldsymbol{r}\right.\\ &\quad \left.+\int_{\mathcal{D}} \chi_t(\boldsymbol{r})\nabla G_{22}(s,\boldsymbol{r})\cdot\nabla p(\boldsymbol{r})\,\mathrm{d}\boldsymbol{r}\right]\boldsymbol{V}(s)\cdot\boldsymbol{n}\,\mathrm{d}s\\ &= \mathrm{Re}\int_{\Gamma_t} \eta\nabla u(s)\cdot\nabla p(s)\boldsymbol{V}(s)\cdot\boldsymbol{n}\,\mathrm{d}s. \end{aligned} \quad (38)$$

2.5. Complementary remarks

At this stage of the investigation, it is seen that one easily gets a negative $\frac{dJ}{dt}$ at time t and, correspondingly, a monotonically decreasing J if one chooses a normal velocity field of deformation V equal to $-\mathrm{Re}\ (g)$ on the contour where the normal shape gradient of the domain, g, of known value at that time t, is calculated as $g = \eta up$ in the TM case and as $g = \eta \nabla u \cdot \nabla p$ in the TE case. Therefore, holding true a relationship of the form $V = -\mathrm{Re}\ (g)$ for any positive or null t throughout $\mathcal{D}$, which is feasible since both u and p are suitably defined everywhere within it once a contour is known, provides a velocity that is fully appropriate to evolving the entire level set ϕ from an initially prescribed level set at $t = 0$.

Let us remark that the shape gradient cancels out in the TM case when p is identically null, i.e. when the scattered field u^{scat} is identical with the data field ζ. This means that the inverse problem at hand is solved exactly and that the obstacle retrieved from the level set function at this t is satisfactory (noting that this might not be the unique obstacle that scatters ζ). In the TE case cancellation of ∇p has same consequence, and the same cause since it results from an exact fit of the data set, again no uniqueness being claimed.

Let us also remark that there is some slight abuse here in equating normal components of the velocity $\boldsymbol{V}$ and shape gradient $\boldsymbol{G}$ found in the integrand of the contour integrals since they do not actually enjoy the same functional space, as is well known. But in numerical practice both V and g take their values in $\mathbb{R}^2$, which obviates the problem.

Let us finally remark that, so far, we have said little about the smoothness of the contour Γ_t of the possibly multiply connected domain Ω_t sought and built with t, except that it had to be smooth enough. A sufficient condition to carry out the min–max differentiability analyses above is that the said contours are C^1—in effect, that the contours of each constitutive part of Ω_t are C^1. Less restrictive assumptions like piecewise C^1 are certainly open to further investigation; this should be in tune with the observation that both direct and adjoint scattering problems are well posed under minor geometric conditions, while in numerical practice, domains simply become distributions of square pixels, boundaries being closed chains of straight segments along x and y, and velocities being calculated at every node of the grid.

3. The numerical experimentation

In this section key ingredients of the numerical implementation are presented and illustrative shape reconstructions of buried obstacles from both TE and TM synthetically generated data fields are displayed and discussed.

3.1. The discrete formulation

3.1.1. The field calculations. The discretization of the wave field formulations introduced previously is simply based on a method of moments (MoM) with pulse basis and point matching; see, for example, Ellis and Peden (1995) for the TM case, and Lambert *et al* (1998) and references therein for the TE case. As usual, it requires the computation of two Green matrices, one corresponding to the interaction between a point on the probing line $\mathcal{M}$ and a point in the test domain $\mathcal{D}$ (terms G_{12} or G_{21}), and the other corresponding to the interaction between two points of $\mathcal{D}$ (terms G_{22}) These two matrices only need to be computed once in the fixed grid spanning $\mathcal{D}$. The latter is made of rectangular pixels of size $\Delta x \times \Delta y$, the electrical contrast χ being assumed to be constant in any given pixel. In the TM case the (electric) field u is calculated at the centres of these pixels, it being assumed to be constant in a given pixel; in the TE case, each pixel is further divided into two triangles in which the (magnetic) field

u is assumed to vary linearly, the field itself being evaluated at every node of the grid. The calculation of the adjoint fields p is carried out accordingly in both TM and TE cases.

The same MoM is used to compute the input data ζ of the inversion problems and to solve both direct and adjoint problems at each chosen time t, i.e. at each iteration of the inversion algorithm; however, *inverse crime* is (mostly) avoided by using different grids. It has been checked by independent means that ζ is computed quite accurately if one uses a grid fine enough (as we do here), whereas one uses a somewhat coarse but still suitable grid within the inversion; this saves computational time and has the side benefit of introducing some model errors which the inversion algorithm is usefully confronted with also.

In terms of computational burden, let us note that if one assumes that $\mathcal{D}$ is a distribution of $n_x \times n_y$ pixels, this corresponds to $n_x \times n_y$ values of the contrast, and to $n_x \times n_y$ values of the electric field and $(n_x + 1) \times (n_y + 1)$ values of the magnetic field (and their adjoints). We denote as (x_i, y_j) the coordinates of the centre of the pixel numbered (i, j) and $(x_{i-\frac{1}{2}}, y_{j-\frac{1}{2}})$, $(x_{i-\frac{1}{2}}, y_{j+\frac{1}{2}})$, $(x_{i+\frac{1}{2}}, y_{j+\frac{1}{2}})$ and $(x_{i+\frac{1}{2}}, y_{j-\frac{1}{2}})$ its four vertex coordinates.

As for the objective function J at given frequency, its discrete normalized version reads as

$$J = \frac{1}{N_s} \sum_{j=1}^{N_s} \frac{\sum_{n=1}^{N_r} \left| u_j^{\text{scat}}(\boldsymbol{r}_n) - \zeta_j(\boldsymbol{r}_n) \right|^2}{\sum_{n=1}^{N_r} \left| \zeta_j(\boldsymbol{r}_n) \right|^2}, \tag{39}$$

where $\boldsymbol{r}_n$ denotes the location of the nth sensor on $\mathcal{M}$.

3.1.2. Initialization of the inversion. The first step of the inversion is the choice of an initial shape of the sought obstacle. This can be done either by selecting the domain Ω_0 and deducing the level set $\phi(0, \boldsymbol{r})$ from it, or vice versa. The Ω_0 must comprise at least one pixel but, otherwise, its choice is arbitrary. It could be the user's best guess, or it can be deduced from a previous processing of the data, for example by a back-propagation scheme (van den Berg and Kleinman 1997)—which however does not work in the TE case within the integral–differential framework chosen here (Lambert *et al* 1998)—or by the level set algorithm applied to data at another frequency (typically within a frequency-hopping scheme). Thus, one equates $\phi(0, \boldsymbol{r})$ for simplicity to the signed distance

$$\phi(0, \boldsymbol{r}) = \begin{cases} -\text{dist}(\boldsymbol{r}, \partial\Omega_0) & \text{if} \quad \boldsymbol{r} \in \Omega_0 \\ +\text{dist}(\boldsymbol{r}, \partial\Omega_0) & \text{elsewhere.} \end{cases} \tag{40}$$

3.1.3. The velocity calculation. The velocity controls the evolution of the level set through (5) and an appropriate choice is essential. In practice, it is to be calculated at every centre of the pixels that cover $\mathcal{D}$. In the TM case it follows directly from the formal equality $V = -\text{Re}(\eta u p)$ that the velocity at the centre of the pixel (i, j) at time t is given by

$$V_{ij}^t = -\text{Re}\left(\eta\, u_{i,j}^t\, p_{i,j}^t\right), \tag{41}$$

where $f_{i,j}^t$ denotes the value taken by the function $f(t, \boldsymbol{r})$ at the point $\boldsymbol{r} = (x_i, y_i)$ at time t, with $u(t, \boldsymbol{r})$ being the (electric) field at the centre of the pixel and $p(t, \boldsymbol{r})$ its adjoint field at the same location. In the TE case the velocity $V = -\text{Re}(\eta \nabla u \cdot \nabla p)$ involves the scalar product between the gradient of the (magnetic) field u and the gradient of its adjoint p at the pixel centres. Since the solution algorithm of the direct problem and of the adjoint problem in the TE case provides u and p only at the vertices of the pixels, the following numerical scheme yields an evaluation of the sought gradients:

$$(\nabla u)_{ij}^t = \begin{pmatrix} (u_{i+1/2,j+1/2}^t - u_{i-1/2,j+1/2}^t + u_{i+1/2,j-1/2}^t - u_{i-1/2,j-1/2}^t)/2\Delta x \\ (u_{i+1/2,j+1/2}^t - u_{i+1/2,j-1/2}^t + u_{i-1/2,j+1/2}^t - u_{i-1/2,j-1/2}^t)/2\Delta y \end{pmatrix} \tag{42}$$

where $u^t_{i+1/2,j+1/2}$, $u^t_{i-1/2,j+1/2}$, $u^t_{i+1/2,j-1/2}$ and $u^t_{i-1/2,j-1/2}$ are the values of u at the four vertices of the pixel (i, j) and at time t, a similar relationship being used for p. The velocity readily follows as

$$V^t_{ij} = -\mathrm{Re}\left(\eta\,(\nabla u)^t_{ij} \cdot (\nabla p)^t_{ij}\right). \tag{43}$$

3.1.4. The numerical Hamiltonian. The evolution of the level set $\phi\,(t, \boldsymbol{r})$ is governed by (5), whose numerical counterpart reads as

$$\frac{\phi^{t+\Delta t}_{ij} - \phi^t_{ij}}{\Delta t} - V^t_{ij}\mathcal{H}\left(\phi^t_{ij}\right) = 0 \tag{44}$$

using notations similar to those above, Δt being a time step. The numerical Hamiltonian $\mathcal{H}$ is an approximation of $|\nabla\phi\,(t, \boldsymbol{r})|$, and is constructed, in particular, so that the motion of a level set contour is outward (resp., inward) when the velocity is positive (resp., negative) (Litman *et al* 1998). The choice of the time step Δt is actually key to the convergence of the algorithm, as will be illustrated next, it being emphasized that no formal relationship of that time step to steps Δx and Δy of the space grid has been proven.

3.2. Illustrative results

3.2.1. Model parameters. The upper half-space is air and the lower half-space (the embedding medium of the buried obstacle) is of relative permittivity $\varepsilon_{r2} = 2$, and it is of null conductivity σ_2, save for the calculations of figure 8 for which a lossy material is considered whose higher and higher conductivity is $\sigma_2 = 1 \times 10^{-3}$, 1×10^{-2} and 5×10^{-2} S m^{-1}. Two different obstacles are investigated:

- One is made of two isolated parts with the same relative permittivity $\varepsilon_{r\Omega} = 3$; one part (on the left with respect to the positively orientated y axis) is squared with side 0.29 m and is centred at ($x = -0.18$ m, $y = -0.68$ m); the other part (on the right) is rectangular with sides 0.18 m (along x) and 0.29 m (along y) and is centred at ($x = 0.28$ m, $y = -0.25$ m).
- The other is singly connected; its relative permittivity is either less than the one of the embedding half-space (one assumes an air void: $\varepsilon_{r\Omega} = 1$) or much larger ($\varepsilon_{r\Omega} = 8$) and it is squared with side 0.29 m and centred at ($x = -0.18$ m, $y = -0.68$ m).

The search domain $\mathcal{D}$, within which these obstacles stay, is a 1 m sided square centred at 0.5 m depth. The measurement apparatus comprises $N_s = 15$ probing sources regularly spaced between -5 m and +5 m at height $y_s = 0.5$ m and possibly radiating at four frequencies 100, 200, 300 and 400 MHz (only one at a time is considered), and $N_r = 47$ sensors regularly spaced between -10 m and 10 m at height $y_r = 0.125$ m. The corresponding input data ζ have been obtained by solving the direct problems with a 44×44 pixel grid whereas the inversions have been carried out with a 30×30 pixel grid.

The results displayed include black-and-white maps of electrical contrasts where black pixels correspond to the interior of the obstacle and white ones to the exterior; maps of level contours (taken of integer magnitudes for convenience) that have been designed from the discrete values of the level set function; three-dimensional representations of the velocity, all those being reached at a certain iteration, say, n, or equivalently at a certain time $n\Delta t$; and variations of the objective function with respect to n. (Recall that the $(n + 1)$th iteration involves the calculation of one direct field distribution and the one of one adjoint field distribution for the obstacle contour Γ_n that has been retrieved at time $n\Delta t$, and the evolution of the level set $\phi^{n\Delta t}$ by one time step to $\phi^{(n+1)\Delta t}$ from which a new contour Γ_{n+1} is inferred as the level set

0.) In addition (see figure 8 again), grey-level maps of electrical contrasts obtained by the binary-specialized modified method are displayed for comparison.

The level set solution procedure itself, unless otherwise indicated, is started from a disc with radius 0.15 m and centred at ($x = 0$ m, $y = -0.5$ m) and from the corresponding signed distance function. It is stopped either when the objective function J becomes less than a given small value or when the number of iterations has reached a given number (here, 500), the 'final' inversion results being always those associated to the least value of J collected in the course of the procedure.

In most examples only monochromatic data are assumed, the main operation frequency being 200 MHz, most of the inversions also being performed in the TE polarization case. At this 200 MHz frequency, the wavelength λ_2 in the lossless burial half-space is about 1.06 m, which means that the obstacles always remain in the near field of the sources and that only near scattered fields are collected, typical dimensions of the obstacle cross sections being less than $\lambda_2/2$ within a search domain of side of about λ_2, while a resolution of the order of one pixel side, $\lambda_2/30$, is aimed at. In the lossy cases the wave field is evidently attenuated within the probed half-space, as shown by complex wavenumbers (at 200 MHz) $k_2 \approx 5.93 + \mathrm{j}0.13$, $6.07 + \mathrm{j}1.30$, and $7.80 + \mathrm{j}5.06$ m^{-1}, and so-called planar skin depths of about 7.51, 0.77 and 0.20 m, which are associated to conductivities σ_2 of 1×10^{-3}, 1×10^{-2} and 5×10^{-2} S m^{-1}, respectively.

Let us emphasize that the value of the cost functional J that would be associated to the discrepancy between the input data ζ calculated with the 44×44 pixel grid for a given obstacle and the scattered field calculated for the same obstacle but with the 30×30 pixel grid is never zero. For instance $J \approx 10^{-2}$ for the two-part obstacle observed at 200 MHz in the lossless case. This model error, implicit in the problem as posed here, indicates that objective functionals plateauing near this level or slightly above or below should be expected, exact reproduction of the obstacles being unlikely.

3.2.2. A typical evolution in the TE case. Typical evolutions of the different functions Ω, ϕ and V during the iterative procedure are sketched in figure 2. The time step is $\Delta t = 3 \times 10^{-3}$. The upper level of the figure corresponds to the initialization stage (iteration number 0) where a single centred obstacle Ω_0 is introduced and the corresponding level set taken as the signed distance function (V is not available at this stage). At the median level of the figure a snapshot of the results of the evolution after five iterations is displayed: Ω_0 has already been split into two smaller domains which are growing in size and moving away from one another, and the velocity remains rather strong in accord with these rapid changes of shapes and locations. At the bottom level of the figure, final results are displayed: the two parts of the buried obstacle are fairly well reconstructed, minor defects showing up here and there, since the boundary is not very smooth (as emphasized by the map of level contours), and correspondingly some pixels near the contours take the wrong shade. The velocity field V is roughly 0 throughout $\mathcal{D}$ and is of considerably smaller magnitude than at the beginning of the inversion, which confirms that a good local minimum has been reached (a null velocity field does not permit further evolution of the level set).

3.2.3. Influence of the time step Δt. The influence of the time step Δt—kept the same all along the iterations, no adaptive scheme having yet been developed—is very important. As a matter of fact Δt is confirmed to be one of the key parameters which govern the evolution of the level set through the numerical Hamiltonian (44). A comparison of the evolution of the objective function for three widely different Δt is found in figure 3. A proper choice of

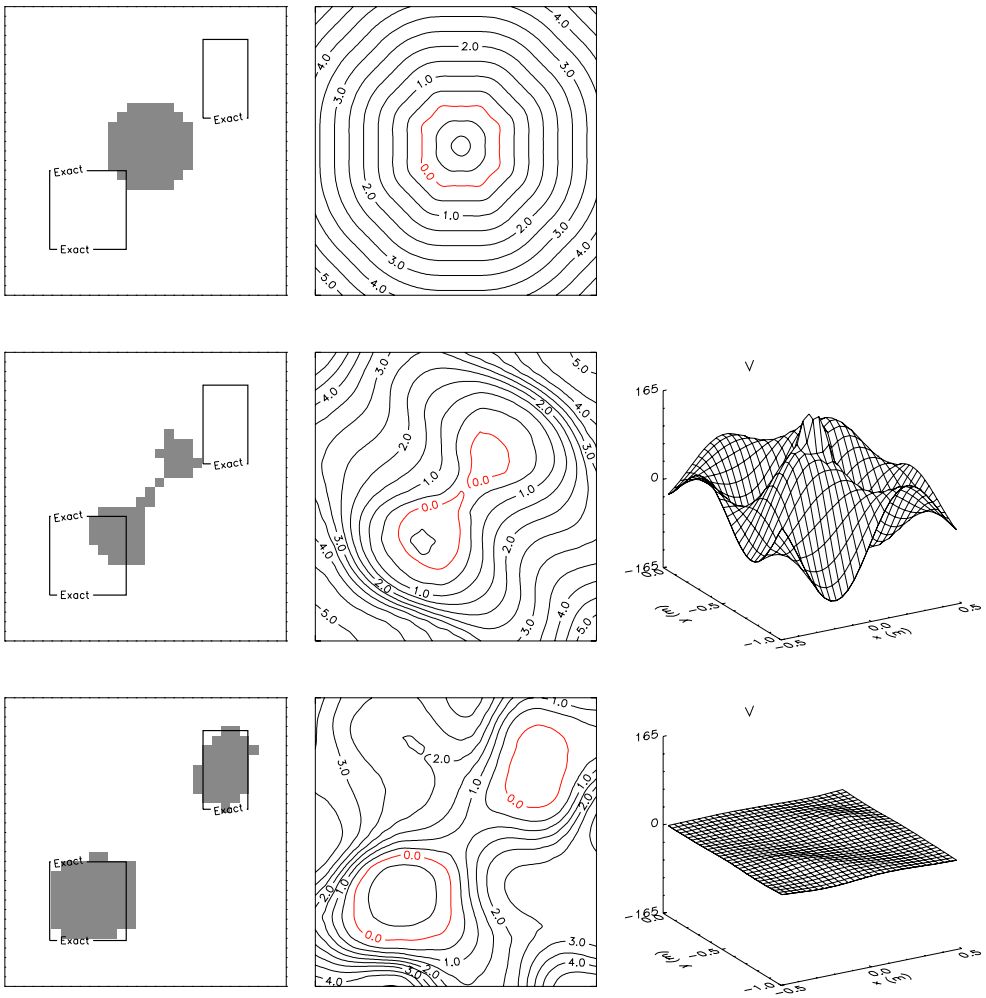

Figure 2. The two-part obstacle: TE case and monochromatic data (200 MHz). Evolution of domain Ω, level set ϕ and velocity V (left, central and right columns, respectively). Upper level: initialization stage (by a disc of 0.15 m radius and a signed distance function); median level: fifth iteration; lower level: best results (421th iteration). Pale grey shows the level set $\phi\,(t, \boldsymbol{r}) = 0$ from which the contour is calculated. Time step $\Delta t = 3 \times 10^{-3}$.

$\Delta t = 3 \times 10^{-3}$—the associated maps are in figure 2—induces a good convergence of the procedure, the objective function (lower curve) oscillating around a plateau of low magnitude of about 3×10^{-3} that is reached beyond about 300 iterations; such oscillations only correspond to small inward or outward motions of the contours, and correspondingly to few pixels near the contour that are alternately changing shade, this phenomenon occuring without affecting any of the main features of the retrieved domains.

Too small a time step ($\Delta t = 3 \times 10^{-4}$, median curve) leads to a much slower, though steady, decrease of the objective functional and a significant growth of the number of iterations needed to reach an acceptable solution. For example, after 500 iterations the magnitude of the objective function as is plotted here is 10 times higher than the previous one, and at this stage the obstacle reconstruction is still poor. It has been observed that about 3000 iterations (the

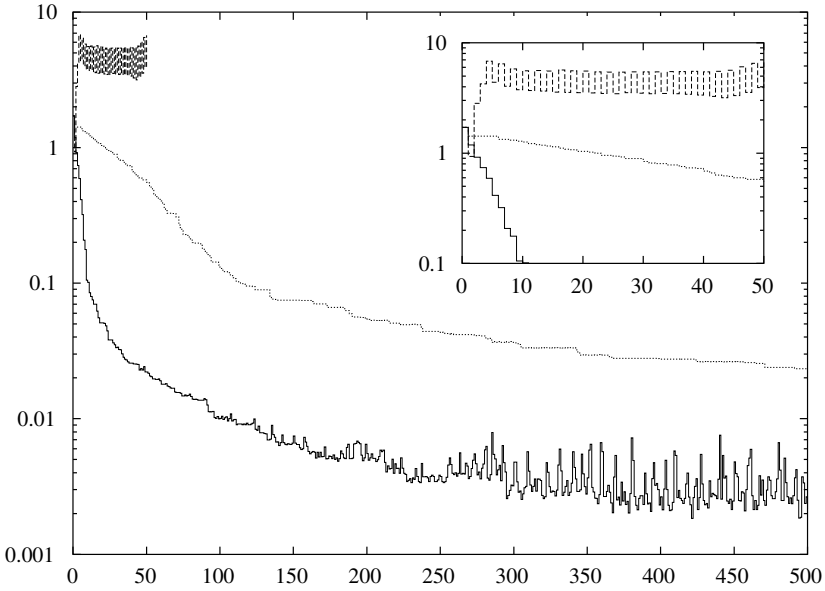

Figure 3. The two-part obstacle: TE case and monochromatic data (200 MHz). Variations of the objective function as a function of the number of iterations for three time steps. Solid curve (lower curve): $\Delta t = 3 \times 10^{-3}$ (corresponding to the results shown in figure 2); dotted curve (median curve): $\Delta t = 3 \times 10^{-4}$; dashed curve (upper curve): $\Delta t = 3 \times 10^{-2}$ (stopped at the 50th iteration because of divergence). The inset describes the first iterations.

results are not shown for brevity) are necessary to reduce this magnitude to the same level as with the reference time step of 3×10^{-3} (again small oscillations occurring around a plateau), the retrieved obstacle map being almost identical to the one observed with the previous time step.

A large time step ($\Delta t = 2 \times 10^{-2}$, upper curve) simply fails us, as is manifested by a brutal growth of the objective function (and a level set function that accordingly jumps to very high values) after the few first iterations, up to some plateau of large value (here, near 8) around which the function oscillates (the procedure here is stopped after 50 iterations).

3.2.4. Influence of data noise. The stability of the inversion with respect to errors affecting the data is rather strong, as is illustrated by variations of J in figure 4. Here the synthetic data have been perturbed by additive white Gaussian noises having different signal-to-noise ratios. Two different signal-to-noise ratios—10 dB (dotted curve) and 5 dB (dashed curve)—and noiseless data (solid curve) are considered. The higher the ratio the higher the minimum of J as is expected, but the results in terms of obstacle domain, level set, and velocity are similar to those obtained from noiseless data (presented in figure 2) with a few pixels near the contour being misplaced at worst.

3.2.5. Comparison with the TM case. So far only results relevant to the TE polarization case have been shown. The performance of the solution procedure in the simpler TM polarization case is illustrated by figure 5. The two-part obstacle configuration is the same as the one studied in the TE case except that the time step Δt is taken as equal to 5×10^{-4}. The procedure converges quite nicely, as was in some sense already true in the TE case (see figure 2).

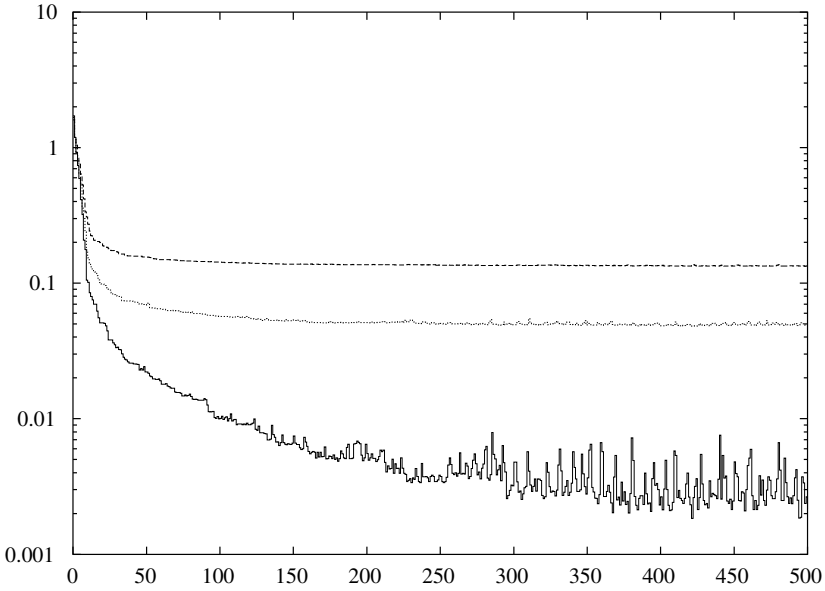

Figure 4. The two-part obstacle: TE case and monochromatic data (200 MHz) as in figure 2. Variations of the objective function as a function of the number of iterations for three different noise levels. Solid curve: noiseless case (the results are shown in figure 2); dotted curve: 10 dB signal-to-noise ratio; dashed curve: 5 dB signal-to-noise ratio. The results (Ω, ϕ, V) are similar in the three cases.

3.2.6. Less and more refractive obstacles. The reconstruction of an air void, associated to a negative contrast, here such as $\chi = -1$, has been carried out for illustration in the isolated obstacle configuration and TE case by means of a frequency-hopping scheme: all four frequencies indicated before are used successively, from the low one (100 MHz) to the high one (400 MHz), the inversion at the second frequency being initialized from the domain retrieved from the data at the first frequency, and so on (at 100 MHz the initial domain is a centred disc with 0.25 m radius). Retrievals at each frequency are presented in figure 6. A rather faithful reproduction of the obstacle is already achieved at the lower frequency, and the introduction of the next frequencies enables us to achieve more and more accurate results. However, the improvement from the two highest frequencies is minor, whereas they require smaller time steps to ensure convergence.

Similarly, a strongly refractive obstacle, associated to a contrast close to its upper bound of 1, here such as $\chi = 0.75$, is successfully retrieved with the frequency-hopping scheme, as is seen from figure 7. Again, time steps have to be adjusted, it being emphazised that the retrieval of the obstacle contour is merely confirmed by frequency hopping since the result at 200 MHz is already excellent. Note that a reconstruction of such a highly refractive obstacle has been experienced as being out of reach with the constrained modified-gradient method developed in Lambert *et al* (1998), while a more refractive obstacle might be retrieved if one pays enough in terms of computational price by using a finer grid.

3.2.7. Conductive embedding: comparison with another method. When the two-part obstacle is buried in a lossy half-space as studied in figure 8 the level set solution method still behaves quite nicely, though in accord with the fact that losses may have a stringent effect on the fields.

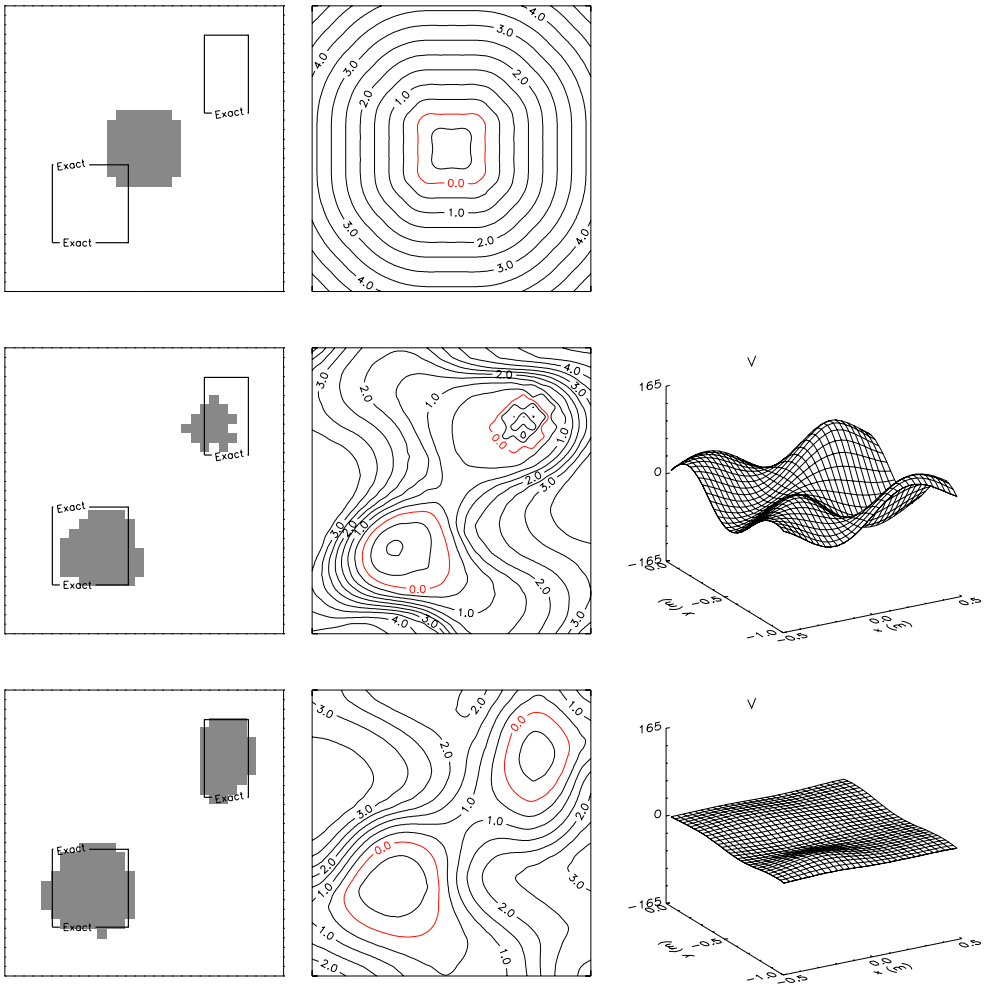

Figure 5. The two-part obstacle: TM case and monochromatic data (200 MHz). Display as in figure 2. Time step $\Delta t = 5 \times 10^{-4}$.

That is, small losses associated to $\sigma_2 = 1 \times 10^{-3}$ S m^{-1}, and correspondingly to a skin depth several times larger than the depths of burial, do not affect the retrieval at all. Higher losses associated to conductivity $\sigma_2 = 1 \times 10^{-2}$ S m^{-1}, and correspondingly to a skin depth of 0.77 m, do not change the retrieval of the shallower part of the obstacle, but the deeper part (buried about one skin depth away from the surface) is rather blurred, though still accurately located. Very large losses ($\sigma_2 = 5 \times 10^{-2}$ S m^{-1}) associated to a skin depth of 0.20 m render the deeper part (buried several skin depths away from the surface) invisible and adversely affect the shallower part: only the upper section comprised between about half a skin depth and a skin depth and half is indeed accurately retrieved; the remaining section is missing and is in effect replaced by some irregularly shaped artefact emerging on its side at roughly the same depth.

The same kind of numerical experimentations considered so far could be equivalently carried out by the binary-specialized modified-gradient method detailed in Lambert and

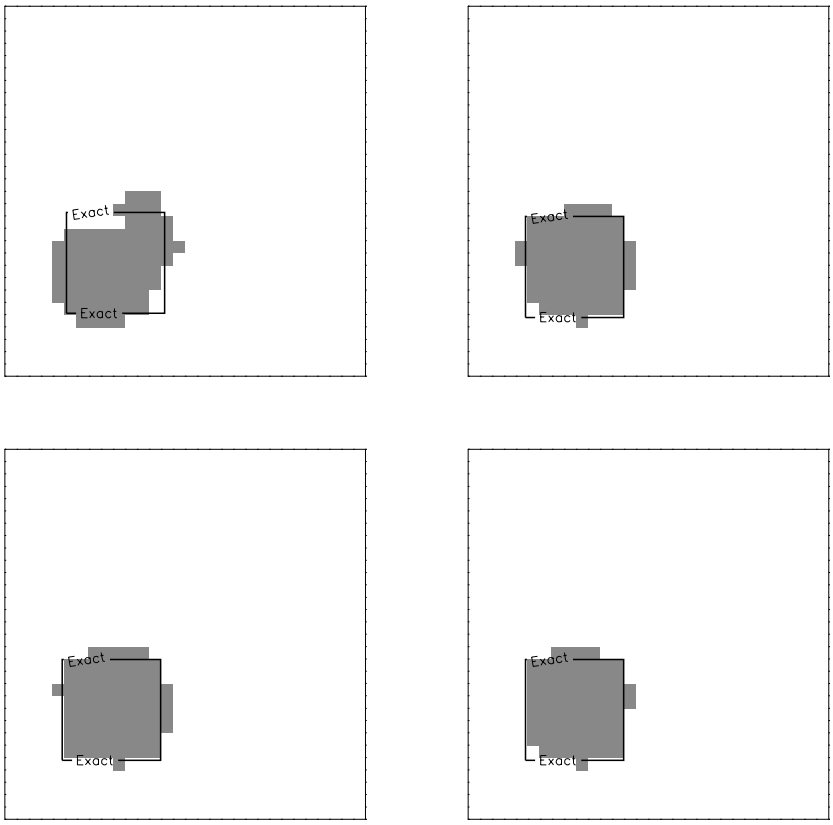

Figure 6. The isolated air void: TE case and frequency hopping from 100 to 400 MHz. Retrievals achieved at 100 MHz (upper left), 200 MHz (upper right), 300 MHz (bottom left) and 400 MHz (bottom right) are displayed. Time steps $\Delta t = 3 \times 10^{-3}$, 3×10^{-3}, 1.5×10^{-3} and 3×10^{-4}, respectively.

Lesselier (2000a). Lack of space precludes us from giving a comprehensive comparison. But the case considered in this section is especially interesting due to two challenging peculiarities: two-part obstacle and increasing losses of the embedding medium. In figure 8 the contrast maps retrieved from the same sets of data by this gradient-type method are displayed. Note that the maps are now the ones of a contrast that is comprised between 0 and 1 in every pixel, though being mostly close to 0—white pixels—or mostly close to 1—black pixels. Also, to keep computations manageable the sampling is now rather coarse (a 21×21 pixel grid is used). However, the final results are comparable with those obtained with the level set method (once one has accommodated for the grey-level representation, and the correspondingly fuzzier contour of the retrieved obstacle) for the low- and median-loss cases (absence of losses leads to the same results as with low losses); they differ greatly in the high-loss case (since the retrieved contrast tends not to be close enough to 1), but the overall location is still fair and emergence of an artefact is confirmed.

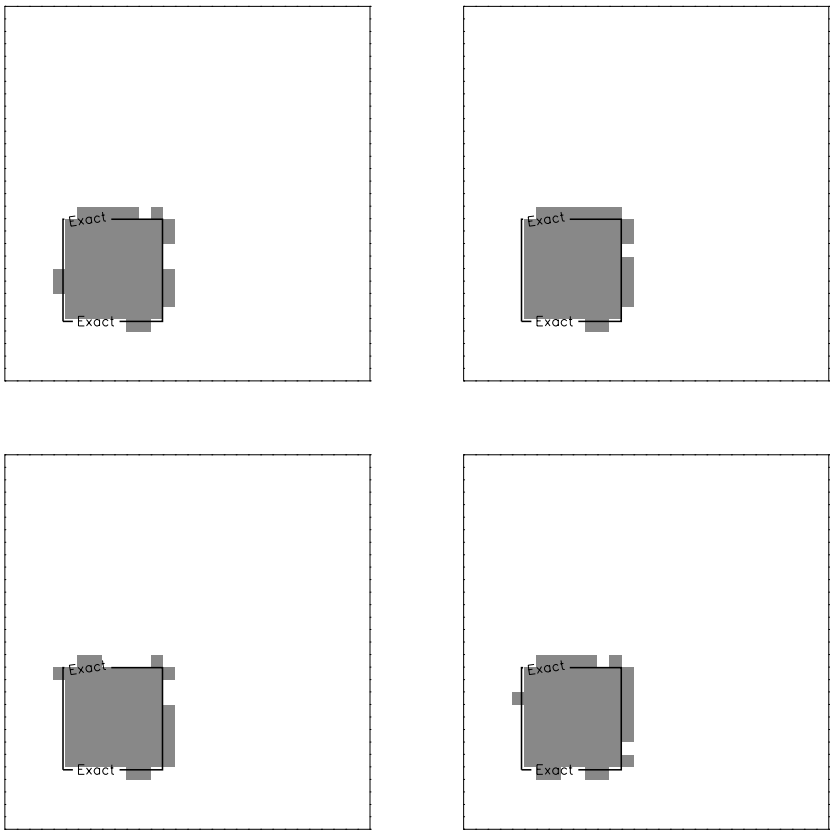

Figure 7. The highly refractive isolated obstacle: TE case and frequency hopping from 100 to 400 MHz. Time steps $\Delta t = 3 \times 10^{-3}, 1.5 \times 10^{-3}, 7.5 \times 10^{-4}$ and 7.5×10^{-5}, respectively. (Display as in figure 6.)

4. Conclusion

The controlled evolution of level sets that combines level set representation of shapes and speed method in the field of contour identification of scattering obstacles from time-harmonic data has many advantages, as is evident from the investigation carried out here and previous works:

- It does not to require any linearization, be it at the level of formulating the wave field (via an exact Green formulation) or when looking for the unknown obstacles themselves (via optimal shape deformations), in contrast, for example, to distorted Born methods and like approaches.
- It is free from most usual topological constraints. Scattering domains merge and split and holes appear or disappear, without knowledge of interior points beforehand; all such properties differ strikingly from those of most shape reconstruction methods which impose a number of restrictive hypotheses: for example, one or a known number of obstacles, singly connected cross sections, star-shaped contours, small deformations.
- Its main requisite is the calculation of proper shape gradients. Those are now derived in closed form from an elegant min–max formulation of the objective function and

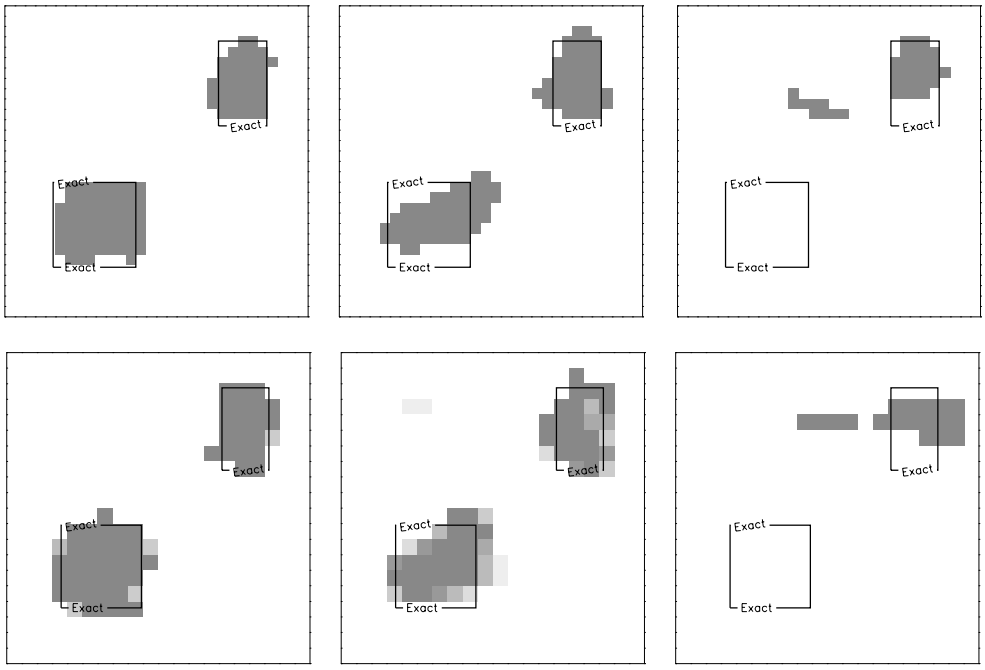

Figure 8. The two-part obstacle in an increasingly lossy half-space ($\sigma_2 = 1 \times 10^{-3}$, 1×10^{-2} and 5×10^{-2} S m^{-1} from left to right) retrieved by the level set method (upper level, time steps $\Delta t = 3 \times 10^{-3}$, 3×10^{-3} and 5×10^{-4}, respectively) and the binary-specialized modified gradient method (bottom level, using a grey-level scale of the magnitude of the contrast): TE case and monochromatic data (200 MHz).

differentiability analysis (conducted under mild conditions) that (in particular) does not require any differentiation of the state fields, as often practised. Furthermore, one remains within wave field formulations deduced from well behaved Green systems of the unperturbed environment, in which most of the complexity of this environment is embodied once and for all.

- It readily works in numerical practice in a fixed grid using precalculated samples of the Green systems, both direct and adjoint problems being tackled in practice by means of the same solution algorithm (once different source fields have been taken account of), and if the grid allows a correct representation of the boundaries, it applies even though those are not smooth.
- Two-dimensional configurations that involve purely scalar wave fields and require moderate computation have been the only ones attacked by us, or by others to the best of our knowledge. Going to three dimensions, and involving vector wave fields, is within reach since level sets, velocity fields and shape gradients can be found by like techniques once dyadic Green systems are set forth, it being noted that accurate numerical solvers of the direct problems are needed (only bulky obstacles are presently studied but a whole field of investigation also opens out on the retrieval of thin cracks in material structures). Let us also emphasize that obstacles hidden in lossy environments can be efficaciously dealt with, the impact of losses being mostly felt on the depth of investigation (roughly less than two skin depths), the solution method actually operating as well as without losses.

However, the great versatility and fair robustness of the method as is emphasized here does not mean that further theoretical and computational developments are not necessary. One should tend to (at least) most of the following and often difficult issues:

- Which functional setting the velocity field enjoys, how that setting relates to the one of the shape gradients, how their discrete versions violate some requirements of the formal calculations though yielding good results, and how brutal topological events (splitting and merging of domains, and emergence of domains where they were none) might be enabled within a certain functional setting are questions whose precise answers would lead to sounder theoretical mechanisms.
- The solution method leaves considerable liberty both in terms of the choice of initial domains—in the absence of any other pertinent information—and in terms of initial level sets, the latter being easily made of signed distance functions. Numerical experimentation in both TM and TE cases has not so far shown that different obstacles with low and roughly equal objective functions can be constructed with different initial domains (here we have displayed the results observed with small discs, bigger discs leading us to close reconstructions). However, this possibility should still not be considered lightly, once it is noticed that uniqueness and even stability in the harsh conditions of inversion prevailing here seem, theoretically speaking, difficult to prove. That a binary-specialized modified-gradient method whose logic is sharply different yields closely similar, even identical, shapes as demonstrated in figure 8 is rather comforting in that respect.
- Whichever the electrical and geometric configurations considered, efficacy means proper choice of the time step Δt, the rule of thumb being that it be neither too small to avoid lengthy computations nor too large to avoid too brutal shape deformations and probable divergence. However, its relationship to the space step(s) remains to be studied beyond pure numerical experimentation once it is pointed out that the velocity is 'unpredictable' throughout the search domain from one time step to the next (it comes from extension of a shape gradient independently estimated) which greatly complicates the matter with respect to standard material on the motion of boundaries that leads to CFL stability conditions.
- Rather fuzzy priors like 'the contours should be smooth enough' might possibly be handled by maintaining the level sets as distance functions, which involves a modification of (5), following that in Gomes and Faugeras (1999) (numerical results, not given here, indicate that in the TE case, if the velocity field is inaccurately computed, the retrieved domains get rather jagged, this phenomenon being alleviated by using the distance function associated to these domains as a new level set and restarting the inversion procedure). More *ad hoc* techniques like shortening an oscillating contour via some evolution superimposed at each iteration step might be preferred (Dorn *et al* 2000), as well as, for example, the direct introduction of constraints linked to least curvature in the evolution equation itself (Ferrayé *et al* 2000). However, simply adding to the objective functional two penalty terms (one of least area and the other of least perimeter) and rigorously deriving the resulting shape gradients within the min–max framework of the objective functional is a good alternative (Ramananjaona *et al* 2001b) (an advection term and a curvature term follow when one does so, as those which were proposed by Santosa (1996)).

References

Brandwood D H 1983 A complex gradient operator and its application in adaptative array theory *IEE Proc.* **130** 11–16

Colton D and Kress R 1983 *Integral Equation Methods in Scattering Theory* (New York: Wiley)

Cuer M and Zolésio J-P 1988 Control of singular problem via differentiation of a min-max *Syst. Control Lett.* **11** 151–8

Dorn O, Miller E L and Rappaport C M 2000 A shape reconstruction method for electromagnetic tomography using adjoint fields and level sets *Inverse Problems, Special Section: Electromagnetic Imaging and Inversion of the Earth's Subsurface* vol 16, ed D Lesselier and T Habashy pp 1119–56

Ellis G A and Peden I C 1995 An analysis technique for buried inhomogeneous dielectric objects in the presence of an air-Earth interface *IEEE Trans. Geosci. Remote Sens.* **33** 535–40

Ferrayé R, Dauvignac J-Y, Pichot C, Barlaud M, Blanc-Féraud L, and Zolésio J P 2000 A boundary-oriented inverse scattering method based on contour deformations by means of PDE-driven level sets for radar imaging *Proc. European Microwave Week: Microwave Imaging Methods and Techniques (Paris La Défense, France)* pp 12–19

Gomes J and Faugeras O 1999 Reconciling distance functions and level sets *Research Report 2666* (Sophia-Antipolis: INRIA)

Kress R 2001 Scattering by Obstacles *Scattering: Part 1- Scattering of Waves by Macroscopic Targets* ed R Pike and P C Sabatier (London: Academic) chapter 2.2 4.2 at press

Lambert M and Lesselier D 2000a Binary-constrained inversion of a buried cylindrical obstacle from complete and phaseless magnetic fields *Inverse Problems* **16** 563–76

——2000b Distributed source method for retrieval of the cross-sectional contour of an impenetrable cylindrical object in a shallow water waveguide *ACUSTICA Acustica united with Acta Acustica* **86** 15–24

Lambert M, Lesselier D and Kooij B J 1998 The retrieval of a buried cylindrical obstacle by a constrained modified gradient method in the H-polarization case and for Maxwellian materials *Inverse Problems* **14** 1265–83

Litman A, Lesselier D and Santosa F 1998 Reconstruction of a two-dimensional binary obstacle by controlled evolution of a level set *Inverse Problems* **14** 685–706

Monebhurrun V, Lesselier D, Duchêne B, Ruosi A, Valentino M, Pepe G and Peluso G 1999 Eddy current nondestructive evaluation using SQUIDs *Electromagnetic Non-Destructive Evaluation* vol 3, ed D Lesselier and A Razek (Amsterdam: IOS Press) pp 171–81

Petry M 1995 Acoustic scattering in a layered medium *Inverse Scattering and Potential Problems in Mathematical Physics* ed R E Kleinman *et al* (Frankfurt: Lang) pp 140–56

Ramananjaona C, Lambert M and Lesselier D 2001a Shape inversion from TM and TE real data by controlled evolution of level sets *Inverse Problems, Special Section: Inversion from Real Data* ed K Belkebir and M Saillard, to be published

Ramananjaona C, Lambert M, Lesselier D and Zolésio J-P 2001b On novel developments of the controlled evolution of level sets in the field of inverse shape problems *Proc. 2001 URSI Int. Symp. on Electromagnetic Theory (Victoria, Canada)* pp 459–61

Ramananjaona C, Lambert M, Lesselier D and Zolésio J-P 2000 On the controlled evolution of level sets and its application to the retrieval of obstacles from microwave laboratory data *Proc. European Microwave Week: Microwave Imaging Methods and Techniques (Paris La Défense, France)* pp 20–7

Santosa F 1996 A level-set approach for inverse problems involving obstacles *ESAIM: COCV* **1** 17–33

Sethian J A 1999 *Level Set Methods and Fast Marching Methods* 2nd edn (Cambridge: Cambridge University Press)

Sokołowski J and Zolésio J-P 1992 *Introduction to Shape Optimization. Shape Sensitivity Analysis* (Berlin: Springer)

Souriau L, Duchêne B, Lesselier D and Kleinman R E 1996 Modified gradient approach to inverse scattering for binary objects in stratified media *Inverse Problems* **12** 463–81

Tai C T 1993 *Dyadic Green Functions in Electromagnetic Theory* 2nd edn (New York: IEEE)

van den Berg P and Kleinman R E 1997 Gradient methods in inverse acoustic and electromagnetic scattering *Large-Scale Optimization with Applications* ed L T Biegler *et al* (Berlin: Springer) pp 173–94

Zolésio J-P, Litman A and Lesselier D Topological identification in electromagnetic wave field inversion *Proc. IABEM 98: Int. Symp. on Boundary Elements Methods (Palaiseau, France)* pp 209–10

F

Application des ensembles de niveaux à des données réelles

[A.11] Shape inversion from TM and TE real data by controlled evolution of level sets
Christophe Ramananjaona, Marc Lambert et Dominique Lesselier
Inverse Problems (Special Section « Testing inversion algorithms against experimental data ») **17** 1585-1595 2001

INSTITUTE OF PHYSICS PUBLISHING INVERSE PROBLEMS

Inverse Problems **17** (2001) 1585–1595 PII: S0266-5611(01)22681-1

Shape inversion from TM and TE real data by controlled evolution of level sets

C Ramananjaona, M Lambert and D Lesselier

Département de Recherche en Électromagnétisme, Laboratoire des Signaux et Systèmes (CNRS-SUPÉLEC-UPS), Plateau de Moulon, 3 rue Joliot-Curie, 91192, Gif-sur-Yvette Cedex, France

E-mail: christophe.ramananjaona@lss.supelec.fr, marc.lambert@lss.supelec.fr and dominique.lesselier@lss.supelec.fr

Received 9 March 2001
Published 13 November 2001
Online at stacks.iop.org/IP/17/1585

Abstract

The retrieval of the cross-sectional contour of a homogeneous, multiply connected cylindrical obstacle located in free space is performed via controlled evolution of a level set from experimental data in either the transverse magnetic (TM) or transverse electric (TE) polarization case as is described in the introductory paper of the special section. Theoretical and algorithmic details on the solution method are found in Ramananjaona *et al* (2001 *Inverse Problems* **17** 1087–111) for the buried object configuration—the free-space configuration is a straightforward simplification—and only key elements are recalled here. Focus is on the display and discussion of shape identification results for the two dielectric circular cylinders (TM data), the rectangularly shaped metal cylinder (TM and TE data), and the U-shaped metal cylinder (TM data). In addition to the fact that TE data are often seen as more of a challenge that TM data, those cases appear to be the most demanding ones in the microwave data base in terms of geometry (the U-shaped one) or in view of the inversion algorithm itself (developed for penetrable objects, the metal case is in principle off limits) whilst the two cylinders illustrate how multiply connected, dielectric objects are retrieved.

1. Introduction

1.1. An overview of the solution method

A significant body of work now exists on controlled evolutions of level sets developed in order to solve in a nonlinearized fashion time-harmonic inverse scattering problems—to our knowledge, only for objects elongated enough in one direction with respect to the probing radiation wavelength to be considered as infinite cylinders. In addition to that conducted since

0266-5611/01/061585+11$30.00

the mid-1990s by the authors and colleagues, we mention the considerable work of Dorn *et al* (2000) on cross-borehole electromagnetic tomography in Earth's subsurface exploration and the investigation summarized in Ferrayé *et al* (2000) for the imaging of perfectly conducting targets in the microwave regime.

The solution method used here has been introduced by, and is thoroughly described in, Litman *et al* (1998), the inverse scattering problem therein being posed in free space and in the TM polarization case only (the electric field is orientated along the cylinder axis). The method has been extended since then by Ramananjaona *et al* (2001a) to the more involved configurational case of the object which is fully buried in a half-space and illuminated and seen from the other half-space only, this case being dealt with in both TM and TE (the magnetic field is orientated along the cylinder axis) polarization cases.

So, the approach as of now combines

- a level-set representation of shapes (see Sethian (1999)) inside an inversion algorithm (as pioneered in Santosa (1996)) evolved in both space $\boldsymbol{r}$ and non-negative pseudo-time t in some prescribed closed box $\mathcal{D}$ according to a Hamilton–Jacobi-type equation of motion at a certain velocity $\boldsymbol{V}$ also varied in space and time;
- the application of the speed or velocity method for shape-optimal design and control (see Sokołowski and Zolésio (1992)) that aims at yielding a decrease of an objective functional J in time t from the flow of a certain velocity of deformation of the shape contour, which provides a proper and determinant choice of $\boldsymbol{V}$.

For us, this shape contour, Γ_t, is the level 0 of the level-set function $\phi(t, \boldsymbol{r})$ that is calculated at time t, and $J(t)$ simply weights in the agreement between the effectively collected field data ζ and those that would be due in the same conditions to a hypothetical obstacle Ω_t of contour Γ_t, the interior (resp. exterior) of the obstacle being associated to negative (resp. positive) values of ϕ.

In summary, the approach

- has been developed from exact contrast-source domain integral formulation (TM) and integral-differential formulation (TE) of the direct scattering problems written from the TM and TE Green systems of the unperturbed environment;
- involves the corresponding integral and integral-differential formulations of their error-driven adjoint scattering problems;
- uses a Min–Max casting of an objective functional J made of the data error to be minimized, and novel differentiability analyses thereof (Cuer and Zolésio 1988), to yield the derivatives of J with respect to the evolution time t in closed form (as integrals along the contour of the obstacle);
- yields a well-defined shape gradient $\boldsymbol{G}$ involving suitable products of the direct and adjoint fields (TM case) or of their gradients (TE case);
- enforces as velocity field $\boldsymbol{V}$ of the entire level-set ϕ a quantity opposite to the shape gradient $\boldsymbol{G}$ once the latter has been heuristically extended throughout $\mathcal{D}$ from its value on the obstacle contour.

In fine, what matters is our ability to calculate the direct field and its adjoint field (or their gradients) for a certain scattering obstacle (the one retrieved at t), not the means to numerically carry out that double calculation (for example, we are not forced to use a computational code also based on a Green formulation), the evolution of the level set only requiring these fields to be made available each time a new contour has been reached.

1.2. Application to the present data

The algorithm is described at length in Litman *et al* (1998) and Ramananjaona *et al* (2001a), and we do not return to it here. Only some items of particular interest are considered below.

The analysis so far is valid for a homogeneous penetrable obstacle made of a known linear, isotropic and non-magnetic material whose electric contrast η with respect to its embedding medium is prescribed at the operating (circular) frequency ω; $\eta = \frac{\varepsilon_\Omega}{\varepsilon_0} - 1$ in the TM case, and $\eta = 1 - \frac{\varepsilon_0}{\varepsilon_\Omega}$ in the TE case where permittivity ε_0 is that of free space and $\varepsilon_\Omega = \varepsilon_0 \varepsilon_{r\Omega}$ is that of the obstacle. $\varepsilon_{r\Omega}$ is real- or complex-valued, i.e. accounts for lossless and lossy materials as well. We have $\varepsilon_{r\Omega}$ real-valued and equal to 3 in the dielectric cases studied later on.

Impenetrable obstacles (such as a metal obstacle in the microwave regime) remain a main hurdle. To proceed in practice, one has to introduce a fictitious conductive material whose large but finite conductivity σ corresponds to $\varepsilon_{r\Omega}$ approximately equal to $\mathrm{j}\sigma/\omega\varepsilon_0$, and allows for some field penetration in the metal. The latter is measured to a good extent by the well known planar skin depth $\delta = \sqrt{2/\sigma\omega\mu_0}$ (μ_0, vacuum permeability), which is therefore taken of the order of the pixel sizes used at the discretization stage. This maintains a good accuracy in the numerical field calculations (almost as if the obstacle is full metal and currents flow only superficially) and still enables the obstacle contour to move inwards as well as outwards within the chosen framework of level-set evolution. σ is valued to 3.1 S m^{-1} in the examples here.

The sought obstacle cross-section Ω itself can be singly or multiply connected, and is possibly hollow as well. No such topological information is necessary to proceed with the solution algorithm. The main topological constraint is that Ω lies inside a user-prescribed search domain $\mathcal{D}$ where the Ω_t are also being built. This is not worrisome since the search domain can be easily appraised beforehand: for example, via data back-propagation.

As for the obstacle contour Γ, the Min–Max analysis mentioned above requires it to be smooth: a sufficient condition is that contours of each constitutive part should be C^1, though this point is open to investigation. Indeed both direct and adjoint problems are well-posed under much more minor geometrical conditions, whilst, in numerical practice, a domain simply becomes a finite distribution of pixels and a level contour a closed chain of straight segments, obstacles with corners being easily tackled in that discrete version.

Sensors have been located, in the investigations which we have led so far, in the near field of the sought obstacle, i.e. the Green functions involved in the calculation of the scattered field (within the so-called data or observation equation) are always calculated from their full-wave representation (using a Fourier expansion in the two half-space case). However, placing such sensors in the far field simply means that some asymptotic representations of such Green functions might be useful—though we have for simplicity kept the full ones whatever the range considered here—without changing the general framework. (We leave aside the difficult question of how the ill-posedness of the retrieval of a target of known material but unknown map is affected by the corresponding lack of evanescent fields.)

Similarly, the sources have been modelled as monochromatic, ideal electric or magnetic current line sources that radiate known incident wavefields with respective TM and TE polarizations, pure plane waves being assumed also. But using effective sources like the horn antennae of the actual experiments leads us to what is actually a 2.5D scattering problem (it seems safe to assume that the cylinders under test are long enough to induce negligible end effects). No attempt is made here to tackle this demanding problem, the incident field throughout $\mathcal{D}$ being still assumed to be of the Hankel type as with line sources. Moreover, the fact that the provided scattered data have been somehow (see below) normalized with respect to the provided incident field data and used as such in the minimized cost functional appears to reduce the effects of field depolarization to a good extent.

The data are normalized as follows. Antennae S_j ($j = 1, \ldots, N_s$) are set at given range from reference point O and de facto surround $\mathcal{D}$. For a given antenna j, N_r incident and total, electric or magnetic, fields are collected at given range (close to the previous one) covering an angle of 240° overall. N_r samples of the scattered field follow by difference, each being multiplied thereafter by a fixed complex-valued factor. The latter is the ratio between two incident fields: the one due to a line source placed at the location of the emitting antenna S_j and calculated at the location of the receiving antenna S_r when this one is placed exactly on the other side of the obstacle in the forward direction, and the one effectively collected by the receiving antenna S_r in that specific situation.

The goal of the inversion is to construct an obstacle which scatters a field u^{scat} close to ζ, ζ being the set of $N_s \times N_r$ properly normalized data samples available at a given frequency. At time t, when one has constructed the obstacle domain Ω_t, the fit is simply appraised via the value of the cost functional

$$J(t) = \frac{1}{N_s} \sum_{j=1}^{N_s} \frac{\sum_{n=1}^{N_r} |u_j^{\text{scat}}(\boldsymbol{r}_{jn}, t) - \zeta_j(\boldsymbol{r}_{jn})|^2}{\sum_{n=1}^{N_r} |\zeta_j(\boldsymbol{r}_{jn})|^2},$$

where $\boldsymbol{r}_{jn}$ denotes the location of the nth receiving antenna which collects the field scattered by Ω_t when it is illuminated by the jth emitting antenna. One chooses an initial shape Ω_0 within $\mathcal{D}$ at will and the corresponding initial level set is taken as a signed distance.

2. The experimentation

In this section illustrative shape reconstructions are displayed and discussed for three different obstacles: the two dielectric circular cylinders (TM data), the rectangularly shaped metal cylinder (TM and TE data), and the U-shaped metal cylinder (TM data), respectively associated to files denoted as twodielTM_4f.exp, rectTM_cent.exp, rectTE_8f.exp, and uTM_shaped.exp.

All results have been obtained with $N_s \times N_r$ data samples where $N_s = 36$ and $N_r = 49$. They consist as usual of black-and-white maps of electrical contrasts η (black pixels correspond to the interior of the obstacle, white ones to the exterior), maps of level contours designed from the discrete values of the level-set function ϕ, and 3D representations of the amplitude V of the component normal to the level contours of the velocity field $\boldsymbol{V}$, all those quantities being reached at a certain iteration, say, n, or equivalently at a certain time $n\Delta t$, and variations of the objective functional J with respect to n, the final results being those associated to the least value of J observed in the course of the procedure.

2.1. The two dielectric cylinders (TM data)

In this example, we have only applied the algorithm to monochromatic datasets, at 6 and at 8 GHz, results of the same overall quality but at the much lower 1 GHz being available in Ramananjaona *et al* (2000). The search domain $\mathcal{D}$ in both cases is a 7.5 cm × 15 cm O-centred rectangle discretized into 16 × 31 cells at 6 GHz and into 21 × 41 cells at 8 GHz. Corresponding cell sides are about 0.48 and 0.36 cm, respectively, to be compared with wavelengths of 5 and 3.75 cm in air and of about 2.9 and 2.2 cm in the dielectric material at the same two frequencies. The initial obstacle Ω_0 is circular with radius 2 cm and O-centred. Results are computed with time step $\Delta t = 10^{-2}$ at 6 GHz and $\Delta t = 2 \times 10^{-2}$ at 8 GHz.

Figure 1 shows a typical evolution of the different functions involved (obstacle domain Ω, level-set ϕ, velocity V), and figure 2 shows the corresponding evolution of J as a function of the number of iterations.

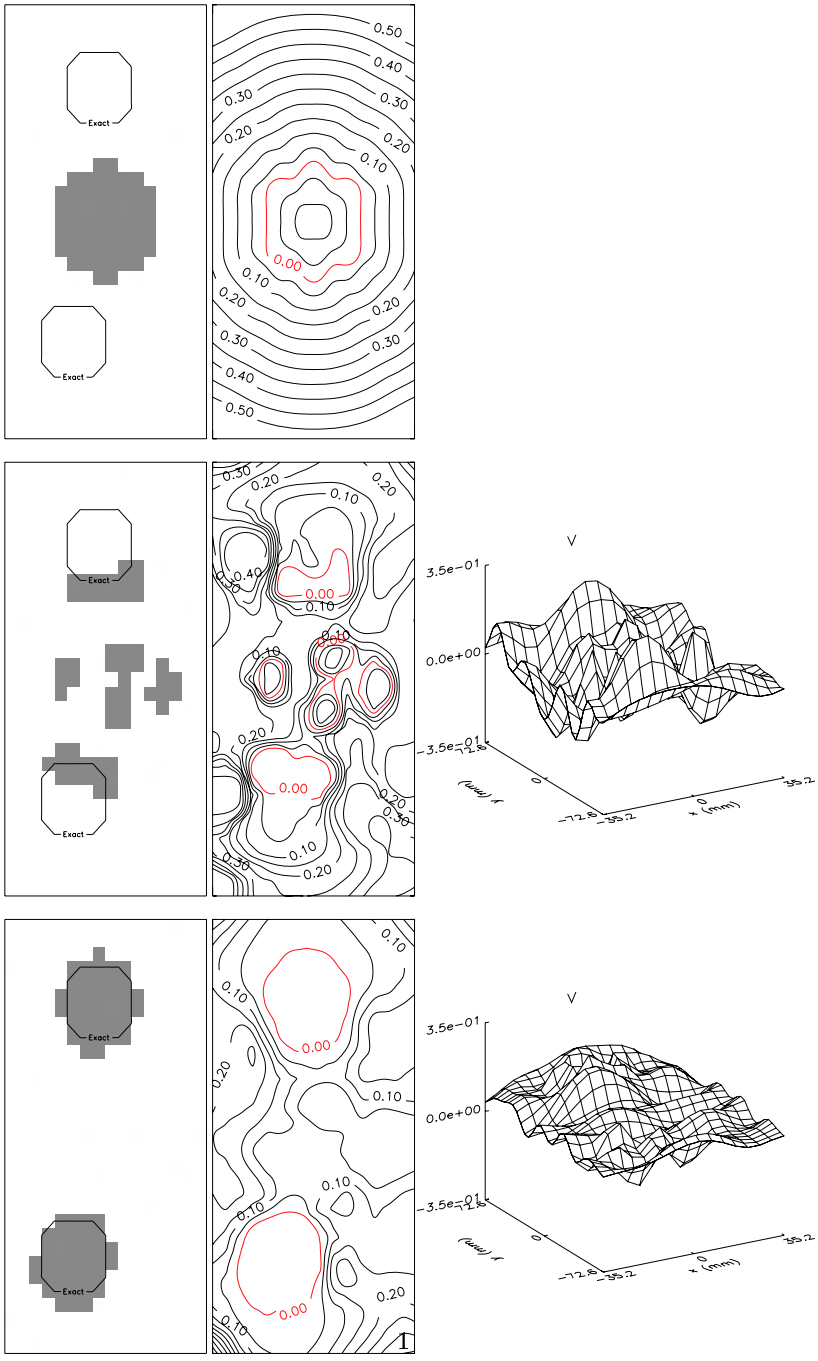

Figure 1. The two dielectric cylinders (TM data, twodielTM_4f.exp): monochromatic data (at 6 GHz). Evolution of the domain Ω, level set ϕ and velocity V (first, second and third columns, respectively). Upper level: initialization stage (by a disc of 2 cm radius and a signed distance function), median level: 35th iteration, and lower level: best results (54th iteration). In red the level-set $\phi(t, \boldsymbol{r}) = 0$ from which the obstacle contour is deduced. The time step is $\Delta t = 10^{-2}$.

(This figure is in colour only in the electronic version)

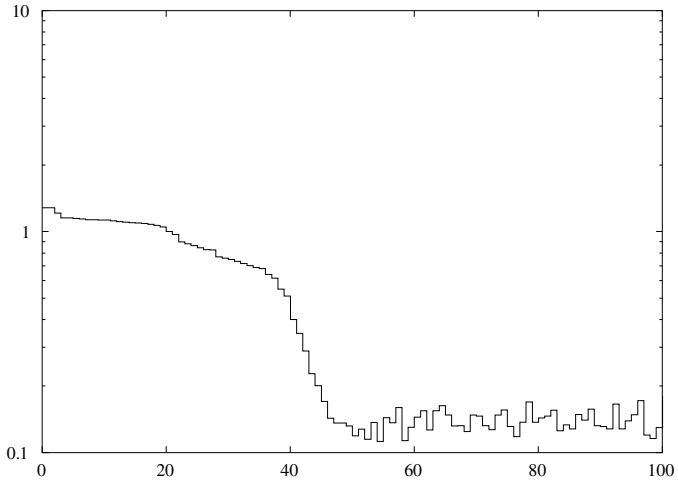

Figure 2. The two dielectric cylinders (TM data, twodielTM_4f.exp): monochromatic data (at 6 GHz). Variations of the objective function as a function of the number of iterations (see figure 1).

The upper level of figure 1 shows these quantities at the initialization stage of the inversion (V is not available at this stage). The median level shows the quantities as they are found near the *splitting time*, i.e. when the obstacle domain Ω starts to be divided into smaller domains, some of which will disappear later on whereas others will enlarge and in practice move towards the right solution. The velocity is still rather strong at this stage and is jagged as well, in accord with the speedy modification of the obstacle shape. The lower level shows the best results (associated to the lowest value of J). The two cylinders appear fairly well retrieved. The velocity is not of very small magnitude yet (as would be observed with nearly exact synthetic data (Ramananjaona *et al* 2001a)), though it varies much more smoothly than before in most parts of $\mathcal{D}$.

Correspondingly, the cost functional J decreases quickly at the early stage of the procedure (notably near the splitting time), before it starts to oscillate around a plateau. The level contour zero remains almost fixed at this stage—other level contours further away can still evolve to a good extent. In short, with the exception of a few pixels near its outer contour, the obstacle domain Ω remains almost the same from one iteration to the next. This is true even though the plateau value is only about 10 times smaller than the one associated with the initial guess and even though the corresponding velocity is not that small.

Figure 3 shows the best shape result (at the 227th iteration) and the variation of the objective functional J obtained with the 8 GHz dataset. Note that J now oscillates significantly during most of the search; this corresponds to a large variation of the retrieved domain Ω from one iteration to the next around the correct solution, a phenomenon at least partly associated with having prescribed a large value of Δt (ideally, Δt should be somehow decreased when J is decreasing, which is presently an option under study).

2.2. The rectangularly shaped metal cylinder (TM and TE data)

The inversion is first performed with the 8 GHz monochromatic TE dataset. The search domain $\mathcal{D}$ is a 3 cm sided square slightly shifted from the reference point O, and centred at (0 cm, -0.75 cm); it is discretized into 30×30 pixels. The supposedly known conductivity of the obstacle is taken as 3.1 S m^{-1}, the corresponding skin depth being $\delta \approx 3.19$ mm at

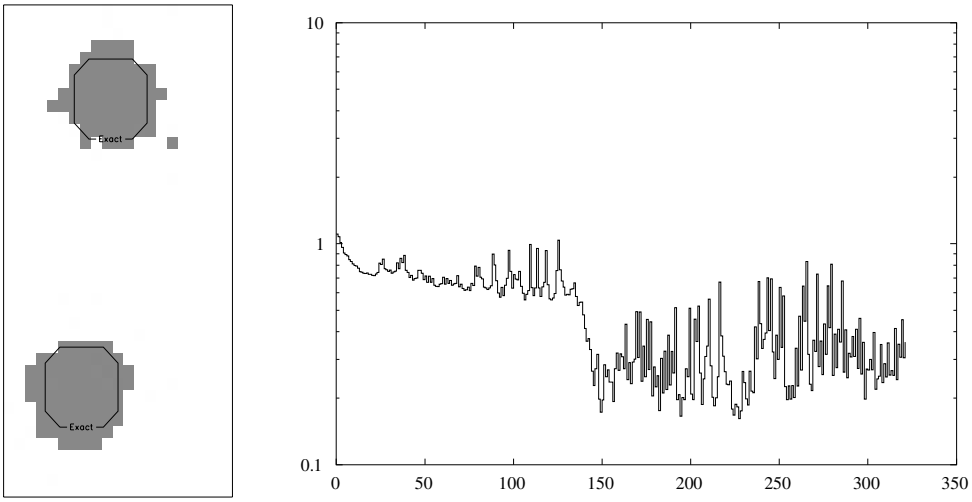

Figure 3. The two dielectric cylinders (TM data, twodielTM_4f.exp): monochromatic data (at 8 GHz). Left: best result (227th iteration); right: variations of the objective function as a function of the number of iterations. The time step is $\Delta t = 2 \times 10^{-2}$.

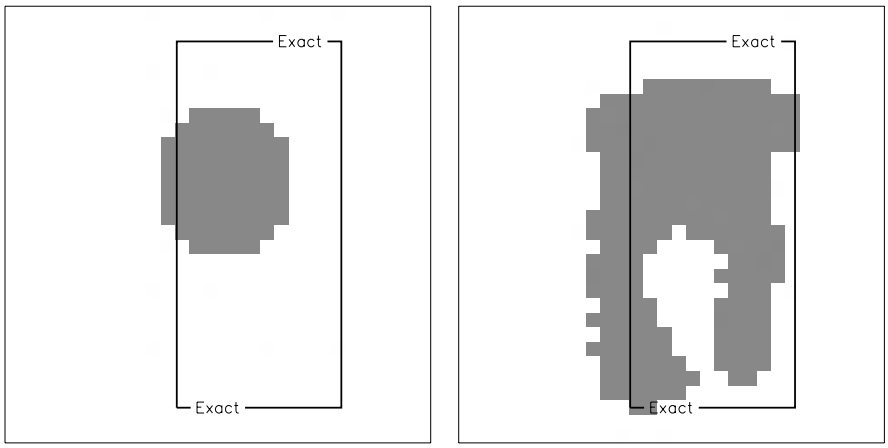

Figure 4. Rectangularly shaped metal cylinder (TE data, rectTE_8f.exp): monochromatic data (at 8 GHz). Left: initialization stage (by a disc of 0.5 cm radius); right: best results (81st iteration). The time step is $\Delta t = 10^{-7}$.

that frequency. The initial obstacle Ω_0 is circular (0.5 cm radius) and centred onto O. The best result (again, we mean the cross-sectional shape associated with the least value of J, not the one closest to the true one) is displayed in figure 4. Reconstruction is at best average, as is exemplified by the open cavity inside the obstacle; had it been closed, this would be a much better result, since the cavity would then be almost invisible due to reflection off the surrounding metal wall. The low decrease of the objective functional J (figure 6) confirms the challenge faced in the inversion.

Let us emphasize here that none of the inversions attempted from experimental data in this configuration (various frequencies, various initial shapes, various σ) have been more

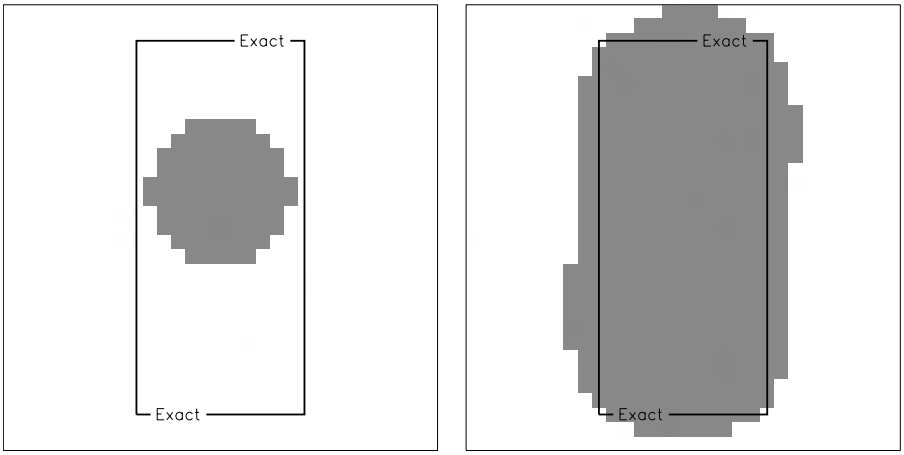

Figure 5. Rectangularly shaped metal cylinder (TM data, rectTM_8f.exp): monochromatic data (at 8 GHz). Left: initialization stage (by a disc of 0.5 cm radius); right: best results (81st iteration). The time step is $\Delta t = 5 \times 10^{-2}$.

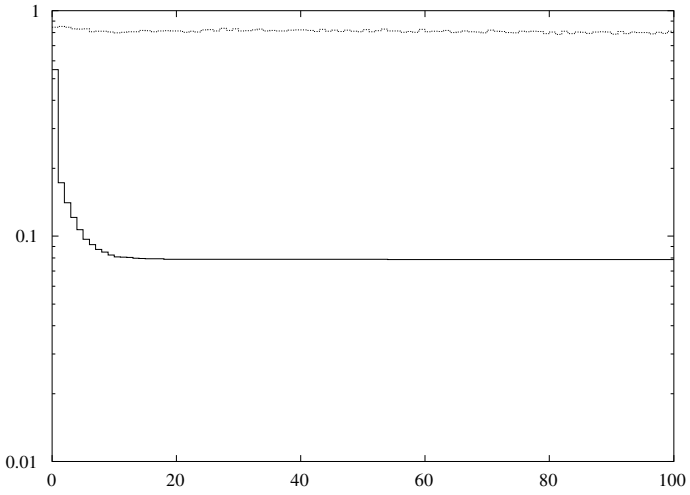

Figure 6. Rectangularly shaped metal cylinder (TM and TE data, rectTM_cent.exp, rectTE_8f.exp): monochromatic data (at 8 GHz). Variations of the objective function as a function of the number of iterations (see figures 4 and 5). Solid curve: TM case, dashed curve: TE case.

successful than this one. However, using synthetic data did not yield much better results in the TE case with an impenetrable obstacle—far fewer problems being encountered with a penetrable obstacle, as exemplified in Ramananjaona *et al* (2001a) in the more demanding case of burials in a half-space. By contrast, the inversion from TM data works well for both penetrable and impenetrable obstacles: this is illustrated in figures 5 and 6 by the retrieval of the rectangularly shaped metal cylinder from the 8 GHz TM dataset. The search domain $\mathcal{D}$ is of the same size as previously, but now centred at (-0.5 cm, -0.75 cm); it is discretized into 31×31 pixels. The initial obstacle Ω_0 is circular (0.5 cm radius) and centred at (-0.5 cm, -0.5 cm). The time step Δt is taken equal to $\Delta t = 5 \times 10^{-2}$.

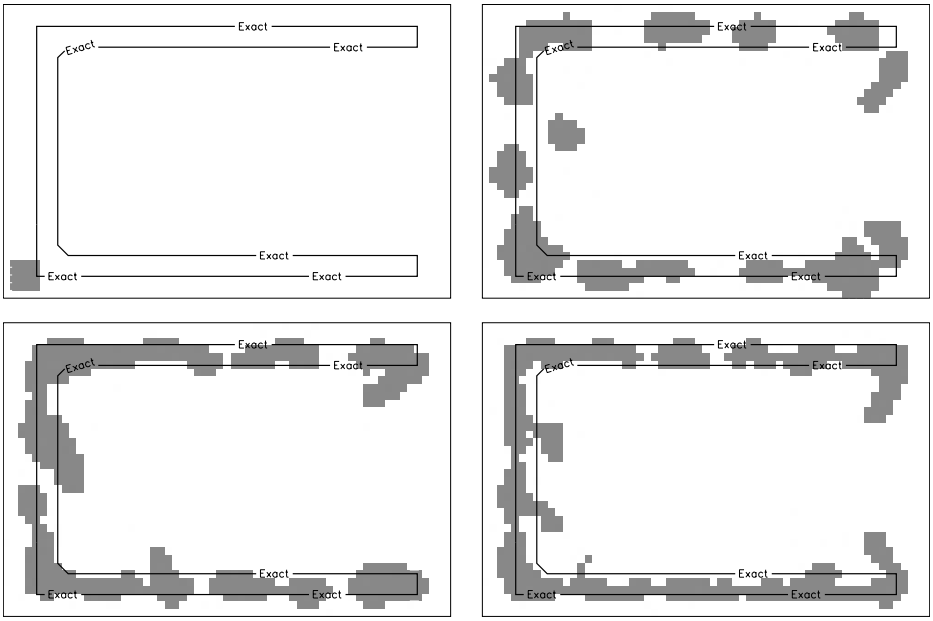

Figure 7. U-shaped metal cylinder (TM data, uTM_shaped.exp): monochromatic data (at 6, 8 and 10 GHz). Initialization by a square of 0.6 cm side (top left); best results at 6 GHz (top right), 8 GHz (bottom left) and 10 GHz (bottom right). The time step is $\Delta t = 10^{-2}$.

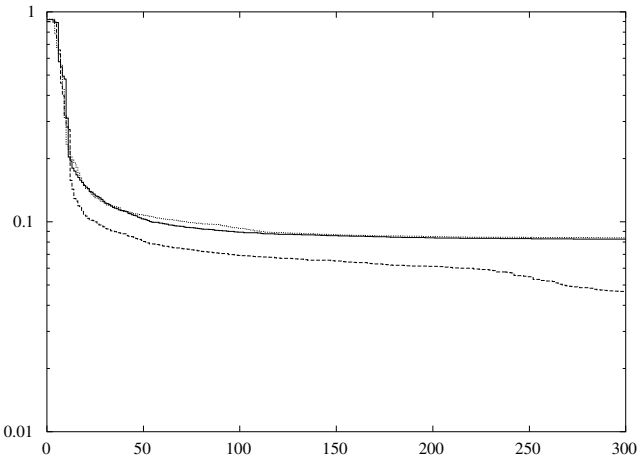

Figure 8. The U-shaped metal cylinder (TM data, uTM_shaped.exp): monochromatic data (at 6, 8 and 10 GHz). Variations of the objective function as a function of the number of iterations. Dashed curve: 6 GHz, solid curve: 8 GHz, dotted curve: 10 GHz.

2.3. The U-shaped metal cylinder (TM data)

The inversion is performed independently with the 6, 8 and 10 GHz monochromatic datasets—hopping from one dataset to the next did not improve the results. The search domain is a

9 cm × 6 cm centred rectangle discretized into 61 × 38 pixels. Conductivity $\sigma = 3.1$ S m^{-1} is kept constant for all three frequencies, the procedure being always started from a small square of 0.6 cm side placed in the left-hand lower corner of the search domain. All results are also computed with fixed time step $\Delta t = 10^{-2}$.

In terms of shape retrieval, in comparison to the true shape, rather good results are obtained for every frequency (figure 7), this being associated with a significant decrease of J (figure 8). Even in the absence of knowledge of the true shape, this is a quality check since the data fit is fair for the three operating frequencies whilst the shape itself is rather insensitive to variations of electrical size—the skin depth δ decreases from 3.69 mm at 6 GHz to 2.85 mm at 10 GHz.

However, this means that a true U-shape and a rather *broken* cross-sectional shape provide us with quite similar results in terms of scattering off the probing wave. Let us emphasize that we have attempted to penalize the shape retrieval in order to get a more regular shape (see Ramananjaona *et al* (2001b) for the corresponding theory and numerics) but the induced variations have been very small. It is necessary to suitably choose the initial shape for retrieving the said U. The initial obstacle here does not cover any metal parts of the U and also it is not located in between its branches. Otherwise, results would be poorer. That is, in this demanding configuration, the location of the initial obstacle has an evident impact on the whole level-set evolution.

One might also profit from the ability of the method to zoom in onto the sought obstacle. In Ramananjaona *et al* (2000) it has been shown that starting from a 10 cm × 10 cm square search domain $\mathcal{D}$ made of 47 × 47 cells provides a fair description of the U-shaped obstacle that can thus be taken as initial guess within the downsized (9 cm × 6 cm) and finer (61 × 38 cells) domain considered here.

3. Concluding remarks

The above results from laboratory-controlled experimental data indicate that the controlled evolution of a level set is a versatile and robust method, if good care is taken of several issues.

- One can treat penetrable and impenetrable objects, provided that the grid step is a fraction of the wavelength in the first case and of the skin depth in the second case. Shapes may be convoluted (the U-shape is typical), again if the grid allows a correct representation of the boundary, and even though this boundary has sharp corners.
- One can handle measurement errors provided that the data coverage (notably, enough directions of illuminations) is sufficiently broad, even at a single frequency. No regularization technique as proposed in Ramananjaona *et al* (2001b) has yet been proven effective with these experimental data.
- One can start from arbitrary initial cross-sectional shapes; for metal parts, it is better they not be included within the initial cross section once it is noted that in this case—for TM data only however—a rather simple back-propagation technique provides excellent first choices for single metal objects viewed from all around.
- One needs to choose an appropriate time step. The rule of thumb so far is that it should be neither too small to avoid lengthy computations nor too large to avoid brutal shape deformations, since divergence occurs beyond a certain threshold. However, the value of this threshold is mostly appraised from numerical experience.
- One should stop the calculation whenever the cost functional stabilizes at a low enough value (in the user's opinion) and the obstacle shape correspondingly freezes—even though the plateau may show successive growths and reductions and few pixels may correspondingly move inwards or outwards—since the resolution of the contour which one can achieve will not be finer than the space step.

References

Cuer M and Zolésio J-P 1988 Control of singular problem via differentiation of a Min–Max *Syst. Control Lett.* **11** 151–8

Dorn O, Miller E L and Rappaport C M 2000 A shape reconstruction method for electromagnetic tomography using adjoint fields and level sets *Inverse Problems* **16** 1119–56

Ferrayé R, Dauvignac J-Y, Pichot C, Barlaud M, Blanc-Féraud L and Zolésio J-P 2000 A boundary-oriented inverse scattering method based on contour deformations by means of PDE-driven level sets for radar imaging *Proc. European Microwave Week: Microwave Imaging Methods and Techniques (Paris, La Défence)* ed C Pichot and J-Y Dauvignac (Microwave Engineering—Europe) pp 12–19

Litman A, Lesselier D and Santosa F 1998 Reconstruction of a 2-D binary obstacle by controlled evolution of a level set *Inverse Problems* **14** 685–706

Ramananjaona C, Lambert M, Lesselier D and Zolésio J-P 2000 On the controlled evolution of level sets and its application to the retrieval of obstacles from microwave laboratory data *Proc. European Microwave Week: Microwave Imaging Methods and Techniques (Paris, La Défence)* ed C Pichot and J-Y Dauvignac (Microwave Engineering—Europe) pp 20–7

—— 2001a Shape reconstruction of buried obstacles by controlled evolution of a level set: from a Min–Max formulation to numerical experimentation *Inverse Problems* **17** 1087–111

—— 2001b On novel developments of the controlled evolution of level sets in the field of inverse shape problems *Proc. 2001 URSI Int. Symp. on Electromagnetic Theory (Victoria, Canada)* pp 459–61

Santosa F 1996 A level-set approach for inverse problems involving obstacles *ESAIM: COCV* **1** 17–33

Sethian J A 1999 *Level Set Methods and Fast Marching Methods* 2nd edn (Cambridge: Cambridge University Press)

Sokołowski J and Zolésio J-P 1992 *Introduction to Shape Optimization. Shape Sensitivity Analysis* (Berlin: Springer)

G

Diffraction par un objet tridimensionnel : développement basse-fréquence

[A.9] Conductive masses in a half-space Earth in the diffusive regime : Fast hybrid modeling in a low-contrast ellipsoid
Gaële Perrusson, Dominique Lesselier, Marc Lambert, Bernard Bourgeois, Antonis Charalambopoulos et George Dassios
IEEE Trans. Geosci. Remote Sensing (Special Issue on Computational Wave Issues in Remote Sensing, Imaging and Target Identification, Propagation and Inverse Scattering) **38** 1585-1599 2000
Préselectionn'e à l'issue de l'URSI Symposium, Salonique, 1998

Conductive Masses in a Half-Space Earth in the Diffusive Regime: Fast Hybrid Modeling of a Low-Contrast Ellipsoid

Gaële Perrusson, Dominique Lesselier, *Senior Member, IEEE*, Marc Lambert, Bernard Bourgeois, Antonios Charalambopoulos, and George Dassios

***Abstract*—Electromagnetic three-component magnetic probes at diffusion frequencies are now available for use in slim mineral-exploration boreholes. When a source is operated at or below the surface of the Earth in the vicinity of a conductive orebody, these probes provide, after appropriate processing, the secondary vector magnetic field attributed to this body. Proper inversion of the resulting datasets requires as a first step a clear understanding of the electromagnetic interaction of model signals with model bodies. In this paper, the response of a conductive ellipsoid buried at shallow depth in a half-space Earth is investigate by a novel hybrid approach combining the localized nonlinear approximation and the low frequency scattering theory. The ellipsoidal shape indeed fits a large class of scatterers and yet is amenable to analytical calculations in the intricate world of ellipsoidal harmonics, while the localized nonlinear approximation is known to provide fairly accurate results at least for low contrasts of conductivity between a scattering body and its host medium. In addition, weak coupling of the body to the interface is assumed. The primary field accounts for the presence of the interface, but multiple reflection of the secondary field on this interface is neglected. After analyzing the theoretical bases of the approach, numerical simulations in several geometrical and electrical configurations illustrate how estimators of the secondary magnetic field along a nearby borehole behave with respect to a general-purpose Method-of-Moments (MoM) code. Perspectives of the investigation and extensions, in particular, to two-body systems, strong coupling to the interface, and high contrast cases, are discussed.**

***Index Terms*—Approximation methods, conducting bodies, ellipsoids, geophysical inverse problems, geophysical measurements, Green function, integral equations, scattering, spheroids.**

I. Introduction

SIGNIFICANT progress in downhole electromagnetic exploration has resulted from the introduction of three-component measurement systems for use in slim mineral exploration boreholes.[1] Such systems provide the three complex components of the magnetic field due to a time harmonic source operated at a number of frequencies from a few tens of Hz to several kHz. The source is a surface loop of electrical current (surface-to-hole configuration), a magnetic dipole in a nearby borehole (cross-hole or tomographic configuration), or a magnetic dipole moved at a fixed, selectable distance from the sensor in the same borehole (single-hole configuration). The SlimBoris system [7] and the Arlett 3-component prototype probe [8] are representative of recent slimhole instruments.

The measured magnetic field components require appropriate processing or reduction since they contain the primary field (due to the source in a given geological background) as well as the secondary field (due to the unknown or partially unknown underground body). This secondary field contains, in an *encoded* fashion, information on the electric and geometric features of this body that can be retrieved by proper inversion (*decoding*). Location, sizing, orientation, shape reconstruction, and/or evaluation of average or local electric parameters may be targeted, depending upon data coverage, prior geological knowledge, inversion algorithms, and user's requirements.

Any satisfactory inversion relies in the first step on a sound understanding of the interaction between the probed body and the probing source. Three-dimensional (3-D) bodies of various geometries and electric properties, layered conductive environments, localized current sources, and vector near fields must be tackled. General-purpose Method-of-Moments (MoM) codes developed from vector volume integral formulations of the electromagnetic field, (e.g., EM3D and others [45], [32], [46], [47]), as well as from surface integral formulations [24], [25] are available. However, these codes may be computationally costly, whereas their internal functioning may not be obvious. Dedicated and computationally fast modeling tools bringing more insight to the behavior of the electromagnetic field thus remain worthwhile even at the price of less generality and less accuracy.

Combining the traditional and rigorous low frequency scattering theory [22], [14] and the localized nonlinear approximation (often termed the "extended Born approximation," and pioneered in a geophysical setting by [17] and recently extended to eddy current nondestructive evaluation [27]) may enable us to achieve this goal [35].

[1]Slim: most such boreholes are drilled with a 46 mm diameter, which is in contrast to the larger boreholes of oil field investigation.

Manuscript received September 19, 1999; revised March 22, 2000. This work was supported in part by a research contract from BRGM, Orléans, France, and in part by the Action Intégrée Franco-Hellénique Platon Contract.

G. Perrusson, D. Lesselier, and M. Lambert are with the Département de Recherche en Électromagnétisme-Laboratoire des Signaux et Systèmes, CNRS-SUPÉLEC-UPS, Gif-sur-Yvette, France (e-mail: lesselier@superlec.fr).

B. Bourgeois is with BRGM ARN/MSO, Orléans, France.

A. Charalambopoulos is with the Department of Mathematical and Physical Sciences, Polytechnic School, Aristotle University of Thessaloniki, Thessaloniki, Greece.

G. Dassios is with the Division of Applied Mathematics, Department of Chemical Engineering, University of Patras, Patras, Greece.

Publisher Item Identifier S 0196-2892(00)05906-4.

Letting k be the complex wavenumber of the host medium at the operation frequency, this *hybrid* modeling provides the low frequency (Rayleigh) dyadic series expansion in positive integral powers of (jk) of the *depolarization dyad*, which is characteristic of the body within the localized nonlinear approximation framework. This dyad acts upon the primary electric field at a given interior point and yields the total electric field at the same location. A wealth of analytical calculations [11] based on the theory of the ellipsoidal harmonics [18] leads to explicit forms of the real-valued dyadic coefficients of this expansion up to power $(jk)^3$ for a homogeneous general triaxial ellipsoid located in a homogeneous space, the materials of the ellipsoid, and the host medium being ideal lossy dielectrics. Spheroidal and spherical specializations are drawn up by exact asymptotic procedures. The expansion of the spherical depolarization dyad, already known up to $(jk)^2$ [17] and long-known static results [40] are retrieved as byproducts.

The low frequency expansion of the secondary magnetic field at any point exterior to the body immediately follows from the one of the primary electric field. The nth coefficient of this secondary field expansion may be interpreted as the field radiated by the nth coefficient of the expansion of volumetric electric sources. This coefficient combines those of the expansions of the depolarization dyad and of the primary electric field at the same order n and/or a lesser order. Alternatively, or in the absence of known expansion of the primary field, we may (or must) resort to numerical integration of the fictitious (Huygens) electric sources within the body calculated from the discrete values of a properly truncated expansion of the depolarization dyad times those of the exact primary electric field.

So far, this hybrid modeling has been applied to an infinite host space. Here, focus is on a more realistic half-space model of the Earth. The scope is larger but theoretical and numerical complexity increases markedly. The ellipsoidal body is buried at somewhat shallow depth and is arbitrarily orientated with respect to the flat Earth's surface (air is above). The electromagnetic source is located just beneath the surface or somewhat deeper so as to fit in both surface-to-hole and hole-to-hole configurations. *Weak* coupling of the body to the interface is assumed and often justified by experimental practice. The primary field accounts for the presence of the interface (new low frequency expansions of this field are established), but multiple scattering between this interface and the body is neglected (the depolarization dyad is the one of the body immersed in an infinite space which has the same electrical characteristics as the half space.

The paper is organized as follows. The main theoretical results already given in the case of a whole-space Earth [35] are discussed in Section II, with no attempt being made to cover the considerable analytical calculations detailed in [11]. The results are completed by a novel expansion of the primary field in a half space evaluated by following the analysis of [42]. Comparisons are shown in Section III between results calculated with the EM3D MoM code (available at BRGM [8]) and low frequency estimators of primary and secondary fields in a half-space and whole-space Earth for several electrical and geometric configurations. In Section IV, conclusive remarks are followed by a brief discussion of perspectives. Many complementary results are found in [33].

II. THEORETICAL RESULTS

A. Geometry, Electrical Parameters, and Main Modeling Assumptions

Let us refer to Fig. 1, in which a fixed Cartesian coordinate system with unit vectors $(\boldsymbol{x}, \boldsymbol{y}, \boldsymbol{z})$ and coordinates (x, y, z) is introduced. The host medium consists of a homogeneous linear isotropic and nonmagnetic half space extending from the $z = 0$ interface plane to $z = +\infty$. A homogeneous linear isotropic and nonmagnetic ellipsoidal body of semi-axes a_i, $a_1 \geq a_2 \geq a_3$ and of volume $V = 4\pi a_1 a_2 a_3/3$ is fully contained in this half space, its center being located on the z axis at depth p. The ellipsoidal coordinate system (ρ, μ, ν–) as a reminder [29] coordinate surfaces are ellipsoids (ρ = const.) and hyperboloids (μ =const., ν =const–) and a second Cartesian coordinate system that coincides with the principal axes of the ellipsoidal body (unit vector $\boldsymbol{x_i}$ and coordinate x_i) are defined. Note that the ellipsoid easily fits a large class of isolated scatterers while benefiting from a separable surface "(...) for which solutions of the boundary value problem may be found using separation of variables" [21]. An ideal time harmonic source (a horizontal thin-wire loop of current or a vertical magnetic dipole) is placed below the half-space interface at $\boldsymbol{r_S}(x_S, y_S, z_S)$. Known primary electric and magnetic fields $\boldsymbol{E_b}$ and $\boldsymbol{H_b}$ are generated at location $\boldsymbol{r}(x, y, z)$, and we are interested in calculating the secondary magnetic field $\boldsymbol{H_s}$ along a nonintersecting borehole R, which will be chosen as vertical in the numerical examples.

The static conductivity and permittivity of the half space and of the body are σ and ε, and ε_e and σ_e, respectively, and are assumed to be independent of angular frequency ω. Permeability $\mu = \mu_0$. The upper half space is air with constants ε_0 and μ_0. Using the dependence $\exp(-j\omega t)$, the complex wavenumbers of the host and body materials k and k_e satisfy $k^2 = j\omega\sigma\mu_0 - (j\omega)^2\varepsilon\mu_0$ and $k_e^2 = j\omega\sigma_e\mu_0 - (j\omega)^2\varepsilon_e\mu_0$, the wave numbers being taken with a positive imaginary part.

The above model is somewhat simple with respect to the full complexity of the Earth. One should refer to [43] for background reading and comments on the inaccuracy of the frequency-independent model in actual geological media. As for the consequences of an anisotropic host medium containing the conductive body, one should refer to [15] for the DC case (this corresponds to the zeroth-order term of the low frequency expansions). In practice, the exact parameters of the Earth are unknown or inaccurately known, and the primary field itself is unknown or inaccurately known. Reduction of the total magnetic field data is required to remove the primary field and retrieve the secondary field. Details of methods routinely employed at BRGM (e.g., reduction by the calculated free space primary field and reduction by the field measured at the lowest frequency), are found in [8]. More sophisticated reduction methods are currently appraised in the case of a significantly conductive layered Earth.

No assumptions are, in principle, made on the value of the body conductivity σ_e with respect to the one of the host medium σ. In the context of mineral exploration, ratio σ_e/σ is usually larger than 1. Moderately conductive bodies ($\sigma_e = 2\times10^{-2}$ and 2×10^{-1} S/m) in a moderately resistive Earth ($\sigma = 2 \times 10^{-3}$

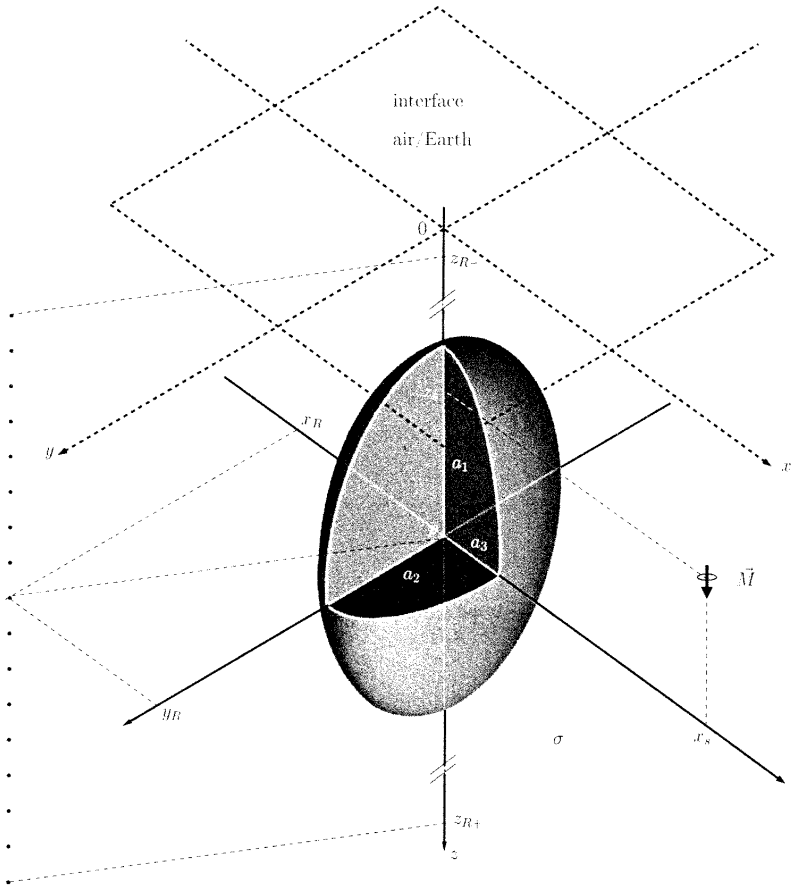

Fig. 1. Ellipsoidal body in a half-space Earth. One displays the particular configuration of a vertically-orientated general triaxial ellipsoid of elongated shape (its semi-axes are in the ratio $a_2/a_1 = a_3/a_2 = 1/2$; see Figs. 4, 7, and 8), which is illuminated by a vertically-orientated magnetic dipole $\boldsymbol{M}$ in the $(x,\ z)$ vertical plane and observed from a vertical borehole nearby. Only the absolute reference frame $(\boldsymbol{x},\ \boldsymbol{y},\ \boldsymbol{z})$ is shown. The ellipsoidal and Cartesian reference frames $(\rho,\ \mu,\ \nu)$ and $(\boldsymbol{x_1},\ \boldsymbol{x_2},\ \boldsymbol{x_3})$ attached to the ellipsoidal body are not represented for simplicity.

S/m) are chosen in the numerical examples. The body permittivity ε_e is not necessarily equal to the one ε of the host medium [35]. In the frequency range considered in mineral exploration, however, the polarization currents are negligible with respect to those of conduction. Here, the low frequency formulation will be specialized to the quasistatic case $k^2 = j\omega\sigma\mu_0$ and $k_e^2 = j\omega\sigma_e\mu_0$. The complete formulation including permittivity and conductivity contrasts and conduction and polarization currents is in [35].

B. Low Frequency Expansions Using the Localized Nonlinear Approximation

One starts from the assumption that a body of conductivity σ_e, specialized to an ellipsoidal body at some later point, is immersed in an infinite space having the same conductivity σ as the half space and is illuminated by primary fields $\boldsymbol{E_b}$ and $\boldsymbol{H_b}$. Combining the localized nonlinear approximation and the theory of low frequency scattering enables us to describe the wave field.

The localized nonlinear approximation [17], [41], [38], [48] is applied to the rigorous contrast-source vector domain integral formulation, which is satisfied by the total electric field $\boldsymbol{E}$ existing at any $\boldsymbol{r'}$ inside the body volume V. This body may not be of ellipsoidal shape (i.e., the formulation holds for any 3-D body with sufficiently smooth boundary). After some calculations that are detailed in the above references, this application yields the linear relationship $\boldsymbol{E}(\boldsymbol{r'}) = \overline{\boldsymbol{\Gamma}}(\boldsymbol{r'})\boldsymbol{E_b}(\boldsymbol{r'})$, where the dyad $\overline{\boldsymbol{\Gamma}}$ is termed as the depolarization dyad of the body. The secondary magnetic field $\boldsymbol{H_s}(\boldsymbol{r})$ induced at any $\boldsymbol{r}$ exterior to the body volume by the fictitious Huygens sources then reads

$$\boldsymbol{H}_s(\boldsymbol{r}) = \frac{1}{j\omega\mu_0}\left(k_e^2 - k^2\right)\int_V \nabla g(\boldsymbol{r}, \boldsymbol{r'}) \times \left[\overline{\boldsymbol{\Gamma}}(\boldsymbol{r'})\boldsymbol{E_b}(\boldsymbol{r'})\right]\, d\boldsymbol{r'} \tag{1}$$

where $g(\boldsymbol{r}, \boldsymbol{r'}) = e^{jk|\boldsymbol{r}-\boldsymbol{r'}|}/4\pi|\boldsymbol{r} - \boldsymbol{r'}|$ is the scalar free space Green's function. The depolarization dyad is derived by dyadic

operations that are effected onto the integral of g over volume V. Letting $\overline{\boldsymbol{I}}$ be the identity dyad, they amount to

$$\overline{\boldsymbol{\Gamma}}(\boldsymbol{r}') = \left[\overline{\boldsymbol{I}} + \frac{k_e^2 - k^2}{k^2}\overline{\boldsymbol{\Gamma}}(\boldsymbol{r}')\right]^{-1} \tag{2a}$$

$$\overline{\boldsymbol{L}}(\boldsymbol{r}') = -\left[k^2\overline{\boldsymbol{I}} + \nabla'\nabla'\right]\int_V g(\boldsymbol{r}', \boldsymbol{r})\, d\boldsymbol{r}. \tag{2b}$$

The above set of formulas can be directly tackled by discretization techniques such as the MoM [48], whereas the sphere case is amenable to a direct method [17] involving closed-form integration of the Green's function from its spherical wave function series, application of the needed differential operators onto the resulting series, and asymptotic expansion of the first terms in powers of the wave number up to $(jk)^2$. But the classical theory of low frequency scattering tells us that all electromagnetic quantities (primary and secondary wave fields, Green's functions) in three dimensions enjoy expansions in positive integral powers of (jk) of the form $\psi = \sum_n \psi_n (jk)^n$, which converge for k small enough. The real-valued nth term ψ_n, which can be scalar, vector, or dyadic and is independent of k, is found for every n by satisfying the wavefield integral equations and the constitutive relationships after expanding them in (jk) and collecting the terms of equal powers $(jk)^n$.

Well-known tutorials are those of [21] and [22], a comprehensive analysis of the state-of-the-art and much new material now being found in [14]. The necessary reading list on low frequency scattering by ellipsoids includes [39], [40], where the first three terms of the power series of the electromagnetic field due to the ellipsoid and its degenerate cases for a variety of boundary conditions are calculated [2]–[4], where the complete expansion of the field due to acoustically hard and acoustically soft spheroids illuminated by a plane pressure wave is constructed, [12] where the interaction of a plane elastic wave with a rigid ellipsoid is treated, and [9] where an acoustically soft ellipsoid is investigated under point source excitation. In these two papers, key material on ellipsoidal harmonics and related topics in the ellipsoidal geometry is given. Polarizability dyads, yielding the first terms of the expansions of scattering amplitudes, are considered in [20], [1], whereas the hollow ellipsoid is treated in [26].

Thus, the method of attack is to rigorously solve the integro-differential equations (1) and (2) within the low frequency realm. From the assumption that $\overline{\boldsymbol{L}}(\boldsymbol{r}') = \sum_n \overline{\boldsymbol{L}}_n(\boldsymbol{r}')(jk)^n$, the expansion of the Green's function and its gradient in power series of (jk) in (2b), the interchange in summation and integration and the subsequent identification of like powers of (jk) lead to

$$\begin{aligned}
4\pi\overline{\boldsymbol{L}}_0 &= -\nabla'\nabla'\int_V \frac{1}{R}\, d\boldsymbol{r} \\
\overline{\boldsymbol{L}}_1 &= \boldsymbol{0}, \\
4\pi\overline{\boldsymbol{L}}_n &= \frac{1}{(n-2)!}\overline{\boldsymbol{I}}\int_V R^{n-3}\, d\boldsymbol{r} \\
&\quad - \frac{1}{n!}\nabla'\nabla'\int_V R^{n-1}\, d\boldsymbol{r},\ n \geq 2
\end{aligned} \tag{3}$$

for any $\boldsymbol{r}'$ in V, letting $R = |\boldsymbol{r}' - \boldsymbol{r}|$. Using (3), the inverse dyad $\overline{\boldsymbol{\Gamma}}^{-1}(\boldsymbol{r}') = \sum_n \overline{\boldsymbol{T}}_n(\boldsymbol{r}')(jk)^n$ is easily calculated from (2a), since the multiplicative factor of the $\overline{\boldsymbol{L}}$ dyad is the frequency-independent contrast $\Delta\sigma/\sigma$, where $\Delta\sigma = \sigma_e - \sigma$. The dyadic coefficients $\overline{\boldsymbol{T}}_n$ are determined in closed form at $\boldsymbol{r}'$ (implied), and the first four coefficients are

$$\begin{aligned}
&\overline{\boldsymbol{T}}_0 = \overline{\boldsymbol{I}} + \frac{\Delta\sigma}{\sigma}\overline{\boldsymbol{L}}_0, \quad \overline{\boldsymbol{T}}_1 = 0, \quad \overline{\boldsymbol{T}}_2 = \frac{\Delta\sigma}{\sigma}\overline{\boldsymbol{L}}_2 \\
&\overline{\boldsymbol{T}}_3 = \frac{\Delta\sigma}{\sigma}\overline{\boldsymbol{L}}_3.
\end{aligned} \tag{4}$$

Since $\overline{\boldsymbol{\Gamma}}^{-1}\overline{\boldsymbol{\Gamma}} \equiv \overline{\boldsymbol{\Gamma}}\overline{\boldsymbol{\Gamma}}^{-1} \equiv \overline{\boldsymbol{I}}$, equating to 1 or canceling out the coefficients of like powers of (jk) in this equality leads to the expansion $\overline{\boldsymbol{\Gamma}}(\boldsymbol{r}') = \sum_n \overline{\boldsymbol{\Gamma}}_n(\boldsymbol{r}')(jk)^n$. The dyadic coefficients $\overline{\boldsymbol{\Gamma}}_n$ follow. At $\boldsymbol{r}'$ (implied), the first four coefficients are

$$\begin{aligned}
&\overline{\boldsymbol{\Gamma}}_0 = \overline{\boldsymbol{T}}_0^{-1}, \quad \overline{\boldsymbol{\Gamma}}_1 = \boldsymbol{0}, \quad \overline{\boldsymbol{\Gamma}}_2 = -\overline{\boldsymbol{T}}_0^{-1}\overline{\boldsymbol{T}}_2\overline{\boldsymbol{T}}_0^{-1} \\
&\overline{\boldsymbol{\Gamma}}_3 = -\overline{\boldsymbol{T}}_0^{-1}\overline{\boldsymbol{T}}_3\overline{\boldsymbol{T}}_0^{-1}
\end{aligned} \tag{5}$$

when the first four coefficients $\overline{\boldsymbol{T}}_n$ are known. Using the above results, the expansion $\boldsymbol{H_s}(\boldsymbol{r}) = \sum_n \boldsymbol{H_s}_n(\boldsymbol{r})(jk)^n$ of the secondary magnetic field at exterior point $\boldsymbol{r}$ can be constructed from the one of the primary electric fields. Since the expansion of the electric field can be demonstrated to begin at least at order 2 in a conductive medium, it is written as $\boldsymbol{E_b}(\boldsymbol{r}') = j\omega\mu_0\sum_n \boldsymbol{E_b}_{(n+2)}(\boldsymbol{r}')(jk)^n$ at interior point $\boldsymbol{r}'$, where the term $j\omega\mu_0 (= -(jk)^2/\sigma)$ has been factored out for the convenience of the calculation. Interchanging in summation and integration, reordering the products of series and collecting the coefficients of equal powers of (jk) in (1) provide the vector coefficients

$$\begin{aligned}
\boldsymbol{H_{s0}} &= \boldsymbol{H_{s1}} = \boldsymbol{0} \\
4\pi\boldsymbol{H_s}_n(\boldsymbol{r}) &= \int_V \frac{\boldsymbol{R}}{R^3} \times \boldsymbol{P}_n(\boldsymbol{r}', \boldsymbol{r})\, d\boldsymbol{r}', \quad n \geq 2
\end{aligned} \tag{6}$$

letting $\boldsymbol{R} = \boldsymbol{r} - \boldsymbol{r}'$ and $R = |\boldsymbol{R}|$. At $\boldsymbol{r}'$ and $\boldsymbol{r}$ (implied), the first four $\boldsymbol{P}_n$ coefficients are

$$\boldsymbol{P}_2 = \frac{\Delta\sigma}{\sigma}\overline{\boldsymbol{\Gamma}}_0\boldsymbol{E_b}_2 \tag{7a}$$

$$\boldsymbol{P}_3 = \boldsymbol{0} \tag{7b}$$

$$\boldsymbol{P}_4 = \frac{\Delta\sigma}{\sigma}\left(\overline{\boldsymbol{\Gamma}}_2\boldsymbol{E_b}_2 + \overline{\boldsymbol{\Gamma}}_0\left[\boldsymbol{E_b}_4 - \frac{R^2}{2}\boldsymbol{E_b}_2\right]\right) \tag{7c}$$

$$\boldsymbol{P}_5 = \frac{\Delta\sigma}{\sigma}\left(\overline{\boldsymbol{\Gamma}}_3\boldsymbol{E_b}_2 + \overline{\boldsymbol{\Gamma}}_0\left[\boldsymbol{E_b}_5 - \frac{R^3}{3}\boldsymbol{E_b}_2\right]\right). \tag{7d}$$

Note that the contribution of polarization currents to the low frequency expansions of the wave field requires us to expand $j\omega$ in power series of $(jk)^2$ using the equality $k^2 = j\omega\mu_0 - (j\omega)^2\varepsilon\mu_0$ in order to correctly calculate the multiplicative factor in (2a), $(k_e^2 - k^2)/k^2$. Additive terms consequently appear in the expressions of $\overline{\boldsymbol{\Gamma}}_2$ and $\boldsymbol{P}_4$ (they simplify somewhat if $\varepsilon = \varepsilon_e = \varepsilon_0$) once $j\omega$ is expanded up to the fourth order as $j\omega = -(1/\sigma\mu_0)(jk)^2 + (\varepsilon/\sigma^3\mu_0^2)(jk)^4$.

The secondary magnetic field in (6) appears to arise from volumetric electric current-like sources $\boldsymbol{P}_n$. Their unit Am^{n-2} depends on order n. The nth such source involves the action of the lth coefficient of the depolarization dyad expansion onto the mth coefficient of the expansion of the primary electric field, where $l + m \leq n$, $m \geq 2$. Note that the first nontrivial coefficient of the secondary magnetic field expansion is of order $n =$

2, even though the primary magnetic field expansion may begin at order $m = 0$ (power $(jk)^0$), as is the case (see Section II-C) of the current loop and the magnetic dipole. For a perfectly conducting body the first nontrivial secondary term would be of the same power $(jk)^0$. The nth source is varying with position $\boldsymbol{r'}$ throughout the body volume but at and beyond order 4, it also varies with the distance R between this source point $\boldsymbol{r'}$ and the observation point $\boldsymbol{r}$. When the body is small enough, however, the scattering phenomenon can be simplified by using constant integrands valued at the body center to bypass the volume integrations. $\boldsymbol{H_{s2}}$ becomes a purely dipolar field radiated by the electric source $\boldsymbol{P}_2 \equiv (\Delta\sigma/\sigma)\overline{\boldsymbol{\Gamma}}_0\boldsymbol{E_{b2}}$ at the body center. The higher-order coefficients $\boldsymbol{H_{s4}}$ and $\boldsymbol{H_{s5}}$ still retain a more complicated geometrical behavior because of the distance factors R^2 [in (7c)] or R^3 [in (7d)].

So far, we have not had recourse to the ellipsoidal shape hypothesis. The first three nontrivial dyadic coefficients of the expansion of $\overline{\boldsymbol{L}}(\boldsymbol{r'})$ and higher orders, whether wished for or not, must be calculated by carrying out repeatedly (for each $\boldsymbol{r'}$ of interest) a 3-D numerical integration of various singular integrands that have to account for the $\nabla'\nabla'$ differentiations. One may question the purpose of the analysis if a numerical solver can be directly applied to (1) and (2) instead. However, for a general triaxial ellipsoid, elegant and both numerically stable and computationally effective expressions of these three dyadic coefficients are rigorously reached. This involves cumbersome calculations based on the ellipsoidal harmonic theory [18]. In particular, appropriate Green's theorems are employed to transform most volume integrals into surface integrals, for which one can fully exploit the orthogonality of ellipsoidal harmonics, which yield much simpler forms of the coefficients involving well tabulated elliptic integrals. Some one-dimensional (1-D) integrals with respect to the ρ coordinate that have no expression in terms of special functions still emerge, but they are easily amenable to standard integration techniques. Note that all dyadic coefficients are reduced to purely analytical forms for the prolate spheroid ($a_1 > a_2 = a_3$), the oblate spheroid ($a_1 = a_2 > a_3$), and the sphere ($a_1 = a_2 = a_3$).

We will not repeat the above derivation. Some results are appended to [35], while the calculations are detailed by [11]. What is the most important to the argument of the paper is that the depolarization dyad $\overline{\boldsymbol{\Gamma}}$ is immediately followed by standard matrix analysis when the nontrivial coefficients of the expansion of $\overline{\boldsymbol{L}}$ up to order 3 are exhibited, which is the case in the general ellipsoidal coordinate system and in its degenerate forms. At any point $\boldsymbol{r'} = \sum_i x_i \boldsymbol{x_i}$ within volume V, the zeroth-, second-and third-order dyads are shown to be

$$\overline{\boldsymbol{\Gamma}}_0 = \sum_i \left[1 + \frac{\Delta\sigma}{\sigma} a_1 a_2 a_3 I_l^i\right]^{-1} \boldsymbol{x_i x_i} \tag{8a}$$

$$\overline{\boldsymbol{\Gamma}}_2 = -a_1 a_2 a_3 \sum_i \left[1 + \frac{\Delta\sigma}{\sigma} a_1 a_2 a_3 I_l^i\right]^{-2} \cdot \left[\frac{\Delta\sigma}{\sigma} \sum_j l_{ij} \boldsymbol{x_i x_j}\right] \tag{8b}$$

$$\overline{\boldsymbol{\Gamma}}_3 = -\frac{2}{9} a_1 a_2 a_3 \frac{\Delta\sigma}{\sigma} \sum_i \left[1 + \frac{\Delta\sigma}{\sigma} a_1 a_2 a_3 I_l^i\right]^{-2} \boldsymbol{x_i x_i} \tag{8c}$$

where I_1^i, $i = 1, \ldots 3$ is the well known elliptic integral

$$I_1^i \equiv I_1^i(a_1) = \tfrac{1}{2} \int_0^\infty \left[(t + a_i^2) R(t)\right]^{-1} dt,$$
$$R(t) = \prod_{j=1}^{3} \left[t + a_j^2\right]^{1/2}. \tag{9}$$

The zeroth-order dyad and the third-order dyad are simple (they are constant diagonal). The static-like coefficients of $\overline{\boldsymbol{\Gamma}}_0$ are those [40] has established with the assumption of incident plane waves, far scattered fields, and lossless embedding. In the spherical geometry, the known result $\overline{\boldsymbol{\Gamma}}_0 = 3\sigma/(2\sigma + \sigma_e)\overline{\boldsymbol{I}}$ [17] is retrieved. Note that when the ellipsoid is small enough, the purely dipolar secondary field $\boldsymbol{H_{s2}}$ may be equated to the field radiated by three mutually orthogonal electric dipoles (one along each semi-axis) whose amplitudes are proportional to $\boldsymbol{E_{b2}}.\boldsymbol{x_i}$. The magnitiude of the coefficients of proportionality (from $\overline{\boldsymbol{\Gamma}}_0$) and the lengths of the semi-axes vary alike for positive $\Delta\sigma$ (a "conductive" anomaly), and the converse is true for negative $\Delta\sigma$ (a "resistive" anomaly).

The second-order dyad $\overline{\boldsymbol{\Gamma}}_2$ is more complicated, though it is symmetric and still becomes purely diagonal at the center of the ellipsoid. The six independent coefficients l_{ij} given in [35] are convoluted but numerically stable combinations of closed-form analytical expressions given in terms of well-known elliptic integrals and of expressions requiring 1-D integration of elliptic functions with respect to ρ. With reference to the formulas in (3), the first expressions result from the $\nabla'\nabla'$ operation on the volume integral of R, whereas the second ones result from the volume integral of $1/R$ that enjoys a closed-form analytical expression for the oblate and prolate spheroids [11] and for the sphere [17] but not for the general triaxial ellipsoid.

Note finally that $\overline{\boldsymbol{L}}_4$ and thus $\overline{\boldsymbol{\Gamma}}_4$, which also involves an expansion of $(j\omega)$ up to $(jk)^6$ when the quasi-static assumption is not made may be found after cumbersome calculations currently in progress. A main problem to be met is that these calculations call for ellipsoidal harmonics of the fourth order, which result from the volume integral of R in (3), and the coefficients of the polynomial expressions of such harmonics in Cartesian coordinates are not known in analytical closed form, in contrast to what is happening with the lower order harmonics that have been employed to calculate the $\overline{\boldsymbol{L}}$ dyads of the third and lesser orders.

C. Low Frequency Expansion of the Primary Field in a Half Space

Let us consider a thin-wire circular loop of radius with a uniform current I (in A), located in a horizontal plane parallel to the flat Earth interface and buried at (in practice, very small) depth $z_S = h$ in the modeling half space of wave number k. Alternatively, we may consider a vertical magnetic dipole with amplitude M (in Am^2) at depth $h > 0$ (in practice, the dipolar source is located in the same borehole as the sensor or in a nearby borehole). Both sources radiate horizontally polarized (transverse electric with respect to the z axis) wave fields. This is true for the loop only if I is uniform, which is a realistic assumption at low frequency, referring to [44] for a general description of the TE and TM waves existing in a horizontally-layered Earth due to

nonuniform I. Such wave fields can, in principle, be expanded in integral powers of (jk). In principle, since an exact derivation of the low frequency expansion of the wave field in the half space does not seem to exist, and the one we sketch below is based on an approximation.

In a cylindrical coordinate system (coordinates (r, φ, z), unit vectors $(\boldsymbol{u_r}, \boldsymbol{u_\varphi}, \boldsymbol{u_z})$) with origin at the center of the loop or at the dipole location, the decomposition of the fields in terms of Hankel transforms to take advantage of the circular symmetry and the application of the boundary and radiation conditions yield the unique (azimuthal) component $E_{b\varphi}$ of the electric field $\boldsymbol{E_b}$

$$E_{b\varphi}(r, z) = j\omega\mu_0 \int_0^\infty \frac{jk\, s(\kappa)}{\sqrt{k^2-\kappa^2}} \cdot \left(e^{j\sqrt{k^2-\kappa^2}|z-h|} + \frac{\sqrt{k^2-\kappa^2}-j\kappa}{\sqrt{k^2-\kappa^2}+j\kappa} e^{j\sqrt{k^2-\kappa^2}(z+h)} \right) \cdot J_1(\kappa r)\, d\kappa \tag{10}$$

where J_1 is the Bessel function of the first kind and of zero order, and the source amplitude $s(\kappa)$ is equal to $(M/4\pi)\kappa$ for the magnetic dipole and to $(Ia/2)J_1(\kappa a)$ for the circular loop. The field is the sum of a direct contribution (the first term of the integrand) and a reflected contribution (the second term). The vertical and radial components of the magnetic field have similar expressions.

The approach employed in deriving the low frequency expansion of the electric field follows the one of [42]. Using $k^2 = j\omega\sigma\mu_0$ and assuming that $|k/\kappa|$ is small with respect to 1, the square roots within the integrand in the right-hand side of (10) are expanded up to power κ^2, the spectral integration being kept from 0 to $+\infty$. Upon reordering terms, we arrive at an expansion of the electric field up to order 4

$$E_{b\varphi}(r, z) = -(jk)^2 \int_0^\infty s(\kappa) \frac{e^{-\kappa|z-h|}}{\sigma} J_1(\kappa r)\, d\kappa + (jk)^4 \int_0^\infty s(\kappa) \cdot \left[\left(\frac{1}{2\sigma\kappa^2} + \frac{|z-h|}{2\sigma\kappa^2} \right) e^{-k|z-h|} - \frac{1}{4\sigma\kappa^2} e^{-\kappa(z+h)} \right] \cdot J_1(\kappa r)\, d\kappa. \tag{11}$$

In the dipolar case, the spectral integrations involved in the two coefficients of expansion (11) can be worked out, and closed-form expressions are obtained in terms of Gauss's hypergeometric functions [16], $\mathrm{F}(1/2, 1; 2, z)$

$$E_{b\varphi}(r=R\sin\theta,\, z=h+R\cos\theta) = -(jk)^2 \frac{M}{4\pi\sigma} \frac{\sin\theta}{R^2} + (jk)^4 \frac{M}{4\pi\sigma} \cdot \left[\begin{array}{l} \dfrac{(1-|\cos\theta|)\cot\theta}{2} + \dfrac{\tan\theta}{4} F\left(\dfrac{1}{2}, 1; 2; -\tan\theta^2\right) \\ -\dfrac{\sin\theta}{8(|\cos\theta|+2h/R)} F\left(\dfrac{1}{2}, 1; 2; -\dfrac{\sin\theta^2}{(|\cos\theta|+2h/R)^2}\right) \end{array} \right]. \tag{12}$$

When the same dipole is radiating in an infinite space with the same wave number k, one calculates

$$E_{b\varphi}(r=R\sin\theta,\, z=h+R\cos\theta) = -(jk)^2 \frac{M}{4\pi\sigma} \frac{\sin\theta}{R^2} + (jk)^4 \frac{M}{4\pi\sigma} \frac{\sin\theta}{2}. \tag{13}$$

The expansion (13) is exact and can be continued to infinity. Note that the fourth-order coefficients in the expansions (11)–(13) include supplementary terms when expanding up to the fourth order the term $j\omega\mu_0$ in factor of the integral in (10).

General expansion (11) and specialization (12) only comprise even powers of (jk) since the square roots in the integrand involve power $(k/\kappa)^2$. The first nontrivial term of either expansion is of power $(jk)^2$. It is the same as the first nontrivial term of the low frequency expansion of the electric field due to the same loop source or to the same dipole source in the infinite space [see (13)]. The next nontrivial term is of power $(jk)^4$. It accounts for the presence of the interface. Correspondingly, the magnetic field components can be expanded into even powers of (jk), the leading terms now being of power 0 (static-like) and equal to the leading terms in the infinite space, the influence of the interface being manifested only from power $(jk)^2$.

Note again that the expansion technique employed here is not traditional compared to the usual low frequency analysis. Other expansions might have been calculated by other means, and (11) and (12) are approximated. This is manifested in particular by the absence of the odd powers from $(jk)^5$ for the electric field and $(jk)^3$ for the magnetic field, though these terms exist in the exact infinite-space field expansions and should exist in those in the half space. Furthermore, there is no need to continue (11) and (12) to power $(jk)^6$, since the imaginary contribution of the sixth-order term should be much smaller than the missing imaginary contribution of the unknown fifth-order term.

III. NUMERICAL SIMULATIONS

A. Comparison Tools and Parameters of the Simulations

Numerical examples are presented for the magnetic dipole only. More results are available in [33], in particular for a current loop. In Figs. 2 and 3, primary electric fields calculated with and without accounting for the interface are compared, as well as exact forms and low frequency expansions. In Figs. 4–8, low frequency results are compared with results from the EM3D code. For application of this code, the ellipsoid is modeled as a parallelepiped of same volume, the sides of which are of the same ratios as those of the semi-axes and are parallel to or perpendicular with the interface. This parallelepiped is then divided into smaller ones according to the same rules.

The bodies under investigation are a general triaxial ellipsoid and an oblate spheroid. The ellipsoid is quite elongated since its semi-axes are in the ratio $a_2/a_1 = a_3/a_2 = 1/2$, letting $a_1 = 62$ m, the major axis being vertical (along the z axis) or horizontal (along the x axis). The oblate spheroid looks like a vertical circular plate, since the major semi-axes lie in the vertical (y, z) plane and are four times ($a_1 = a_2 = 62$ m) larger than the minor semi-axis ($a_3 = 15.5$ m).

Conductivity contrasts σ_e/σ between the body and the background medium are 10 : 1 or 100 : 1 ($\sigma_e = 2 \times 10^{-2}$ S/m or

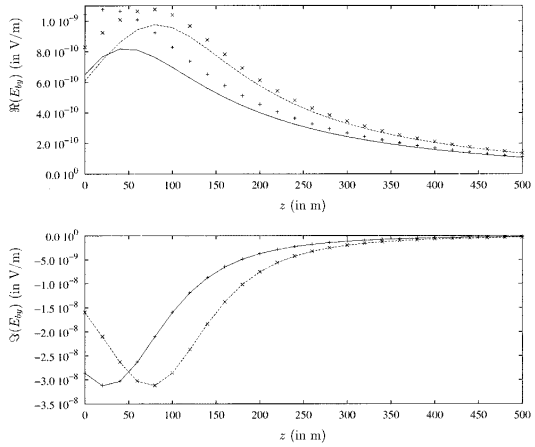

Fig. 2. Primary electric field due to a 500 Hz, 1 Am^2 vertically-orientated magnetic dipole (along $\boldsymbol{z}$) in an infinite or half space ($\sigma = 2 \times 10^{-3}$ S/m). Real and imaginary parts of the exact values of the y-component along the z axis are compared for a shallower source ($z_S = 25$ m) and a deeper ($z_S = 75$ m) source at fixed range ($x_S = 100$ m, $y_S = 0$) with those observed within an infinite Earth. $z_S = 25$ m, half space (—), infinite space $(+\ +\ +)$, $z_S = 75$ m, half space (- - -), infinite space $(\times\ \times\ \times)$.

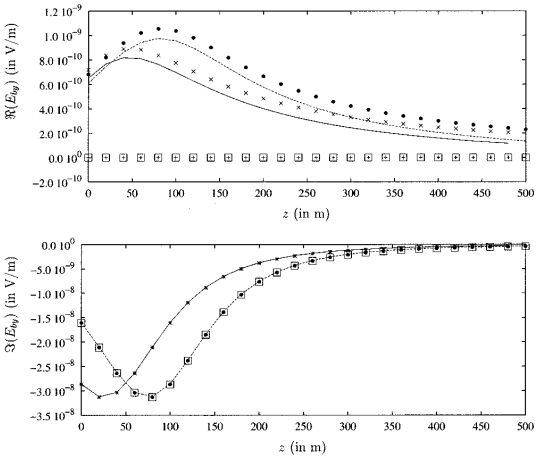

Fig. 3. Primary electric field due to a 500 Hz, 1 Am^2 vertically-oriented magnetic dipole (along $\boldsymbol{z}$) in the half-space Earth ($\sigma = 2 \times 10^{-3}$ S/m). Same as in Fig. 2, but the exact y-component values are now compared to those of its expansions up to powers $(jk)^2$ and $(jk)^4$. $z_S = 25$ m, exact (—), $(jk)^2(+\ +\ +)$, and $(jk)^4(\times\ \times\ \times)$; $z_S = 75$ m, exact (- - -), $(jk)^2$ (o o o), and $(jk)^4(\square\square\square)$.

2×10^{-1} S/m, $\sigma = 2 \times 10^{-3}$ S/m). Frequency is 500 Hz or 1000 Hz. Corresponding planar skin depths in the 2×10^{-2} S/m ellipsoid material, and the 2×10^{-3} S/m host material at 500 Hz are $\delta_e \approx 159$ m, and $\delta \approx 503$ m, respectively. They decrease to $\delta_e \approx 36$ m and $\delta \approx 356$ m, respectively, in the 2×10^{-1} S/m ellipsoid material and the 2×10^{-3} S/m host material at 1000 Hz.

The magnetic dipole with amplitude 1 Am^2 is orientated vertically downward and lies in the (x, z) vertical plane at $x_S = 100$ m and z_S smaller than or equal to the depth p of the body center. The calculated values are the real and imaginary parts of the components of the secondary magnetic field along a vertical line passing near the ellipsoidal body. Note that we are in a transmission mode since the borehole R is in the $(x < 0, y > 0)$ quadrant, and the source is in the $(x > 0, z \leq p)$ domain, and that the body in this configuration is *a priori* providing a predominantly galvanic response to which it is known that the localized nonlinear approximation is well suited. These values are calculated by the aforementioned EM3D MoM code and by low frequency expansions, an exact expansion (denoted as EE), a full expansion (FE) and a short expansion (SE).

For EE, the depolarization dyad is calculated from its closed-form expansion up to $(jk)^3$. The primary electric field is calculated from its exact integral form (10) in the half space, while in the case of the infinite space, the well-known dipolar field formula is used. The secondary magnetic field results from (1), the integration over volume V being performed numerically.

For FE, the depolarization dyad is calculated from its expansion up to $(jk)^2$. Correspondingly, the primary electric field in the half space is calculated from its expansion up to $(jk)^4$. The secondary magnetic field results from its expansion up to $(jk)^4$, the needed integration over volume V being performed numerically.

For SE, the depolarization dyad is equated to its static-like term. Correspondingly, the primary electric field is equated to the term of power $(jk)^2$, the same as in an infinite space, and is valued at the ellipsoid center. The secondary magnetic field results from the $(jk)^2$ term in (6) and (7a), the volume integration in (6) being reduced to a multiplication by V.

B. Main Comments

In Fig. 2, it is observed that the interface does not influence the preponderant imaginary part of the primary electric field even within a few meters of the interface and for the shallower 25-m-deep dipole ($z_S \approx \delta/20$). Only the much smaller real part is affected, the difference being stronger in the neighborhood of the source and quite visible only down to depths $\approx \delta/3$. Results not shown here also indicate that for a 150-m-deep dipole ($z_S \approx \delta/3$), the influence of the interface is negligible.

The agreement between the low frequency expansions and the exact values that are displayed in Fig. 3 is excellent for the imaginary part, and this is true both in the half space and in the infinite space since the term of power $(jk)^2$ is the same in both cases. The real part provided by the expansion to power $(jk)^4$ is varying with depth as the exact real part does, a small discrepancy, which is about constant to large depths for a given source location and of similar magnitude for the shallower source and for the deeper source being observed in the half-space case. This discrepancy may be attributed at least partially to the absence of terms of power $(jk)^5$ in the primary electric field expansion, which has no consequence on the large imaginary parts arising from power $(jk)^2$ but may be significant for the small real parts arising from power $(jk)^4$.

When the elongated ellipsoid of contrast 10 : 1 is considered at 500 Hz (Figs. 4 and 5), the vertical component of the secondary magnetic field calculated by the EE approach is in good agreement with the one calculated by the MoM code for both real and imaginary parts. This agreement is somewhat better

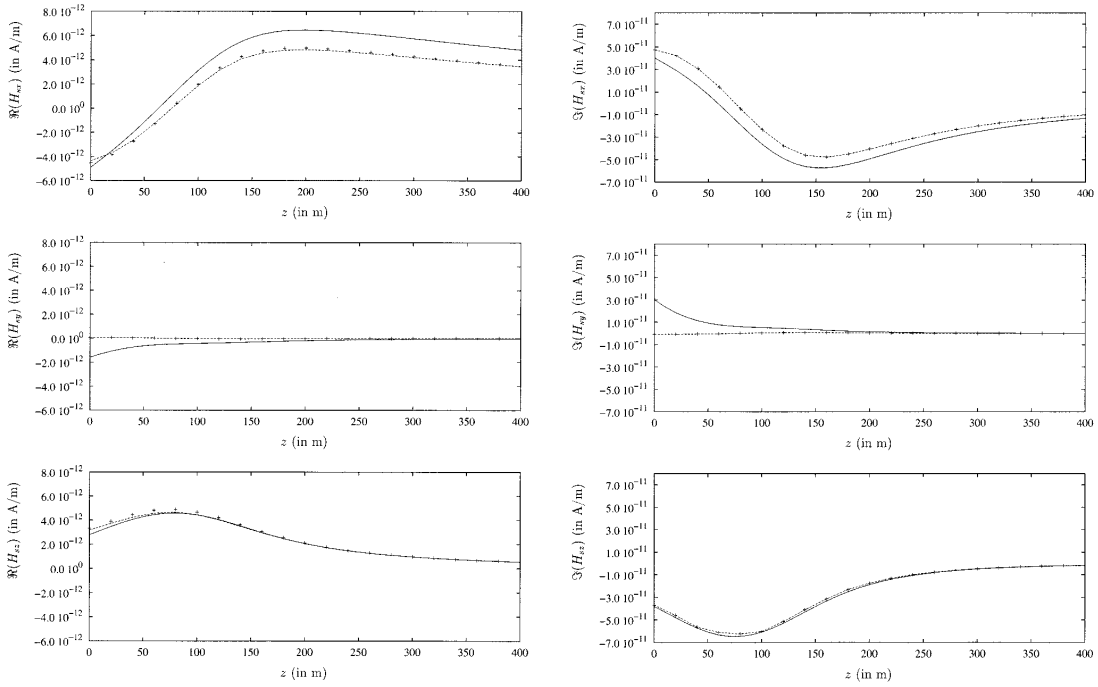

Fig. 4. Vertically-oriented elongated triaxial ellipsoid ($a_1 = 62$ m, $\boldsymbol{x_1}//\boldsymbol{z}$, $a_2 = 31$ m, $\boldsymbol{x_2}//\boldsymbol{y}$, $a_3 = 15.5$ m, $\boldsymbol{x_3}//\boldsymbol{x}$) of conductivity $\sigma_e = 2 \times 10^{-2}$ S/m is buried at $p = 75$ m in a less conductive Earth ($\sigma = 2 \times 10^{-3}$ S/m) and is illuminated by a 500 Hz, 1 Am^2 vertically-orientated magnetic dipole at ($x_S = 100$ m, $y_S = 0$, $z_S = 75$ m). (a) Real parts and (b) imaginary parts of the components of the secondary magnetic field are calculated along a ($x_R = -50$ m, $y_R = 90$ m) vertical line: exact expansion (EE) results in the case of the half space (- - -) and for an infinite space ($+ \ + \ +$), MoM results (—).

with the vertical orientation of the ellipsoid than with the horizontal orientation. As for the influence of the interface, it is weak (absent on the imaginary part, as expected from the primary field behavior) even if the dipole source is 75-m-deep ($z_S \approx \delta/7$) and the tip of the vertically-orientated ellipsoid is at only 38 m ($\approx \delta/14$) below the interface.

The horizontal components calculated by the MoM code and the exact expansion (EE) approach differ more from one another than the vertical parts do. The weak and fast-decaying y-component yielded by the MoM code (with no guarantee of accuracy) is not duplicated, the secondary magnetic field provided by the EE approach being much closer to 0 (it would be zero for symmetry with the SE approach). The real parts of the x-component are similar to one another, the vertical ellipsoid again yielding somewhat closer results than the horizontal one. The much stronger imaginary parts vary likewise, the agreement being better than for the real parts, in particular since the discrepancy between the MoM and EE imaginary parts vanishes below $\approx 2\delta/3$ while the MoM and EE real parts still differ by a small and constant additive term below $\approx \delta$. Again the influence of the interface is very weak (none on the imaginary part, very small on the real part).

When the response of the vertical plate-like spheroid with the same 10 : 1 contrast is considered at the same 500 Hz frequency (Fig. 6), the match of the vertical components appears quite good again. However, the interface has more influence on the real part than previously. This is expected since the spheroid is twice bigger than the ellipsoid and since, in view of its shape and orientation, the integration domain near the interface becomes much larger. The x-component is fairly reproduced but the y-component is not.

Increasing conductivity contrast (by a factor of 10) and operation frequency (by a factor of 2) should reduce the accuracy of the EE approach. Nevertheless, as shown in Fig. 7, the imaginary parts of the field, which are much stronger than with the lower contrast and frequency, remain fairly reproduced. Here the source is at $z_S \approx 0.4\delta$, and the interface has a small role. Other results (not shown) indicate that the EE approach is more accurate for a vertical orientation of the ellipsoid than for other orientations for the type of illumination considered so far.

The EE approach is more time consuming than the FE and SE approaches since it does not use the low frequency expansions of the primary field, and they use them. Results of the three approaches are compared in Fig. 8 for the 10 : 1 vertical ellipsoid at 500 Hz with reference to the MoM results. The SE approach, extremely fast since no integration is carried out, yields null real parts since it is confined to the zero-order static term of the secondary magnetic field, and due to symmetry, it ensures a null y-component in our configuration. The imaginary parts of the z-and x-components are very close to the MoM

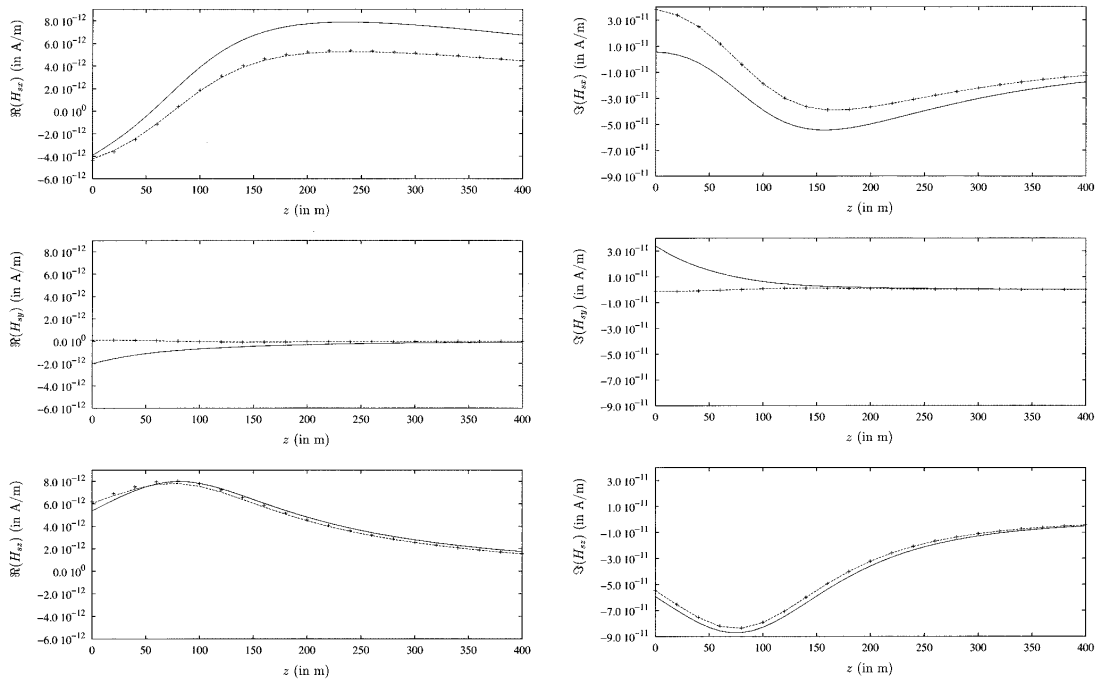

Fig. 5. Horizontally-oriented elongated triaxial ellipsoid ($a_1 = 62$ m, $\boldsymbol{x_1}//\boldsymbol{x}$, $a_2 = 31$ m, $\boldsymbol{x_2}//\boldsymbol{y}$, $a_3 = 15.5$ m, $\boldsymbol{x_3}//\boldsymbol{z}$) of conductivity $\sigma_e = 2 \times 10^{-2}$ S/m (see Fig. 4) is buried at $p = 75$ m in a less conductive Earth ($\sigma = 2 \times 10^{-3}$ S/m) and is illuminated by a 500 Hz, 1 Am^2 vertically-orientated magnetic dipole at ($x_S = 100$ m, $y_S = 0$, $z_S = 75$ m). (a) Real parts and (b) imaginary parts of the components of the secondary magnetic field are calculated along a ($x_R = -100$ m, $y_R = 80$ m) vertical line: EE in the case of the half space (- - -) and for an infinite space ($+\ +\ +$), MoM results (—).

results below ≈100 m ($\approx \delta/5$), the vertical component being reproduced well at shallower depths except near the source depth. The FE approach yields the same imaginary parts as the EE approach, which well reproduces the imaginary parts of the z-component and, to a lesser extent, of the x-component. The real parts the FE approach provides are fairly good for both components. For reasons not known to us, the x-component agrees better with the MoM results than the one calculated by the EE approach even though the plateau observed at large depth (e.g., beyond about 250 m ($\approx \delta/2$) is erroneous. This is not the case with the z-component for which the EE approach works successfully from very shallow depths, whereas some discrepancies are observed with the FE approach.

As noted earlier, expanding the primary field to $(jk)^4$ yields imaginary parts indistinguishable from the exact ones, but real parts that differ somewhat even at large depths. Since the secondary field results from depolarization dyad estimators acting on primary field estimators and involves integration over the whole ellipsoidal volume, small errors on the real parts of the components of the primary field may have adverse effects on the real parts of the components of the secondary field. Note that real parts of the magnetic fields are at least one order of magnitude smaller than imaginary parts. A strong discrepancy with a real part does not mean a strong discrepancy with the magnitude of the field component. The same phenomenon is observed with the sphere from the results of [17].

IV. Conclusion and Perspectives

Formulating the heuristic localized nonlinear approximation within the low frequency scattering theory yields a hybrid modeling of the electromagnetic behavior of a conductive general ellipsoidal body buried in a conductive half space when a magnetic dipole source or a current loop is on or below the interface. The analytical calculations to determine the low frequency expansion of the depolarization dyad of the ellipsoid are cumbersome. To a much lesser degree, this is also the case for the primary field in the half space. But the estimators of the exterior magnetic field are computationally simple and remain stable in the case of degeneracy to spheroidal and spherical bodies, and they are reasonably accurate for moderate but still realistic conductivity contrasts and commensurate exploration frequencies. Though limited to a low frequency range, further use of the results can be found in checking numerical solvers designed for general shapes. Last but not least, the intricate 3-D inversion of electromagnetic geophysical data can sometimes be viewed as the simpler search of an "equivalent" body with few geometric and constitutive parameters. An ellipsoidal body gives much geometric freedom in the search, while the hybrid electromagnetic modeling brings good insight into the diffusive wave field scattering involved and may enable us to associate individual terms in the low frequency expansions with particular properties of the body. All of this might be good justification

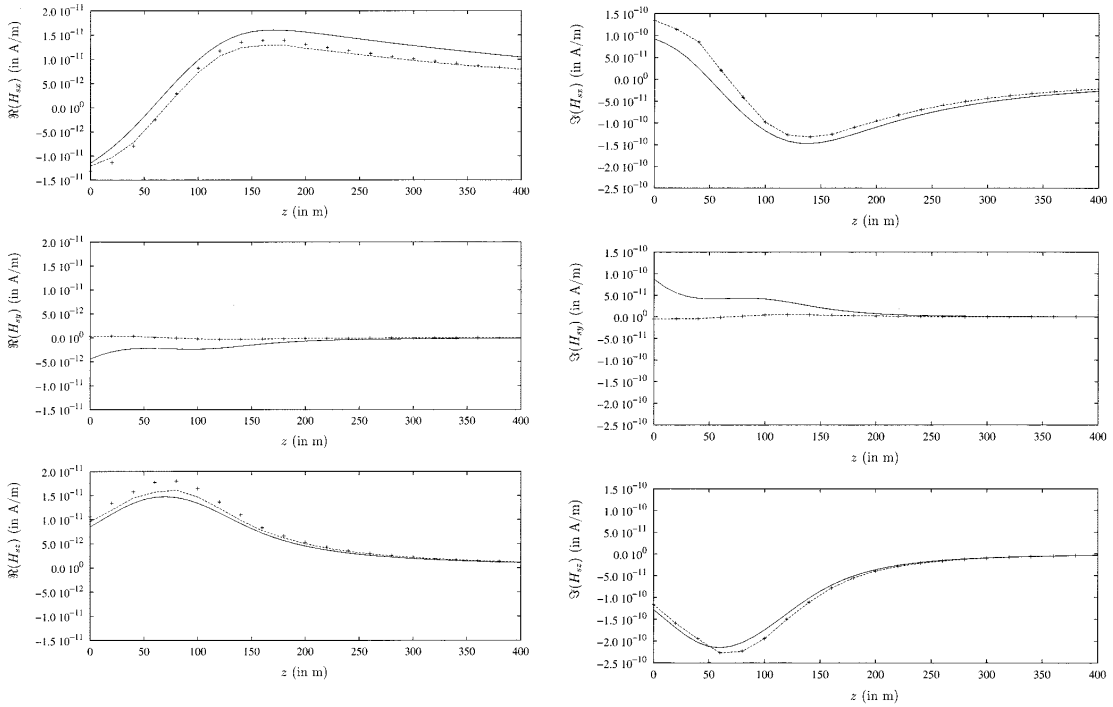

Fig. 6. Plate-like, vertically-oriented oblate spheroid ($a_1 = 62$ m, $\boldsymbol{x_1}//\boldsymbol{z}$, $a_2 = 62$ m, $\boldsymbol{x_2}//\boldsymbol{y}$, $a_3 = 15.5$ m, $\boldsymbol{x_3}//\boldsymbol{x}$) of conductivity $\sigma_e = 2 \times 10^{-2}$ S/m is buried at $p = 75$ m in a less conductive Earth ($\sigma = 2 \times 10^{-3}$ S/m) and is illuminated by a 500 Hz, 1 Am^2 vertically-orientated magnetic dipole at ($x_S = 100$ m, $y_S = 0$, $z_S = 25$ m). (a) Real parts and (b) imaginary parts of the components of the secondary magnetic field are calculated along a ($x_R = -50$ m, $y_R = 80$ m) vertical line: EE in the case of the half space (- - -) and for an infinite space ($+ \ + \ +$), MoM results (—).

for presenting the results, but several issues thought to restrict the scope of the modeling still deserve the following comments.

A. Specialization to an Ellipsoidal Shape

The ellipsoid is a highly versatile single body. Its surface of the second degree easily matches many bodies of smooth boundary with no imposed symmetries and proportions through free choice of the three semi-axes. Furthermore, it enjoys the advantages of the most general form of separable coordinate systems: the ellipsoidal one. Most other separable systems [29] are so peculiar that they have no use in the geophysical mining context, and the simpler spheroidal and spherical cases directly proceed from the general case by asymptotic arguments. Also, we still know very little about ellipsoidal or Lamé wave functions, as was underlined almost 50 years ago in [6]. But the low frequency method of attack obviates the need to expand the Green's function in terms of these functions and enables us to benefit from the accessible theory of ellipsoidal harmonics without recourse to general numerical solvers.

As for parallelepipeds, lack of separability in the Cartesian coordinate system evidently forbids us to proceed likewise. Nevertheless, their low frequency behavior [22] is close to the one of the corresponding ellipsoids except for extreme values of material, source, and sensor parameters. This observation in effect underpins the comparison with the results provided by the EM3D code, though one should keep in mind that accuracy of this code requires a careful parametrization and may still not be assured, especially in the absence of many comparison results.[2]

B. Use of a Canonical Source Only

The source is specialized in the simulations to the ideal magnetic dipole, which is a safe assumption for sources commonly used in boreholes. Current sources placed on the Earth's surface (surface-to-hole configuration), especially if they are modeled as a circular loop of the same area as the approximately square loop of common use, are considered likewise. Indeed, both situations enable explicit low frequency expansions of the primary electric fields, at least up to power $(jk)^4$. The wave field due to an electric dipole could be worked out similarly. Complicated sources may require us to stop the analytical work at the depolarization tensor expansion and estimate its action on the primary electric field by numerical integration in the absence of low frequency expansions of this field.

[2]Results are available for the penetrable sphere in a conductive infinite space illuminated by a magnetic dipole [17] via exact Mie series expansions. Spheroidal wave function expansions for spheroidal bodies in a vacuum illuminated by a plane wave exist for a perfectly conducting spheroid [37] or a dielectric one, but a corresponding solution for a dipole is not known by us. Such expansions do not exist for the general ellipsoid. T-matrix approaches pioneered by [5] and exemplified by [36] may be used.

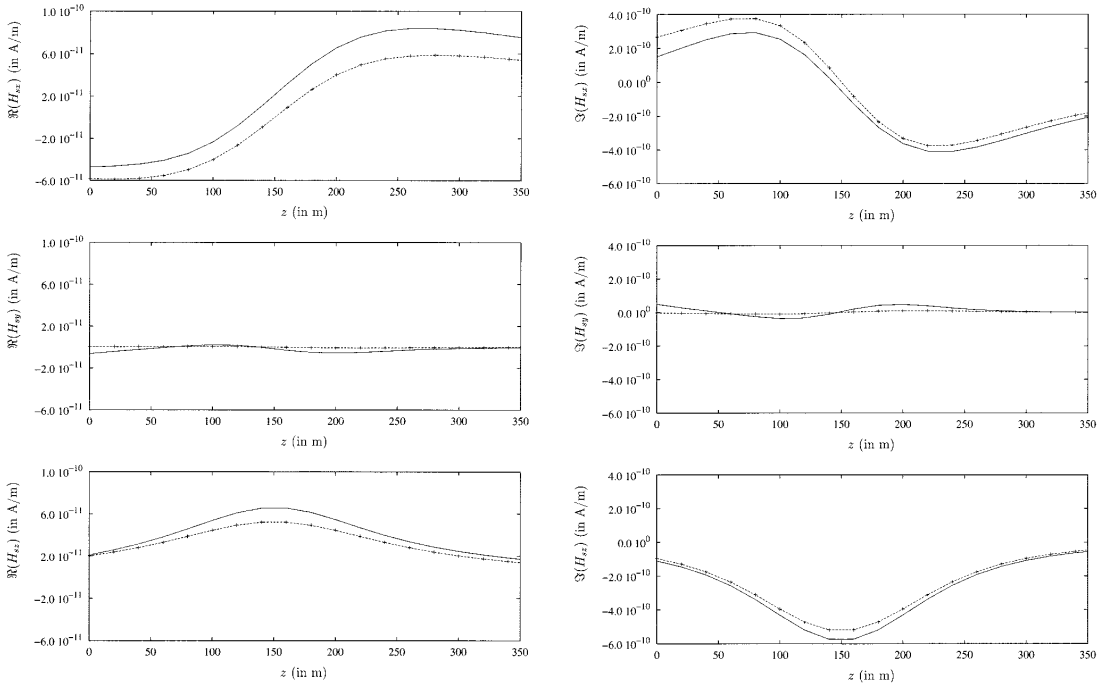

Fig. 7. Vertically-oriented elongated triaxial ellipsoid ($a_1 = 62$ m, $\boldsymbol{x_1}//\boldsymbol{z}$, $a_2 = 31$ m, $\boldsymbol{x_2}//\boldsymbol{y}$, $a_3 = 15.5$ m, $\boldsymbol{x_3}//\boldsymbol{x}$) of conductivity $\sigma_e = 2 \times 10^{-1}$ S/m (see Fig. 4) is buried at $p = 150$ m in a much less conductive Earth ($\sigma = 2 \times 10^{-3}$ S/m) and is illuminated by a 1000 Hz, 1 Am^2 vertically-orientated magnetic dipole at ($x_S = 100$ m, $y_S = 0$, $z_S = 150$ m). (a) Real parts and (b) imaginary parts of the components of the secondary magnetic field are calculated along a ($x_R = -50$ m, $y_R = 90$ m) vertical line: EE in the case of the half space (- - -) and for an infinite space ($+\ +\ +$), MoM results (—).

C. Depolarization Dyad in an Infinite Space

Here the ellipsoid is assumed to be weakly coupled to the medium interface with only the primary field accounting for it. This is, in particular, compatible with somewhat deep metallic ores since the secondary field is a few orders of magnitude less than the primary field in the borehole and multiple reflections on the interface are invisible. However, this assumption may fail for shallower objects (e.g., in the 50 m range) at higher frequencies (e.g., in the 100 kHz range), and *a fortiori* in ground penetrating radar (GPR) applications [47].

A remedy might be a (possibly repeated) three-step procedure. Calculate the secondary electric and magnetic fields at the interface from the action of the depolarization dyad of the body in infinite space onto the primary field (which includes the interface effects), determine their reflection on the interface via a proper spectral analysis, and use the resulting electric field as the new primary field in the body volume. There seem not to be many attempts in that direction except [24], [25]. Here the critical task is the calculation of the reflected fields. In harmony with the hybrid analysis, the static-like equivalence of the ellipsoid with three electric dipoles could be employed, the new primary electric field being calculated by modeling to the same zeroth order the interaction of these dipoles with the interface.

A satisfactory approach would be to use a low frequency expansion of the depolarization dyad, which better accounts for the coupling. To our knowledge, low frequency expansions of this type have not been exhibited in electromagnetics even in the simplest spherical geometry. [13] handles the planar acoustic illumination of a 3-D, arbitrarily shaped scatterer above a plane when Dirichlet and/or Neumann boundary conditions are imposed. But the analysis must be specialized to a sphere in the bispherical coordinate system. Unfortunately, no generalization of this system exists for the ellipsoid that would get the first nontrivial term explicitly and forego the solution of boundary value problems for the body and its image with respect to the plane.

The exact image theory [23], [30] has produced the polarizability dyad. Acted upon by the primary field, it yields the far-field of a dielectric body placed near a dielectric half space when illuminated by a plane wave in air. This dyad accounts for the polarizability dyad of the body in free space and reflection on the interface, but this is only valid for a sphere small enough to contain a uniform primary field. Using the zeroth-order polarizability dyad of the ellipsoid seems an easy step forward. However, near fields, localized sources, and conductive materials are highly challenging.

The localized nonlinear approximation is an excellent model of the behavior of a metal plate or tube affected by a 3-D void or inclusion at eddy current frequencies [27], [28]. Discrete values of the depolarization dyad are obtained from the volume integration of the diagonal components of the electric-electric dyadic Green's function (known in closed-form in the spectral plane

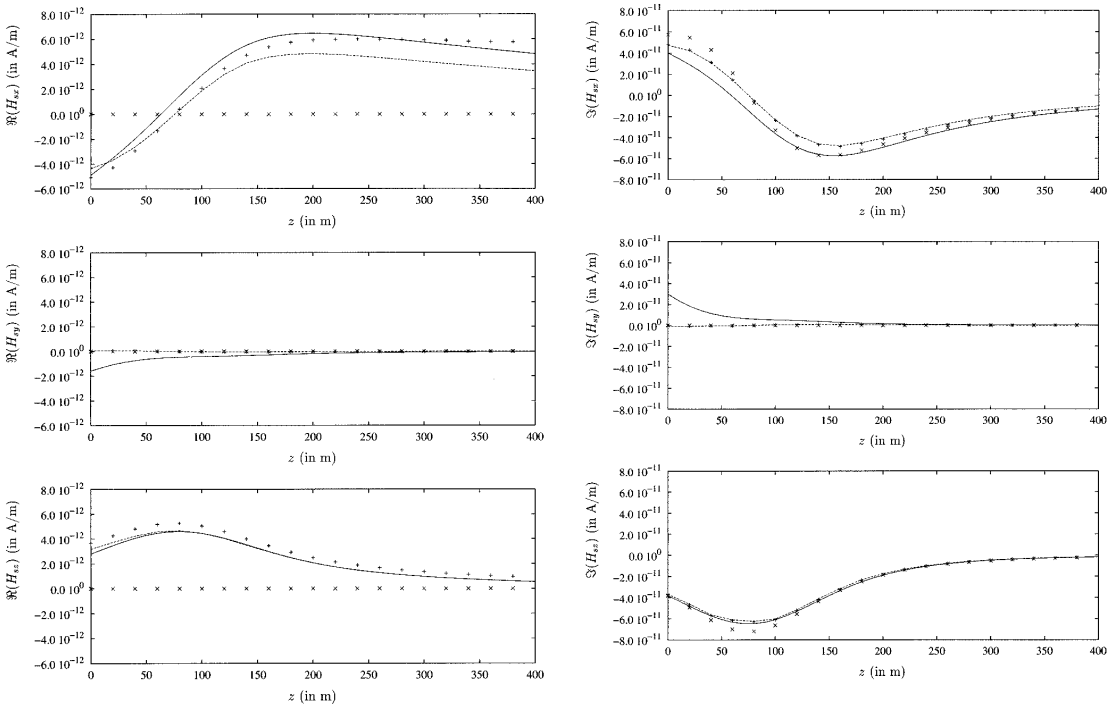

Fig. 8. Same as in Fig. 4, but several low frequency estimates of (a) the real parts and (b) imaginary parts of the components of the secondary magnetic field are now compared for the same half space. EE (- - -), full expansion (FE) (+ + +), short expansion (SE) (x x x), MoM results (—).

associated with the lateral coordinates) after application of a MoM to the contrast-source vector integral formulation of the electric field. This approach is promising for geophysical applications in the diffusive regime. A more physically interpretable and less computationally involved model should result from a low frequency expansion of the dyadic Green's function itself.

D. Limitation to an Isolated Body

A two-body system (e.g., two interacting ellipsoidal bodies) and even a multiple-body system may be modeled by successively considering primary fields that are accounting for the presence of the other body(ies), the degree of complexity being expected low when the three-dipole ellipsoidal equivalence is used. That the lack of separable coordinates associated to the two-body system considerably hinders the theoretical analysis of this multiple scattering problem is obvious in the ellipsoidal geometry. So far, acoustically soft spheres of unequal radii are rigorously treated in the low frequency realm [10] using bispherical coordinates, for which the Laplace equation is separable, and the Helmholtz equation is not. If lossy dielectric prolate spheroids are analyzed by [31], who employ the rotational-translational addition theorems of the spheroidal vector wave functions to transform the wave scattered by one spheroid into the one impinging onto the other, asymptotic extraction of low frequency expansions from their results seems almost intractable.

E. Application to Low-Contrast Cases Only

The accuracy of the hybrid model is not greater than that of its components. Our investigation here, the results of [35], the pioneering studies of [17], and the subsequent works of [41] and [38] show that, in the diffusive regime, the localized nonlinear approximation is excellent for bodies more resistive than their environment (contrasts σ_e/σ less than 1) and moderately conductive ones (σ_e/σ less than 10 or so) and remains satisfactory up to contrasts of at least 100 for a spherical body. However, there is a clear dependence on the source and sensor location. The slower the preponderant components of the primary electric field vary in the body volume, the better the accuracy, whereas reciprocity is not satisfied. As for the low frequency modeling, it appears robust provided that the primary field expansion is of sufficient order.

An alternative path may be followed, which is somewhat novel in theoretical terms and is *a priori* computationally effective. Work is currently in progress [34][3] Consider the

[3]Kaufman and Keller [19] show that a low frequency approximation of the first nontrivial terms of the series representing the exact secondary fields reproduces the fields due to the interaction of a conductive sphere with a transverse magnetic dipole or an axial dipole in a conductive host medium. The source radiating such approximated secondary fields consists of two magnetic dipoles and one electric dipole that are mutually orthogonal and coincident at the sphere center. However, this approach fails to accommodate for a highly conductive sphere, especially since the magnitude of the first neglected term is not smaller than the one of the term kept.

interaction of a magnetic dipole with a "perfectly conducting" ellipsoid, by which it is meant that the body is conductive to extremely conductive (a few S/m to a few 10^3 S/m) and is located in a resistive host medium (a few 10^{-3} S/m and less) [8], the frequency of excitation being such that the skin depth in the body material is much smaller than the body dimensions. Two potential problems in ellipsoidal coordinates that are coupled together (since the source of the second one is expressed from the solution of the first) can be defined. Their solutions are the zeroth-and second-order coefficients of the low frequency expansion of the exterior magnetic field and are developed in series of weighted ellipsoidal harmonics.

ACKNOWLEDGMENT

The authors wish to thank the keen interest of T. Habashy, Schlumberger Doll, Ridgefield, CT, in the investigation. The contribution of B. Duchêne to other avenues of the research summarized here is also acknowledged.

REFERENCES

[1] T. S. Angell and R. E. Kleinman, "Polarizability tensors in low frequency inverse scattering," *Radio Sci.*, vol. 22, no. 7, pp. 1120–1126, 1987.

[2] J. S. Asvestas and R. E. Kleinman, "Low frequency scattering by spheroids and disks 1. Dirichlet problem for a prolate spheroid," *J. Inst. Math. Applicat.*, vol. 6, pp. 42–56, 1969.

[3] ——, "Low frequency scattering by spheroids and disks 2. Neumann problem for a prolate spheroid," *J. Inst. Math. Applicat.*, vol. 6, pp. 57–75, 1969.

[4] ——, "Low frequency scattering by spheroids and disks 3. Oblate spheroids and disks," *J. Inst. Math. Applicat.*, vol. 6, pp. 157–163, 1970.

[5] P. Barber and C. Yeh, "Scattering of electromagnetic waves by arbitrarily shaped dielectric bodies," *Appl. Opt.*, vol. 14, no. 12, pp. 2864–2872, 1975.

[6] H. Bateman, "Higher transcendental functions," in *The Bateman Manuscript Project*, A. Erdelyi, Ed. New York: Mac Graw Hill, 1953, vol. 3, pp. 91–166.

[7] B. Bourgeois and C. Alayrac, "The borehole Slingram method in mineral exploration using the SlimBoris system," in *Proc. 61st Eur. Assoc. Geosci. Eng. Meeting*, Helsinki, Finland, June 8–12, 1999.

[8] B. Bourgeois, D. Legendre, M. Lambert, and G. Hendrickson, "ARLETT: A prototype 3-component borehole electromagnetic system," in *Three-Dimensional Electromagnetics*, ser. Soc. Expl. Geophys., M. L. Oristaglio and B. R. Spies, Eds. Tulsa, OK, 1999, pp. 625–657.

[9] A. Charalambopoulos and G. Dassios, "Scattering of a spherical wave by a small ellipsoid," *IMA J. Appl. Math.*, vol. 62, pp. 117–136, 1999.

[10] A. Charalambopoulos, G. Dassios, and M. Hadjinicolaou, "An analytic solution for low frequency scattering by two soft spheres," *SIAM J. Appl. Math.*, vol. 58, pp. 370–386, 1998.

[11] A. Charalambopoulos, G. Dassios, G. Perrusson, and D. Lesselier, "The localized nonlinear approximation in ellipsoidal geometry. A novel approach to the low frequency scattering problem," , to be published.

[12] G. Dassios and K. Kiriaki, "The rigid ellipsoid in the presence of a low frequency elastic wave," *Quart. Appl. Math.*, vol. 43, no. 4, pp. 435–456, 1986.

[13] G. Dassios and R. E. Kleinman, "Half space scattering problems at low frequencies," *IMA J. Appl. Math.*, vol. 62, no. 1, pp. 61–79, 1999.

[14] ——, *Low Frequency Scattering*. Oxford, U.K.: Oxford Univ. Press, 2000.

[15] M. J. Flykt, E. H. Eloranta, K. I. Nikoskinen, I. V. Lindell, and A. H. Sihvola, "DC potential anomalies caused by a conducting body in an anisotropic conducting half space," *IEEE Trans. Geosci. Remote Sensing*, vol. 34, pp. 27–32, Jan. 1996.

[16] S. Gradshteyn and I. M. Ryzhik, *Table of Integrals, Series, and Products*. New York: Academic, 1965, pp. 711–712 and 1039–1042.

[17] T. M. Habashy, R. W. Groom, and B. R. Spies, "Beyond the Born and Rytov approximations: A nonlinear approach to electromagnetic scattering," *J. Geophys. Res.*, vol. 98, no. B2, pp. 1759–1775, 1993.

[18] E. W. Hobson, *The Theory of Spherical and Ellipsoidal Harmonics* New York, 1955.

[19] A. A. Kaufman and G. V. Keller, *Inductive Mining Prospecting*. Amsterdam, The Netherlands: Elsevier, 1985.

[20] J. B. Keller, R. E. Kleinman, and T. B. A. Senior, "Dipole moments in Rayleigh scattering," *J. Inst. Math. Applicat.*, vol. 9, no. 1, pp. 14–22, 1972.

[21] R. E. Kleinman, "The Rayleigh region," *Proc. IEEE*, vol. 53, pp. 818–856, Aug. 1965.

[22] R. E. Kleinman and T. B. A. Senior, "Rayleigh scattering," in *Acoustic, Electromagnetic and Elastic Wave Scattering, Low and High Frequency Asymptotics*, V. K. Varadan and V. V. Varadan, Eds. Amsterdam, The Netherlands, 1987, vol. 2, pp. 1–70.

[23] I. V. Lindell, A. H. Sihvola, K. O. Muinonen, and P. W. Barber, "Scattering by a small object close to an interface. I. Exact-image theory formulation," *J. Opt. Soc. Amer.*, vol. 8, no. 3, pp. 472–482, 1991.

[24] E. H. Liu and Y. Lamontagne, "Geophysical application of a new surface integral equation method for EM modeling," *Geophysics*, vol. 63, no. 2, pp. 411–423, 1998.

[25] ——, "Electromagnetic modeling using surface integral equations," in *Three-Dimensional Electromagnetics*, ser. Soc. Expl. Geophys., M. L. Oristaglio and B. R. Spies, Eds. Tulsa, OK, 1999, pp. 76–89.

[26] S. F. Mahmoud and J. R. Wait, "Magnetic response of a hollow ellipsoid," *Antennas Propagat. Mag.*, vol. 41, no. 2, pp. 7–12, 1999.

[27] V. Monebhurrun, D. Lesselier, and B. Duchêne, "Evaluation of a 3-D bounded defect in the wall of a metal tube at eddy current frequencies: The direct problem," *J. Electromagn. Waves Applicat.*, vol. 12, no. 3, pp. 315–347, 1998.

[28] V. Monebhurrun, D. Lesselier, B. Duchêne, A. Ruosi, M. Valentino, G. Pepe, and G. Peluso, "Eddy current nondestructive evaluation using SQUIDs," in *Electromagnetic Non-Destructive Evaluation (III)*, D. Lesselier and A. Razek, Eds. Amsterdam, The Netherlands: IOS, 1999, pp. 171–181.

[29] P. Moon and D. Spencer, "Eleven coordinate systems," in *Field Theory Handbook*. Berlin, Germany: Springer-Verlag, 1961, sec. 1, pp. 1–48.

[30] K. O. Muinonen, A. H. Sihvola, I. V. Lindell, and K. A. Lumme, "Scattering by a small object close to an interface. II. Study of backscattering," *J. Opt. Soc. Amer.*, vol. 8, no. 3, pp. 477–482, 1991.

[31] S. Nag and B. P. Sinha, "Electromagnetic plane wave scattering by a system of two uniformly lossy dielectric prolate spheroids in arbitrary orientation," *IEEE Trans. Antennas Propagat.*, vol. AP-43, pp. 322–327, Mar. 1995.

[32] G. A. Newman and G. W. Hohmann, "Transient electromagnetic responses of high contrast prisms in a layered earth," *Geophysics*, vol. 18, pp. 341–344, 1988.

[33] G. Perrusson, "Caractérization électromagnétique d'objets conducteurs enfouis. Application à la prospection géophysique," Ph.D. dissertation, Univ. PVersailles, St. Quentin-en-Yvelines, Versailles, St. Quentin-en Yvelines, France, Oct. 1999.

[34] G. Perrusson, B. Bourgeois, D. Lesselier, M. Lambert, and B. Duchêne, "Probing conductive masses in the diffusive regime: Equivalent sources and bodies," in *Proc. 61st EAGE Meeting*, Helsinki, Finland, June –812, 1999.

[35] G. Perrusson, M. Lambert, D. Lesselier, A. Charalambopoulos, and G. Dassios, "Electromagnetic scattering by a triaxial homogeneous penetrable ellipsoid: Low-frequency derivation and testing of the localized nonlinear approximation," , to be published.

[36] J. B. Schneider and I. C. Peden, "Differential cross-section of a dielectric ellipsoid by the T-matrix extended boundary condition method," *IEEE Trans. Antennas Propagat.*, vol. 36, pp. 1317–1321, Sept. 1988.

[37] B. Sinha and R. H. MacPhie, "Electromagnetic scattering by prolate spheroids for plane waves with arbitrary polarization and angle of incidence," *Radio Sci.*, vol. 12, no. 2, pp. 171–184, 1977.

[38] B. R. Spies and T. M. Habashy, "Sensitivity analysis of crosswell electromagnetics," *Geophysics*, vol. 60, no. 3, pp. 834–845, 1995.

[39] A. F. Stevenson, "Solution of electromagnetic scattering problems as power series in the ratio (dimension of scatterer)/wavelength," *J. Appl. Phys.*, vol. 24, no. 9, pp. 1134–1142, 1953a.

[40] ——, "Electromagnetic scattering by an ellipsoid in the third approximation," *J. Appl. Phys.*, vol. 24, no. 9, pp. 1143–1151, 1953.

[41] C. T. Verdin and T. M. Habashy, "Rapid 2.5-dimensional forward modeling and inversion via a new nonlinear scattering approximation," *Radio Sci.*, vol. 29, no. 4, pp. 1051–1079, 1994.

[42] J. R. Wait, *Geo-Electromagnetism*. London, U.K.: Academic Press, 1982.

[43] ——, "Complex resistivity of the earth," in *Pier 1*, J. A. Kong, Ed. New York: Elsevier, 1989, pp. 1–173.

[44] ——, "Fields of a horizontal loop antenna over a layered half space," *J. Electromagn. Waves Applicat.*, vol. 9, no. 10, pp. 1301–1311, 1995.

[45] P. E. Wannamaker, G. W. Hohmann, and W. A. San Filipo, "Electromagnetic modeling of three-dimensional bodies in layered earths using integral equations," *Geophysics*, vol. 49, pp. 60–74, 1984.
[46] Z. Xiong and A. C. Tripp, "Electromagnetic scattering of large structures in layered earths using integral equations," *Radio Sci.*, vol. 30, no. 4, pp. 921–929, 1995.
[47] ——, "3-D electromagnetic modeling for near-surface targets using integral equations," *Geophysics*, vol. 62, no. 4, pp. 1097–1106, 1997.
[48] M. S. Zhdanov and S. Fang, "Quasilinear approximation in 3-D electromagnetic modeling," *Geophysics*, vol. 61, no. 3, pp. 646–665, 1996.

Gaële Perrusson was born in France in 1971. She received the Dr. Sci. degree from the Université de Versailles Saint-Quentin (UVSQ), Saint-Quentin, France, in 1999.

Since 1996, her research activities have been with the Laboratoire des Signaux et Systèmes (L2S), now Joint Laboratory of Supélec, Centre National de la Recherche Scientifique (CNRS) and Université Paris Sud (UPS), Orsay, France, and she is also with the Département de Recherche en Electromagnétisme (Supélec-L2S), Gif-sur-Yvette. She has spent several short research periods with the University of Patras, Patras, Greece. She is currently a Teaching and Research Assistant at UVSQ.

Her work focuses on the modeling and numerical simulation of the interaction of wave fields with mineral masses and other bodies in the Earth and their application to subsurface electromagnetic imaging and inversion, notably in the low frequency scattering realm.

Dr. Perrusson was the recipient of the Young Scientist Award from the Union Radio-Scientifique Internationale (URSI) in 1998, and is a member of URSI Commission B.

Dominique Lesselier (M'99) was born in France in 1953. He received the engineer degree from the Ecole Supérieure d'Electricité (now Supélec), Paris, France, in 1975, and the degrees of Dr. de 3ème Cycle and Dr. d'Etat es Sciences Physiques from the Université Pierre et Marie Curie, Paris, France, in 1978 and 1982, respectively.

Since 1975, he has been with the Laboratoire des Signaux et Systèmes (L2S), now Joint Laboratory of Supélec, Centre National de la Recherche Scientifique (CNRS) and Université Paris Sud (UPS), Orsay, France, and also with the Département de Recherche en Electromagnétisme (Supélec-L2S), Gif-sur-Yvette. From 1982 to 1983, he was a Visiting Scholar with the Department of Electrical Engineering, University of California, Los Angeles. Since 1988, he has been Directeur de Recherche with CNRS. His main scientific activity pertains to the development and the analysis of solution methods of electromagnetic and acoustic wave field inverse problems, from mathematical theory to numerical solutions to interpretation of experimental data and vice versa. He is on the Editorial Board of *Inverse Problems*, and is also Guest Editor (with T. Habashy) of an Autumn 2000 Topical Issue of *Inverse Problems*, "Electromagnetic Imaging and Inversion of the Earth's Subsurface." Applied topics of his interest include eddy current nondestructive evaluation, Earth's low frequency inversion, acoustic characterization in shallow waters, and electromagnetic imaging of shallowly buried obstacles in the ground.

Dr. Lesselier is on the Standing Committee of the Electromagnetic Non-Destructive Evaluation (ENDE) workshop series, and the International Steering Committee of the International Symposia on Non-Linear Electromagnetic Systems (ISEM). He was the recipient of the 1982 R. W. P. King Award from the Antennas and Propagation Society of the IEEE, and he was elected Fellow of the Institute of Physics in 1999. He is a member of the Electromagnetics Academy and the Union Radio-Scientifique Internationale (URSI) Commission B.

Marc Lambert was born in France in 1966. He received the Dr. Sci. degree from the Université Paris Sud, Orsay, France, in 1994.

Since 1991, he has mainly carried out his research activities within the Laboratoire des Signaux et Systèmes (L2S), now Joint Laboratory of Supélec, Centre National de la Recherche Scientifique (CNRS) and Université Paris Sud (UPS), and he is also with the Département de Recherche en Electromagnétisme, Supélec and L2S, Gif-sur-Yvette. Before completion of his doctoral thesis, he spent the Summer of 1993 as Summer Research Assistant with the Saclant Undersea Research Center, La Spézia. He was Teaching and Research Assistant with UPS in 1993 and 1994, and Research Engineer with the Bureau de Recherche Géologique et Minière (BRGM), Orléans, France, for most of 1995, before he became Chargé de Recherche with CNRS in October 1995. His main research is concerned with solutions of direct and inverse scattering problems in both electromagnetics and acoustics and their applications to the characterization of complex objects buried in complex environments from limited datasets, most of his attention being devoted to the many theoretical and computational issues this characterization entails.

Dr. Lambert is a member of URSI Commission B.

Bernard Bourgeois was born in France in 1954. He received the degree from the Ecole des Mines de Paris (majoring in earth sciences), Paris, France, in 1978.

From 1978 to 1982, he taught mathematics in Morocco, and then was with the Department of Geophysics, Bureau de Recherche Géologique et Minière (BRGM), Orléans, France, in 1982. He was first involved in commercial operations in France and abroad (Morocco, Greece, West Indies, Rwanda), encompassing all domains of geophysics for diverse applications (mineral exploration, geothermal, groundwater, civil engineering). In 1988, he was with a research group of BRGM devoted to electrical and electromagnetic methods (surface, borehole, airborne), focusing on borehole methods for mineral exploration (field campaigns and demonstrations in Canada, Alaska, Spain, and Finland). His present research interests are in shallow electromagnetic exploration for geotechnical and environmental applications.

Dr. Bourgeois is a member of the European Association of Geoscientists and Engineers and of the Société pour l'Avancement et l'Interprétation de Diagraphies.

Antonios Charalambopoulos was born in Greece in 1965. He received the Dipl. Ing. degree in electrical engineering and the Ph.D. degree in applied mathematics, both from the National Technical University of Athens, Greece, in 1988 and 1992, respectively. He received the M.Sc. degree in applied mathematics from Brown University, Providence, RI, in 1989.

Since July 1997, he has been with the Department of Mathematical and Physical Sciences, Polytechnic School, Aristotle University of Thessaloniki, Thessaloniki, Greece, where he is currently Assistant Professor of Mathematics. From 1995 to 1997, he has been a Postdoctoral Researcher with the Division of Applied Mathematics, Department of Chemical Engineering, University of Patras, Patras, Greece, and Institute of Chemical Engineering and High Temperature Chemical Processes-Foundation for Research and Technology, Hellas, Patras. His research interests include direct and inverse scattering problems of acoustics, electromagnetics and elasticity, partial differential equations (with emphasis on general theory, boundary value problems, conservation laws and exterior calculus), integral equations, and the applications of partial differential equations and scattering theory to biomechanics and biotechnology.

George Dassios was born in Greece in 1946. He received the Diploma degree from the University of Athens, Athens, Greece, in 1970, and the the M.S. and Ph.D. degrees from the University of Illinois, Urbana, in 1972 and 1975, respectively. He did his doctoral dissertation in scattering theory under Victor Twersky.

Since 1981, he has been Chair Professor of Applied Mathematics, University of Patras, Patras, Greece, and is with the Division of Applied Mathematics, Department of Chemical Engineering, University of Patras, and Institute of Chemical Engineering and High Temperature Chemical Processes, Foundation for Research and Technology, Hellas, Greece. His interests lie in scattering theory, low frequencies, wave propagation, partial differential equations, and mathematical methods in sciences and engineering. In 2000, he published an extensive monograph on *Low Frequency Scattering*, co-authored with Ralph Kleinman.

Dr. Dassios is a member of a number of scientific societies, including the American Mathematical Society and the Society for Industrial and Applied Mathematics.

H

Diffraction par un objet tridimensionnel : méthode de moments

[A.12] On the modeling of 3-D inclusions in conductive media using extended Born models in the diffusive regime
Daniel Dos Reis, Marc Lambert et Dominique Lesselier
J. Applied Electromagnetics and Mechanics à paraître

Int. J. Applied Electromagnetics and Mechanics (à paraître)

On the modeling of 3-D inclusions in conductive media using extended Born models in the diffusive regime

D. Dos Reis, M. Lambert, D. Lesselier
Département de Recherche en Électromagnétisme – Laboratoire des Signaux et Systèmes
CNRS-SUPÉLEC-UPS, Plateau de Moulon, 3 rue Joliot-Curie,
91192 Gif-sur-Yvette Cedex, France
E-mail: name@lss.supelec.fr, phone: 33 1 69 85 15 61, fax: 33 1 69 85 17 65

Abstract

Diffusive fields in 3-D configurations, e.g., as those faced when searching for inclusions in conductive planar layered media (a metal slab, a half-space subsoil) at low frequencies, can be modeled via Green's integral formulations that require Green dyads. Such formulations make good use of extended Born approximations in order to express the secondary sources existing within the probed inclusion from the primary fields at same location. Here it is sketched how several such approximations perform in cases of interest by comparison with full solutions and benchmark measurements.

1 Introduction

The purpose of this contribution is the analysis of the electromagnetic behavior of 3-D bounded inclusions affecting a conductive, non-magnetic and isotropic planar-layered metal probed by a low-frequency current source operated nearby in air with an application to eddy current Non-destructive Evaluation. A comparison between measured data and data obtained from exact and approximated models will be discussed. Among all methods available to model eddy currents in a damaged conductive structure, an integral formulation, resulting from the application of the Green's theorem onto the equations governing the fields propagation, has been chosen. This formulation requires the expressions of the Green dyads for layered structures which are known in closed-form in the spectral domain. Two integral equations are solved: the coupling equation which links the total field in the inclusion to itself, the incident field and the contrast through an appropriate Green dyad, and the observation (or data) equation which links the scattered field on the receivers to the total field in the inclusion and the contrast through another Green dyad. The integral equations are discretized using a Method of Moments and the discrete counterpart of the coupling equation is solved with a Conjugate-Gradient-FFT-based method taking into account its convolutional structure. This is very demanding in terms of computational time and partially-linearized approximations pioneered in [1] and investigated also in [2, 3] are introduced and their effectiveness is discussed (one should also refer to earlier works [4]).

2 Exact and approximated models

The configuration of study is as follows: all materials being linear, isotropic with permeability μ_0 and permittivity ϵ_0, the space is divided in two air half-spaces (numbered 1 and 3) with, in between, a planar slab of conductivity σ_2 (numbered 2). This slab contains a 3-D defect of finite support Ω and conductivity $\sigma(\mathbf{r})$. A time-harmonic source (circular-frequency ω and implied time dependence $\exp(-\mathrm{j}\omega t)$) is placed in medium 1. The so-called vector domain (contrast-source) integral formulations of the electric and magnetic fields in this configuration are yielded by application of the Green theorem onto the (diffusive) vector wave equations —involving Green dyads of the layered environment. They read as

$$\mathbf{E}_i(\mathbf{r}) = \mathbf{E}_{i0}(\mathbf{r}) + \mathrm{j}\omega\mu_0 \int_\Omega \underline{\mathbf{G}}_{i2}^{ee}(\mathbf{r},\mathbf{r}')\,\mathbf{J}_2(\mathbf{r}')\,d\mathbf{r}' \tag{1}$$

$$\mathbf{H}_i^s(\mathbf{r}) = \int_\Omega \underline{\mathbf{G}}_{i2}^{me}(\mathbf{r},\mathbf{r}')\,\mathbf{J}_2(\mathbf{r}')\,d\mathbf{r}'. \tag{2}$$

INT. J. APPLIED ELECTROMAGNETICS AND MECHANICS (À PARAÎTRE)

In the above $\mathbf{E}_{i0}(\mathbf{r})$ —given by $\mathbf{E}_{i0}(\mathbf{r}) = \mathrm{j}\omega\mu_0 \int_S \underline{\mathbf{G}}_{i1}^{ee}(\mathbf{r},\mathbf{r}')\,\mathbf{J}_S(\mathbf{r}')\,d\mathbf{r}'$— is the incident field due to the electrical current $\mathbf{J}_S$ carried by the source (e.g., a coil probe), $\mathbf{J}_2(\mathbf{r})$ are the contrast sources of Ω-support given by $\mathbf{J}_2(\mathbf{r}) = \sigma_2\chi(\mathbf{r})\,\mathbf{E}_2(\mathbf{r})$, $\chi(\mathbf{r}) = \sigma(\mathbf{r})/\sigma_2 - 1$ is the electric contrast, $\mathbf{E}_i(\mathbf{r})$ and $\mathbf{H}_i^s(\mathbf{r})$ are the total electric field and the scattered magnetic field in medium i respectively, and $\underline{\mathbf{G}}_{ij}^{ee}(\mathbf{r},\mathbf{r}')$ and $\underline{\mathbf{G}}_{ij}^{me}(\mathbf{r},\mathbf{r}')$ are the electric-electric and magnetic-electric Green dyads made of the electric and magnetic fields at $\mathbf{r}$ in medium i due to a Dirac electrical current at $\mathbf{r}'$ in medium j, respectively. The latter are given by

$$\nabla\times\nabla\times\underline{\mathbf{G}}_{ij}^{ee}(\mathbf{r},\mathbf{r}') - k_i^2\underline{\mathbf{G}}_{ij}^{ee}(\mathbf{r},\mathbf{r}') = \underline{\mathbf{I}}\delta(\mathbf{r}-\mathbf{r}')\,\delta_{ij}, \underline{\mathbf{G}}_{ij}^{me}(\mathbf{r},\mathbf{r}') = \nabla\times\underline{\mathbf{G}}_{ij}^{ee}(\mathbf{r},\mathbf{r}'), \tag{3}$$

completed with appropriate transmission and radiation conditions. The expressions of the Green dyads for layered structures are known in closed-form in the spectral domain. The reciprocity theorem yields the variation ΔZ of the probe impedance as:

$$I_0^2\Delta Z = -\int_\Omega \mathbf{E}_{20}(\mathbf{r})\cdot\mathbf{J}_2(\mathbf{r})\,d\mathbf{r}, \tag{4}$$

where I_0 is the feeding current of the probe.

The scattering problem requires solving for all $\mathbf{r}$ in Ω

$$\mathbf{J}_{20}(\mathbf{r}) = \mathbf{J}_2(\mathbf{r}) - \eta(\mathbf{r})\int_\Omega \underline{\mathbf{G}}_{22}^{ee}(\mathbf{r},\mathbf{r}')\,\mathbf{J}_2(\mathbf{r}')\,d\mathbf{r}', \eta(\mathbf{r}) = \mathrm{j}\omega\mu_0\sigma_2\chi(\mathbf{r}), \tag{5}$$

$\mathbf{H}_i^s(\mathbf{r})$ and ΔZ being deduced from $\mathbf{J}_2(\mathbf{r})$. For the exact model, the solution of equation (5) is obtained via a Conjugate-Gradient-FFT-based method. This operation can be time-consuming and partially-linearized approximations are introduced to simplify the solution of (1) or (5). These approximations are based on the observation that $\underline{\mathbf{G}}_{ij}^{ee}(\mathbf{r},\mathbf{r}')$ peaks for $\mathbf{r}=\mathbf{r}'$ which implies that the field in $\mathbf{r}$ strongly depends on domains close to $\mathbf{r}=\mathbf{r}'$ in Ω [1]. Three approximations are briefly described below:

- LN (Localized Nonlinear approximation): in the LN approximation —originally introduced in [1]— as we apply it here, one assumes in the first step that an approximated expression of (1) for the total electric field in medium $i=2$ is given by

$$\mathbf{E}_2(\mathbf{r}) = \mathbf{E}_{20}(\mathbf{r}) + \left[\mathrm{j}\omega\mu_0\sigma_2\int_\Omega \underline{\mathbf{G}}_{22}^{ee}(\mathbf{r},\mathbf{r}')\,\chi(\mathbf{r}')\,d\mathbf{r}'\right]\mathbf{E}_2(\mathbf{r}) \tag{6}$$

  and can be re-written as $\mathbf{E}_2(\mathbf{r}) = \underline{\Gamma}(\mathbf{r})\,\mathbf{E}_{20}(\mathbf{r})$, where the *depolarization* dyad $\underline{\Gamma}(\mathbf{r})$ is given by $\underline{\Gamma}(\mathbf{r}) = \left(\underline{\mathbf{I}} - \mathrm{j}\omega\mu_0\sigma_2\int_\Omega \underline{\mathbf{G}}_{22}^{ee}(\mathbf{r},\mathbf{r}')\,\chi(\mathbf{r}')\,d\mathbf{r}'\right)^{-1}$. Then, in a second step, one assumes that the depolarization can be neglected, which is leading as to $\underline{\Gamma}(\mathbf{r})$ diagonal.

- QL (Quasi-Linear approximation): introduced in [2], the QL approximation involves that the total electric field is given by $\mathbf{E}_2(\mathbf{r}) = [\underline{\mathbf{I}} + \underline{\Lambda}(\mathbf{r})]\,\mathbf{E}_{20}(\mathbf{r})$, where $\underline{\Lambda}(\mathbf{r})$ is an *electrical reflectivity dyad*. Adding the hypothesis that $\underline{\Lambda}(\mathbf{r})$ is a $\mathbf{r}$-independent scalar dyad (slow variation in Ω-domain) given by $\lambda\underline{\mathbf{I}}$ and using a least-square analysis of (1) provide the scalar simplification of the QL approximation, denoted QLS in the following. λ reads as

$$\lambda = \frac{\int_\Omega \left[\mathbf{E}_{20}(\mathbf{r}) - \mathbf{E}_2^B(\mathbf{r})\right]^*\cdot\mathbf{E}_2^B(\mathbf{r})\,d\mathbf{r}}{\int_\Omega \left|\mathbf{E}_{20}(\mathbf{r}) - \mathbf{E}_2^B(\mathbf{r})\right|^2 d\mathbf{r}}, \mathbf{E}_2^B(\mathbf{r}) = \mathrm{j}\omega\mu_0\sigma_2\int_\Omega \underline{\mathbf{G}}_{22}^{ee}(\mathbf{r},\mathbf{r}')\,\chi(\mathbf{r}')\,\mathbf{E}_{20}(\mathbf{r}')\,d\mathbf{r}', \tag{7}$$

  where $\mathbf{E}_2^B(\mathbf{r})$ is the second-order Born field and where * stands for complex conjugate.

- QA (Quasi-Analytic approximation): introduced in [3], the QA approximation blends the QL and LN approximations. It starts from the hypothesis that the total electric field can be written as $\mathbf{E}_2(\mathbf{r}) = [\underline{\mathbf{I}} + \underline{\Lambda}(\mathbf{r})]\,\mathbf{E}_{20}(\mathbf{r})$. Assuming that $\underline{\Lambda}(\mathbf{r})$ is now a $\mathbf{r}$-dependent scalar

dyad (but still with slow variation in Ω-domain) given by $\lambda(\mathbf{r})\,\underline{\mathbf{I}}$, a scalar projection onto $\mathbf{E}_{20}(\mathbf{r})$ leads to

$$\lambda(\mathbf{r}) = \frac{\mathbf{E}^*_{20}(\mathbf{r}) \cdot \mathbf{E}^B_2(\mathbf{r})}{|\mathbf{E}_{20}(\mathbf{r})|^2 - \mathbf{E}^*_{20}(\mathbf{r}) \cdot \mathbf{E}^B_2(\mathbf{r})}. \tag{8}$$

Numerically speaking the discrete counterparts of the integral equations are obtained from an appropriate Methods of Moments where one is discretizing the obstacle with parallelepipeded voxels. The singular part of the Green dyad is expressed in closed-form in the spatial domain and numerically integrated over a voxel via a Gauss-Legendre scheme whereas its regular part is expressed and integrated in closed-form in the spectral domain and calculated in the spatial domain via FFT. Due to the convolution structure the integration over Ω is performed using FFT in space along the lateral coordinates x and y and in an usual manner according to the depth coordinate z.

3 Numerical results

The modeling has been compared with synthetic and real results either in geophysics ([2, 3]) or in NdE (JSAEM problem n°2 [5, 6], benchmarks from the Center for Nondestructive Evaluation at Iowa State). This paper is focused onto the comparison with the benchmarks of this Center (available at http://www.cnde.iastate.edu/ec/Projects/Project.html). The configuration of measurement is as follows: a planar void crack (5.435 mm long, 0.269 mm wide and 0.46 mm deep) cut into a 1.265 mm thick metal slab of Inconel 600 ($\sigma_2 = 0.8$ MS/m) is observed by a pancake probe moved 0.458 mm above the crack in x (the mouth of the cut) and y (orthogonal to the mouth). The crack is cut either from the top of the slab (ID) or from the bottom (OD). The variation of impedance of the probe ΔZ is measured at two frequencies (150 kHz and 300 kHz). The numerical simulation is performed with an obstacle discretization of $31 \times 3 \times 11$ voxels. In figure 1 the real part (a) and the imaginary part (b) of ΔZ along x are displayed for the crack denoted as ID40; the measured data and the simulated results have the same shape and magnitude except with the QLS. In figure 2 the real part (a) and imaginary part (b) of ΔZ are shown versus y. The exact modelization and the LN approximation are still good. The QLS is off again but now the QA does not behave properly also. At 300 kHz the results for the ID void remain of similar qualities and are not presented here for lack of place. The case of the OD crack seems much more difficult however. Results at 300 kHz (figure 3 (a) and (b)) show a relatively large discrepancy between the models and the measurements even though the shapes are quite similar. Let us emphasize that the results given by the LN and the QA approximations are still acceptable compared to those given by the exact modeling.

Finally let us notice that, once the Green dyads have been pre-calculated (about 1 hour CPU-time on a standard workstation), for the ID40 at 150 kHz the exact modeling takes about 4 hours for getting 46 values of ΔZ whereas each approximation (LN, QLS or QA) needs less than 1 minute CPU-time.

4 Conclusion

Models of the interaction of a probe with a void in a metal plate based on a contrast-source vector integral equation using proper Green dyads are introduced. An exact solution based on a Conjugate-Gradient-FFT-based Method-of-Moments is developed and three heuristic, Born-extended approximations are applied. The solutions are compared with benchmarks from the Center for Nondestructive Evaluation at Iowa State. The exact modelization shows a fair agreement with the measured data. Using the partially-linearized approximations results in an important saving of CPU-time (by a factor of 250) compared to the exact modeling but only the LN gives acceptable results in every case whereas the QLS always fails and the QA fails in some cases.

References

[1] T. M. Habashy *et al.* Beyond the Born and Rytov approximations: a nonlinear approach to electromagnetic scattering. *J. Geophys. Res*, 98:1759–1775, 1993.

[2] M. S. Zhdanov and Sheng Fang. Quasi-linear approximation in 3-D electromagnetic modeling. *Geophys.*, 61, 1996.

[3] M. Zhdanov and G. Hursan. 3D electromagnetic inversion based on quasi-analytical approximation. *Inverse Probl.*, 16:1297–1322, 2000.

[4] A. Ruosi *et al.* High Tc SQUIDs and eddy current NDE: a comprehensive investigation from real data to modeling. *Measurement Scie. Technol.*, 11:1639–1648, 2000.

[5] T. Takagi *et al.* Ect research activities in JSAEM – benchmark models of eddy current testing for steam generator tube part 1 & part 2. In R. Collins *et al.*, editor, *Nondestructive Testing of Materials*, pages 253–264 & 313–320. IOS Press, Amsterdam, 1995.

[6] V. Bertrand *et al.* On the numerical modeling of eddy current nondestructive evaluation with the FEM-BEM TRIFOU software in controlled configurations. In S. Udpa *et al.*, editor, *Electromagnetic Non-Destructive Evaluation*, volume IV, pages 32–41. IOS Press, Amsterdam, 2000.

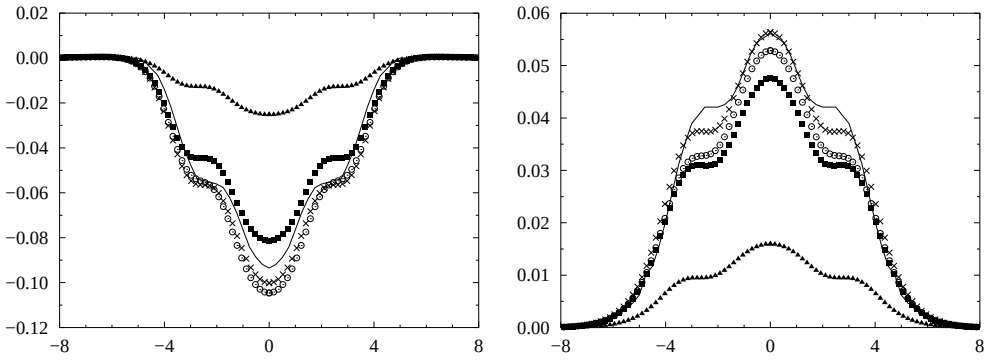

(a) (b)

Figure 1: ID40 at 150 kHz, real part (a) and imaginary part (b) of the variation of the probe impedance ΔZ (Ω) along the x-axis (mm); measurement (solid line), full solution (crosses), LN (open circle), QLS (solid triangle), QA (solid square)

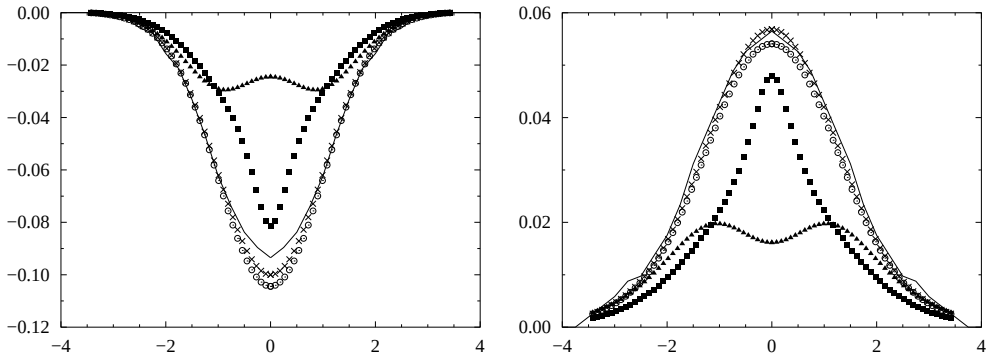

(a) (b)

Figure 2: ID40 at 150 kHz, real part (a) and imaginary part (b) of the variation of the probe impedance ΔZ (Ω) along the y-axis (mm); measurement (solid line), full solution (crosses), LN (open circle), QLS (solid triangle), QA (solid square)

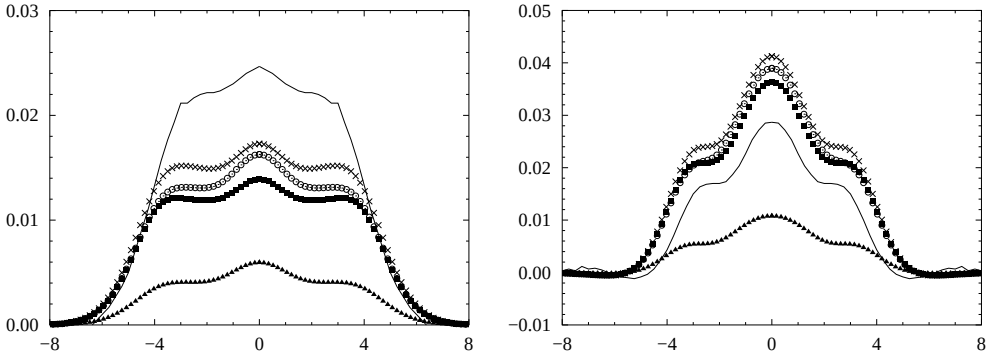

(a) (b)

Figure 3: OD40 at 300 kHz, real part (a) and imaginary part (b) of the variation of the probe impedance ΔZ (Ω) along the x-axis (mm); measurement (solid line), full solution (crosses), LN (open circle), QLS (solid triangle), QA (solid square)

I

Méthode de contraste source

[L5.5] Eddy-current evaluation of 3-D defects in a metal plate, a first analysis of a contrast-source gradient method
Daniel Dos Reis, Marc Lambert et Dominique Lesselier
Electromagnetic Non-Destructive Evaluation (V) Studies in Applied Electromagnetics and Mechanics IOS Press Amsterdam soumis mai 2001

Eddy-current evaluation of 3-D defects in a metal plate: a first analysis of a contrast-source gradient method

D. Dos Reis, M. Lambert, D. Lesselier
Département de Recherche en Électromagnétisme – Laboratoire des Signaux et Systèmes
CNRS-SUPÉLEC-UPS, Plateau de Moulon, 3 rue Joliot Curie,
91192 Gif-sur-Yvette Cedex, France, http://www.supelec.fr/lss/

Abstract Retrieval of voluminous defects in a non-magnetic metal plate from maps of time-harmonic anomalous magnetic fields in air due to a source nearby is performed by a contrast-source, gradient-type technique which uses the binary aspect of the sought conductivity distributions. The functional analysis within a Green-based vector integral formulation of the diffusive fields is sketched and the efficiency of the approach is discussed from synthetic data in demanding defect configurations.

1 Introduction

We investigate the evaluation of 3-D bounded (voluminous) defects of known conductivity (voids, inclusions) inside a flat, horizontal non-magnetic metal plate from anomalous magnetic fields observed when a low-frequency source is operated nearby. The source consists of an air-core coil probe positioned above the expectedly damaged zone, and the data consist of a 2-D map of one single component (the vertical one) or of all three components of the anomalous magnetic field at discrete locations in a planar surface above the plate. Our main aim is not to introduce fully novel modeling tools of, and solution methods to, that demanding 3-D shape inversion problem, but to study whether approaches recently put forth

- to calculate the eddy-current pattern in a planarly-layered conductive environment affected by a localized inhomogeneity of arbitrary geometry using exact solutions as well as extended-Born approximations developed within a rigorous, *full-wave* vector domain integral formulation of the diffusive fields inside and outside the affected sample [1, 2],
- to extract from a magnetic field observed nearby a 3-D, possibly multiply-connected voluminous object buried in an infinite conductive space its distribution of conductivity by using a contrast-source-based gradient-type method [3, 4] in an Earth's subsurface imaging context,
- to use the prior information that the sought defects are of prescribed conductivity contrast with respect to their environment, their 3-D maps ideally consisting of distributions of black and white voxels (in the exterior and in the interior of the defects) as is the case already in [5] and as much studied in 2-D geometries since the early approach [6] of binary-specialized modified gradient methods,

could effectively be combined when the embedding environment is a planar (conductive) layer, when the scattering obstacles are three-dimensionally bounded, when illumination and observation are made from above it (aspect-limited data), and even when a single component of the vector magnetic field is collected on a limited, coarse mesh.

Previous investigations [1, 2] have shown that anomalous magnetic fields are modeled with fair accuracy –in manageable computational time on a standard work-station– by the aforementioned integral formulation, and we do not come back to this topic here. We mostly outline below how this *hybrid* inversion method can be properly developed, and give a few typical results. Test cases at this still preliminary stage come from synthetic data calculated on canonical 3-D models of mm-sized parallelepipeded void defects in an Inconel 600 plate probed in the 150 – 300 kHz frequency range.

2 The algorithm

Let us refer to the configuration sketched in Fig. 1. A possibly multiply-connected 3-D defect Ω of constant conductivity σ (it will be 0 in the numerical examples) is embedded within a non-magnetic linear isotropic metal plate of conductivity σ_2. Eddy currents are generated in the plate using a time-harmonic (circular frequency ω, time-dependence $\exp(-\mathrm{j}\omega t)$) coil source carrying electrical currents J_C at fixed location in air (permeability μ_0, permittivity ϵ_0). Perturbation of the eddy current pattern produces an anomalous magnetic field that is observed in a prescribed planar surface $\mathcal{S}$ in air.

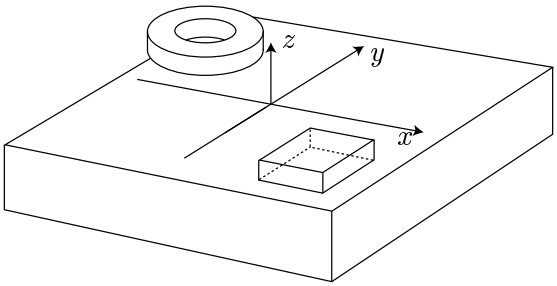

Figure 1: Configuration of study: a pancake-type source probe is set at fixed location above the damaged metal plate, here sketched as a void parallelepiped, the time-harmonic magnetic field being sampled in a plane of observation at fixed height above the plate.

The electromagnetic field $\mathbf{E}, \mathbf{H}$ at any $\mathbf{r}$ in the plate (corresponding quantities will be marked by subscript 2) and in air (using subscript 1 if above the plate, and 3 if below) are cast into a rigorous vector domain (contrast-source) integral formulation from application of the Green theorem onto the quasi-static Maxwell's PDE –involving the Green dyads of the layered environment. So, the field modeling requires the calculation of a fictitious contrast source $\mathbf{J}_2(\mathbf{r}) = \sigma_2 \chi(\mathbf{r}) \mathbf{E}_2(\mathbf{r})$, where $\chi(\mathbf{r})$, equal to 0 outside Ω and to $\chi_c = \sigma/\sigma_2 - 1$ inside Ω, is the electrical contrast between the metal and the defect Ω (for a void, $\chi_c = -1$). For any $\mathbf{r}$ in Ω,

$$\mathbf{J}_2(\mathbf{r}) = \mathbf{J}_{20}(\mathbf{r}) + \mathrm{j}\omega\mu_0\sigma_2\chi(\mathbf{r}) \int_\Omega \underline{\mathbf{G}}_{22}^{ee}(\mathbf{r}, \mathbf{r}') \mathbf{J}_2(\mathbf{r}')\, d\mathbf{r}', \tag{1}$$

whilst the anomalous magnetic field $\mathbf{H}_1^{\mathcal{S}}$ in $\mathcal{S}$ follows from

$$\mathbf{H}_1^{\mathcal{S}}(\mathbf{r}) = \int_{\Omega} \underline{\mathbf{G}}_{12}^{me}(\mathbf{r},\mathbf{r}')\,\mathbf{J}_2(\mathbf{r}')\,d\mathbf{r}'. \tag{2}$$

In the above $\mathbf{J}_{20} = \sigma_2\chi\mathbf{E}_{20}$, where $\mathbf{E}_{20}(\mathbf{r}) = \mathrm{j}\omega\mu_0\int_{\mathcal{S}}\underline{\mathbf{G}}_{21}^{ee}(\mathbf{r},\mathbf{r}')\,\mathbf{J}_C(\mathbf{r}')\,d\mathbf{r}'$ represents primary currents associated to the electrical current $\mathbf{J}_C$ in the coil source C in medium 1; $\underline{\mathbf{G}}_{ij}^{ee}(\mathbf{r},\mathbf{r}')$ and $\underline{\mathbf{G}}_{ij}^{me}(\mathbf{r},\mathbf{r}')$ are the electric-electric and magnetic-electric Green dyads made of the electric and magnetic fields at $\mathbf{r}$ in medium i due to a Dirac electrical current at $\mathbf{r}'$ in medium j, respectively.

Upon iteratively solving (1) by a Conjugate-Gradient Fast-Fourier-Transform Method of Moments using pre-calculated samples of the Green dyads the anomalous field follows from (2) (extended-Born approximations enabling us to bypass the solution of (1)) [1, 2, 7]. Correspondingly, the inversion problem requires us to determine within each voxel of a prescribed 3-D box $\mathcal{D}$ containing the unknown defect of Ω support some conductivity contrast such as an anomalous magnetic field close in some sense to data $\boldsymbol{\zeta}$ collected in $\mathcal{S}$ is produced, being assumed that the true distribution is binary.

As already indicated, binary-specialized modified gradient methods and contrast-source gradient-type methods have been investigated for nonlinearized wave field inversion. Lack of place precludes us to go into their respective machineries. Combining both methods by specializing the contrast-source approach to a binary contrast –in original fashion and with promising results as shown in section 3 by numerical experimentation– is done as follows.

The formulation of interest is written into shorthand operator form using Green dyadic operators: $\underline{\mathcal{G}}_{22}^{ee}\mathbf{J}_2 = \mathrm{j}\,\omega\,\mu_0\int_{\mathcal{D}}\underline{\mathbf{G}}_{22}^{ee}(\mathbf{r},\mathbf{r}')\,\mathbf{J}_2(\mathbf{r}')\,d\mathbf{r}'$ and $\underline{\mathcal{G}}_{12}^{me}\mathbf{J}_2 = \int_{\mathcal{D}}\underline{\mathbf{G}}_{12}^{me}(\mathbf{r},\mathbf{r}')\,\mathbf{J}_2(\mathbf{r}')\,d\mathbf{r}'$. Two equations are of interest: the data equation

$$\boldsymbol{\rho} = \boldsymbol{\zeta} - \underline{\mathcal{G}}_{12}^{me}\mathbf{J}_2^n \tag{3}$$

tells us that some contrast source $\mathbf{J}_2$ in $\mathcal{D}$ radiates a certain magnetic field in $\mathcal{S}$ whose discrepancy with data $\boldsymbol{\zeta}$ is measured by vector residual $\boldsymbol{\rho}^n$; the state equation

$$\boldsymbol{\epsilon} = \sigma_2\,\chi\,\mathbf{E}_2 - \mathbf{J}_2 \tag{4}$$

tells us that this contrast source is consistent with a contrast distribution χ in $\mathcal{D}$, the degree of consistency being appraised by vector residual $\boldsymbol{\epsilon}$, letting $\mathbf{E}_2 = \mathbf{E}_{20} + \underline{\mathcal{G}}_{22}^{ee}\mathbf{J}_2$.

As for the sought binary aspect of the contrast distribution (valued to χ_c or to 0 at any $\mathbf{r}$ in $\mathcal{D}$), and in order to use gradient methods that require us to restore differentiability with respect to this distribution, it is enforced via the nonlinear transformation

$$\chi = \chi_c\,\Psi(\tau),\ \Psi(\tau) = (1+\exp\,(-\tau/\theta))^{-1}, \tag{5}$$

where θ is a strictly positive, real-valued tuning parameter which is controlling the slope of the strictly monotonous real function Ψ (bounded between 0 and 1 and varying from 0 to 1 when τ is increased), the $\mathbf{r}$-dependence being implied. In practice, decreasing θ yields an electrical contrast χ closer to χ_c (resp., to 0) for a given positive (resp. negative) τ at same $\mathbf{r}$.

The solution itself now relies on the construction of two sequences of τ^n and $\mathbf{J}_2^n$ (correspondingly, of $\mathbf{E}_2^n$) that are both function of space $\mathbf{r}$ (implied) in $\mathcal{D}$ –once chosen proper first guesses at $n = 1$– so as a suitable cost functional $\mathbf{F}$ is decreased from one iteration to the

next. Using $\|.\|_{\mathcal{S}}$ and $\|.\|_{\mathcal{D}}$ as norms on $L_2(\mathcal{S})$ et $L_2(\mathcal{D})$ and (later on) corresponding scalar products $\langle , \rangle_{\mathcal{S}}$ and $\langle , \rangle_{\mathcal{D}}$, the general expression of $\mathbf{F}$ reads as

$$\mathbf{F} = \eta_{\mathcal{S}} \, \|\boldsymbol{\rho}\|_{\mathcal{S}}^2 + \eta_{\mathcal{D}} \, \|\boldsymbol{\epsilon}\|_{\mathcal{D}}^2 \,, \tag{6}$$

where weight $\eta_{\mathcal{S}} = \|\boldsymbol{\zeta}\|_{\mathcal{S}}^{-2}$ is constant for given data $\boldsymbol{\zeta}$ and where weight $\eta_{\mathcal{D}} = \|\sigma_2 \, \chi \, \mathbf{E}_{20}\|_{\mathcal{D}}^{-2}$ is contrast-dependent.

The determination of the contrast source $\mathbf{J}_2^n$ is carried out first. At iteration n, one simply chooses $\mathbf{J}_2^n = \mathbf{J}_2^{n-1} + \alpha^n \mathbf{v}^n$, where the complex-valued, $\mathbf{r}$-dependent (3-component) vector $\mathbf{v}^n$ is a conjugate-gradient direction of displacement of the Polak-Ribière type and where the complex-valued constant parameter α^n is a coefficient of displacement. One sets for $n > 1$

$$\mathbf{v}^n = \mathbf{g}^{v,n} + \frac{\langle \mathbf{g}^{v,n}, \mathbf{g}^{v,n} - \mathbf{g}^{v,n-1} \rangle_{\mathcal{D}}}{\langle \mathbf{g}^{v,n-1}, \mathbf{g}^{v,n-1} \rangle_{\mathcal{D}}} \tag{7}$$

(at $n = 1$, $\mathbf{v}^1 = \mathbf{g}^{v,1}$). $\mathbf{g}^{v,n}$ is the gradient of $\mathbf{F}$ with respect to the contrast source $\mathbf{J}_2$; it is valued at $\mathbf{J}_2^{n-1}$, the contrast being kept fixed at χ^{n-1} in that operation (i.e., τ^{n-1} is kept fixed). It reads as

$$\mathbf{g}^{v,n} = -\eta_{\mathcal{S}} \, \underline{\mathcal{G}}_{12}^{me^*} \, \boldsymbol{\rho}^{n-1} - \eta_{\mathcal{D}}^{n-1} \left(\boldsymbol{\epsilon}^{n-1} - \underline{\mathcal{G}}_{22}^{ee^*} \, \sigma_2 \, \overline{\chi^{n-1}} \, \boldsymbol{\epsilon}^{n-1} \right) , \tag{8}$$

where * denotes the adjoint operation and where the upper bar denotes complex conjugation, weight $\eta_{\mathcal{D}}^{n-1}$, and residuals $\boldsymbol{\rho}^{n-1}$ and $\boldsymbol{\epsilon}^{n-1}$ being those associated with the iterates of order $n-1$. Minimizer α^n of $\mathbf{F}$ for the set of directions $\mathbf{v}^n$, is written in closed form as

$$\alpha^n = \frac{\eta_{\mathcal{S}} \langle \boldsymbol{\rho}^{n-1}, \underline{\mathcal{G}}_{12}^{me} \, \mathbf{v}^n \rangle_{\mathcal{S}} + \eta_{\mathcal{D}}^{n-1} \langle \boldsymbol{\epsilon}^{n-1}, \mathbf{v}^n - \sigma_2 \, \chi^{n-1} \, \underline{\mathcal{G}}_{22}^{ee} \, \mathbf{v}^n \rangle_{\mathcal{D}}}{\eta_{\mathcal{S}} \left\| \underline{\mathcal{G}}_{12}^{me} \, \mathbf{v}^n \right\|_{\mathcal{S}}^2 + \eta_{\mathcal{D}}^{n-1} \left\| \mathbf{v}^n - \sigma_2 \, \chi^{n-1} \, \underline{\mathcal{G}}_{22}^{ee} \, \mathbf{v}^n \right\|_{\mathcal{D}}^2} . \tag{9}$$

Contrast source and field have now been updated to $\mathbf{J}_2^n$ and to $\mathbf{E}_2^n = \mathbf{E}_2^{n-1} + \alpha^n \, \underline{\mathcal{G}}_{22}^{ee} \, \mathbf{v}^n$. However, the residual of the *updated* state equation, written as $\boldsymbol{\epsilon} = \sigma_2 \, \chi \, \mathbf{E}_2^n - \mathbf{J}_2^n$, valued at $\widetilde{\boldsymbol{\epsilon}}^n$ when the contrast is the present iterate $\chi^{n-1} = \chi_c \, \Psi(\tau^{n-1})$, might not be close enough to zero in order to be satisfied with. Proper updating of the contrast comes by letting $\tau^n = \tau^{n-1} + \beta^n d^n$, where real-valued $\mathbf{r}$-dependent scalar d^n is again of the Polak-Ribière type and where real-valued parameter β^n is a displacement coefficient. For $n > 1$

$$d^n = g^{d,n} + \frac{\langle g^{d,n}, g^{d,n} - g^{d,n-1} \rangle_{\mathcal{D}}}{\langle g^{d,n-1}, g^{d,n-1} \rangle_{\mathcal{D}}} \tag{10}$$

(at $n = 1$, $d^1 = g^{d,1}$). $g^{dv,n}$ is the gradient at τ^{n-1}, contrast source $\mathbf{J}_2^n$ and field $\mathbf{E}_2^n$ being kept fixed, of a weighted-in squared norm $\mathbf{F}_{\mathcal{D}}$ of the above state residual $\boldsymbol{\epsilon}$; in conveniently expanded form, $\mathbf{F}_{\mathcal{D}}$ reads as

$$\mathbf{F}_{\mathcal{D}} = \eta_{\mathcal{D}}^{n-1} \, \|\sigma_2 \, \chi_c \, \Psi(\tau) \, \mathbf{E}_2^n - \mathbf{J}_2^n\|_{\mathcal{D}}^2 \,, \tag{11}$$

where weight $\eta_{\mathcal{D}}^{n-1} = \|\sigma_2 \, \chi_c \, \Psi(\tau^{n-1}) \, \mathbf{E}_{20}\|_{\mathcal{D}}^{-2}$. One shows that

$$g^{d,n} = -2 \, \eta_{\mathcal{D}}^{n-1} \, \Psi' \left(\tau^{n-1} \right) \Re \left(\sigma_2 \, \overline{\chi_c \, \mathbf{E}_2^n} \cdot \widetilde{\boldsymbol{\epsilon}}^n \right) , \tag{12}$$

where Ψ' is the derivative of Ψ with respect to τ, residual $\widetilde{\boldsymbol{\epsilon}}^n$ at τ^{n-1} having been defined previously; here, $(\cdot)$ represents the usual scalar product of (3-component) vectors at given

location. As for β^n, the minimizer of $\mathbf{F}_{\mathcal{D}}^n$ into the set of directions d^n, it is obtained in closed form as

$$\beta^n = -\frac{\Re\langle d^n\,\sigma_2\,\chi_c\,\Psi'\left(\tau^{n-1}\right)\mathbf{E}_2^n, \widetilde{\boldsymbol{\epsilon}}^n\rangle_{\mathcal{D}}}{\|d^n\,\sigma_2\,\chi_c\,\Psi'\left(\tau^{n-1}\right)\mathbf{E}_2^n\|_{\mathcal{D}}^2}. \tag{13}$$

The algorithm now proceeds by alternating an update of contrast source $\mathbf{J}_2$ and an update of contrast τ inside each voxel of $\mathcal{D}$ until the value reached by the cost functional $\mathbf{F}$ is small enough, or until some plateau is reached. In the latter case, the tuning parameter θ might be reduced in order to push contrast values either to 0 or to χ_c, and equivalently to re-distribute voxels into darker ones and lighter ones, from which the construction of the two sequences is then started again.

3 Numerical results

A number of results has been obtained by the above inversion algorithm. Those shown in figures 2 and 3 consist of gray-level 2-D cross-sectional maps at successive depths (0.1 mm step) of the retrieved 3-D distributions of the contrast χ (after about 2500 iterations, when the cost functional has notably decreased) and of evolution curves of the cost functional $\mathbf{F}$ as a function of the number of iterations.

The example is the one of a 2 mm thick slab of conductivity σ_2 = 1 MS/m where voluminous void defects are sought. A thick circular coil (0.6 and 1.6 mm inner and outer radii, 0.8 mm height) is centered 0.9 mm above the slab at $x = -0.75$ mm and $y = 0$ to avoid undue symmetries with respect to the search domain $\mathcal{D}$ (the latter is centered on the z axis and discretized into $52 \times 52 \times 20$ cubical voxels of $0.1\ \mathrm{mm}^3$ volume). The frequency of operation is 150 kHz, which is corresponding with a plane-wave skin depth δ in metal of about 1.3 mm. One considers in figure 2 and 3 two void parallelepipeds opening in air (the top surface of the slab), both of $1.1 \times 1.1\ \mathrm{mm}^2$ squared horizontal cross-section, the first one 1 mm deep and centered at $x = -1.1$ mm, $y = -1.1$ mm, the other 0.5 mm deep and symmetrically located at $x = 1.1$ mm, $y = 1.1$ mm; one considers a single void opening in air in figure 4, which is still of $1.1 \times 1.1\ \mathrm{mm}^2$ squared horizontal cross-section and 1 mm depth, but its axis is now inclined by $22.5°$.

Data consist of the three components of the anomalous magnetic (Figs. 2-4) or of its single vertical (z) component (Fig. 4) collected at nodes 0.1 mm apart in a planar surface $\mathcal{S}$ of overall area $10\ \mathrm{mm}^2$ and centered 1.55 mm above $\mathcal{D}$. The inversion is started from a two-level contrast map valued at $\chi = 0.5\,\chi_c$ for the three shallower layers of voxels of $\mathcal{D}$ and at $0.01\,\chi_c$ for the deeper ones, or from a contrast map that evolves with depth as $\chi = 0.5\,\chi_c \exp\left(-z/\delta\right)$ (Fig.4). No refreshment (decrease of θ) has been made at this stage of the study, a proper θ having been equated to 1 by numerical experimentation.

From those results retrievals appear almost identical (and the cost functionals evolve similarly) when all three components of the field are used and when the vertical one is used, which is rather comforting in terms of application to real measurement configurations (e.g., by displacing a small coil probe throughout a plane of observation). However, only the shallower parts of the voids, down to about $2/3$ of a skin depth, are fairly well retrieved, the volume of those shallower parts being increased with respect to the exact one and those of the deeper parts being decreased. Such shadowing and blurring due to skin effect are expected phenomena faced independently of the inversion algorithm.

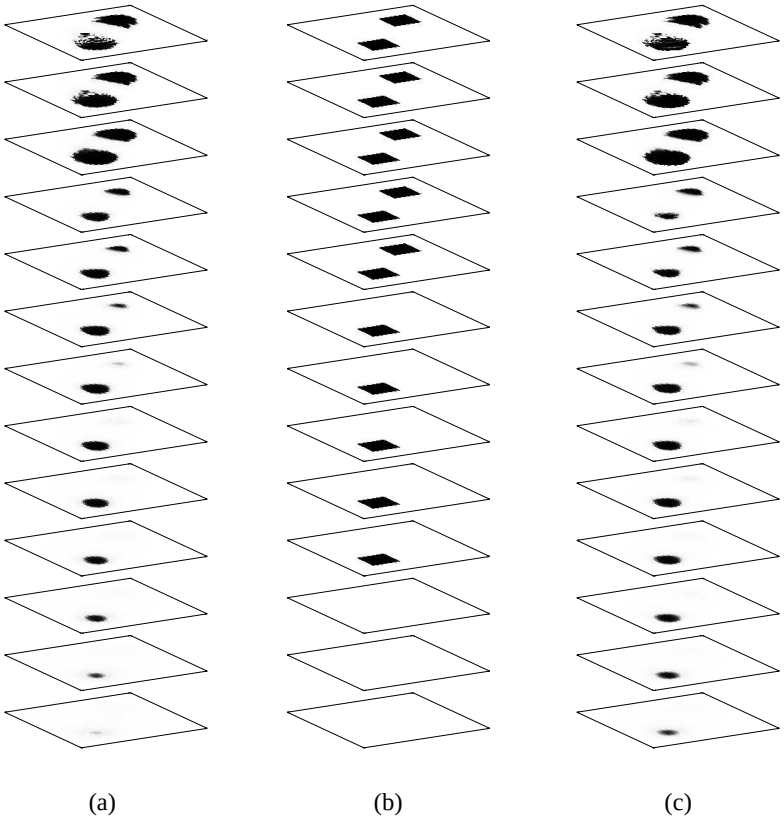

Figure 2: Retrieval of two voids of different depths in a metal slab (see text for details). Cross-sectional gray-level maps of the conductivity contrast χ at successive 0.1 mm-stepped depths using all three components of the anomalous magnetic fi eld (a), and the vertical component only (c). Exact maps are given in (b) for comparison.

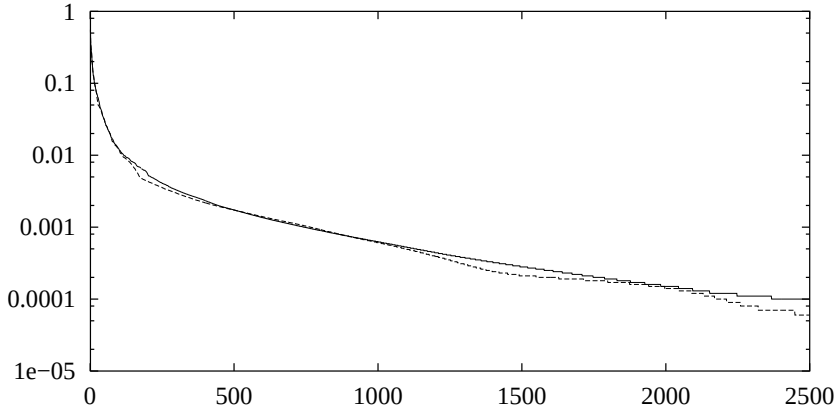

Figure 3: Evolution of the cost functional $\mathbf{F}$ as a function of the number of iterations for the two voids as studied in Fig. 2. Dotted line, case (c); solid line, case (a).

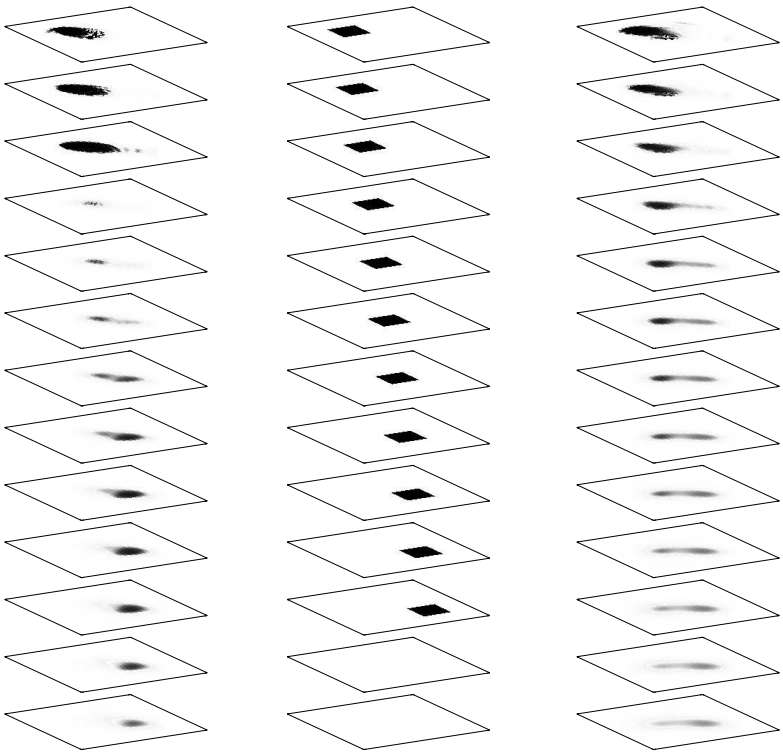

(a) (b) (c)

Figure 4: Retrieval of an inclined void in a metal slab (see text for details). Cross-sectional gray-level maps of the conductivity contrast χ at successive 0.1 mm-stepped depths (using all three components of the anomalous magnetic field). The initial contrast χ is chosen as the two-level one in (a), and is chosen as the one exponentially decreasing with depth in (c). Exact maps are given in (b) for comparison.

Nevertheless, the results displayed here show that the hybrid technique is rather effective. This is illustrated by the retrieval of two close voids (Fig. 2-3) that appear both fairely located and well discriminated, the inclination of a single one (Fig.4) being well reproduced. Obviously one needs an appropriate initial guess to do so. An initial contrast that exponentially decreases as a function of the depth-to-skin-depth ratio from the usual mid value of $\chi_c/2$, does not lead to a better retrieval than a contrast that is set to $\chi_c/2$, in the three first layers of voxels and to almost 0 below (the cost functional reaches a value one-third larger in the first case than in the second case).

4 Concluding remarks

So far data have been assumed to be collected throughout a planar surface (not only along a probing line within a user-prescribed symmetry plane of a defect as is often assumed); this appears to be a pre-requisite when mapping geometrically unknown 3-D objects. Two configurations, other than this multistatic configuration (fixed source – moving field probe), could be attacked similarly, e.g., when source and probe devices are moved together (a reference case would be a SQUID-based magnetometer [7]), or when the variation of the impedance of

the probe itself is observed [8]. Work is presently in progress for such two configurations.

However the difficulty in dealing with such new configurations does not lie in the functional analysis, which is carried out as the one sketched here, but in the numerical burden, (one has to construct induced sources for each location of the source device) and in the lack of information (in the second situation, one has to extract pertinent information from a quantity expected to vary more smoothly than the anomalous field).

In addition it remains to study in further detail the influence of the initial guess and of refreshment, and the advantages of frequency-hopping (using data at successive frequencies, from a low one to a high one), whereas the consequence of data noise and model errors should be appraised closely, the synthetic data here having been modeled using the same discretization as the one used in the inversion itself.

References

[1] D. Dos Reis *et al.*, Extended Born domain integral models of diffusive fields, Proc. COMPUMAG'01 Evian, 2001, to appear.

[2] D. Dos Reis *et al.*, On the modeling of 3-D inclusions in conductive media using extended Born models in the diffusive regime, Int. J. Appl. Electromagn. Mechan. (2001) submitted.

[3] A. Abubakar and P. M. van den Berg, Three-dimensional inverse scattering applied to cross-well induction sensors, IEEE Trans. Geosci. Remote Sensing 38 (2000) 1669-81.

[4] A. Abubakar *et al.*, A conjugate gradient contrast source technique for 3D profile inversion, IEICE Trans. Electron. E83-C (2000) 1864-1874.

[5] V. Monebhurrun *et al.*, 3-D inversion of eddy current data for Nondestructive Evaluation of steam generator tubes, Inverse Problems 14 (1998) 707-24.

[6] L. Souriau *et al.*, Modified gradient approach to inverse scattering for binary objects in stratified media, Inverse Problems 12 (1996) 463-81.

[7] A. Ruosi *et al.*, High Tc SQUIDS and eddy-current NDE: a comprehensive investigation from real data to modelling, Meas. Sci. Technol. 12 (2000) 1639-48.

[8] T. Takagi *et al.*, ECT research activities in JSAEM Benchmark models of eddy current testing for steam generator tube, Parts 1 and 2. In: R. Collins *et al.* (ed.), Nondestructive Testing of Materials. IOS Press, Amsterdam, 1995, pp. 253-64 and 313-20.

J

Dipôles équivalents

[C.10] On the identification of a simple conductive body buried in a conductive Earth at low frequencies
Gaële Perrusson, Marc Lambert, Dominique Lesselier, Bernard Duchêne, George Dassios et Gregory Kamvyssas
Proc. URSI International Symposium on Electromagnetic Theory Salonique 575-577 1998

ON THE IDENTIFICATION OF A SIMPLE CONDUCTIVE BODY BURIED IN A CONDUCTIVE EARTH AT LOW FREQUENCIES

G. Perrusson, M. Lambert, D. Lesselier, and B. Duchêne
Département de Recherche en Électromagnétisme – Laboratoire des Signaux et Systèmes
CNRS-SUPÉLEC, Plateau de Moulon, 91192 Gif-sur-Yvette Cedex, France
G. Dassios and G. Kamvyssas
Division of Applied Mathematics, Departement of Chemical Engineering,
University of Patras, and ICEHT-FORTH, GR 265 00, Patras, Greece

Abstract: One considers the characterization of a conductive body buried in a conductive earth from magnetic fields acquired along a borehole when a localized source at a low frequency is placed at a fixed position nearby. From real and synthetic data, equivalent electric and magnetic dipole sources are shown to provide us with a fair model of the interaction, while the theoretical framework behind such solutions is sketched, and preliminary results on low-frequency expansions of the resulting dyadic fields are introduced.

INTRODUCTION

Great progress is being made on low-frequency (induction) electromagnetic characterization of 3-D orebodies in the Earth with today's development of miniature 3-component receiver probes, e.g., *Bourgeois et al.* [1]. But interpretation of the vector data now available lacks effective tools based on a sound understanding of the interaction between probing wavefields and probed masses. In this context, one is aiming at the characterization of a homogeneous, nonmagnetic conductive body in a homogeneous, nonmagnetic conductive space, from 3-component magnetic fields measured along a borehole when an electric current loop is placed at a fixed position nearby and made to radiate at a given (low-)frequency.

THE ELECTROMAGNETIC INTERACTION

Some figures of interest. The frequency range is ≈ 50 Hz - 500 Hz, the size of the scattering body is ≈ 50 m or somewhat larger, center-source and (minimum) center-receivers distances are in the 200 m – 400 m range, conductivity of the body, σ_i, varies from a few mS/m (highly resistive) to a few 10 S/m (highly conductive) while the one of the environment, σ_b, is less than 1 mS/m (highly resistive) and up to a few 10 mS/m (conductive). Thus all distances are less than a few tenths of the plane-wave skin depth δ_b in the embedding –the skin depth δ_i in the body material is often much smaller than δ_b.

Complexity of the electromagnetic modeling. The above geometrical modeling may appear simple to anyone aware of the complexity of induction mining prospecting –though it corresponds with practical cases when the interaction with the surface is negligible. But localized sources, near-fields, frequency-dependence, conductive media, are more intricate than the plane-wave, far-field, zero-order expansion, vacuum embedding hypotheses often assumed with low-frequency inversion, e.g., Angell and Kleinman [2]. Also, the contrast of the body with the embedding (σ_i/σ_b is at least 10 and may reach 10^5) results in inadequacy of weak-scattering assumptions while the localized nonlinear approximation, e.g., Habashy *et al.* [3], breaks down at high contrasts; on the other hand, the body is not perfectly conducting even then. Furthermore, the limited measurement space (single borehole, fixed source) considerably hinders the inversion. Therefore, in mineral exploration, finding that an orebody is, from some closeness of observed and calculated fields, equivalent to a homogeneous triaxial ellipsoid whose geometry and conductivity are estimated, is near optimality –we limit ourselves to a sphere; and the retrieval of equivalent sources is useful –we focus onto a dipolar equivalence. Finally the transmitter in practice is a square loop (≈ 300 × 300 m^2) at the Earth surface. One shows elsewhere that its assimilation to a circular loop of same area is good deeper than ≈ 50 m (if the borehole is not crossing the loop) but a dipole equivalence is at most fair, and only at depths below ≈ 200 m; so the incident field modeling is not as easy as it may seem –we assume a Vertical Magnetic Dipole (VMD).

THE INVERSION

Inversion of experimental data. A number of representative data sets have been acquired by BRGM at several sites with the ARLETT set-up. As is exemplified in Fig. 1, data are reproduced with a fair accuracy by a single couple of electric and magnetic dipoles which, for simplicity, are taken as radiating in air. Data are either the real parts, or the imaginary parts –the choice depends upon which part is the largest– of the magnetic field components (H_{Down}, H_{North}, H_{East}) which are considered as being induced by the orebody

and which are found as such after processing the raw data (e.g., "reduction": the incident field is taken as the field measured at the lowest frequency, 69 Hz). Unknowns are source coordinates and the electric and magnetic moment components. The cost functional is obtained by summing up on all measuring stations (each 20 m) and all components the amplitude of the difference between a measured and a calculated *H*-field, and is minimized by a constrained quasi-Newton algorithm.

Equivalence with electric and magnetic dipoles. One considers a sphere (radius a, volume V) centered at the origin O of a spherical coordinate system and illuminated by a time-harmonic ($-j\omega t$) VMD with moment M_b located at $\dot{r}_b$. The latter projects into two dipoles, one radial to the sphere, with moment $M_{br}\bar{u}_r$, and the other transverse, with moment $M_{bt}\bar{u}_\theta$, which create at O incident fields $H_{bt}\bar{u}_\theta, H_{br}\bar{u}_r, E_{bt}\bar{u}_\phi$. Kaufman and Keller's analysis [4] amounts to keep the first terms only of the exact series expansions of the field, and it provides the scattered field $\bar{H}_s$ as being due to two magnetic and one electric dipoles whose moments are $\bar{M}_r = (3V/2)DH_{br}\bar{u}_r$, $\bar{M}_t = -(3V/2)DH_{bt}\bar{u}_\theta$, $\bar{P}_t = -3V\chi\sigma_b E_{bt}\bar{u}_\phi$, with $D = J_{5/2}(k_i a)/J_{1/2}(k_i a)$, $k_i = (1+j)/\delta_i$, $\chi = (\sigma_i - \sigma_b)/(\sigma_i + \sigma_b)$. Consequently, looking for three mutually orthogonal dipoles at the same location, by minimizing via an appropriate optimization algorithm the discrepancy between a given data set and the field they induce, seems a worthwhile inversion strategy; typical results are shown in Fig. 2. However, emphasize that when carrying out the inversion one gets only an electric dipole at small σ_i/σ_b (Fig. 2c) and magnetic dipoles at high ones (Fig. 2a), retrieval of both types occurring only for a limited range of medium contrasts (Figs. 2b, d) –so one cannot hope to retrieve independently V and σ_i except in that range. Notice also that the inversion results are rather poor when M_{br} and M_{bt} are of same amplitude but are excellent when they differ enough (compare Fig. 2b to Fig. 2d), while the dipoles' location is always slightly shifted toward the source position, this shift being significantly larger at high contrasts (Fig. 2a, ≈ 6 m) –Kaufman and Keller's analysis fails at high $k_i a$, magnitudes of the saved and neglected terms in the expansions being too close.

Towards a higher order of generality. Dyadic fields, e.g., Dassios *et al.* [5], embody in the incident dyadic wave the two fundamental axial and transverse polarizations of a dipole source with respect to the sphere. Thus, dyadic low-frequency field expansions, $\bar{\bar{\Psi}} = \Sigma\, \bar{\bar{\Psi}}_p (jk_b)^p$, p running from 0 to ∞, $k_b = (1+j)/\delta_b$, can be derived recurrently as done for a less intricate scalar scattering case by Dassios and Kamvyssas [6]. Here, once taken into account that for a magnetic dipole source coefficients $\bar{\bar{H}}_1, \bar{\bar{E}}_0, \bar{\bar{E}}_1, \bar{\bar{E}}_3, \ldots$ are zero, divergence-free $\bar{\bar{H}}_p$ and $\bar{\bar{E}}_p$ coefficients of the total field satisfy $\nabla \times \bar{\bar{H}}_p = \sigma_n \bar{\bar{E}}_p$ ($n = i, b$) and $\nabla \times \bar{\bar{E}}_p = -\bar{\bar{H}}_{(p-2)}/\sigma_b$, $p \geq 2$, plus usual tangential continuity at the body surface; the coefficients $\bar{\bar{H}}_0$ and $\bar{\bar{H}}_3$ are reduced to those of the incident field. So the solution now involves a single potential problem, $\nabla \times \bar{\bar{\Psi}}_p = \bar{\bar{Q}}_p$, for known successive source terms $\bar{\bar{Q}}_p$, which is tackled within the framework of the spherical potential theory. (The influence of permittivity has been neglected so far, but the analysis readily extends to a full Maxwell model, while the perfectly conducting body is easily handled.) Work is in progress and no final conclusions on the practicality of the approach are being drawn yet, but it is worthwhile to emphasize that a triaxial ellipsoid is handled similarly, once introduced ellipsoidal harmonic functions to solve the potential problem.

REFERENCES

[1] Bourgeois, B., *et al.*, "ARLETT: a prototype 3-component frequency-em system for efficient downhole mineral exploration," in *Three-Dimensional Electromagnetics*, SEG, 1998, to be published.

[2] Angell, T. S., and R. E. Kleinman, "Polarizability tensors in low-frequency inverse scattering," *Radio Science*, **vol. 22**, no. 7, Dec. 1987, pp. 1120-1126.

[3] Habashy, T. M., *et al.*, "Beyond the Born and Rytov approximations: a nonlinear approach to electromagnetic scattering," *J. Geophys. Res.*, **vol. 98**, no. B2, Feb. 1993, pp. 1759-1775.

[4] Kaufman, A. A., and G. V. Keller, *Inductive Mining Prospecting*, Elsevier, Amsterdam, 1985.

[5] Dassios, G.*, et al*., "Scattering theorems for complete dyadic fields," *Int. J. Engng. Sci.*, **vol. 33**, no. 2, 1995, pp. 269-277.

[6] Dassios, G., and G. Kamvyssas, "The impedance scattering problem for a point source field: The small resistive sphere," *Q. J. Mech. appl. Math.,* **vol. 50** , Pt. 2, 1997, pp. 321-332.

ACKNOWLEDGEMENTS

Experimental data are courtesy of B. Bourgeois, BRGM, DR-GIG Orleans. Exact scattered field calculations have been carried out with a code provided by T. Habashy, Schlumberger-Doll Research, Ridgefield. The support of a BRGM research contract and of Action Intégrée Franco-Hellénique Platon 97 is acknowledged.

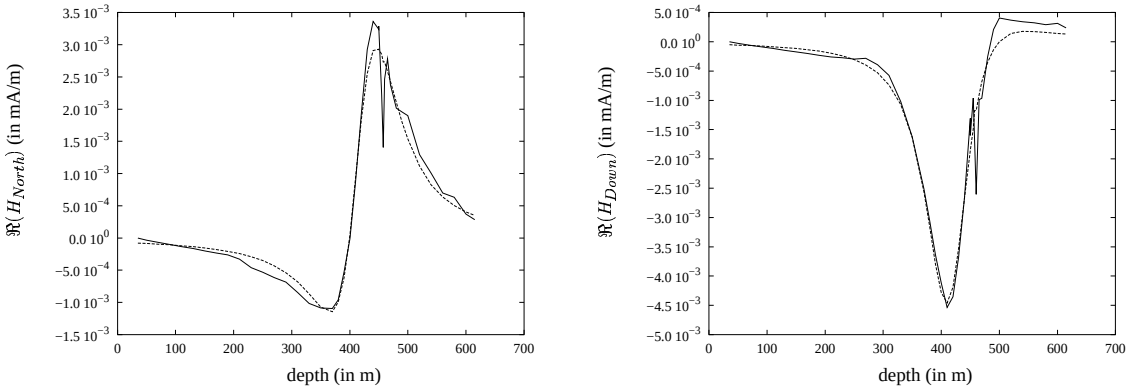

Figure 1: *The reduced magnetic field (solid line) and the magnetic field (broken line) created by the two equivalent electric and magnetic dipoles at same location found by optimization at 140 Hz in air.*

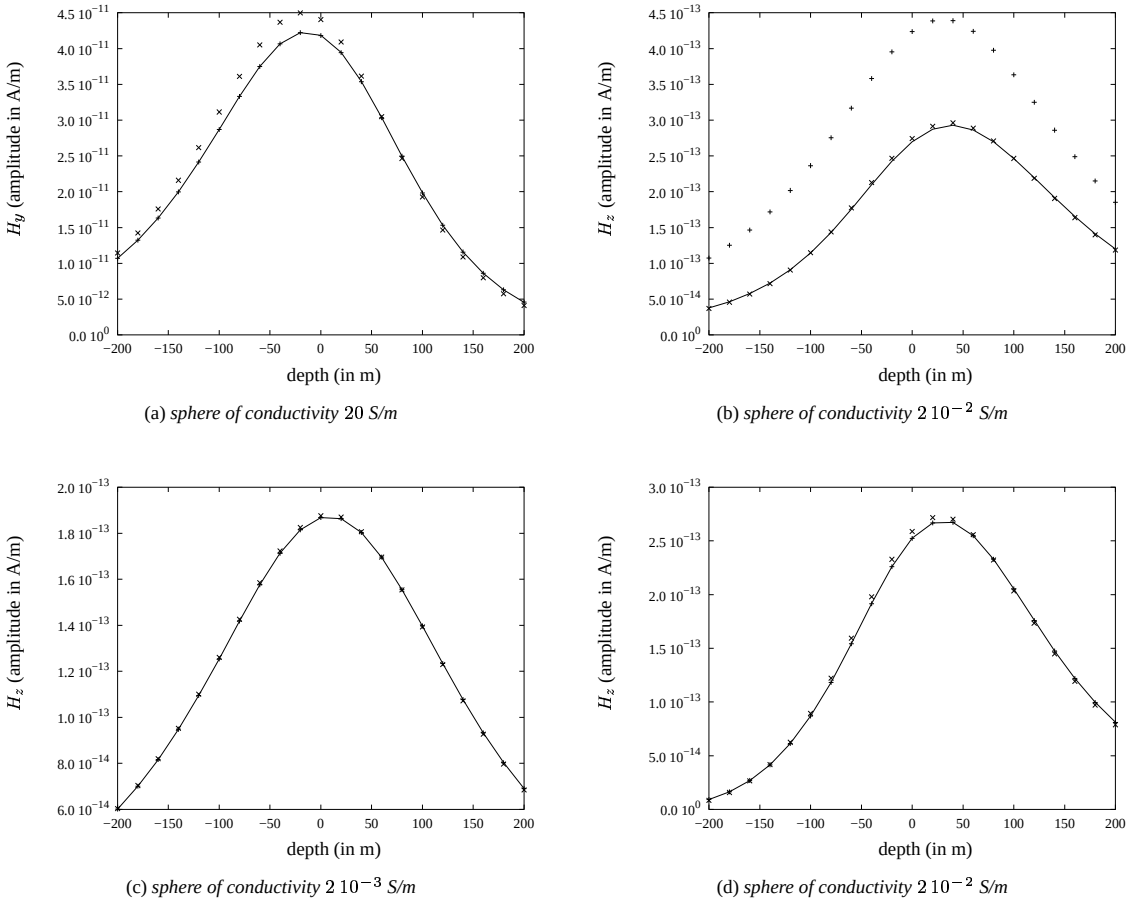

(a) *sphere of conductivity* 20 *S/m*

(b) *sphere of conductivity* $2\,10^{-2}$ *S/m*

(c) *sphere of conductivity* $2\,10^{-3}$ *S/m*

(d) *sphere of conductivity* $2\,10^{-2}$ *S/m*

Figure 2: *The field (solid line) scattered by a conductive sphere (radius 50 m) illuminated by a VMD of unit amplitude, is compared to the fields created by the three equivalent dipoles given by the theory of [4] (×) and found by inversion (+) at 100 Hz, in a homogeneous conductive medium (2 10^{-4} S/m). For figures 2(a) to 2(c) the VMD is situated at $x = -200$ m, $y = 0$ m, $z = 200$ m, and at $x = 141.42$ m, $y = 0$ m, $z = 244.95$ m for figure 2(d). The probing line is a vertical line at $x = 141.42$ m and $y = 141.42$ m, with depth from -200 m to 200 m.*

Bibliographie

[Abubakar et van den Berg, 2000] Abubakar, A. et van den Berg, P. M. (2000). Three-dimensional inverse scattering applied to cross-well induction sensors. *IEEE Trans. Geosci. Remote Sensing*, 38, 1669–1681.

[Abubakar et van den Berg, 2001] Abubakar, A. et van den Berg, P. M. (2001). Total variation as a multiplicative constraint for solving inverse problems. *IEEE Trans. Image Processing*, 10, 1384–1392.

[Angell et Kleinman, 1987] Angell, T. S. et Kleinman, R. E. (1987). Polarizability tensors in low-frequency inverse scattering. *Radio Sci.*, 22, 1120–1126.

[Angell et Kleinman, 1997] Angell, T. S. et Kleinman, R. E. (1997). Radiation condition and uniqueness. Rapport technique 97-2, Center for the Mathematics of Waves, University of Delaware.

[Angell *et al.*, 1996] Angell, T. S., Kleinman, R. E., Rozier, C., et Lesselier, D. (1996). Uniqueness and complete families for an acoustic wave guide problem. Rapport technique 96-4, Center for the Mathematics of Waves, University of Delaware.

[Belkebir et Tijhuis, 1996] Belkebir, K. et Tijhuis, A. G. (1996). Using multiple frequency information in the iterative solution of a two-dimensional nonlinear inverse problem. Dans *Proc. Progress In Electromagnetic Research Symposium*, p 353.

[Bertero et Pike, 1991] Bertero, M. et Pike, E. R., éditeurs (1991). *Inverse Problems in Scattering and Imaging*. Malvern Physics. Adam Hilger.

[Bonnard *et al.*, 1998] Bonnard, S., Vincent, P., et Saillard, M. (1998). Cross-borehole inverse scattering using a boundary finite-element method. *Inverse Problems*, 14, 521–534.

[Bonnard *et al.*, 1999] Bonnard, S., Vincent, P., et Saillard, M. (1999). Improved inverse scattering for dielectric homogeneous cylinders. *J. Opt. A : Pure Appl. Opt.*, 1, 566–572.

[Bonnet, 1999] Bonnet, M., éditeur (1999). *Problèmes Inverses : de l'Expérimentation à la Modélisation*, volume 22 de *Arago*. Observatoire Français des Techniques Avancées (OFTA), tec & doc édition.

[Borup *et al.*, 1987] Borup, D. T., Sullivan, D. M., et Gandhi, O. P. (1987). Comparison of the FFT conjugate gradient method and the finite-difference time-domain method for the 2-D absorption problem. *IEEE Trans. Microwave Theory Tech.*, 35, 383–395.

[Bourgeois et Alayrac, 1999] Bourgeois, B. et Alayrac, C. (1999). The borehole slingram method in mineral exploration using the SlimBoris system. Dans *Proc. 61st Eur. Assoc. Geosci. Eng. Meeting*, Helsinki.

[Bowler, 1994] Bowler, J. R. (1994). Eddy-current interaction with an ideal crack. i. the forward problem. *J. Appl. Phys.*, 75, 8128–8137.

[Buchanan *et al.*, 2000] Buchanan, J. L., Gilbert, R. P., Wirgin, A., et Xu, Y. S. (2000). Identification, by the intersecting canonical domain method, of the size, shape and depth of a soft body of revolution located within an acoustic waveguide. *Inverse Problems*, 16.

[Carrion et Boehm, 1994] Carrion, P. et Boehm, G. (1994). Tomographic imaging of opaque and low-contrast objects in range-independent waveguides. *J. Acoust. Soc. Am.*, 91, 1440–1446.

[Chew, 1995] Chew, W. C. (1995). *Waves and Fields in Inhomogeneous Media*. Electromagnetic waves. IEEE Press, New-York.

[Chiu et Kiang, 1991] Chiu, C.-C. et Kiang, Y.-W. (1991). Inverse scattering of a buried conducting cylinder. *Inverse Problems*, 7, 187–202.

[Chiu et Kiang, 1992] Chiu, C.-C. et Kiang, Y.-W. (1992). Image reconstruction for an imperfectly conducting cylinder buried in a half-space. *J. Electromagn. Waves Appli.*, 6, 1413–1431.

[Collins et Kuperman, 1994] Collins, M. D. et Kuperman, W. A. (1994). Inverse problems in ocean acoustics. *Inverse Problems*, 10, 1023–1040.

[Cuer et Zolésio, 1988] Cuer, M. et Zolésio, J.-P. (1988). Control of singular problem via differentiation of a min-max. *Systems Control Lett.*, 11, 151–158.

[Das et Mc Fee, 1991] Das, Y. et Mc Fee, J. (1991). A simple analysis of the electromagnetic response of buried conducting objects. *IEEE Trans. Geosci. Remote Sensing*, 29, 343–344.

[Das *et al.*, 1990] Das, Y., Mc Fee, J., Toews, J., et Stuart, G. (1990). Analysis of an electromagnetic induction detector for real-time location of buried objects. *IEEE Trans. Geosci. Remote Sensing*, 28, 278–288.

[Dassios et Kleinman, 2000] Dassios, G. et Kleinman, R. E. (2000). *Low Frequency Scattering*. Oxford University Press, Oxford.

[Ellis et Peden, 1995] Ellis, G. A. et Peden, I. C. (1995). An analysis technique for buried inhomogeneous dielectric object in the presence of an air-earth interface. *IEEE Trans. Geosci. Remote Sensing*, 33, 535–540.

[Gan et Chew, 1995] Gan, H. et Chew, W. C. (1995). A discrete BCG-FFT algorithm for solving 3D inhomogeneous scatterer problems. *J. Electromagn. Waves Appli.*, 9, 1339–1357.

[Gilbert *et al.*, 1998] Gilbert, R. P., Scotti, T., Wirgin, A., et Xu, Y. S. (1998). The unidentified object problem in a shallow ocean. *J. Acoust. Soc. Am.*, 103, 1320–1328.

[Golub *et al.*, 1979] Golub, G. H., Heath, M., et Wahba, G. (1979). Generalized cross-validation as a method for choosing a good ridge parameter. *Technometrics*, 21, 215–223.

[Gosh Roy *et al.*, 1997] Gosh Roy, D. N., Couchman, L., et Warner, J. (1997). Scattering and inverse scattering of sound-hard obstacles via shape deformation. *Inverse Problems*, 13, 585–606.

[Guicking *et al.*, 1998] Guicking, D., Gork, K., et Peine, H. (1998). Classification of underwater objects using resonance scattering and neural networks. Dans Alippi, A. et Cannelli, G. B., éditeurs, *Underwater Acoustics*, pp 567–570, Rome. CNR-IDAC.

[Habashy *et al.*, 1993] Habashy, T. M., Groom, R., et Spies, B. (1993). Beyond the Born and Rytov approximations : a nonlinear approach to electromagnetic scattering. *J. Geophys. Res*, 98, 1759–1775.

[Hansen, 1992] Hansen, P. C. (1992). Numerical tools for analysis and solution of Fredholm integral equations of the first kind. *Inverse Problems*, 8, 849–872.

[Hansen et O'Leary, 1993] Hansen, P. C. et O'Leary, D. P. P. (1993). The use of the L-curve in the regularization of discrete ill-posed problems. *SIAM J. Sci. Comput.*, 14, 1487–1503.

[Harrington, 1989] Harrington, R. F. (1989). Boundary integral formulations for homogeneous material bodies. *J. Electromagn. Waves Applic.*, 3, 1–15.

[Jin *et al.*, 1988] Jin, J. M., Liepa, V. V., et Tai, C. T. (1988). A volume-surface integral equation for electromagnetic scattering by inhomogeneous cylinders. *J. Electromagn. Waves Applic.*, 2, 573–588.

[Joachimowicz et Pichot, 1990] Joachimowicz, N. et Pichot, C. (1990). Comparison of three integral formulations for the 2-D TE scattering problem. *IEEE Trans. Microwave Theory Tech.*, 38, 178–185.

[Kaufman et Keller, 1985] Kaufman, A. et Keller, G. (1985). *Inductive Mining Prospecting*. Methods in Geochemistry and Geophysics. Elsevier, Amsterdam.

[Kleinman et Senior, 1987] Kleinman, R. E. et Senior, T. B. A. (1987). Rayleigh scattering. Dans Varadan, V. K. et Varadan, V. V., éditeurs, *Acoustic, Electromagnetic and Elastic Wave Scattering, Low and High Frequency Asymptotics*, pp 1–70, Amsterdam. Elsevier.

[Kleinman et van den Berg, 1992a] Kleinman, R. E. et van den Berg, P. M. (1992a). An extended range modified gradient technique for profile inversion. *Radio Sci.*, 29, 877–84.

[Kleinman et van den Berg, 1992b] Kleinman, R. E. et van den Berg, P. M. (1992b). A modified gradient method for two dimensional problems in tomography. *J. Comput. Appl. Math.*, 42, 17–35.

[Kong, 1986] Kong, J. A. (1986). *Electromagnetic Wave Theory*. John Wiley and Sons, New-york.

[Kottmann et Martin, 2000] Kottmann, J. P. et Martin, O. J. F. (2000). Accurate solution of the volume integral equation for high-permittivity scatterers. *IEEE Trans. Antennas Propagat.*, 48, 1719–1726.

[Lesselier et Duchêne, 1996] Lesselier, D. et Duchêne, B. (1996). Wavefield inversion of objects in stratified environments. From backpropagation schemes to full solutions. Dans Stone, W. R., éditeur, *Review of Radio Science 1993-1996*, pp 235–268. Oxford University Press, Oxford.

[Litman *et al.*, 1998] Litman, A., Lesselier, D., et Santosa, F. (1998). Reconstruction of a two-dimensional binary obstacle by controlled evolution of a level-set. *Inverse Problems*, 14, 685–706.

[Liu et Lamontagne, 1998] Liu, E. H. et Lamontagne, Y. (1998). Geophysical application of a new surface integral equation method for EM modeling. *Geophys.*, 63, 411–423.

[Liu et Lamontagne, 1999] Liu, E. H. et Lamontagne, Y. (1999). Electromagnetic modeling using surface integrale equations. Dans Oristaglio, M. L. et Spies, B. R., éditeurs, *Three-Dimensional Electromagnetics*, pp 76–89. Society of Exploration Geophysicists (SEG).

[Lixin *et al.*, 1995] Lixin, W., Kleinman, R. E., et van den Berg, P. M. (1995). Modified gradient profile inversion using H-polarized waves. Dans *Proc. IEEE Antennas and Propagation Society International Symposium*, volume 3, pp 1598–1601.

[Lobel *et al.*, 1997] Lobel, P., Blanc-Féraud, L., Pichot, C., et Barlaud, M. (1997). A new regularization scheme for inverse scattering. *Inverse Problems*, 13, 403–410.

[Maleki et Devaney, 1993] Maleki, M. H. et Devaney, A. J. (1993). Phase-retrieval and intensity-only reconstruction algorithms for optical diffraction tomography. *J. Opt. Soc. Am. A*, 10, 1086–1092.

[Maleki *et al.*, 1992] Maleki, M. H., Devaney, A. J., et Schatzberg, A. (1992). Tomographic reconstruction from optical scattered intensities. *J. Opt. Soc. Am. A*, 9, 1356–1363.

[Monebhurrun *et al.*, 1998] Monebhurrun, V., Duchêne, B., et Lesselier, D. (1998). 3-D inversion of eddy current data for nondestructive evaluation of steam generator tubes. *Inverse Problems*, 14, 707–724.

[Newman et Hohmann, 1988] Newman, G. A. et Hohmann, G. W. (1988). Transient electromagnetic responses of high contrast prisms in layered Earth. *Geophys.*, 16, 341–344.

[Peterson, 1988] Peterson, A. F. (1988). A comparison of integral, differential and hybrid methods for TE-wave scattering from inhomogeneous dielectric cylinder. *J. Electromagn. Waves Applic.*, 3, 87–106.

[Pincemin *et al.*, 1994] Pincemin, F., Sentenac, A., et Greffet, J.-J. (1994). Near field scattered by a dielectric rod below a metallic surface. *J. Opt. Soc. Am. A*, 11, 1117–1125.

[Rozier *et al.*, 1997] Rozier, C., Lesselier, D., Angell, T. S., et Kleinman, R. (1997). Shape retrieval of a cylindrical obstacle in shallow water from a single-frequency farfield using a complete family method. *Inverse Problems*, 13, 487–508.

[Ruosi *et al.*, 2000] Ruosi, A., Valentino, M., Pepe, G., Monebhurrun, V., Lesselier, D., et Duchêne, B. (2000). High Tc SQUIDs and eddy current NDE : a comprehensive investigation from real data to modeling. *Measurement Scie. Technol.*, 11, 1639–1648.

[Sabatier, 1987] Sabatier, P. C., éditeur (1987). *Inverse Problems : an Interdisciplinary Study*, volume 19 de *Advances in Electronics and Electron Physics*. Academic Press.

[Sabatier, 2000] Sabatier, P. C. (2000). Past and future of inverse problems. *J. Math. Phys.*, 41, 4082–4124.

[Saillard et Toso, 1997] Saillard, M. et Toso, G. (1997). Electromagnetic scattering from bounded or infinite subsurface bodies. *Radio Scie.*, 32, 1347–1360.

[Santosa, 1996] Santosa, F. (1996). A level-set approach for inverse problems involving obstacles. *ESAIM : Control, Optimisation and Calculus of Variations*, 1, 17–33.

[Sethian, 1999] Sethian, J. A. (1999). *Level Set Methods and Fast Marching Methods*. Cambridge University Press, Cambridge, 2nd édition.

[Sokolowski et Zolésio, 1992] Sokolowski, J. et Zolésio, J.-P. (1992). *Introduction to Shape Optimization. Shape Sensitivity Analysis*. Springer, Berlin.

[Souriau *et al.*, 1996] Souriau, L., Duchêne, B., et Lesselier, D. (1996). Modified approach to inverse scattering for binary objects in stratified media. *Inverse Problems*, 12, 463–81.

[Takagi *et al.*, 1995a] Takagi, T., Fukutomi, H., Hashimuoto, M., Yoshida, Y., Miya, K., Tsuboi, H., Harada, Y., et Shimone, J. (1995a). Ect research activities in JSAEM – benchmark models of eddy current testing for steam generator tube part 1. Dans Collins, R., Dover, W. D., Bowler, J. R., et Miya, K., éditeurs, *Nondestructive Testing of Materials*, pp 253–264. IOS Press, Amsterdam.

[Takagi *et al.*, 1995b] Takagi, T., Fukutomi, H., Hashimuoto, M., Yoshida, Y., Miya, K., Tsuboi, H., Harada, Y., et Shimone, J. (1995b). Ect research activities in JSAEM – benchmark models of eddy current testing for steam generator tube part 2. Dans Collins, R., Dover, W. D., Bowler, J. R., et Miya, K., éditeurs, *Nondestructive Testing of Materials*, pp 313–320. IOS Press, Amsterdam.

[Takenata *et al.*, 1997] Takenata, T., Wall, D. J. N., Harada, H., et Tanaka, M. (1997). Reconstruction algorithm of the refractive index of cylindrical object from the intensity measurements of the total field. *Microwave Opt. Technol. Lett.*, 14, 182–188.

[van den Berg et Kleinman, 1995] van den Berg, P. M. et Kleinman, R. E. (1995). A total variation enhanced modified gradient algorithm for profile reconstruction. *Inverse Problems*, 11, L5–L10.

[van den Berg et Kleinman, 1997a] van den Berg, P. M. et Kleinman, R. E. (1997a). A contrast source inversion method. *Inverse Problems*, 13, 1607–1620.

[van den Berg et Kleinman, 1997b] van den Berg, P. M. et Kleinman, R. E. (1997b). Gradient methods in inverse acoustic and electromagnetic scattering. Dans Chavent, G. et Sabatier, P. C., éditeurs, *Large-Scale Optimization with Applications*, pp 143–158. Berlin : Springer.

[van den Berg *et al.*, 1999] van den Berg, P. M., Van Broekhoven, A. L., et Abubakar, A. (1999). Extended contrast source inversion. *Inverse Problems*, 15, 1325–1344.

[Wannamaker *et al.*, 1984] Wannamaker, P. E., Hohmann, G. W., et San Filipo, W. A. (1984). Electromagnetic modeling of three-dimensional bodies in layered Earths using integral equation. *Geophys.*, 49, 60–74.

[Wilton, 1992] Wilton, D. R. (1992). Review of current status and trends in the use of integral equations in computational electromagnetics. *Electromagnetics*, 12, 287–341.

[Wirgin et Scotti, 1998] Wirgin, A. et Scotti, T. D. (1998). Complete family of functions methods, based on the Rayleigh hypothesis and on the extinction theorem, for inverse acoustic wave scattering problems. *ACUSTICA - acta acustica*, 84, 1083–1090.

[Xiong et Tripp, 1995] Xiong, Z. et Tripp, A. C. (1995). Electromagnetic scattering of large structures in layered Earths using integral equations. *Radio Sci.*, 30, 921–929.

[Xiong et Tripp, 1997] Xiong, Z. et Tripp, A. C. (1997). 3-D electromagnetic modeling for near-surface targets using integral equations. *Geophys.*, 62, 1097–1106.

[Xu et Yan, 1993a] Xu, X. B. et Yan, W. (1993a). A hybrid integral equation solution of scattering of TE excitation by inhomogeneous cylinder near a medium interface. *J. Electromagn. Waves Applic.*, 7, 919–942.

[Xu et Yan, 1993b] Xu, X. B. et Yan, W. (1993b). Modification of hybrid integral equation for determining scattering by an inhomogeneous cylinder of discontinous electromagnetic parameters near a media interface. *J. Electromagn. Waves Applic.*, 7, 1389–1394.

[Yang et Yates, 1994] Yang, T. C. et Yates, T. W. (1994). Scattering from an object in a stratified medium. II extraction of scattering signature. *J. Acoust. Soc. Am.*, 96, 1020–1031.

[Yoshida et Bowler, 2000] Yoshida, Y. et Bowler, J. R. (2000). Vector potential integral formulation for eddy-current probe response to cracks. *IEEE Trans. Magn.*, 36, 461–469.

[Zhdanov et Hursan, 2000] Zhdanov, M. et Hursan, G. (2000). 3-D electromagnetic inversion based on quasi-analytical approximation. *Inverse Problems*, 16, 1297–1322.

[Zhdanov et Fang, 1996] Zhdanov, M. S. et Fang, S. (1996). Quasi-linear approximation in 3-D electromagnetic modeling. *Geophys.*, 61, 646–665.

[Zwamborn et van den Berg, 1991] Zwamborn, P. et van den Berg, P. M. (1991). A weak form of the conjugate gradient FFT method for two-dimensional TE scattering problems. *IEEE Trans. Microwave Theory Tech.*, 39, 953–960.

[Zwamborn et van den Berg, 1992] Zwamborn, P. et van den Berg, P. M. (1992). The three-dimensional weak form of the conjugate gradient FFT method for solving scattering problems. *IEEE Trans. Microwave Theory Tech.*, 40, 1737–1766.

Table des matières